UNIVERSITY OF CALIFORNIA, SAN DIEGO

Imaging the Oceanic Crust with Broadband Seismic and Pressure Data

A dissertation submitted in partial satisfaction of the
requirements for the degree
Doctor of Philosophy

in

Earth Sciences

by

Adrian K. Doran

Committee in charge:

Professor Gabi Laske, Chair
Professor Li-Tien Cheng
Professor LeRoy Dorman
Professor Alistair Harding
Professor Peter Shearer

2019

The dissertation of Adrian K. Doran is approved, and it is acceptable in quality and form for publication on microfilm and electronically:

_____

_____

_____

_____

_____

Chair

University of California, San Diego

2019

DEDICATION

For Princess Sunflower

EPIGRAPH

When you have eliminated the impossible, whatever remains,

however improbable, must be the truth.

– Sherlock Holmes

TABLE OF CONTENTS

LIST OF FIGURES

LIST OF TABLES

ACKNOWLEDGEMENTS

First and foremost I would like to thank Gabi for giving me the opportunity of a lifetime. I received the good news that I was accepted into the IGPP doctorate program while working the night shift on an oil exploration rig in Stratford, New Zealand. That moment marked the beginning of an incredible opportunity here at SIO that has profoundly influenced my life for the better. Gabi has taught me innumerable things throughout my PhD, and I am grateful for the help she has given me. I would also like to thank the rest of my thesis committee, Alistair Harding, Peter Shearer, LeRoy Dorman, and Li-Tien Cheng, for making time and providing guidance over the past years.

I am also thankful for the tremendous support network of individuals here at SIO and IGPP. I have spent time with too many people at SIO to list here, but they have all contributed meaningfully to my experience. I would especially like to thank my first year cohort (Matt Cook, John DeSanto, Dara Goldberg, Jessie Saunders, Wei Wang, and Yongfei Wang) and my Barnyard officemates (Bei Zhang, Katia Tymofyeyeva, Wes Neely, Wenyuan Fan, Dallas Sherman, and honorary members Nick Lau and Susheel Adusumilli) for the support through easy and tough times. The SIO Basketball League has been another tremendous source of joy for me.

Scripps has provided incredible opportunities to grow personally and professionally. I have been involved with a number of projects outside my direct research that aided my development as a scientist. Thanks to Kerry Key for inviting me on an EM research cruise in Alaska, thanks to Kerry, Steve Constable, Adrian Borsa, and Jessie for helping to organize the Silver Lake geophysical field project, thanks to Jeff Gee and Sarah Maher for including me on the Pito Deep cruise, thanks to Gabi for including me in the Glacier de la Plaine Morte seismic experiment, and special thanks to Gabi, Martin Rapa, Sean McPeak, Mark Gibaud, Ernie Aaron, and the rest of the SIO OBS lab for the hours and hours of help with the research cruises we undertook offshore San Diego. I would also like to acknowledge funding from the UC Ship Funds program, the IGPP Paul G. Silver Research Enhancement Award program, the SIO Shepard

Funds, and the Chateaubriand Fellowship, all of which enabled exciting research opportunities. For the Chateaubriand Fellowship, I appreciate the mentorship and assistance of Wayne Crawford and others at IPGP, particularly Javier Escartìn and visiting scholar Paul Johnson.

I have also had the opportunity to gain valuable teaching experience while at SIO. Thanks to Dave Stegman, Dave Sandwell, Helen Fricker, Guy Masters, and Steve Constable for the encouragement while TAing. Thanks to Debi Kilb for years of guidance and for getting me involved with the Sally Ride Science Summer Program. Special thanks to Anne Pommier for the hours of help while I taught SIO 001: The Planets during the summer of 2018. Anne provided consistent support and encouragement that I greatly appreciated. Peter Shearer also provided valuable assistance during this class.

Finally, a PhD is made significantly easier through the support and love of family and friends. I appreciated the good times to be found at the Soft Loft and at the Ladies Venue, as well as my reliable chauffeurs, Drs. R. Nick Tuttle and Dara E. Goldberg. I am thankful to Clint Coon, who provided consistent friendship at SIO, and to Zhigang Peng of Georgia Tech, without whom my entire endeavor in seismology would not have been possible. I am also thankful to the numerous people I have not listed here but whom undoubtedly deserve praise and thanks. Finally, and most importantly, I am infinitely grateful to my wife Dr. Rev. Elizabeth L. Howland, as well as my sister Dana, my parents, and my extended family, who have all surrounded me with love throughout my life. I am an immeasurably fortunate individual.

Chapter 2, in full, is a reformatted version of a publication in Bulletin of the Seismological Society of America: Doran, A.K., and G. Laske (2017), Ocean-bottom seismometer instrument orientations via automated Rayleigh-wave arrival angle measurements, Bull. Seism. Soc. Am. 107, 691-708. DOI: 10.1785/0120160165. I was the primary investigator and author of this paper.

Chapter 3, in full, is a reformatted version of material that has been accepted for pub-

lication in the Journal of Geophysical Research: Doran, A.K., and G. Laske (2019), Seismic structure of marine sediments and upper oceanic crust surrounding Hawaii. I was the primary investigator and author of this paper.

Chapter 4 describes unpublished measurements and analysis of surface wave dispersion using ambient noise correlations between PLUME OBS sites. This work was undertaken in collaboration with Gabi Laske. I was the primary investigator and author of this project.

Chapter 5, in full, is a reformatted version of a publication in Journal of Geophysical Research: Doran, A.K., and G. Laske (2016), Infragravity waves and horizontal seafloor compliance, J. Geophys. Res. 121, 260-278, DOI: 10.1002/2015JB012511. I was the primary investigator and author of this paper, which describes our attempts to measure and analyze horizontal seafloor compliance data.

Chapter 6 describes my work modeling the temporal evolution of crustal structure beneath Axial Volcano using seafloor compliance data. This work was undertaken in collaboration with Wayne Crawford. I was the primary investigator and author of this project, which is currently in preparation for journal submission.

Chapter 7 includes concluding remarks and ideas for future work.

Appendix A contains details from two student-led cruises occurring in 2015 and 2018. I was the chief scientist on these cruises. This work was done in collaboration with Gabi Laske, Martin Rapa, and Jeff Babcock.

Appendix B contains details of modeling I performed as part of an experiment analyzing high-frequency surface wave phase velocities measured on an alpine glacier. The appendix also includes a reformatted version of the resulting publication in the Annals of Glaciology: Lindner, F., and Laske, G., and Walter, F., and A.K. Doran (2018), Crevasse-induced Rayleigh wave azimuthal anistropy on Glacier de la Plaine Morte, Swizterland, Ann. Glaciol., DOI: 10.1017/aog.2018.25.

Appendix C has notes from my research that didn't make it into any specific chapters

but may be of use to future students. It contains a compilation of parameter scaling relationships in the oceanic crust and sediments, as well as observations of changes in OBS tilt that occurred during the PLUME deployment.

VITA

2019	Ph.D. in Earth Sciences, University of California, San Diego
2013-2019	Research Assistant, University of California, San Diego
2018	Associate-In Lecturer, University of California, San Diego
2016-2019	Teaching Assistant, University of California, San Diego
2014	M.Sc. in Earth Sciences, University of California, San Diego
2012-2013	Surface Logging Geologist, Schlumberger Limited, New Plymouth, NZ
2011-2012	Seismic Field Engineer, Institute of Earth Science and Engineering, Auckland, NZ
2011	B. A. in Earth Sciences and Physics with Honors, Dartmouth College

PUBLICATIONS

Doran, A.K. and G. Laske (2019), "Seismic structure of marine sediments and upper oceanic crust surrounding Hawaii", *Journal of Geophysical Research*, doi: 10.1029/2018JB016548. *Accepted*.

Lindner, F. and G. Laske and F. Walter and A.K. Doran (2018), "Crevasse-induced Rayleigh-wave azimuthal anisotropy on Glacier de la Plaine Morte, Switzerland", *Annals of Glaciology*, 1-16, doi: 10.1017/aog.2018.25.

Doran, A.K. and G. Laske (2017), "Ocean-bottom seismometer instrument orientations via automated Rayleigh-wave arrival angle measurements", *Bulletin of the Seismological Society of America*, 107, 691-708, doi: 10.1785/0120160165.

Doran, A.K. and G. Laske (2016), "Infragravity waves and horizontal seafloor compliance", *Journal of Geophysical Research*, 121, 260-278, doi: 10.1002/2015JB012511.

ABSTRACT OF THE DISSERTATION

Imaging the Oceanic Crust with Broadband Seismic and Pressure Data

by

Adrian K. Doran

Doctor of Philosophy in Earth Sciences

University of California, San Diego, 2019

Professor Gabi Laske, Chair

The oceanic crust, the uppermost layer of the rigid oceanic lithosphere, has a well defined general architecture, but the magnitude and wavelength of heterogeneities in crustal structure remain poorly observed in detail. In this thesis, I have characterized the seismic structure of the marine sediments and crust surrounding the Hawaiian islands. I primarily analyzed seafloor compliance data, the deformation of the seafloor in response to infragravity wave loading. These long-period (50+ seconds) measurements are estimated from broadband ocean-bottom seismic data and are sensitive to the elastic structure of oceanic sediments and crust, particularly shear-velocity structure. I produced a map of sediment thickness and shear velocity, which includes high-velocity volcanic sediments and low-velocity pelagic sediments. I then used surface wave

dispersion data to constrain the structure of the lower crust and the uppermost mantle beneath the Hawaiian Islands. Initial results indicate that the uppermost mantle may exhibit variations in shear velocity on the order of several percent. These variations could be explained through a combination of thermal anomalies and partial melting.

Another focus of this thesis is the analysis of seafloor compliance data as a function of time to investigate melt content in the lower crust before and after the submarine eruption of 2015 at Axial Volcano. I found that Vs dropped dramatically following the eruption and took several years to recover to pre-eruption levels. The changes can be explained by variations in the geometry of melt. The station distribution also allowed me to constrain the lateral extent of the variations to within several hundred meters of the center of the caldera.

In the course of these studies, I developed tools and theory to improve OBS data quality. I wrote automated software to determine the orientation of horizontal seismometer components using surface wave arrival angles, and spent considerable time characterizing the long-period response of differential pressure gauges. Finally, I demonstrated the viability of measuring horizontal seafloor compliance, although I was limited in my geologic interpretations due to instrument response issues and data quantity.

The techniques and results developed in this thesis should provide insight into the dynamics of the oceanic lithosphere, including the mechanics of intraplate plumes and crustal accretion. These results will become more valuable as OBS instrumentation progresses and expands data coverage into the furthest reaches of the world's oceans.

1 Introduction

1.1 The Oceanic Crust

The lithosphere is the rigid outermost shell of the Earth that comprises the Earth's tectonic plates. Oceanic lithosphere, approximately 100 km thick beneath most of the world's oceans, is constantly being created at seafloor spreading centers, as the plates diverge and hot mantle rock ascends to the surface and freezes, and destroyed in subduction zones, where the lithosphere plunges deeper into the mantle. The classical model of the oceanic crust, the uppermost layer of the oceanic lithosphere, contains three layers and averages 6-7 kilometers thick. Layer 1 is composed primarily of unconsolidated sediments and can vary in thickness from tens to thousands of meters. Layer 2, often subdivided into Layers 2A and 2B, is composed of pillow basalts overlying sheeted dikes and is typically 1.5 km thick. Layer 3 is comprised of gabbros and cumulates and usually estimated at 4.5 km in thickness. This model was first proposed by Raitt (1963), and has been subsequently refined but not significantly altered (Fig. 1). These layers were originally associated with distinct seismic velocities and later identified compositionally. Inadequacies of this model have long been recognized (Spudich and Orcutt, 1980a), but this simplified one-dimensional assumption for the oceanic crust continues to be used in many tomographic investigations that analyze data sensitive to deeper structures, including surface waves, free oscillations, and long-period body waves. Uncertainties in crustal structure can limit the resolution of seismic analyses at all scales (e.g., Dahlen and Tromp, 1998).

Despite covering the majority of the Earth's surface, the nature of heterogeneity in the oceanic crust remains poorly documented. Strong variations in nearly all crustal properties have been reported. A summary of seismic refraction studies revealed oceanic crustal thicknesses ranging from 2 to 37 kilometers (Mutter and Mutter, 1993). Density (ρ), compressional velocity (Vp), shear velocity (Vs), anisotropy, and attenuation profiles all show regional differences as well, due primarily to thermal and compositional differences and often related to the crustal age (e.g., Orcutt, 1987; Swift and Stephen, 1989; Carlson, 1998). The most dramatic variations are

seen in marine sedimentary layers. Previous studies of pelagic sediments throughout the deep Pacific (>2 km water depth) have yielded a wide range of shear velocity estimates (e.g., Bratt and Solomon, 1984; Bromirski et al., 1992). Hamilton (1979a) made *in situ* measurements of sedimentary V_p/V_s ratios and found values ranging from 1.7 to over 13. Dorman (1997) reviewed the wide ranges for all sedimentary physical parameters, noting that V_s is much more variable and difficult to measure than V_p.

Uncertainties about the elastic structure of the crust can have far-reaching consequences. Seismicity locations, dependent on accurate three-dimensional velocity models, may be biased by overly simplistic assumptions about the crust. Inaccurate crustal structure may also affect seismic imaging results of deeper structure, particularly the uppermost mantle. The sensitivity of even long-period seismic data to near-surface structure is well documented, as are the nonlinear effects of strong lateral variations in crustal structure (e.g., Montagner and Jobert, 1988; Marone and Romanowicz, 2007). This effect is not limited to seismic tomography. Interpretations of many geophysical observables, including gravity data (e.g., Basuyau et al., 2013; Herceg et al., 2016) and heat flow measurements (e.g., von Herzen et al., 1989), can be biased by inaccurate assumptions about the crust.

In order to characterize the oceanic crust, I analyzed seafloor acceleration and pressure data. These data are collected using ocean-bottom seismometers (OBSs), which typically include three-component seismometers and differential-pressure gauges (DPGs; Cox et al., 1984). In the following chapters I will focus on broadband OBSs, with flat velocity response to periods of 120 seconds or longer. Figure 1.2 displays the median hourly vertical acceleration (LHZ) and pressure (DPG) spectra at OBS site PL37, which is located southwest of Hawaii at 4676 meters of water depth and deployed as during PLUME (Plume-Lithosphere Undersea Mantle Experiment ; Laske et al. (2009)) . Only frequencies of 0.5 Hz and less are shown; at higher frequencies, marine mammals, local earthquakes, anthropogenic activities, and weather and ocean-atmospheric interactions are the primary influences (Wilcock et al., 2014; Berger et al., 2018).

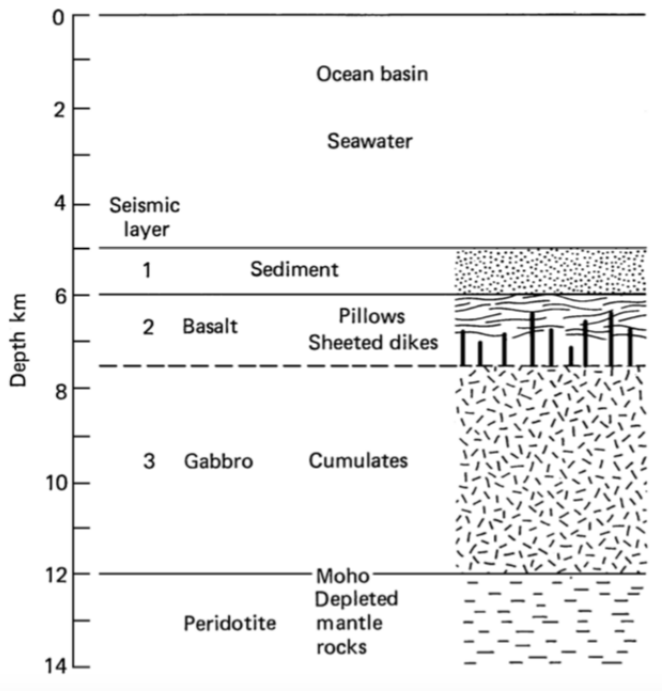

Figure 1.1: Typical structure of oceanic crust from Turcotte and Schubert (2002, 2014).

The major structures of the ambient noise spectrum are visible (see: Webb, 1998). Most of the analysis in this dissertation will focus on the infragravity band, encompassing frequencies between 1 and 33 mHz (periods between 30 and 1000 seconds).

1.2 Infragravity Waves & Seafloor Compliance

Energy from oceanic infragravity waves dominates the long-period power spectra of broadband ocean-bottom seismometers and DPGs. Infragravity waves in the deep ocean have small wave heights ($\leq$ 1cm), long wavelengths (1-20 km), long periods (30-300 s), high phase velocities ($>$ 100 m/s in 2 km water depth), and propagate great distances over the ocean while experiencing minimal attenuation (e.g., Webb, 1998; Yang et al., 2012). Observations were first made near the coast (Munk, 1949; Tucker, 1950) but infragravity energy is now routinely observed in the open ocean as well (Webb et al., 1991; Godin et al., 2013). The mechanism of infragravity wave generation remains a target of intense study. Significant correlation has been

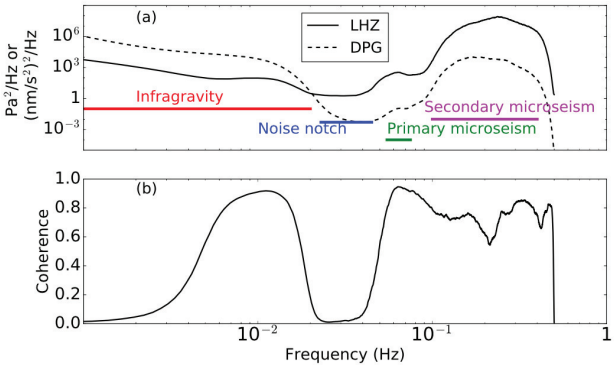

Figure 1.2: (a) Median hourly vertical acceleration (LHZ) and pressure (DPG) spectra at OBS site PL37, located southwest of Hawaii at 4676 meters water depth. Significant features of the spectrum are labeled (see Webb, 1998). The acceleration data were corrected for instrument tilt following Bell et al. (2015a). (b) Coherence between the DPG and tilt-corrected LHZ signals.

reported between infragravity waves and local short period wind and swell waves (e.g., Herbers et al., 1995a; Ardhuin et al., 2014). Consensus is slowly building that infragravity waves are formed by nonlinear interactions of short-period ocean waves in the near-shore environment that either become trapped on the continental shelf or leak outwards into the deep ocean (e.g., Herbers et al., 1995b; Webb, 1998; Rhie and Romanowicz, 2006; Aucan and Ardhuin, 2013; Ardhuin et al., 2014; Godin et al., 2014; Crawford et al., 2015).

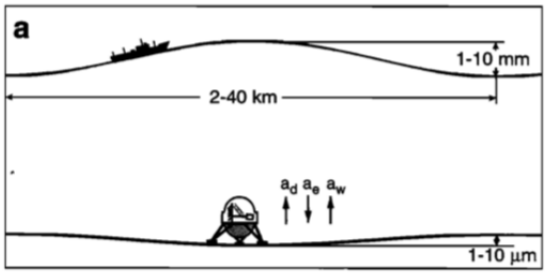

Figure 1.3: A cartoon showing the seafloor compliance measurement from Crawford et al. (1998). In addition to the compliance acceleration (a_d), the sensor measures acceleration terms due to the changing water column (a_w) and the changing relative position of the center of mass of the Earth (a_e). These terms must be removed to accurately measure compliance data.

Seafloor compliance measurements provide a way to resolve crustal structure at depths between 0-6+ kilometers, a much shallower range than most other broadband teleseismic methods. Long-period (>30 s) oceanic infragravity waves stress and displace the seafloor, and the

displacement is a function of the water depth, the frequency of the waves, and the elastic parameters of the underlying sediment and crust (Fig. 1.3). Seafloor compliance, the transfer function between seafloor displacement and stress, was first developed by Crawford et al. (1991), who demonstrated the strong dependence of the measurements on shear velocity and the sensitivity of different frequencies to structure at different depths. Subsequent research has often focused on characterizing zones of low shear velocities, including partial melt zones at spreading centers (e.g., Crawford et al., 1998, 1999; Iassonov and Crawford, 2008), large sedimentary units (e.g., Crawford and Singh, 2008), and fluid and gas intrusions (e.g., Willoughby and Edwards, 2000; Willoughby et al., 2008).

The seafloor pressure at a water depth H caused by a surface gravity wave of height ζ is given by

$$P_{bottom} = \frac{\rho g \zeta}{\cosh(kH)} \simeq P_{surface} e^{-kH} \tag{1.1}$$

where k is the wave number, ρ is the water density and g is the gravitational acceleration (e.g., Dolenc et al., 2005). Infragravity waves are freely propagating surface gravity waves (Webb et al., 1991), and the frequency and wavenumber are related through the dispersion relation (Apel, 1987)

$$\omega^2 = gk \tanh(kH) \tag{1.2}$$

where ω is the angular frequency of the wave. The water depth controls the maximum frequency to which either horizontal or vertical coherence in the infragravity frequency band can be analyzed (Crawford et al., 1991). The ground deformation is a function of the underlying elastic structure. An analytic normalized compliance expression (the ratio of deformation to vertical stress, ξ, normalized by the wavenumber) can be derived for an isotropic elastic half-space (Crawford, 2004):

$$\eta = k\xi = k\frac{\mathbf{u}}{\tau_{zz}} = k\frac{u_x\hat{x} + u_z\hat{z}}{\tau_{zz}} = \frac{-i}{2(\lambda+\mu)}\hat{x} + \frac{\lambda+2\mu}{2\mu(\lambda+\mu)}\hat{z} \tag{1.3}$$

where $\mathbf{u}$ is the displacement, τ_{zz} is the vertical stress, and λ and μ are the Lamé parameters. Displacement is expected in both the vertical and horizontal directions, but all studies currently focus on vertical compliance due to both an intrinsically higher-amplitude signal and high noise at long periods on OBS horizontal components. Vertical compliance can be rewritten as a function of seismic velocities:

$$\eta_Z = k\xi_Z = \frac{\lambda+2\mu}{2\mu(\lambda+\mu)} = \frac{V_p^2}{2\rho V_s^2(V_p^2 - V_s^2)} \tag{1.4}$$

Although overly simplistic for realistic models, examination of Equation 1.4 is informative. Calculation of the partial derivatives reveals that the sensitivity is highly nonlinear, and that all three elastic parameters affect compliance data:

$$\frac{\partial\eta_Z}{\partial V_p} = -\frac{V_p}{\rho(V_p^2 - V_s^2)^2} \qquad \frac{\partial\eta_Z}{\partial V_s} = -\frac{V_p^2(V_p^2 - 2V_s^2)}{\rho V_s^3(V_p^2 - V_s^2)^2} \qquad \frac{\partial\eta_Z}{\partial\rho} = -\frac{V_p^2}{2\rho^2 V_s^2(V_p^2 - V_s^2)} \tag{1.5}$$

Note that each partial derivative is negative, indicating that an increase in the velocity or density of the crust leads to a decrease in compliance. Unlike path-averaged measurements, such as surface wave or body wave travel times, compliance data are essentially *in situ* point measurements. Hulme et al. (2005) demonstrated with a 2D forward modeling code that the sensitivity of compliance data is typically restricted to structure within 5 km of the instrument. In this study we modeled compliance data using a 1D propagator matrix code (Gomberg and Masters, 1988; Crawford et al., 1991). Figure 1.4 plots the sensitivity of compliance data as a function of depth and frequency for a realistic oceanic crustal model lacking a sedimentary layer. Lower frequencies are sensitive to deeper structure, but the data have maximum sensitivity to

different elastic parameters at different depths. Furthermore, all parameters have non-negligible contributions in the upper crust. Unlike the analytic solution for a half-space, in which the partial derivatives are always negative, note that for realistic Earth structures, the sensitivity changes sign in the uppermost crust for Vs while remaining negative for Vp and ρ. However, compliance sensitivities are highly dependent on the starting model, and when sediments are present, all frequencies are most sensitive to the sedimentary properties. Chapter 3 goes into great detail regarding the sensitivity of compliance data.

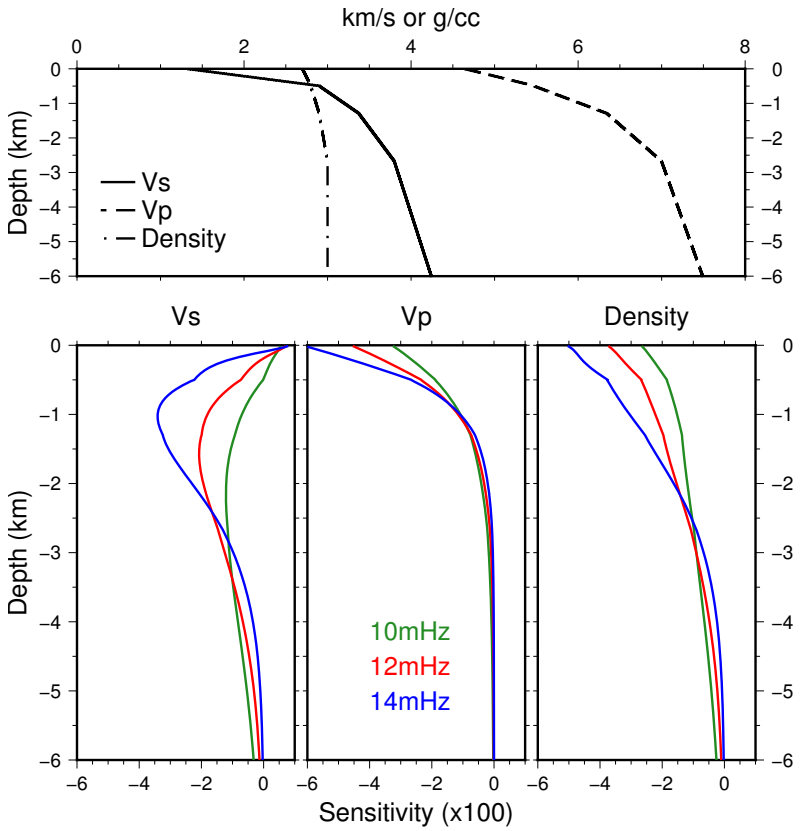

Figure 1.4: The sensitivity of the compliance function to fractional changes in model parameters. The starting model is shown on top, while the sensitivity functions for 10, 12, and 14 mHz are shown below. The kernels are calculated assuming a water depth of $H = 5000$ meters, typical of PLUME data.

Figure 1.2 displays the magnitude-squared coherence calculated between the vertical acceleration and the DPG for PLUME station PL37. We see a high coherence between the signals in the infragravity band, primarily between frequencies of 8 and 17 mHz. The highest

frequency waves that can exert pressure on the bottom are those with wavelengths between 1/2 and 2 times the water depth (Crawford et al., 1991):

$$f_{max} = \left(\frac{g}{2\pi nH}\right)^{1/2} \qquad 0.5 < n < 2 \tag{1.6}$$

For a water depth of 5000 meters (typical of the PLUME stations) and $n = 1$, the maximum frequency would be approximately 18 mHz, which is very nearly what we observe. Infragravity waves can continue to periods of 1000 seconds and longer (Aucan and Ardhuin, 2013), but the lowest frequency compliance measurements are determined by the long-period response of the instruments. Notice that the traces also show high coherence in the microseism band (0.06 - 0.2 Hz). The coherence is caused by microseism-generated Rayleigh waves rather than water wave forcing, and so obeys a different dispersion relation (Ruan et al., 2014). While techniques have been developed to derive structural constraints from data in this frequency range, for now we ignore this part of the spectrum.

Compliance can be modeled using a number of techniques. The most common method remains a 1D solution that assumes a layered Earth and was detailed by Crawford et al. (1991). Forward modeling is accomplished numerically by propagating the solution through a layered Earth (Gomberg and Masters, 1988). The 1-D solution is fast and numerically stable, but subsequent research suggests it may be unsuitable for regions with rapid lateral variations in subsurface shear structure. Subsequent research found that 1D models tend to overestimate shear velocities in an LVZ, and therefore underestimate the velocity anomaly (e.g., Crawford et al., 1998; Iassonov and Crawford, 2008; Zha et al., 2014a). However, compliance data are typically sensitive to structure within 3-5 km of an OBS site, a smaller inter-station distance than most broadband OBS deployments (Hulme et al., 2005). The majority of analyses in this dissertation utilize 1D modeling and inversions, except where noted.

1.3 Scientific Motivation & Thesis Outline

The primary objective of this thesis is to characterize the elastic structure of the oceanic crust and uppermost mantle, addressing a major source of uncertainty in interpreting a wide range of geophysical data and contributing to our understanding of the chemical and thermal processes on the surface and interior of the Earth. My research primarily relies on the analysis of broadband ocean-bottom seismic and pressure data.

One difficulty of working with OBS data is that the geographic orientation of the horizontal seismometer components is unknown during deployment and cannot be directly measured. Knowledge of this parameter is crucial to a variety of seismic analyses, yet no satisfactory method existed to produce consistent, accurate orientations during data post-processing. To address this deficiency, I developed an automated algorithm to measure surface wave arrival angles as a function frequency from teleseismic earthquakes (**Chapter 2**). The arrival angles can be used to infer the orientation of the horizontal components with respect to geographic north. This software is freely available online at `https://igppweb.ucsd.edu/~adoran/`.

Following this, I discuss my efforts to characterize the seismic structure of the oceanic sediments, crust, and uppermost mantle beneath the Hawaiian Swell (**Chapter 3**). I measured seafloor compliance data at 40+ sites deployed during the Plume-Lithosphere Undersea Mantle Experiment (PLUME; Laske et al. (2009)). This study incorporated measurements of the delay times of converted body-wave phases generated at the sediment-bedrock interface in order to further constrain sediment properties. I present maps of sediment and uppermost crust shear velocity. **Chapter 4** discusses my efforts to constrain lower crustal and uppermost mantle structure using dispersion measurements made from ambient noise correlation functions. Initial results indicate that the uppermost mantle may exhibit variations in shear velocity on the order of several percent. These variations could be explained through a combination of thermal anomalies and partial melting.

I then present the first observations of horizontal seafloor compliance, the horizontal deformation fo the seafloor in response to infragravity wave loading (**Chapter 5**). These measurements were made from buried seismometer data from the Ocean Seismic Network Pilot Experiment (Stephen et al., 2003b) and the Monterey Bay Broadband Ocean-Bottom Seismic Observatory (Romanowicz et al., 2006), which exhibit significantly less noise than traditional OBS sites. Although interpretation of these data were limited by instrument response issues and a lack of suitable data, I demonstrated that the technique is capable of providing additional constraints on sedimentary structure.

Finally, I describe my work modeling changes in shear structure in the lower crust following a submarine eruption at Axial Volcano (**Chapter 6**). I analyzed a unique continuous 3.5+ year time series of broadband seismic data to compute seafloor compliance values as a function of time and frequency. I was able to place constraints on the size and shape of the lower crustal melt conduit and to estimate the temporal evolution of melt fraction and geometry. This work was undertaken in collaboration with Dr. Wayne Crawford at the Institut de Physique du Globe de Paris.

Chapter 7 contains a summary of the conclusions of this thesis, as well as potential avenues to continue this research.

During the research for this thesis I recognized that uncertainties in the instrument response function of the differential pressure gauges (DPGs) were inhibiting my analysis. Calibrating these instruments at long periods ($>$ 60 seconds) has been a persistent problem in the OBS community. I worked with the SIO OBS lab and led a student research cruise to deploy instruments with *in situ* calibration devices. These tests confirmed that DPGs require individual calibration for the highest-accuracy measurements at long periods. Details of these research cruises and experiments are described in **Appendix A**.

I have also included a reprint of a paper that describes an experiment to investigate alpine glacier structure using Rayleigh wave anisotropy (**Appendix B**). I was fortunate to be involved

in several aspects of this project, including assisting with the initial fieldwork and modeling and inverting the high-frequency (10 - 30 Hz) dispersion data, in which I gained valuable experience constraining near-surface structure in a novel environment. **Appendix C** has notes from my research that didn't make it into any specific chapters but may be of use to future students. It contains a compilation of parameter scaling relationships in the oceanic crust and sediments, as well as observations of changes in OBS tilt that occurred during the PLUME deployment.

Chapter 2, in full, is a reformatted version of a publication in Bulletin of the Seismological Society of America: Doran, A.K., and G. Laske (2017), Ocean-bottom seismometer instrument orientations via automated Rayleigh-wave arrival angle measurements, Bull. Seism. Soc. Am. 107, 691-708. DOI: 10.1785/0120160165. I was the primary investigator and author of this paper. **Chapter 3**, in full, is a reformatted version of material that has been accepted for publication in the Journal of Geophysical Research: Doran, A.K., and G. Laske (2019), Seismic structure of marine sediments and upper oceanic crust surrounding Hawaii. I was the primary investigator and author of this paper. **Chapter 4** describes unpublished measurements and analysis of surface wave dispersion using ambient noise correlations between PLUME OBS sites. I was the primary investigator and author of this project. **Chapter 5**, in full, is a reformatted version of a publication in Journal of Geophysical Research: Doran, A.K., and G. Laske (2016), Infragravity waves and horizontal seafloor compliance, J. Geophys. Res. 121, 260-278, DOI: 10.1002/2015JB012511. I was the primary investigator and author of this paper, which describes our attempts to measure and analyze horizontal seafloor compliance data. **Chapter 6** describes my work modeling the temporal evolution of crustal structure beneath Axial Volcano using seafloor compliance data. I was the primary investigator and author of this project, which is currently in preparation for journal submission. **Chapter 7** includes concluding remarks and ideas for future work. **Appendix A** contains details from two student-led cruises occurring in 2015 and 2018. I was the chief scientist on these cruises. **Appendix B** contains details of model-

ing I performed as part of an experiment analyzing high-frequency surface wave phase velocities measured on an alpine glacier. The appendix also includes a reformatted version of the resulting publication in the Annals of Glaciology: Lindner, F., and Laske, G., and Walter, F., and A.K. Doran (2018), Crevasse-induced Rayleigh wave azimuthal anistropy on Glacier de la Plaine Morte, Swizterland, Ann. Glaciol., DOI: 10.1017/aog.2018.25.

2 Ocean-bottom seismometer instrument orientations via automated Rayleigh-wave arrival angle measurements

2.1 Abstract

After more than ten years of operations of the U.S. ocean bottom seismometer instrument pool (OBSIP), there is still need for a consistent and accurate procedure to determine the orientation of the horizontal seismometer components of passive-source free-fall broadband OBSs with respect to Geographic North. We present a new Python-based, automated and high-accuracy algorithm to obtain this information during post-processing of the data. Like some previous methods, our new method, DLOPy, is based on measuring intermediate-period surface wave arrival angles from teleseismic earthquakes. A crucial new aspect of DLOPy is the consultation of modern global dispersion maps when setting up the analysis window. We repeat measurements at several frequencies to lower biases from wave propagation in laterally heterogeneous structure. We include measurements from the first minor and major great-circle arcs to further lower biases caused by uneven geographical data coverage. We demonstrate the high accuracy of our technique through benchmark tests against a well-established "hands-on" but slow technique using data from instruments of the Global Seismographic Network (GSN) for which orientations are well documented. We present results for all Cascadia Initiative (CI) deployments, along with a number of other OBS experiments. Compared to other widely used automated codes, DLOPy requires fewer events to achieve the same or better accuracy. This advantage may be greatly beneficial for OBS deployments that last as short as a few months. Our computer code is available for download. It requires minimal user input, and is optimized to work with data disseminated through the Incorporated Research Institutions for Seismology Data Management Center (IRIS DMC).

2.2 Introduction

Many if not most seismic applications that use horizontal seismometer components are crucially dependent on the accurate knowledge of the instrument orientation, i.e. the alignment

of the nominal 1- and 2-components with geographic North and East. Seismometers on land can be oriented quite accurately, e.g., to within a fraction of a degree using a gyro (see e.g., Ekstrom and Busby (2008); Ringler et al. (2013) for reviews). Network operators then either align the components with the geographic coordinates, or report a misalignment in the corresponding metadata that accompany a data stream. A data user can take this information into account and rotate the horizontal components accordingly.

The determination of the orientation of free-fall ocean bottom seismometers (OBSs) is a much greater challenge. Attempts to use a fluxgate magnetometer to gauge the component orientation upon arrival on the seafloor are subject to large errors (John Collins, personal communication). In active-source experiments, the instrument orientation can be determined through airgun shots from several locations (e.g., Anderson et al., 1987; Duennebier et al., 1987; Riedel et al., 2014), but this practice is not common for most of the recent passive broadband OBS deployments because of ship-time costs and permitting challenges. The data user - which includes the PI of a specific experiment - often has to determine the component orientation during post-processing. Very often, this is done concurrently with the analysis of seismic observables such as shear-wave splitting or receiver functions (RFs). Accurate determination of instrument orientations requires global azimuthal coverage to remove biasing effects from 3-D structure, a requirement that is often violated (Laske et al., 1994). Instrument orientations obtained during post-processing may be documented in publications (e.g., Stachnik et al., 2012b; Zha et al., 2013; Janiszewski and Abers, 2015; Rychert et al., 2013), but these results are rarely reported to the Incorporated Research Institutions for Seismology Data Management Center (IRIS DMC) and disseminated as metadata to the seismic datasets. In addition, no method has emerged as a standardized and widely-accepted practice, leading to inconsistencies in reported OBS orientations.

A number of numerical approaches and seismic techniques exist to obtain instrument orientations. Some investigators exploit the particle motion of P-waves, either by examining

the first-arrival particle motion (e.g., Yoshizawa et al., 1999; Schulte-Pelkum et al., 2001) or by minimizing the energy on the transverse component in a selected window (e.g., Niu and Li, 2011). Janiszewski and Abers (2015) describe a method to orient horizontal OBS components by minimizing the receiver function energy on the transverse component. Zha et al. (2013) use the inter-station Rayleigh-wave impulse response recovered from ambient noise correlations. Ekstrom and Busby (2008) generate synthetic seismograms using previously calculated moment tensor solutions and find the arrival angle that best correlates with the surface-wave time series. Stachnik et al. (2012b) developed an automated procedure to measure arrival angles of first-arriving Rayleigh wave trains (R_1), averaged over a wide frequency band. This algorithm is currently used by the IRIS OBS Management Office (IRIS OMO) to provide initial OBS orientation estimates for OBS community experiments such as the Cascadia Initiative (CI; Toomey et al., 2014). The OBSIP website offers a corresponding Matlab toolbox under the "data" tag for use by others (version date as downloaded and at the time of writing of this chapter: 11/14/2014) and that is described in Sumy et al. (2015). For comparison purposes with our new technique, we wrote a Python version of this toolbox and verified its consistency with the Matlab tool box as well as the strategy of the original Stachnik et al. (2012b) publication, except for the way the Matlab toolbox computes error bars. In the following we will refer to this Python implementation as the Stachnik et al. (2012b) method, or STACHPy. One of the first techniques to determine instrument orientation at Global Seismographic Network (GSN) stations during post-processing was the "hands-on" approach of Laske et al. (1994), who measured surface wave arrival angles interactively at a range of frequencies, for both Rayleigh and Love waves, for the first-arriving but also later wave trains. This Fortran and C-based interactive-screen tool is quite accurate but considered too slow and labor-intensive for many modern networks with large numbers of stations on one hand and the need for rapid, community-service-type determinations of instrument orientations on the other.

Here, we introduce a Python- and Fortran-based hybrid, automated method, DLOPy

(Doran-Laske-Orientation-Python), that takes advantage of both approaches, the automated Stachnik et al. (2012b) R_1-only method but also some features of the interactive but slow Laske et al. (1994) method. With regards to datasets used, we benchmark results using GSN stations but also several legacy OBS deployments such as the Ocean Seismic Network (OSN) pilot deployment (Collins et al., 2001). The ultimate goal of this chapter is to report an internally consistent set of instrument orientations for all four one-year OBS deployments for the CI. The CI was the first amphibious (onshore/offshore) community experiment. Seismic data were not subject to the usual 2-year proprietary hold but were made available to all users as soon as the OBS operators uploaded the data to the IRIS DMC. New instruments were built specifically for the CI by the three OBSIP Institutional Instrument Contributors (IICs): Lamont-Doherty Earth Observatory (LDEO), Scripps Institution of Oceanography (SIO) and Woods Hole Oceanographic Institute (WHOI). As a first for OBS engineering, two groups (LDEO and SIO) developed shielded, trawl-resistant instruments to allow noise-reduced deployment in shallow water on the continental shelf. We find that the SIO "Abalone" instruments provide consistently high-quality results at water depths greater than 200 meters. The advantage of this design seems to hold in deeper waters off Cascadia beyond water depths of 2500 meters, though a few non-shielded instruments also yielded high-quality results.

2.3 Method

The basic idea behind DLOPy is to measure broadband surface-wave arrival angles for individual earthquakes. The statistical average over all measurements is then taken as the misalignment of the horizontal seismometer components with respect to the geographic coordinate system. We assume that the horizontal components are orthogonal and that the sensor is level. On a heterogeneous Earth, and with uneven source coverage, the statistical average most likely has an often ignored contribution from lateral refraction. We will cover this aspect in the discus-

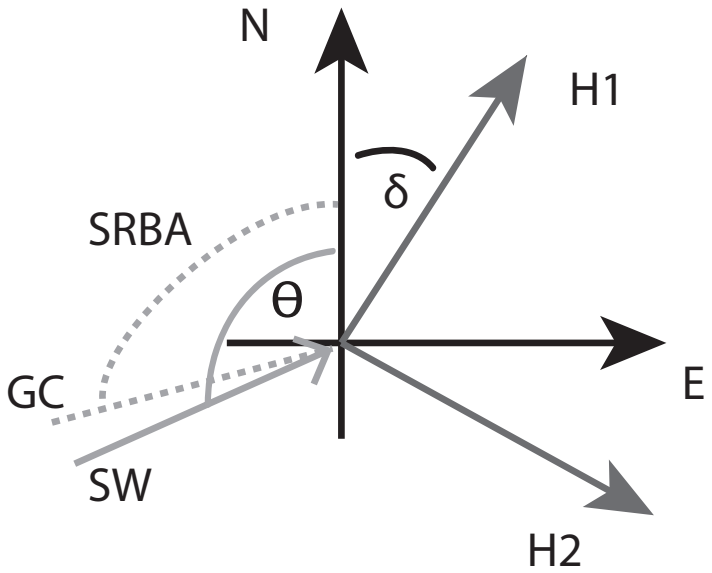

Figure 2.1: Orientation of the horizontal seismometer components (N, E) using the GSN/SEED naming convention for a left-handed coordinate system. Component Z emerges out of the page towards the reader. Misaligned components are named H1 and H2 accordingly. The angle δ is the instrument orientation. Angle $\alpha = \theta + \delta$ is determined by grid search (see text for details). The measured arrival angle as used for further processing is α - SRBA (source-receiver back azimuth). In a heterogenous Earth, the actual approach of a surface wave (SW) may deviate from the source-receiver great-circle (GC) by several degrees.

sion section.

With respect to channel names, we use the SEED/GSN naming convention: the H1, H2 and Z components form a left-handed coordinate system, with H1 ideally being horizontal component N, H2 being horizontal component E, and Z being up (e.g., Ahern et al., 2012). The H1, H2 naming convention is used instead of N, E when the horizontal components are misaligned by more than a few degrees (Figure 2.1). In many OBS deployments, the components are named using a right-handed coordinate system, with component H1 being the E component. We will explicitly state when a right-handed convention is used.

Our automated method builds upon the approach of Stachnik et al. (2012b), which in turn is based on the principles of previous back azimuth estimation studies (e.g., Baker and Stevens, 2004; Chael, 1997; Selby, 2001). The basic idea is that an isolated Rayleigh wave in a three-component seismogram, that is rotated into a ray-based coordinate system, appears only on the radial component but not on the transverse. The radial component then correlates with the Hilbert-transformed vertical component. In a grid search, we rotate the horizontal components by an angle α, with

$$\begin{bmatrix} H_1' \\ H_2' \end{bmatrix} = \begin{bmatrix} \cos\alpha & -\sin\alpha \\ \sin\alpha & \cos\alpha \end{bmatrix} \begin{bmatrix} H_1 \\ H_2 \end{bmatrix} \tag{2.1}$$

where α varies between 0 and 360°, at 0.25° intervals. We search for α that maximizes the cross-correlation between the Hilbert-transformed vertical component and H_1'. In this case, we find $\alpha = \theta + \delta$ as defined in Figure 2.1, and H_1' is the radial component. After correction for the source-receiver back azimuth, this angle is the measured arrival angle. As proposed by Stachnik et al. (2012b), we use the unbounded cross-correlation C_{zr}^{*} to determine the arrival angle because it has clear maxima and minima, but use the normalized correlation C_{zr} to determine the quality of the measurement because the value is bounded on the interval [-1,1]. The relevant functions are defined as

$$C_{zr} = \frac{S_{zr}}{\sqrt{S_{zz}S_{rr}}} \qquad C^*_{zr} = \frac{S_{zr}}{S_{zz}} \qquad S_{ij} = \sum_{\tau=1}^{N} x_i(\tau)x_j(\tau) \tag{2.2}$$

where S_{ij} is the zero-lag cross-correlation coefficient (we also use the term cross-correlation value) between two time series x_i (the radial component H_1') and x_j (the Hilbert-transformed vertical component Z). A user can choose a threshold for the cross-correlation below which a measurement is discarded.

Both methods discussed here use a 10% Tukey window as a data taper (Harris, 1978). The most fundamental difference between DLOPy and STACHPy is the timing of the data taper used for analysis in combination with the protocol of bandpass-filtering the wave packets. Starting with the latter, for a given source-receiver R_1 wave packet, STACHPy makes a single measurement for a wave packet filtered between 20 and 40 mHz. The choice of a relatively short window at a fixed length of 10 min 20 s provides uniform spectral smoothing for an entire arrival-angle database though it does not take into account the different dispersive properties in the wave packets that change with varying epicentral distances. We choose to make individual measurements on wave packets that were bandpass-filtered around a suite of frequencies between 10 and 40 mHz, at 5 mHz intervals. Associated 4-pole, zero-phase Butterworth filters have corner frequencies at $\pm$ 5 mHz around the target frequency. The individual measurements enter the final averaging process for the retrieval of the instrument orientation with equal weight, which we will discuss later. The reason why we include lower frequencies than Stachnik et al. (2012b) is that low-frequency arrival angles are usually less affected by wave propagation in the heterogeneous Earth. In fact, global broadband studies use frequencies as low as 5 mHz (e.g., Laske et al., 1994; Larson and Ekstrom, 2002). In ocean environments, high noise levels from infragravity waves inhibit useful analysis at frequencies much below 10 mHz (Webb, 1998), and noise levels are particularly high at shallow sites (Webb and Crawford, 2010). On the other hand, our experience has been that many deep-ocean OBSs provide high-quality and consistent dispersion data to frequencies as low as 10 mHz. The background noise on OBSs is

depth-dependent (e.g., Webb and Crawford, 1999; Yang et al., 2012), and we will investigate the relationship between orientation uncertainty and ocean depth later in this chapter.

The most crucial difference between our methods is the timing of the data taper. STACHPy uses a fixed R_1 time window that always starts 20 s before "a predicted 4.0-km/s phase arrival" that varies with epicentral distance. The taper extends to 600 s after this arrival (Figure 2.2), regardless of epicentral distance. In contrast, the timing of our tapers depends on frequency and is determined using modern global dispersion maps (Ma and Masters, 2014; Ma et al., 2014) that are sampled in equal-area 1° cells. For each source-receiver pair, we integrate the group travel time to determine the center time of our taper. The determination of this time is currently the only piece of code written in Fortran (courtesy Zhitu Ma) while the rest is in Python. The taper length varies with frequency and was determined somewhat empirically. We started out using a length of 600 s, similar to what Stachnik et al. (2012b) did, but we subsequently varied the length to optimize the cross-correlation between the radial and Hilbert-transformed vertical components. For each frequency, we then picked the length that gave the best correlation for most epicentral-distance ranges. Taper lengths range from 500 s at 40 mHz to 700 s at 10 mHz, which means that the taper for 40 mHz is 20 periods long but that at 10 mHz only seven. These values are currently embedded in our code but could be changed by an experienced user.

An example of the dramatic difference in the application of tapers between DLOPy and STACHPy is shown in Figure 2.2. While Stachnik et al. (2012b) do not analyze data at 10 mHz, the associated wave packet would be the only one to be considered sufficiently well windowed for analysis, while the waveforms for 20 and 35 mHz that are analyzed using STACHPy are nearly missed completely as the window begins too late. We can only speculate that the default velocity of 4 km/s was chosen upon inspecting group velocity curves for reference Earth models such as PREM (Dziewonski and Anderson, 1981) to determine the beginning of the time window (-20 s). For such a model, the group velocity never reaches 4 km/s for frequencies between 20 and 40 mHz. For PREM, the velocities range between 3.60 km/s at 40 mHz and 3.89 km/s

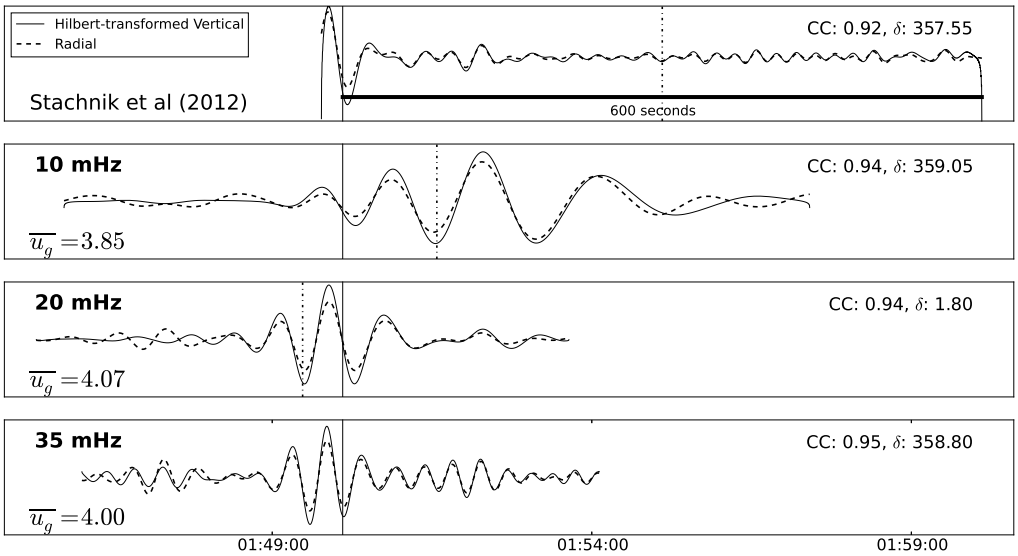

Figure 2.2: R_1 wave packets for the M_W=8.0, 6 February 2013 Santa Cruz Islands earthquake (01:12:27 UTC, source depth 24 km) recorded at Cascadia Initative station G20B at epicentral distance $\Delta = 81^\circ$. The wave packets are shown as filtered and windowed but not yet tapered for analysis by STACHPy (top panel), and by DLOPy at three frequencies (lower three panels). Each panel shows the match between the Hilbert-transformed vertical trace (solid) and the optimally-rotated BH1 trace ("Radial"; dashed). Corresponding correlation coefficients (CC) and the inferred instrument orientation for this particular event (δ) are shown in the upper right corner. The traces are amplitude-normalized in each panel for optimal display. The solid vertical bar marks the arrival time for a 4km/s default group velocity, u_g, chosen by Stachnik et al. (2012b), while the dotted lines in the low three panels mark the center of our taper. Associated path-averaged source-receiver group velocities are given in the left corner of each panel. The dotted line in the top panel marks the center of the STACHPy window and corresponds to a path-averaged group velocity of 3.53 km/s. This window nearly completely misses R_1, which decreases the likelihood for a high-quality arrival-angle estimate.

at 20 mHz (frequencies associated with a group velocity of 4 km/s are around 2.9 mHz). The group velocity associated with the center of a Stachnik window (as opposed to the beginning) depends on epicentral distance. In the case shown in Figure 2.2 it is 3.53 km/s and still seems reasonable for a PREM velocity. However, oceanic paths have particularly high path-averaged group velocities as is documented by the timing of our new windows, and PREM values are poor representers. We should note that the example shown may be an extreme case, but most paths associated with OBS deployments most likely are significantly oceanic. We should also note that an experienced user may code a more fitting group velocity. However, this would presuppose that the user inspects the data, which is not typically done using automated tools. Surprisingly enough, we obtain reasonable agreement between individual arrival angles measured with both techniques, as discussed below. It is interesting to note that the maximum in the envelope of our wave packets lag our predicted arrival times for 10 mHz but leads for 20 mHz. This indicates some small inconsistencies between our data and the modern group velocity maps of Ma et al. (2014). However, the study of this is not the topic of this chapter.

Rounding up the basic differences between STACHPy and DLOPy, the former analyzes only R_1. We include the analysis of the major arc, R_2, as was done in our previous global studies (e.g., Laske and Masters, 1996). Surface waves experience different lateral refraction on the minor-arc and major-arc great-circle paths, and therefore provide independent arrival angle estimates. Quite often, R_2 has a superb signal-to-noise ratio, particularly for the larger earthquakes. R_2 is also often "cleaner" than R_1 in the sense that we get higher correlation between the radial and the Hilbert-transformed vertical components. We also observe higher singular values with the older Laske et al. (1994) method, which indicates that single, isolated signals approach the station (as opposed to multiple, interfering signals). R_1 can be contaminated by coda signals from the Love wave, G_1, as well as from Rayleigh wave overtones. Due to different dispersion, their effects on R_2 is different so that R_2 may be more isolated.

2.4 Implementation and Application

For our analyses, we use all global shallow earthquakes with M_W or $M_S \geq 5.5$. We exclude events with source depths greater than 150 km to lower the risk of overtone contamination. We also exclude events with epicentral distances $\Delta < 5^\circ$ and $\Delta > 175^\circ$ to avoid bias from near-source and antipodal multipathing effects. This choice also ensures that all sources are at least one wavelength away from the station for our longest-period measurements. Our computer code utilizes the recently-developed seismic package ObsPy (Beyreuther et al., 2010; Megies et al., 2011; Krischer et al., 2015) to download data from the IRIS DMC. The code is written primarily using Python 2.7 (as opposed to Python 3.0 or later releases) to simplify user interaction as much as possible. For each station separately, we determine the final station orientation and uncertainty using the following protocol:

1. Retain all measurements with $C_{zr} \geq 0.80$ (adjusted as needed depending on noise conditions at individual instrument locations)

2. Remove outliers by computing the median of data and retaining all values within five times the median absolute deviation (MAD)

3. Use the bootstrap method of random sampling with replacement (Efron, 1979) to compute the arithmetic mean after 5000 runs on the remaining values and the 95% confidence interval of the mean. We report the uncertainty as twice this confidence interval.

In step (2), using the MAD to identify outliers is preferable to methods involving the standard deviation or variance of the data, as these statistics yield biased results for datasets with severe outliers. As datasets are resampled during bootstrapping, this strategy may allow us to remove some of the biasing effects caused by the uneven azimuthal distribution of earthquakes. A MAD cutoff of 5 was determined empirically. It may seem somewhat conservative but produces robust results.

Step (3) is a new way to determine error bars that was not implemented by Stachnik et al. (2012b). Since the error of the mean is inversely proportional to the square root of the number of calculations (standard error $\approx \sigma/\sqrt{n}$), more calculations generally lead to a more precise estimate, if the underlying dataset has no systematic biases. While many investigators present orientation uncertainties using the 95% confidence interval of the mean, we choose twice this value, effectively reporting the 4-σ uncertainty. As will be discussed below, this more conservative choice accounts for some systematic biases in the datasets. It also ensures internal consistency and repeatability within the dataset as well as more consistency when using different measurement strategies. We should add that, since we use the bootstrap method to determine error bars, repeat runs yield different error bars. Our experience is that errors may change by 0.05° for stations having high signal-to-noise ratios, which is actually a very small number compared to the actual error bars.

As an example, Figure 2.3 displays an entire arrival angle dataset for CI station G20B. Obviously, DLOPy gives more measurements than STACHPy since the latter gives only frequency averages. In both cases, the vast majority of data have low cross-correlation values, which implies low quality. However, high-quality data associated with cross-correlation values higher than a certain threshold tend to cluster around an average which we take as the station orientation. For a given threshold, our data tend to scatter more than those using STACHPy, most likely because of the implicit spectral averaging in the latter. Hence, the scatter alone does not rank the quality of one method over the other. Quite often, only one or two frequencies produce high-quality results for R_1, so a measurement using STACHPy may produce a low-quality result that is ultimately discarded, whereas they are retained as data using our code. Also recall that the dataset using our code includes many high-quality R_2 measurements.

For CI station G20B station, we obtain an orientation of $2.39^\circ \pm 2.82^\circ$ from 209 high-quality measurements for 76 events. This includes 180 R_1 data and 29 R_2 data. Application of STACHPy yields an orientation of $0.26^\circ \pm 6.08^\circ$ from only 10 events. We should expect that

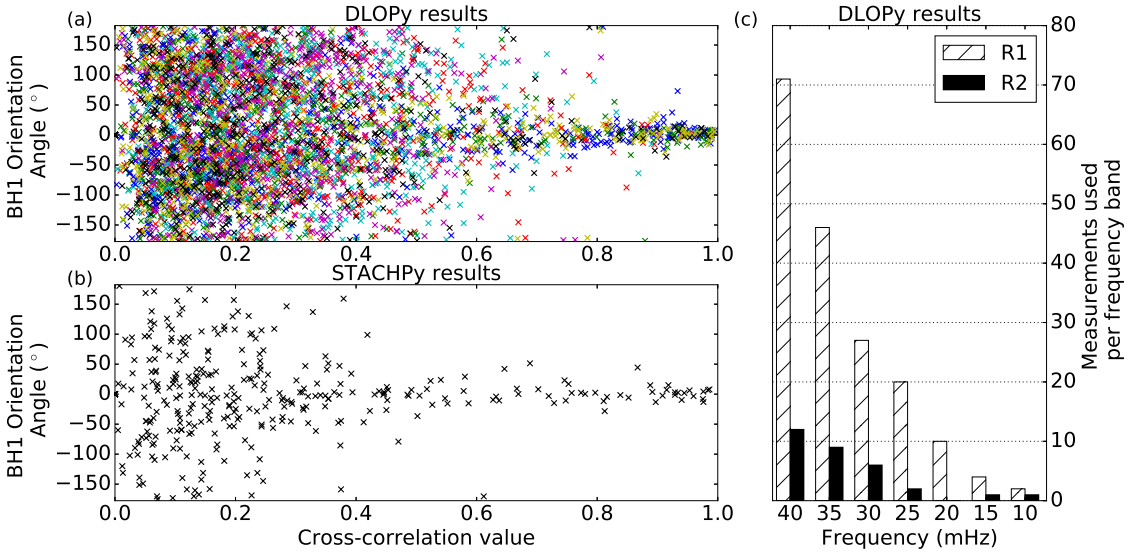

Figure 2.3: A complete set of arrival angle measurements as a function of cross-correlation value for CI station G20B. (a) Doran & Laske [2016] method DLOPy; (b) Implementation of Stachnik et al. (2012b) method, STACHPy. The cross-correlation value is a measure for data quality. "BH1 Orientation Angle" is the optimum rotation angle, α that maximizes cross-correlation between component H_1' and the Hilbert-transformed vertical component. Different shades of grey in (a) mark measurements at different frequencies and wave orbit number (1 or 2). High-quality data tend to cluster around a common value, the inferred instrument orientation, δ. Coincidentally, this instrument was almost naturally oriented. (c) provides a count of the number of high-quality measurements used from each great-circle arc and frequency. At G20B, the greatest number of usable measurements are made for R_1 at 40 mHz. Final instrument orientations: STACHPy: 0.26 $\pm$6.08°; DLOPy: $2.39 \pm 2.82°$; IRIS OMO report: $3.00 \pm 15°$

the vastly lower number of events used in the latter bears an increased risk of biasing effects by dominant ray corridors on a laterally heterogeneous Earth. Nevertheless, both our methods yield consistent station orientations, with statistically insignificant discrepancies. Note however, that our error bar is smaller than that obtained using STACHPy for which we did NOT multiply the error by a factor 2. The IRIS OMO has recently started implementing the Stachnik et al. (2012b) method to determine the OBS orientations for community experiments such as the CI. OMO used 28 events to obtain a orientation angle of $3.00^\circ \pm 15^\circ$. The IRIS OMO Matlab implementation computes errors in a different way, namely choosing the standard deviation in the dataset. In the strict statistical sense, this is too conservative on one hand, but gives unrealistically small errors for small datasets.

2.5 Benchmark Methods and Datasets

In this section, we attempt to validate several aspects of the measurement process. A crucial question is whether relatively short deployments (or a collection of only a few earthquakes) can provide reasonably accurate estimates of instrument orientations. We address this using data from GSN stations ESK (Eskdalemuir, Scotland) and HRV (Harvard, Massachusetts).

We also assess the validity and repeatability of our results, and the automated methods in general. For this, we compare our results for GSN station SACV (Santiago Island, Cape Verde) against those obtained using the interactive Laske et al. (1994) benchmark method. In this method, the frequency-dependent surface-wave arrival angles are measured by hand via an interactive screen tool. The data analyst chooses the window that best visually isolates the desired waveforms in the three-component seismogram. A singular value decomposition (SVD) of the complex three-component spectrum then yields frequency-dependent eigenvectors that govern the principal particle motion. The associated singular values give information on the quality of the motion. In the ideal case of an isolated signal with particle motion in one plane

(including linear motion), one singular value is one and the other two are zero. If needed, the data analyst finds the best window iteratively that yields the highest singular value. A multi-taper approach optimizes between spectral leakage effects and bias from noise in the seismic records. The orthogonal multi-tapers also provide statistically independent estimates, allowing the assignment of formal error bars for each individual measurement. The interactive choice of the data window is particularly effective and important in the case of Love waves to make sure that no signal of the earlier or concurrent Rayleigh-wave overtones nor the later Rayleigh wave fundamental mode is in the window.

We then proceed with some past temporary and permanent OBS deployments. We compare surface and buried OBSs during the short-term Ocean Seismic Network (OSN) pilot experiment near Hawaii (Collins et al., 2001). We also investigate the instrument orientation of the buried OBS at the high-quality, long-term MOnterey Bay Broadband Observatory (MOBB; Romanowicz et al., 2006) off-shore California. Finally, we benchmark our results for the Plume-Lithosphere Undersea Mantle Experiment (PLUME) Phase 2 deployment near Hawaii (Laske et al., 2009) against published values obtained with the Laske et al. (1994) method.

2.5.1 Internal Consistency and Deployment Length on the Examples of ESK and HRV

We begin our benchmark testing by applying DLOPy at a particular station for different time periods. For this test, we need a station that has had a consistent seismometer deployment without interruption for a long time, and we choose IRIS-IDA (II) station ESK. According to IRIS DMC metadata information, this station operated a Wielandt-Streckeisen very broadband (VBB) STS-1 seismometer without interruption for six years between January 1st 2004 and January 1st 2010. This includes no downtime, no changes to the instrument response, no recovery and redeployment of the sensor, nor any other adjustments. The STS-1 is the primary sensor at ESK and carries the location code 00.

For our test, we determine instrument orientations using data for the entire six-year period, as well as several subsets of the data spanning one full year, six months and three months. The results are summarized in Figure 2.4. As expected, the dataset of the full six years yields the final instrument orientation with the smallest error bar: $3.34 \pm 0.48^\circ$. Results obtained for shorter time spans, e.g., 1-year or several months yield orientations that slightly vary, but the 6-year benchmark result is within the respective error bars. Some of this variation may be due to differing azimuthal distributions of earthquakes during the time periods considered. Larger variations have to be expected for shorter time spans that implicitly incorporate a smaller number of earthquakes, but the larger error bars make these variations statistically insignificant. This indicates that it is possible to obtain reasonably well the instrument orientation for deployments as short as a few months. Note, however, that orientations of short deployments may have error bars of 2.5° or more.

For the epoch spanning the six years, the IRIS DMC metadata database currently shows an orientation of the N component as 0.1° but the two horizontal components are not orthogonal. The STS-1 components are physically distinct packages, so unintentional non-orthogonal setups are possible though unlikely. The azimuth of the E component is reported as 89.5°, so the angle between the two components is 89.4°. Our code does not account for this. The orientation at ESK is reported at the DMC as being the same since operations started in 1987, so we also compare our results with previously published results. Laske (1995) reported $0.07 \pm 0.37^\circ$, and her subsequent but unpublished updates in the mid-2000s were as high as 0.28°. These angles were obtained during joint inversions for station orientation and laterally heterogeneous structure. Larson and Ekstrom (2002) obtained $1.1 \pm 0.72^\circ$ after inversion and 0.9° through simple averaging. We currently cannot explain the relatively large discrepancy with our results of more than 2°. The previous studies included Love wave angles in their analyses. Our experience is that in some cases this does make a significant difference. We confirmed with the station operator that no realignment of the sensor was performed at ESK (Pete Davis, personal com-

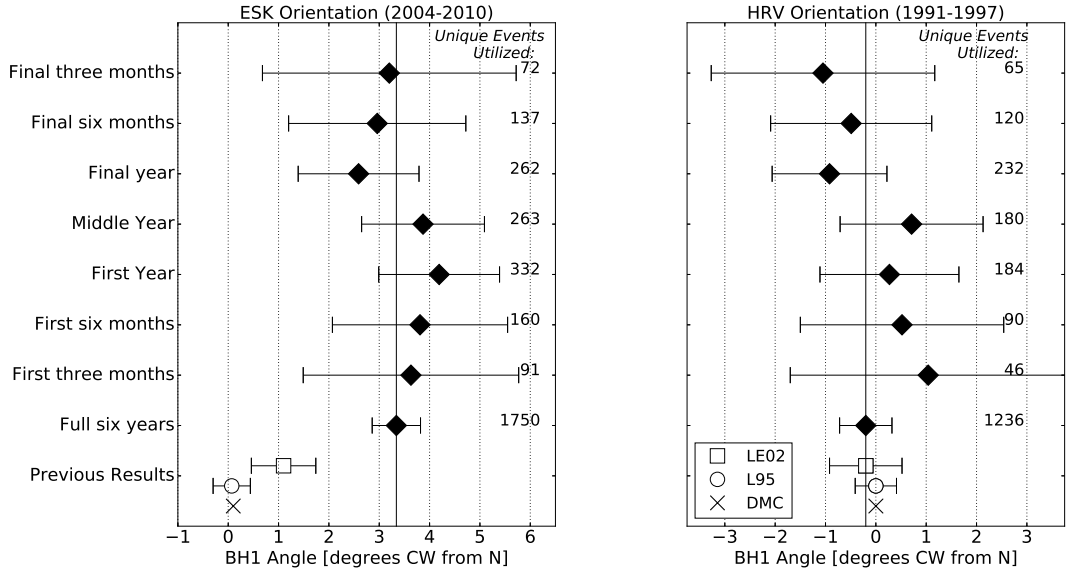

Figure 2.4: Instrument orientation consistency check at GSN stations ESK and HRV. Results are shown when obtained using the full dataset for six years and several subsets thereof. The "benchmark" results for the full six-year dataset is 3.34±0.48° for ESK and -0.2±0.52° for HRV. Also shown are the number of unique earthquakes contributing to each data subset and the results of previous misorientation analyses: LE02 refers to Larson and Ekstrom (2002), L95 refers to Laske (1995), and DMC refers to the BH1 orientation reported on the IRIS DMC. The orientation of BH1 component is shown in degrees clockwise (CW) from geographic north (N).

munication), thereby ruling out the possibility that the sensor orientation was changed between studies. Here, we take the 2° difference as a threshold for how accurately and consistently the station orientation can be determined at low-noise stations.

We repeat this procedure at IRIS-USGS (IU) station HRV to further test the consistency and accuracy of DLOPy. This station also operates a VBB STS-1 seismometer (location code 00), and the DMC reports perfect orthogonality between the horizontal components. The HRV BH channels ran with very few interruptions between January 1st 1991 and January 1st 1997. The IRIS DMC reports intermittent data gaps between December 3 - 8 1996 while construction was occurring in the vault. An instrument response correction affecting December 1996 data was performed retroactively in March 2006. As shown in Figure 2.4, we see the same consistency in these data as achieved at ESK. The final orientation we obtain is -0.2±0.52°. Our results agree closely with those of Laske (1995) and Larson and Ekstrom (2002), who report orientations of 0.00±0.41 and -0.2±0.64, respectively.

2.5.2 Repeatability of Final Instrument Orientation on the Example of SACV

A possible reason for the discrepancy in the instrument orientation for station ESK could be because different workers used earthquakes from different time periods. We therefore repeat a test for the time period between 2011.169 and 2012.202 (13 months) using data collected at station SACV. This is a time period when no changes to the instrument responses were made and no data gaps occurred. The station has two seismometers where the primary sensor is a Geotech-Teledyne KS54000 VBB sensor (SEED location code 00), while a broadband Güralp CMG-3T seismometer serves as secondary sensor (location code 10). The KS54000 is a borehole sensor, and the IRIS DMC reports an emplacement depth of 97 meters. At the time of this study, there is some debate on how accurately the sensor orientations are known for this station (Pete Davis, personal communication). This is one reason why we choose this station for our tests.

Applying the automated methods as described above, we determine the instrument orientation for both sensors (Table 2.1). Using our new approach, the results are based on high-quality measurements from 454 events for sensor 00 and 343 events for the noisier sensor 10. STACHPy yields error bars that are about twice as large as the ones we obtain with DLOPy, but our orientations of 28.75° and 4.04° for both sensors lie within the error bars of the STACHPy results. This indicates once again that at low-noise GSN stations, both methods yield mutually consistent results for a 1-year long deployment.

Using the Laske et al. (1994) interactive-screen method, the data analyst usually discards measurements for a wave train if the largest singular value remains below 0.6 or so. Unlike with our new method, those low-quality results never enter the database. For this study only results with singular values greater than 0.7 are included in further processing. We determine the median of all minor and major arc results at 6 frequencies: 5, 8, 11, 14, 17 and 20 mHz, for each Love and Rayleigh waves. The average of the measurements gives the final instrument orientation, and the standard deviation divided by 12 gives the uncertainty. We choose to work with the median rather than the weighted averages in this particular test because we do no further vetting against outlier data that we otherwise discard during secondary screening. For the location code 00 sensor, we obtain about 180 Rayleigh wave high-quality measurements and 160 Love wave measurements, at each of the six frequencies. The location code 10 sensor is less well constrained, with about 80 Rayleigh wave and 100 Love wave measurements. For the two sensors, we obtain instrument orientations of 28.59° and 4.02° (Table 2.1). Both values are in excellent agreement with those obtained with DLOPy. The Laske et al. (1994) values are now reported as instrument orientations in the metadata at the IRIS DMC. We note that the DMC reports that the horizontal components are not quite orthogonal, with a 90.4° angle between them.

Since the Laske et al. (1994) method includes Love wave angles but our new method does not, Table 2.1 also lists final instrument orientations when excluding Love waves. While results for the quieter 00 sensor agree with those using DLOPy to within less than a degree, the

noisier 10 sensor for which less data are available now has a larger discrepancy of 1.4°. This is still within our error bars though.

To test the repeatability of the obtained instrument orientations, a novice data analyst repeated the Laske et al. (1994) method on the dataset for sensor 00. The analyst required much more time than Laske to make the measurements, but his efforts yielded an internally more consistent dataset, particularly at low frequencies. The final instrument orientation he obtained is $28.69 \pm 1.66^\circ$ and is in excellent agreement with Laske's result. Addressing the outlier issue, we repeat our procedure after we discarded outliers in Laske's dataset. Histograms reveal that the data distribution is somewhat one-sided, probably as a result of uneven earthquake distribution and wave propagation on a heterogeneous Earth. We therefore choose cut-off limits by hand instead of applying a standard n-σ cut-off but leave the bounds constant across all frequencies. Overall, we discard data that are about 2.5 σ or more away from the median at high frequencies but only 1.5 σ at low frequencies. The final instrument orientations after this data vetting are $29.43 \pm 0.87^\circ$ and 4.41 ± 1.01. The data-cleaning process clearly yields smaller error bars, by a factor of almost 2, but does not significantly change the final instrument orientations. Nevertheless, these changes are larger than the original 2-σ error bars obtained with our new automated method DLOPy. To accommodate all these discrepancies we choose to work with 4-σ errors instead, as noted above.

2.5.3 Repeatability of Individual Measurements on the Example of SACV

After exploring consistencies and discrepancies in the final estimates of instrument orientation, we now investigate the consistency of each individual measurement. This check is particularly important for the use of surface wave arrival angles in interpretations of lateral heterogeneity (e.g., Laske and Masters, 1996, 1998; Larson et al., 198; Yoshizawa et al., 1999; Larson and Ekstrom, 2002). A quick comparison between the individual measurements taken by Laske using the Laske et al. (1994) method agree reasonably well with those taken by the

novice data analyst in that most measurement lie within their respective error bars. Some outliers include the assignment of the wrong wave orbit or wave type and likely would not pass secondary screening. The interesting and important question is how the Laske et al. (1994) dataset compares to the one obtained with our new method. This is demonstrated in Figure 2.5.

Table 2.1: Comparison of orientation results at GSN station SACV*.

Method	SACV.00	SACV.10
DLOPy	28.75 ± 0.96	4.04 ± 1.28
STACHPy	30.05 ± 2.10	4.48 ± 2.04
Laske et al. (1994)	28.59 ± 1.67	4.02 ± 1.99
Laske et al. (1994) R_1+R_2	29.38 ± 3.34	5.42 ± 3.94

*Results for time period 2011.169 through 2012.202 as obtained with the three methods. We consider both the primary sensor (location code 00) and secondary sensor (location code 10).

Here, we use different selection thresholds to consider only high quality data. For the Laske et al. (1994) method, we increased the singular-value threshold to 0.85 for R_2, while we increase the C_{rz} value for DLOPy to 0.85 for R_1 to include only high-quality data but lower it to 0.7 for R_2 angles to allow for more data to be considered. Uncertainties are only shown for Laske et al. (1994) because only this technique provides formal error bars for individual measurements. Overall, our measurements are in close agreement, with most of our data placing within the error bars obtained with the Laske et al. (1994) method. As discussed above, R_2 wave packets sometimes appear to be cleaner than R_1, resulting in measurements with smaller errors, and the agreement between our methods supports this impression (by the higher correlation coefficients between the two datasets).

However, we also note some discrepancies. The different windowing of the data may explain some of this. A screen-interactive method allows the analyst to select slightly different window positions and lengths to emphasize the wave packet of interest. While our new automated approach centers the window around a group arrival time using modern dispersion maps, that window may still include some other signals. Unwanted signals, such as the earlier-arriving overtones may then still be included in our new analysis while the Laske et al. (1994) windowing

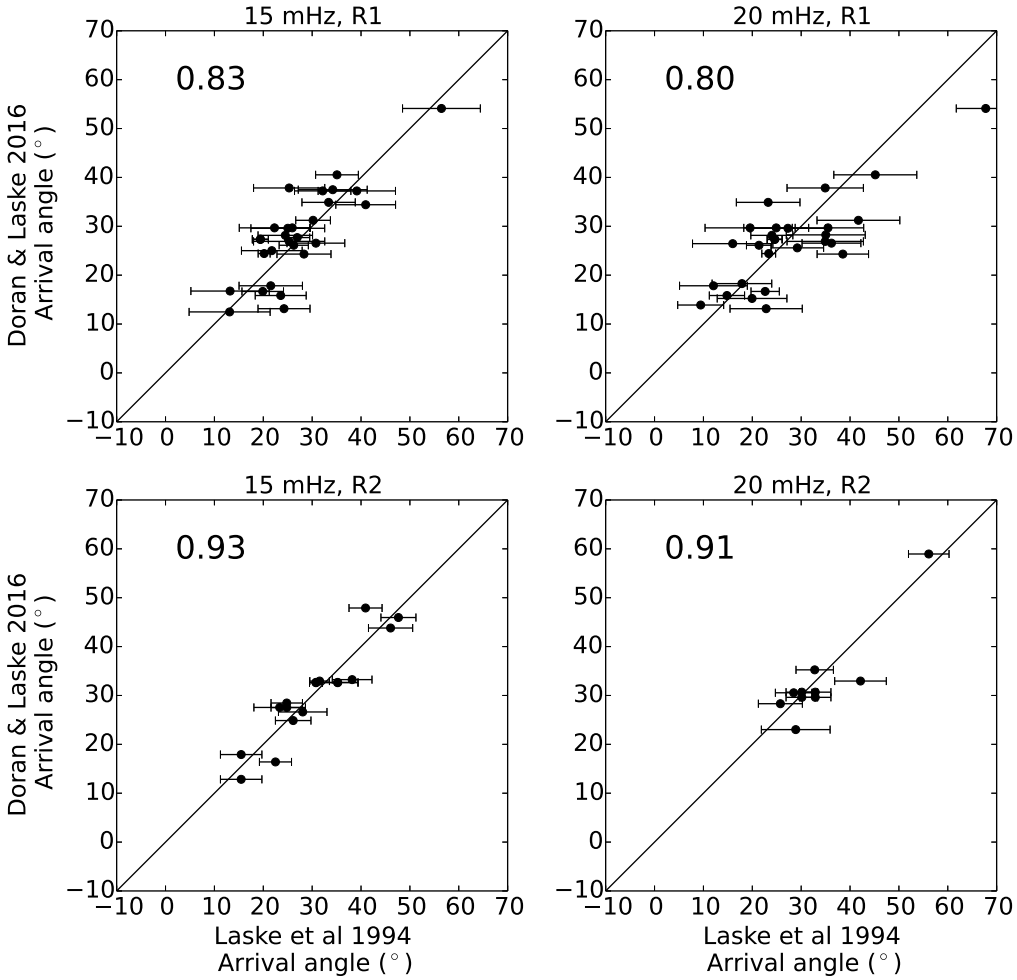

Figure 2.5: A comparison of individual measurements for GSN station SACV location 00 using the Laske et al. (1994) method and DLOPy. Results are shown for two frequencies, 15 and 20 mHz, for both R_1 and R_2. Only a subset of high-quality data are considered: measurements with singular values ≥ 0.75 for R_1 and ≥ 0.85 for R_2 are used from the method of Laske et al. (1994), and measurements with correlation coefficients $C_{zr} \geq 0.85$ for R_1 and $C_{zr} \geq 0.70$ for R_2 are used from DLOPy. The method of Laske et al. (1994) gives formal uncertainties for individual estimates, while DLOPy does not. Numbers in the top left denote correlation coefficients between the two datasets.

explicitly allows an analyst to exclude them. Similarly, multipathing can affect late-arriving energy and affect results obtained using our new approach. On the other hand, a data analyst using the Laske et al. (1994) approach may cut too much into the wave packet, thereby inadvertently eliminating low-amplitude signals. Our experience is that measurements at low frequencies that are not considered here (e.g., 5 mHz) are particularly vulnerable. On the other hand, since the Laske et al. (1994) method determines arrival angles at all frequencies at once, a long window is often required (up to 30 minutes) to ensure that all of the dispersed energy is captured. This may be too long for the highest frequencies considered (e.g., 20 mHz), and so the Laske data at 20 mHz may be less accurate. Another difference between the methods is the set of tapers used. At the least, the multi-tapers treat noise in a different way than the single taper we use here. By implementing the same set of multi-tapers as used in the Laske et al. (1994), we may achieve better agreement. And finally, the underlying method to determine the optimal angle may also play a significant role. While Laske et al. (1994) perform a formal inversion of the complex spectra of the 3-component seismogram, we perform a grid search in the time domain using the cross-correlation of two components.

Table 2.2: A comparison of results for the three OBSs deployed for the OSN Pilot Experiment (Stephen et al., 2003b).

Method	OSN1	OSN1S	OSN1B
Laske et al. (1994)	126.41 ± 0.90	282.36 ± 2.24	147.99 ± 0.87
STACHPy	125.88 ± 1.87	281.28 ± 3.16	148.79 ± 2.73
DLOPy	126.72 ± 1.86	281.46 ± 3.64	148.57 ± 1.68
DLOPy, R1 Only	126.54 ± 1.86	281.03 ± 3.58	148.59 ± 1.72
DLOPy, R2 Only	127.91 ± 5.46	283.29 ± 11.52	148.42 ± 3.62

2.5.4 Short- and Long-term OBS Observatory Sites

We now move from working with land seismometers to those on the ocean floor. We start our investigations at two observatory-quality installations, first at the short-term OSN pilot

deployment near Hawaii (Stephen et al., 2003b; Collins et al., 2001), and then at the permanent cabled observatory MOBB off-shore California (Romanowicz et al., 2006).

The OSN pilot experiment operated for four months between February and June of 1998 and provides a unique dataset for comparison. For this experiment, three different OBSs were deployed: site OSN1 had a Geotech-Teledyne KS54000 VBB borehole seismometer that is routinely installed at GSN land stations. At this site, the water depth was about 4400 m, and the seismometer was emplaced in Ocean Drilling Project (ODP) Hole 843B and 248 m below the seafloor. Site OSN1S had a Güralp CMG-3T broadband seismometer installed on the ocean floor, and OSN1B had the same sensor as but pushed into the mud about 1 m deep. As of the writing of this chapter, the metadata at the IRIS DMC report an instrument orientation of 0° (i.e. alignment with the geographical coordinate system; or orientation unknown) for all three sensors.

The borehole installation at OSN1 was expected to have the lowest noise levels, particularly at frequencies below 10 mHz. Unfortunately fluid circulation in the borehole caused noise levels to be unexpectedly high so that OSN1B actually produced the seismically quietest data (Stephen et al., 2003b). The borehole sensor outperformed the Güralp systems at frequencies beyond the microseism peak at frequencies above 0.3 Hz on the vertical components. The difference was even more striking for the horizontal components, for which the buried sensor at OSN1B clearly outperformed the KS54000 at frequencies below 50 mHz, while the KS54000 was clearly the best sensor at frequencies higher than 0.2 Hz. For our analysis, which is performed at low frequencies, we therefore expect to obtain the most stable results for OSN1B. We should also note that burial greatly reduced the noise on the Güralp sensor at frequencies below 50 mHz, on all components, but had virtually no effect at high frequencies though an improvement may be observed on the horizontal components at frequencies above 5 Hz.

Table 2.2 summarizes our results together with those obtained with the Laske et al. (1994) method and STACHPy, and the results are included in Figure 2.6. As expected, the error bars

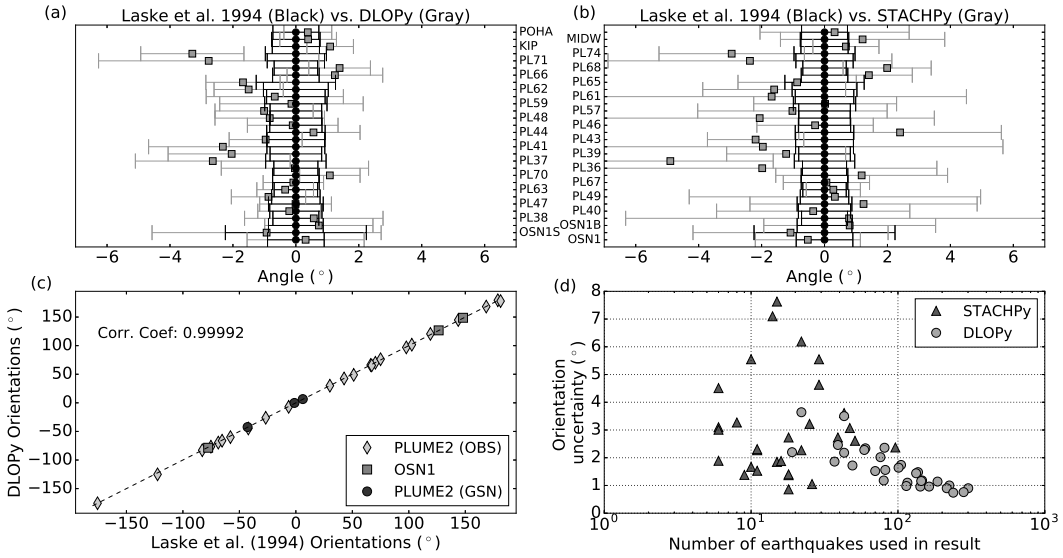

Figure 2.6: A comparison of results obtained with DLOPy, the method of Laske et al. (1994) and STACHPy for 30 stations of the OSN and PLUME deployments. (a) and (b) compare the final instrument orientations with respect to those found using the Laske et al. (1994) method. (c) shows a comparison between Laske et al. (1994) and DLOPy. PLUME2 GSN denotes GSN stations IU.KIP, IU.MIDW, and IU.POHA. (d) compares the instrument orientation uncertainties obtained using DLOPy to those of STACHPy.

for the instrument orientation are smallest for OSN1B and largest for OSN1S using DLOPy and the Laske et al. (1994) method. It is unclear why the error is relatively large for OSN1B when using STACHPy, or why the error at OSN1S is larger for DLOPy than for STACHPy. The Laske et al. (1994) method produces the smallest error bars for each station. Note however that the orientations using the different methods place within the respective error bars so that discrepancies are statistically insignificant, for all three stations. We also present orientations obtained when using only R_1 or R_2 measurements. Due to the very small number of data, the error bars for the R_2 orientations are relatively large. Remarkably, the obtained instrument orientations still place within the error bars of the complete dataset. All these results indicate that, at least in the deep ocean, deployments of only several months are sufficient to orient the sensors reliably during post-processing using long-period surface waves.

We also check the instrument orientation at the cabled ocean observatory MOBB (Ro-

manowicz et al., 2006). The cable allows GSN-like real-time access to the data. At this site, the water depth is 1000 meters, and a Güralp CMG-1T was installed 0.5 meters under the seafloor. The data can be obtained through the Northern California Earthquake Data Center (NCEDC) while some metadata are included at the IRIS DMC in the metadata for the Berkeley Digital Seismograph Network (BK). An investigation of infragravity energy on the horizontal components of MOBB and OSN seismometers was the initial motivator for the work presented here (Doran and Laske, 2016) as understanding the directionality of infragravity waves requires precise knowledge of the instrument orientations.

We use data between August 1st, 2011 and September 1st, 2012, which compares to the duration of a typical modern temporary passive seismic OBS deployment. Using DLOPy, we obtain an orientation of 8.73 ± 1.82 using 575 measurements from 205 events, while STACHPy computes an orientation of 7.36 ± 6.45 using 31 events. Choosing a slightly different time period from November 1st, 2011 through November 1st, 2012 gives $7.99 \pm 1.78^\circ$ from 564 measurements on 184 events in DLOPy and $6.92 \pm 6.47^\circ$ based on 28 events in the Stachnik et al. (2012b) implementation. For both methods, the orientation varies on the order of 1° which lies within the error bars and so is statistically insignificant. Using the Laske et al. (1994) method, we examined six frequencies between 8 and 23 mHz and obtained an orientation of $8.39 \pm 1.11^\circ$. These results were calculated after excluding outliers during secondary screening. Higher frequencies were examined here than ESK and SACV because of high noise at lower frequencies. While analyzing these data, we noticed that the Love wave measurements produce more internally consistent results than the Rayleigh wave measurements, with cleaner waveforms and lower uncertainties associated with the individual measurements. The Laske et al. (1994) method produces the smallest error bars and STACHPy produces the largest, but all three results agree within their respective uncertainties. Discussion with MOBB station operators recently confirmed that a misorientation of 6 to 8 degrees is quite possible (Barbara Romanowicz, personal communication).

Compared to the results obtained for the OSN sensors, the error bars for STACHPy are surprisingly large, which we cannot fully explain at this point. DLOPy allows the inclusion of many more earthquakes, resulting in a drastic reduction of formal uncertainties. We do note that in raw-data plots similar to that in Figure 2.3 the fewer measurements cluster more tightly around an average value for OSN sensors than for the MOBB sensor for which we have vastly more data.

The actual orientation of the sensor is probably not known as the metadata at both the IRIS DMC and the NCEDC report an orientation of 0°. To conclude, at low-noise OBS sites, we should expect to be able to determine instrument orientations with error bars as small as 2° or less when using DLOPy. Whether this also means that we can determine instrument orientations to that accuracy is addressed in the final discussion at the end of this chapter.

2.5.5 OBSIP Deployments: the Hawaiian PLUME Phase 2 Deployment

We now examine a dataset obtained from one of the early OBSIP deployments: the phase-2 deployment for the Hawaiian Plume-Lithosphere Undersea Mantle Experiment (PLUME2 Laske et al., 2009; Rychert et al., 2013). The PLUME2 deployment provided useful 3-component seismograms for 24 broadband OBSs and 10 land stations from May 2006 through June 2007. Here we concentrate on the OBSs. The sensors were Güralp CMG-3T sensors in WHOI OBS packages and Nanometrics Trillium T-240s in the SIO packages. All OBSs were deployed at water depths between 4500 and 5800 meters on and off the Hawaiian Swell. The temporary PLUME deployment was complemented by three permanent GSN stations: Kipapa (IU.KIP; a STS-1 sensor), Pohakuloa (IU.POHA; a KS54000) and Midway Island (IU.MIDW; a STS-2). For these 27 stations, we use our new technique to determine the instrument orientation and compare our results to those of Rychert et al. (2013), which used the Laske et al. (1994) high-quality ”benchmark” method (published in their online supplement).

Figure 2.6 displays a comprehensive summary of the results. There is excellent agree-

ment between the results using DLOPy and the Laske et al. (1994) method (see Panels 6(a) and 6(c)). Note that the latter yields consistently smaller errors bars than DLOPy but, except for station PL74 all of our results agree with those obtained with the Laske et al. (1994) method, to within our error bars but not necessarily the Laske error bars. Station PL74 shows a discrepancy of about 4°. The sensor is nearly naturally polarized so that the BH1 component is almost aligned with Geographic North. Upon inspection of Laske's original arrival angle data, we notice that the 6 Rayleigh wave frequencies yield an orientation result similar to what we get with the new method (-2°), but the Love wave frequencies consistently have the opposite sign, are internally more consistent and therefore dominate the averaging process, leading to an orientation of about +2°. Since STACHPy also only uses Rayleigh waves, this method yields a similar inconsistency for PL74 against the Laske et al. (1994) method but agrees with the results from DLOPy. A discrepancy of 4° seems unacceptable but note that this is an exception in a set of 27 stations. We note that seven SIO OBS orientations published by Rychert et al. (2013) differ from our results by $\pm 180°$. The method of Laske et al. (1994) currently does not distinguish between δ and $\delta \pm 180°$. A comparison with synthetic seismogram could remove this ambiguity but is not implemented. The stations affected are: PL38, PL40, PL47, PL49, PL63, PL67, PL70 (for more information, see Table S2, available online at `https://igppweb.ucsd.edu/~adoran/DLOPy.html`).

Overall, STACHPy yields much larger error bars, sometimes being well over 5°, and the instrument orientations seems to agree less well with those by Laske. Nevertheless, the differences are never statistically significant. It is also revealing to investigate the dependency of the orientation error bars on the number of unique earthquakes used. Our new method consistently uses many more earthquakes than STACHPy, by an order of magnitude. As discussed earlier, measuring multiple frequencies and multiple wave trains allows a much greater number of events to be utilized. This usually yields significantly smaller error bars, by a factor of nearly 2 on average.

2.6 Results for the OBSs of the Cascadia Initiative

We now turn our attention to the four 1-year OBS deployments of the Cascadia Initiative community experiment (Toomey et al., 2014). CI was an amphibious experiment, i.e. there was a land component, but we analyze only the OBS records using both DLOPy as well as STACHPy. The complete table of instrument orientations for 223 OBSs can be found in Table S1, available online at `https://igppweb.ucsd.edu/~adoran/DLOPy.html`, while Table 2.3 provides an overall summary. As of 5/23/2016, the IRIS DMC MetaData Aggregator (MDA) contained no information on the azimuths of CI horizontal channels. Lodewyk and Sunny (2015) report that all data have been converted to a left-hand coordinate system, with H2 being 90 degrees clockwise from H1, as of 5/2/2014. We accessed the data between 30/10/2015 - 28/03/2016 and assume this convention.

Table 2.3: Summary comparison for the Cascadia Initiative OBSs between results of DLOPy, STACHPy, and those disseminated by OBSIP.

Method	Deployments	# Stations	Median Error (°)	Median # of Events
DLOPy	1 - 4	223	4.92	31
OBSIP	1 - 3	161	17.0	10
STACHPy	1 - 4	213	5.73	7

Applying DLOPy to OBS records of all four deployments, we obtain instrument orientations and related uncertainties for 223 stations. With STACHPy, we obtain orientations for only 213 stations. At the time of writing of this chapter, IRIS OMO disseminates reports containing estimated instrument orientations for the first three deployments (Lodewyk et al., 2014; Lodewyk and Woodward, 2014; Lodewyk and Sunny, 2015). While their number of events per station generally agrees with that using STACHPy, OMO obtains much larger error bars than we get with both Python codes. We speculate that this is a result of OMO's usage of the standard deviation of the data as error bars instead of determining a smaller error of the mean (Sumy et al., 2015). As documented in Figure 2.7, most of our errors are about 6° or smaller, with a

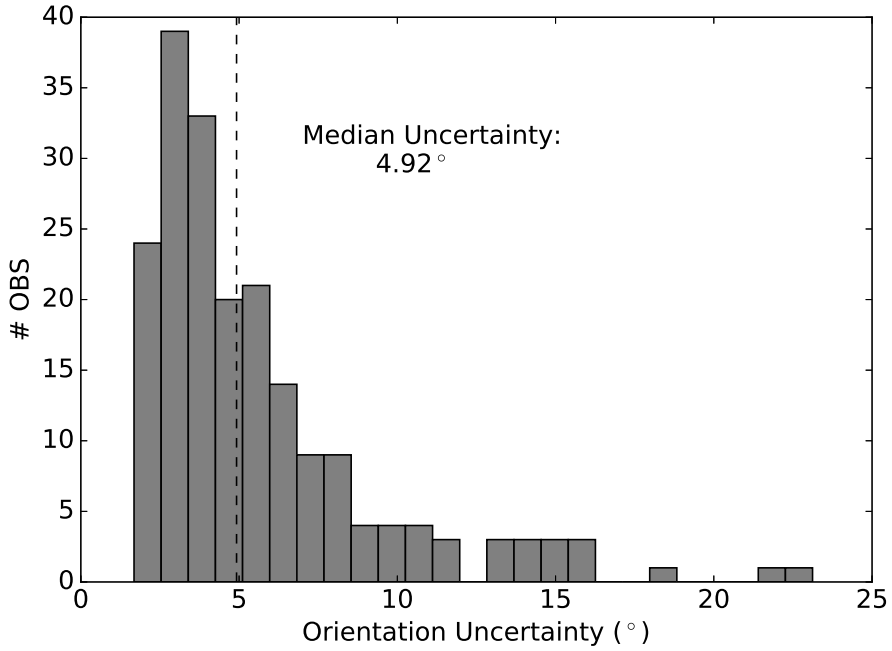

Figure 2.7: Histogram of station orientation uncertainties obtained for the four 1-year Cascadia Initiative deployments using DLOPy. Most uncertainties are smaller than 7°, though a few uncertainties in our database are larger than 100° (not shown).

median of 4.92° (Table 2.3). Our minimum error is 1.68°.

Having a closer look at individual stations, a wide range of errors in the station orientation may be due to widely different ambient noise levels at the OBSs as a result of deployment in a wide range of water depths between less than 100 m and nearly 4500 m. As found by many other investigators of OBS data, shallow-water environments tend to be significantly noisier than those in the deep ocean, particularly at long periods. Consequently, our error bars at shallow stations (water depth $z \leq 500$ m) are three or more times greater than those at deeper stations (Figure 2.8). This tends to be the case for all three algorithms. There also appears to be a relationship between the number of events useful for analysis and water depth, for all three implementations, supporting the idea that deep ocean environments are quieter at long periods (25 to 100 s, as used in this study). As already documented in Table 2.3 but also obvious from Figure 2.8 our results are based on many more earthquakes than those using other algorithms. DLOPy is most

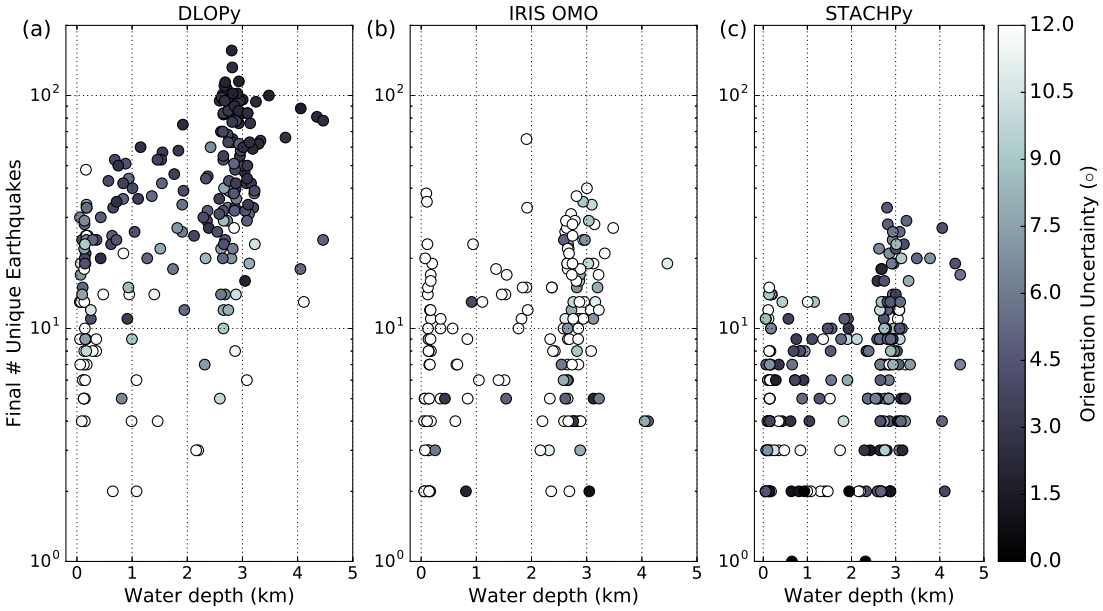

Figure 2.8: Number of unique earthquakes utilized (y-axis) and uncertainty of CI station orientations (gray shades) as a function of water depth. (a) Results using DLOPy; (b) Results reported by IRIS OBS Management Office (IRIS OMO); (c) Results using STACHPy.

consistent in assigning larger error bars for results that are based on only few events. Recall that the two other implementations are based on purely statistical treatment of data samples, which can result in unrealistically small error bars for small datasets, unlike our bootstrapping approach.

We also investigate the dependence of the orientation error on the OBS design. For the Cascadia Initiative, many instruments were newly designed to serve two purposes. Firstly, for deployment on the continental shelf, the instruments needed to be trawl-resistant. The danger of OBSs being disturbed or even displaced by fishing trawlers is particularly great on the wider shelf along the U.S. east coast, but also exists along the narrower west coast shelf. Secondly, the OSNPE clearly showed that burial of a sensor reduces long-period noise in the seismic records. Burial of the sensors is prohibitively costly and time-consuming and was not an option for the CI, but some type of shielding of the sensor should go a long way to reduce current- and wave-induced noise, particularly at shallow sites. While all three OBSIP IICs provided instru-

ments, LDEO designed the trawl-resistant TRM and SIO designed the ABALONE. All three groups used the Nanometrics Trillium Compact 120 as sensor. In addition, WHOI provided traditional broadband OBSs using a Güralp CMG-3T sensor that were deployed primarily in the deep ocean at water depths greater than 2000 m. Furthermore, two traditional SIO instruments were deployed in year 4 (See Data and Resources for additional information). Figure 2.9 shows orientation uncertainties as function of depth and instrument type. As already mentioned, errors tend to be larger for shallow deployments, particularly at water depths less than 200 m. Some large-error deeper deployments tend to be ones with technical problems and/or premature shutdown. For example, for WHOI's year 4 station FS16D deployed at 1080 m water depth, we have only 3 useful measurements from 2 events. While hoping that shielding the seismic sensor would help reduce noise levels particularly on the horizontal components in shallow water, we cannot document that because no standard OBS for comparison was deployed at depths shallower than 716 m. At this depth, the WHOI year 4 instrument at G09D (for which we have 63 data from 24 earthquakes) performed just as well as the shielded OBSs. However, remarkably and perhaps somewhat unexpectedly, the SIO ABALONE has nearly consistently smaller orientation errors than most other instruments for larger water depths. A relatively large error of 15° at year 2 SIO site G12B is the result of a dearth of useful data, with only 17 measurements from 6 earthquakes. While our error bars are not a direct measure for ocean noise on the horizontal seismometer components, we are confident that we can use it as proxy. It seems therefore that the SIO ABALONE competes well with more traditional OBS packages in the deep ocean along Cascadia. Our results are consistent with those of Bell et al. (2015a), who examine tilting on the horizontal components of OBSs from Cascadia year 1 deployment at long periods (50 seconds) and conclude that SIO shielded instruments are quieter than unshielded OBSs at similar depths.

As with PLUME, we conduct a preliminary investigation of the internal consistency of our CI measurements. Figure 2.10 shows 30 mHz R_1 arrival angle measurements for two events in the Solomon Islands that occurred within some 20 km of each other during the year-3 deploy-

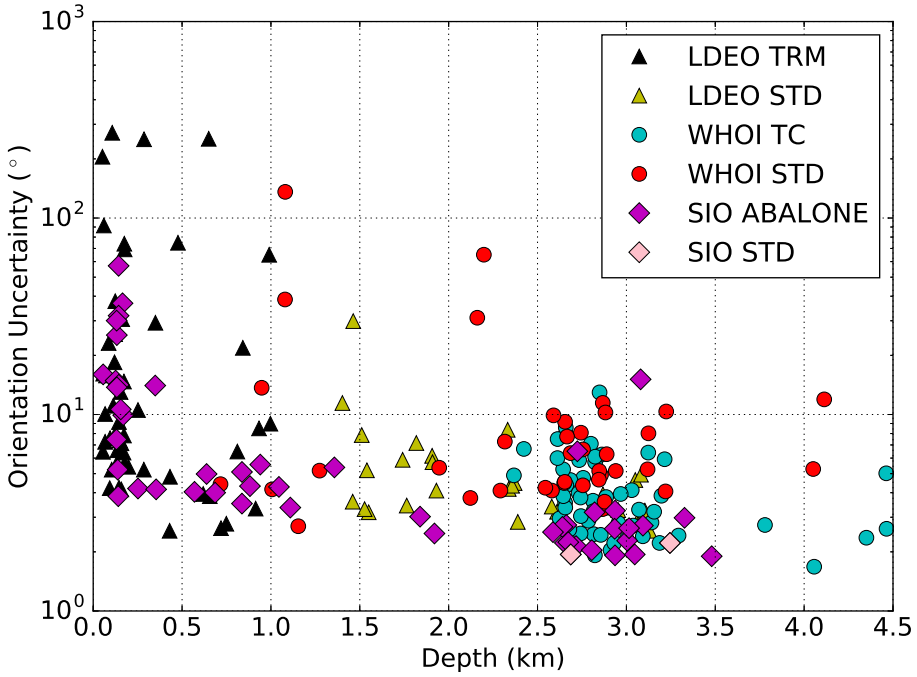

Figure 2.9: Instrument orientation uncertainties determined using DLOPy for the Cascadia Initiative OBSs, as function of water depth and sorted by instrument type. SIO ABALONE and LDEO TRM are shielded, trawl-resistant instruments. LDEO TRM OBSs were deployed only in shallow water ($z < 1000$ m). LDEO STD were standard LDEO OBSs. WHOI TC (Trillium Compact) were newly designed for CI deployments. All these used a Nanometrics Trillium Compact 120s as sensor. The WHOI STD OBSs used a broadband Güralp CMG-3T sensor, and the SIO STD OBSs used a Nanometrics Trillium 240 sensor.

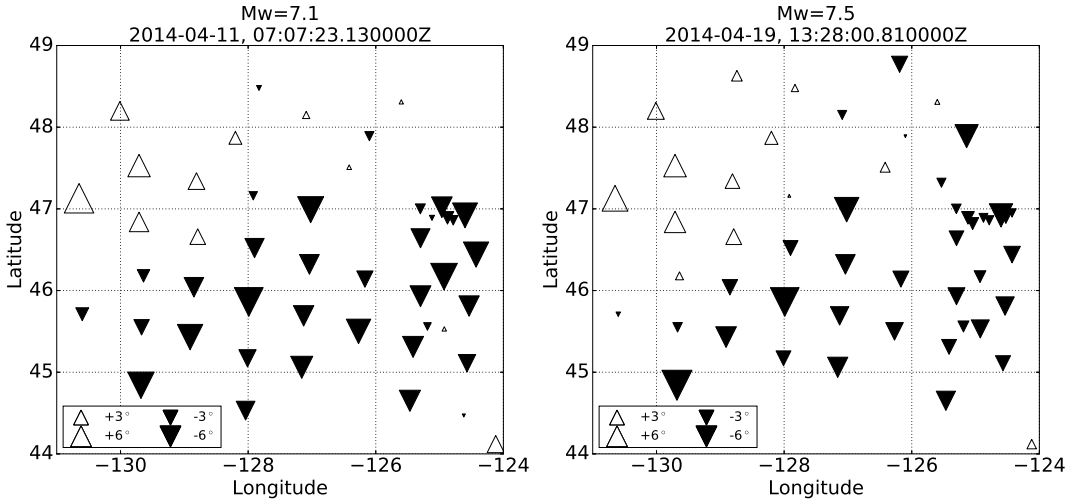

Figure 2.10: Arrival angle deviations from the source-receiver great-circle for R_1 measured at 30 mHz for two close events during the year-3 CI deployment. The events occurred in April 2014 in the Solomon Islands region, at epicentral distances of about 85° (from center of network), with a back azimuth of about −105°. The events were large, with M_W = 7.1 and 7.5, and occurred about 8 days apart. Only stations with a high cross-correlation value (cc>0.9) are shown. The individual measurements were corrected for the final instrument orientation. The shapes of the symbols represent arrival angle deviations in degrees from the great-circle path (GCP). Clockwise rotations are shown in white, while counter-clockwise rotations are shown in black. The triangles are scaled by the magnitude of the deviations.

ment. These events produced high-quality ($C_{zr} \geq 0.90$) measurements on nearly every station. The progression of the arrival angle anomaly across the CI network is spatially coherent and gives consistent measurements between the events, except for a small number of outliers. Arrivals are systematically rotated clockwise in the northwest of the network but counter-clockwise in most of the rest, documenting complex lateral refraction of the Rayleigh waves between the source region and the network. Wave field complexity as expressed by surface-wave arrival angle anomalies has recently been documented on the larger USArray Transportable Array (Foster et al., 2014a).

2.7 Comparison with other Seismic Techniques

Several other seismic approaches have been utilized to determine the station orientation during data post-processing. A number of studies analyze *P*-wave particle motion to estimate horizontal orientations (e.g., Stachnik et al., 2012b; Niu and Li, 2011; Schulte-Pelkum et al., 2001; Toomey et al., 1998), either alone or in combination with surface wave arrival angles. Although both approaches should and often do produce consistent results, we prefer to analyze surface wave arrival angles for a number of reasons. First and foremost, *P*-wave arrivals tend have a small amplitude and are much more likely to be contaminated by noise than surface wave arrivals, particularly on OBS records. Stachnik et al. (2012b) found a factor of 5 more events with acceptable signal-to-noise ratios (SNR) using surface waves as opposed to *P*-waves. Another reason against teleseismic body-wave arrivals is that events have to be in a specific distance range to avoid interference with other phases. This dramatically narrows the number of suitable events compared to a surface-wave study, thus limiting much-needed azimuthal coverage. Not lastly, long-period *P*-waves can display 10° or more deviation from the source back azimuth (Schulte-Pelkum et al., 2001), and thus, as waves propagating in the 3-D Earth may accumulate more effects from lateral refraction than surface waves propagating on a 2-D surface.

Other seismic techniques that determine the instrument orientation during post-processing include shear-wave splitting and receiver function (RF) analyses. Janiszewski and Abers (2015) utilize the receiver function method, whereby the seismometer orientation is determined by minimizing the RF energy on the transverse component, to orient a number of Cascadia Deployment 1 & 3 stations. Zha et al. (2013) use ambient noise correlations to orient the instruments of an OBS network in the Eastern Lau Spreading Center (Zha et al., 2014b). This method calculates the three-component Empirical Green's Function from ambient seismic noise and determines the arrival angle based on principles similar to those described in our chapter. Regardless of the approach, all methods should yield similar values for the instrument orientation to within their

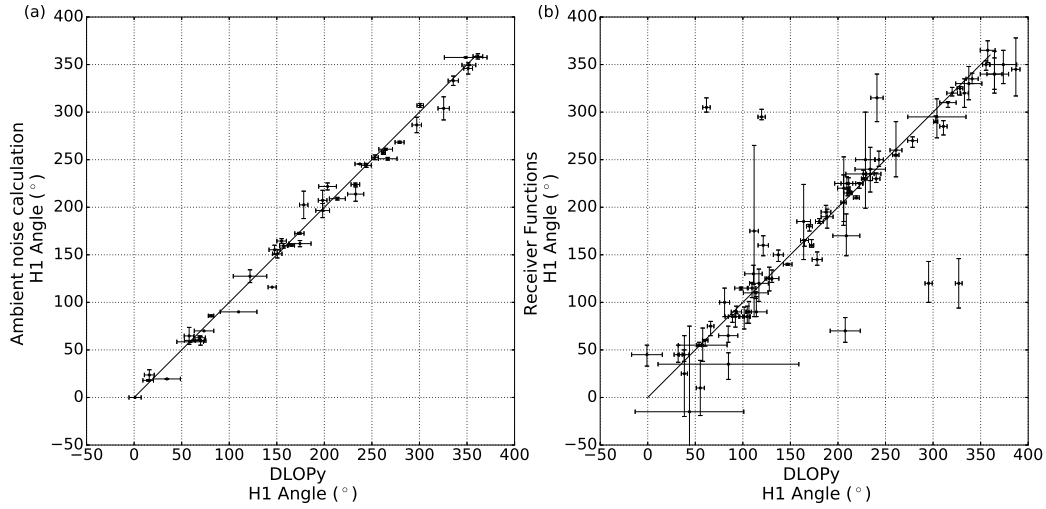

Figure 2.11: A comparison of results obtained for OBS deployments using DLOPy and two other methods. (a) Instrument orientations for the Eastern Lau Spreading Center (ELSC) deployment using ambient noise correlations (Zha et al., 2013, 2014b). (b) Instrument orientations for the CI year-1 and year-3 deployments using receiver functions (Janiszewski and Abers, 2015). Both cases comparisons exhibit significant disagreement. Compare these results with those shown in Figure 2.6(c).

respective error bars. Figure 2.11 compares the results from these methods with those obtained with DLOPy. It should be mentioned here that Zha et al. (2013) use a right-handed coordinate system in their representation and we converted their published results by subtracting them from 180°. Although there is general agreement in the instrument orientations between using these methods and DLOPy, disagreements are much larger than those between using DLOPy and the surface wave arrival angle method of Laske et al. (1994) (see Figure 2.6). Some of the discrepancy may stem from the fact that these methods are based on different seismic observables, and therefore are subject to different errors and biases. However, all methods should give statistically compatible results since there is only one true orientation of the instrument (assuming it does not vary with time), and the methods discussed here show some significant disagreement. Perhaps these examples support the idea that at least for OBSIP deployments, it may be beneficial that instrument orientations be determined using consistently one and the same technique.

2.8 Discussion

This chapter introduces an automated technique to measure Rayleigh wave arrival angles on OBS deployments, with the ultimate goal of determining the orientation of the horizontal seismometer components. Obtaining instrument orientations through the analysis of surface waves has several advantages over using other approaches: surfaces waves are typically the largest signal in a seismogram so signal-to-noise ratios are typically best. There are fewer restrictions on earthquake choices compared to other teleseismic techniques, usually leading to a better azimuthal event coverage. This is important in the light that the arrival direction of seismic phases are typically influenced by lateral refraction in the heterogeneous Earth. For stations with only few earthquakes, particularly when they cluster in a certain source region, the resulting instrument orientation may be in error by as much as 5° or even larger. To obtain unbiased instrument orientations, the arrival angles should therefore undergo a non-linear joint inversion for structure and instrument orientation (e.g., Laske, 1995; Larson and Ekstrom, 2002). Here, we did not do this but simply determined the medians in our datasets. DLOPy tries to accommodate this omission through larger error bars that result automatically for smaller datasets when applying the bootstrap process.

Larson and Ekstrom (2002) determined surface wave arrival angles for GSN stations and other permanent, observatory-quality seismic stations using events between 1989 and 1998 and then compared the differences in the resulting station orientations when including or omitting Earth structure in a joint inversion. For stations with more than 100 measurements, the median discrepancy between both results is only 0.2°. But when the number of measurements drops below this, the discrepancy can be much larger, and the median in the discrepancy for the stations in Larson and Ekstrom (2002) that fall in this category increases to 1.1°. For GSN stations, and using the 10-year dataset, the number of high-quality measurements can drop to below 10 but the discrepancy between simple average and result from joint inversion never reaches beyond 5.6°.

With 23 high-quality data, station SMTC (Superstition Mountain of the Southern Californian TERRAscope/Trinet Network) had the largest discrepancy at 5.6°. However, the error obtained from the inversion was 6.5° so this discrepancy is statistically insignificant. We also demonstrated that the repeatability of individual measurements using the same or different techniques can results in differences in instrument orientations on the order of 1-2°. The main point here is that, for temporary OBS deployments and studies that do not perform a joint inversion for structure to determine instrument orientations, we should probably expect a possible bias on the order of a few degrees. We therefore feel that increasing the error bar from 2-sigma (as reported in other studies) to 4-sigma (this study) is well justified.

Both Laske (1995) and Larson and Ekstrom (2002) analyze both Rayleigh and Love waves. Since Love waves sense shallower structure at the same frequency as Rayleigh waves (e.g., Laske and Widmer-Schnidrig, 2015), some argue that Love waves in general are subject to greater lateral refraction (e.g., Guy Masters, personal communication). Others argue that Love waves are subject to severe interference with Rayleigh-wave overtones (e.g., Foster et al., 2014b; Jin and Gaherty, 2015) and should therefore be excluded from analysis. We find that high singular values in the Laske et al. (1994) method, together with the ellipticity of the particle motion are excellent indicators for the purity of Love waves, and we maintain that including Love waves in the process yields less bias in station orientations. In fact, it is not uncommon that the high-quality Love-wave arrival-angle datasets are larger than the corresponding Rayleigh wave datasets. In a noisy seismogram, it is often easier to make high-quality Love wave measurements than Rayleigh wave measurements using the Laske et al. (1994) method because the waveforms are less dispersed in the frequency band of interest. Consequently, windows are shorter and less noise or other signals enter the measurement. We attempted to analyze Love waves with DLOPy. Using the dispersion maps of Ma et al. (2014) to determine our analysis windows we would expect that the correct angle is found when the rotated H2 component, H2', has no correlation with the Hilbert-transformed vertical (i.e. it is zero). It turns out that in this case,

we again achieve maximum correlation between H1' and the Hilbert-transformed vertical, so we used the latter as criterion. However, Rayleigh wave overtone signals in the same window also lead to increased correlations between these components. To make matters worse, random checks of the corresponding 3-component seismograms indicate that in highly correlating cases, the front end of the Rayleigh wave is present, implying that our automated windows are too long to separate out the Love wave effectively. We therefore exclude the analysis of Love waves at this point.

The exclusion of Love waves is an important weakness of Rayleigh-wave only methods such as DLOPy, and may explain much of the discrepancy seen in the final orientation estimate at ESK. Also, if we deal with uneven event coverage on a heterogeneous Earth, then orientations based solely on statistical averages instead of on a joint inversion for structure may well be biased. Considering only the year 2004 and only statistical averages, the Laske et al. (1994) method calculates an overall orientation of 0.17 ± 0.82 for ESK, but using only Rayleigh waves yields an orientation of 1.32 ± 1.97, which is statistically consistent with the DLOPy results. Although ESK may be an extreme case, a systematic error of some 2° must be considered a realistic possibility. Using only Rayleigh wave data is probably a sufficient and appropriate strategy for quick determination of instrument orientations for OBS and temporary networks. Permanent observatory stations such as those of the GSN should include high-quality Love wave data to reduce potential bias.

2.9 Summary

We have developed an automated method, DLOPy, to determine the geographic orientation of horizontal seismometer components. Our automated procedure measures frequency-dependent arrival angles of intermediate- and long-period fundamental mode Rayleigh waves from the first major and minor great-circle arcs. Our technique uses optimized but conservative

confidence intervals to provide realistic orientation estimates and uncertainties, and can produce reliable sensor orientations for deployments as short as several months. We validated our method by comparing our overall instrument orientations as well as our individual arrival angle measurements with results from well-established techniques at high-quality GSN stations and OBS deployments of various lengths. While DLOPy can be applied to all broadband three-component instruments, it is particularly intended for use with free-fall OBSs and other temporary deployments in need of quick determination of instrument orientations. We presented orientations for all OBS stations with sufficient data from the large-scale Cascadia Initiative amphibious project. We provided evidence that newly-developed shielded OBSs provide substantial improvement to long-period data quality even in the deep ocean. Our technique was designed with accuracy, automation, and ease-of-use in mind. DLOPy provides a simple, stable, and standardized method to compute accurate orientations and meaningful uncertainties with minimal bias without undergoing a formal joint inversion for Earth structure.

2.10 Acknowledgements

We wish to thank OBSIP and their IICs at SIO, WHOI and LDEO, and the principal investigators of OSNPE and MOBB for producing and releasing data of the OBS deployments discussed in this study. All data are publicly available through the IRIS and NCEDC data management centers. We wish to thank Pete Davis and Wenyuan Fan for stimulating discussions and Alex Burky for help with the data analysis. We wish to thank Barbara Romanowicz for helpful discussions about MOBB orientation. We thank Associate Editor Thomas Brocher, along with three anonymous reviewers, for very helpful reviews that helped clarify and improve the manuscript. This research was funded through NSF grants EAR-1215636, EAR-1415763 and EAR-1446978.

Waveforms, station metadata, and earthquake catalogs are publicly available and were ac-

cessed through the IRIS DMC (last accessed May 2016) and the NCEDC (doi:10.7932/NCEDC) for station MOBB (last accessed May 2016). GSN operator IRIS-IDA provided the data for stations ESK and SACV. IRIS OMO provides the MATLAB implementation of the Stachnik et al. (2012b) code on the OBSIP website at http://www.obsip.org/data/ obs-horizontal-orientation/ (last accessed May 2016). Site http://www.obsip.org/instruments/cascadia-instruments/ was last accessed May 2016. More information about the Cascadia Initiative can be found at http://cascadia.uoregon.edu (last accessed May 2016). More information on OBSIP and CI instrumentation can be found at http://www.obsip.org/instruments/cascadia-instruments/ (last accessed September 2016). Zhitu Ma provides his surface wave dispersion maps on the LITHO1.0 website at http://igppweb.ucsd.edu/∼ gabi/litho1.0.html (last accessed April 2016). Many of the geodesic calculations utilize the methods of Karney (2013), and implementations in several languages can be found at http://geographiclib. sourceforge.net (last accessed March 2016). Figure 1 was drawn using Adobe Illustrator while all other figures were drawn using Python 2.7 (Python Software Foundation, http://www.python.org, last accessed September 2016). A distribution of our code is available at http://igppweb.ucsd.edu/∼gabi/ and http:// igppweb.ucsd.edu/∼adoran/. The full table of Cascadia orientations and a table of PLUME2 orientations can also be found on these websites.

Chapter 2, in full, is a reformatted version of a publication in Bulletin of the Seismological Society of America: Doran, A.K., and G. Laske (2017), Ocean-bottom seismometer instrument orientations via automated Rayleigh-wave arrival angle measurements, Bull. Seism. Soc. Am. 107, 691-708. DOI: 10.1785/0120160165. I was the primary investigator and author of this paper.

3 Seismic structure of marine sediments and upper oceanic crust surrounding Hawaii

3.1 Abstract

We present models of compressional and shear velocity structure of the oceanic sediments and upper crust surrounding the Hawaiian islands. The models were derived from analysis of seafloor compliance data and measurements of Ps converted phases originating at the sediment-bedrock interface. These data were estimated from continuous broadband ocean-bottom seismometer acceleration and pressure records collected during the Plume-Lithosphere Undersea Mantle Experiment, an amphibious array of wideband and broadband instruments with an aperture of over 1000 kilometers. Our images result from a joint inversion of compliance and Ps delay data using a nonlinear inversion scheme whereby deviation from *a priori* constraints is minimized. In our final model, sediment thickness increases from 50 meters at distal sites to over 1.5 kilometers immediately adjacent to the islands. The sedimentary shear velocity profiles exhibit large regional variations. While sedimentary structure accounts for the majority of the compliance signal, we infer variations in shear velocity in the uppermost bedrock on the order of $\pm 5\%$. We also require relatively high values of Poisson's ratio in the uppermost crust. Lower crustal velocities are generally seen to the north and west of the islands but do not appear well correlated with the Hawaiian Swell bathymetry. A region of strong low velocity anomalies to the northeast of Hawaii may be associated with the Molokai Fracture Zone.

3.2 Introduction

The Hawaiian island chain is often viewed as the archetypal example of hotspot volcanism affecting a moving plate, with buoyant melt fed to the surface from a stable mantle plume, a thermal upwelling rooted deep in the mantle. The structure of the Hawaiian hotspot controls surface volcanism and provides essential insight into mantle dynamics, melt transport, and the evolution of intraplate volcanoes. No single hypothesis explaining the dominant cause of the Hawaiian Swell, the bathymetric uplift around the islands, has gained widespread acceptance.

In one model, the lithosphere reheats and thins over a hotspot, causing seafloor uplift ("thermal rejuvenation"; e.g., Detrick and Crough (1978)). In another, the mantle plume itself causes the entire unaltered lithosphere to rise by exerting normal stresses at the base ("dynamic support"; e.g., Olson (1990)). Existing geophysical data are seemingly inconclusive or contradictory. For example, Cadio et al. (2012) analyzed geoid measurements and ruled out thermal rejuvenation as an important mechanism, while recent tomographic images were most consistent with a hybrid model of thermal rejuvenation and dynamic support (e.g., Li et al., 2004; Laske et al., 2007, 2011). Other studies have introduced ideas of chemical buoyancy in the form of crustal underplating to reconcile the observed bathymetry with heat flow measurements (Phipps Morgan et al., 1995). To complicate matters further, some researchers still question the necessity of invoking a deep-rooted mantle plume at all, preferring to explain the Hawaiian hotspot through cracks in the lithosphere, sublithospheric convection, or other processes restricted to the upper mantle (e.g., Natland and Winterer, 2005; Anderson, 2011).

One major impediment to improved understanding of the Hawaiian hotspot is uncertainty in the elastic parameters of the near-surface, namely the sediments and crust beneath and near Hawaii. Such uncertainties can affect seismic imaging results of the crust and uppermost mantle (e.g., Leahy et al., 2010; Laske et al., 2011). Although density (ρ), compressional velocity (Vp), and shear velocity (Vs) are all known to vary in the oceanic crust, basic questions remain regarding the amplitude and wavelength of such variations. The sensitivity of even long-period seismic data to near-surface structure is well documented, as are the nonlinear effects of strong lateral variations in crustal structure (e.g., Montagner and Jobert, 1988; Marone and Romanowicz, 2007). This effect is not limited to seismic tomography. Interpretations of many geophysical observables, including gravity data (e.g., Basuyau et al., 2013; Herceg et al., 2016) and heat flow measurements (e.g., von Herzen et al., 1989), can be biased by inaccurate assumptions about the crust.

A standard model of the oceanic crust includes low-velocity marine sediments (Layer

1), an upper crust comprised of sheeted dikes and pillow basalts (Layer 2, often subdivided into 2A and 2B), and a lower crust comprised primarily of gabbros (Layer 3). This model was first proposed by Raitt (1963), and has been subsequently refined but not significantly altered. Seismically, we now typically assume Layer 2 to be 1.5 km thick and have Vp gradients of 1 [km/s]/km or greater, and Layer 3 to be 4.5 km thick and have shallower Vp gradients of 0.1-0.2 [km/s]/km (e.g., Spudich and Orcutt, 1980a; White et al., 1992; Harding, 2001). A number of studies have documented the heterogeneity of very young crust, which can exhibit very strong lateral Vp gradients on the scale of several kilometers (Henig et al., 2012; Arnulf et al., 2012, 2014a). While strong local horizontal gradients have been observed away from spreading centers (e.g., Stephen, 1988), Pacific crust older than 20 Ma is generally assumed to be largely uniform (White et al., 1992; Christeson et al., 2017). Around the Hawaiian islands, the oceanic crust increases from a typical thickness of approximately 6 km off the Swell to nearly 20 km beneath the island of Hawaii (e.g., Zucca et al., 1982; Watts et al., 1985; Watts and ten Brink, 1989; Leahy et al., 2010). Local variation in crustal structure has been attributed to lithospheric flexure (ten Brink and Brocher, 1987), and evidence has also been presented for systematic differences in crustal thickness across the Molokai Fracture Zone (ten Brink and Brocher, 1988). The thickness and velocity of local sediments show strong regional differences, and thickness has been observed to increase from 100 m far from the islands to over 2 km within the Hawaiian Moat (Rees et al., 1993; Leslie et al., 2002).

The Hawaiian Plume-Lithosphere Undersea Mantle Experiment (PLUME; Laske et al., 2009) sought to improve our understanding of the Hawaiian hotspot by deploying onshore and offshore seismic instruments with a wide aperture around the Hawaiian hotspot (Fig. 3.1). Data collected during the PLUME deployment have contributed significant evidence for a mantle plume rooted in the transition zone or deeper (Wolfe et al., 2009, 2011) with complex non-vertical pathways of upwelling mantle melt (Laske et al., 2011; Rychert et al., 2013; Agius et al., 2017). A coincident MT experiment observed a narrow conductive plume extending from

the islands into the lower mantle (Constable and Heinson, 2004). However, the near-surface structure of the crust, particularly shear structure, has yet to be investigated in detail.

This chapter aims to image the sediments and upper oceanic crust around Hawaii and provide constrains on the scale of spatial variations in this region. We have measured seafloor compliance, the displacement of the seafloor in response to oceanic infragravity wave loading. Compliance data are sensitive to near-surface elastic structure, particularly low-velocity zones and sediments (e.g., Crawford et al., 1991; Crawford and Webb, 2002; Zha and Webb, 2016). We complemented these data by measuring Ps converted phases originating at the sediment-bedrock interface. These measurements provide an independent constraint on the thickness and velocity structure of seafloor sediments (e.g., Shen et al., 1997; Harmon et al., 2007a; Agius et al., 2018), a significant source of ambiguity for compliance analyses. We incorporated *in situ* borehole measurements of density and Vp in the sediments and uppermost crust along with the previous structural results of Lindwall (1991) as *a priori* information to further constrain our modeling. Together these data allowed an investigation of unprecedented lateral detail of upper crustal structure both on and off the Hawaiian Swell. We jointly inverted compliance data and Ps delay measurements for sedimentary and crustal structure around the Hawaiian islands through a nonlinear constrained minimization. We found significant variation in sediment thickness and shear velocity profiles across the array. Our results also suggest that shear velocity of the uppermost crust varies on the order of $\pm 5\%$ over lateral scales of tens of kilometers. Our data are consistent with largely uniform compressional velocity in the uppermost crust over these same length scales.

3.3 Data

Seafloor compliance is a measure of the deformation of the seafloor in response to loading from infragravity waves. Infragravity waves propagate through the deep oceans with periods

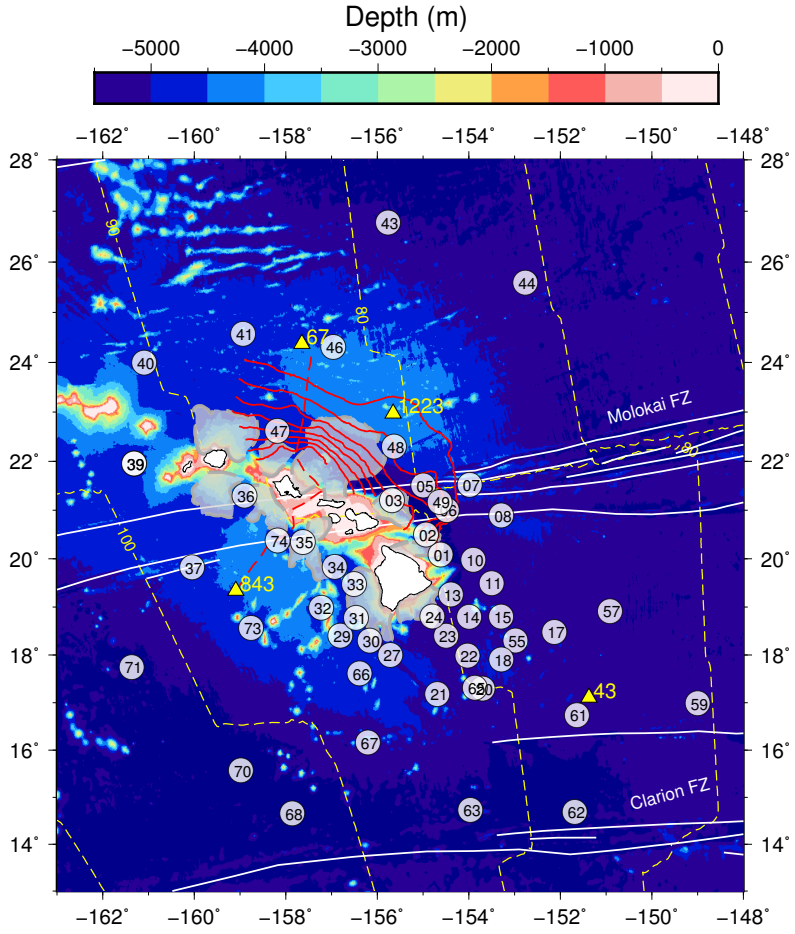

Figure 3.1: Locations of all PLUME OBSs used in this study. Crustal ages from Müller et al. (2008) are shown in 10 Ma intervals in dashed yellow lines. The shaded gray areas are volcanic sedimentary deposits mapped by Moore et al. (1989). The yellow triangles show the locations of, clockwise from the northernmost: DSDP site 67, ODP site 1223, DSDP site 43, and ODP site 842/843. The red dashed line running north-south to the east of Oahu shows the seismic profile line of Watts et al. (1985). The red lines to the north of the islands represent 100 millisecond two-way travel time sediment isochrons (from 100 ms on the furthest lines to 800 ms on the closest) as presented by Rees et al. (1993). The bathymetry is taken from the Hawai'i Mapping Research Group at the University of Hawai'i at Manoa (http://www.soest.hawaii.edu/HMRG/multibeam/index.php) and the two-minute averaged grids of Smith and Sandwell (1997) (http://topex.ucsd.edu/marine_topo/). Estimated traces of the Molokai and Clarion Fracture Zones as presented by Matthews et al. (2011) are shown in white.

longer than 30 seconds and amplitudes of several millimeters, and are the dominant source of energy recorded by ocean-bottom seismometers and pressure sensors between microseism and tidal frequencies (e.g., Webb, 1998; Ardhuin et al., 2014). Normalized seafloor compliance $\eta(\omega)$, the transfer function between vertical displacement and seafloor pressure multiplied by the wavenumber $k(\omega)$ of the forcing waves, is defined as

$$\eta(\omega) = k(\omega)\gamma(\omega)\sqrt{\frac{|S_d(\omega)|}{|S_p(\omega)|}} = \frac{k(\omega)\gamma(\omega)}{\omega^2}\sqrt{\frac{|S_a(\omega)|}{|S_p(\omega)|}} \tag{3.1}$$

where $S_d(\omega)$ is the displacement spectrum, $S_a(\omega)$ is the displacement spectrum, $S_p(\omega)$ is the pressure spectrum, $\gamma(\omega)$ is the signal coherence between the two signals, and ω is angular frequency (Crawford et al., 1991, 1998, 1999). We prefer to start our data processing in terms of acceleration in order to simplify corrections for additional terms described later. The compliance of a uniform half-space can be solved analytically, and was shown by Crawford (2004) to be

$$\eta(\omega) = k\frac{\mathbf{u}}{\tau_{zz}} = \frac{\lambda+2\mu}{2\mu(\lambda+\mu)} = \frac{V_p^2}{2\rho V_s^2(V_p^2-V_s^2)} \tag{3.2}$$

where $\mathbf{u}$ is the seafloor displacement, τ_{zz} is the component of stress in the vertical direction at the seafloor, and λ and μ are the Lamé parameters. Examination of the partial derivatives reveals that the sensitivity is highly nonlinear, and that all three elastic parameters affect compliance data:

$$\frac{\partial\eta}{\partial V_p} = -\frac{V_p}{\rho(V_p^2-V_s^2)^2} \qquad \frac{\partial\eta}{\partial V_s} = -\frac{V_p^2(V_p^2-2V_s^2)}{\rho V_s^3(V_p^2-V_s^2)^2} \qquad \frac{\partial\eta}{\partial\rho} = -\frac{V_p^2}{2\rho^2 V_s^2(V_p^2-V_s^2)} \tag{3.3}$$

Note that each partial derivative is negative, indicating that an increase in the velocity or density of the crust leads to a decrease in compliance. Unlike path-averaged measurements, such as surface wave or body wave travel times, compliance data are essentially *in situ* point

measurements. Hulme et al. (2005) demonstrated with a 2D forward modeling code that the sensitivity of compliance data is typically restricted to structure within 5 km of the instrument. In this study we modeled compliance data using a 1D propagator matrix code (Gomberg and Masters, 1988; Crawford et al., 1991). Figure 3.2a plots the sensitivity of compliance data as a function of depth and frequency for a realistic oceanic crustal model lacking a sedimentary layer. Lower frequencies are sensitive to deeper structure, but the data have maximum sensitivity to the different elastic parameters at different depths. Furthermore, all parameters have non-negligible contributions in the upper crust. Unlike the analytic solution for a half-space, in which the partial derivatives are always negative, note that for realistic Earth structures, the sensitivity changes sign in the uppermost crust for Vs while remaining negative for Vp and ρ. However, compliance sensitivities are highly dependent on the starting model, and when sediments are present, all frequencies are most sensitive to the sedimentary properties (Figs 3.2b, 3.2c). This can pose an acute problem when the precise thickness and velocity structure of the sediments are unknown, since inaccuracies in the sediments can bias interpretations of underlying crustal structure.

PLUME consisted of two year-long deployments of wideband and broadband ocean bottom seismometers (OBS) at over 60 seafloor sites with an array aperture of over 1000 km (Fig. 3.1). The experiment included ten additional temporary land stations and took advantage of three GSN stations (KIP, POHA, and MAUI), but in this study we incorporated only the seafloor instruments. The majority of the OBSs were provided by Woods Hole Oceanographic Institute (WHOI) and contained Güralp CMG-3Ts (corner period at 120 seconds). The remaining instruments were provided by Scripps Institution of Oceanography (SIO), of which the PLUME phase 1 instruments contained Nanometrics Trillium 40 wideband seismometers (corner period at 40 s) and the PLUME phase 2 instruments contained Nanometrics Trillium 240 broadband seismometers (corner period at 240 s). All instruments contained Cox-Webb differential pressure gauges (DPGs; Cox et al. (1984)). Adjustments to the nominal instrument responses were required for the SIO seismometers (Figure S1) and all DPGs. We individually calibrated the

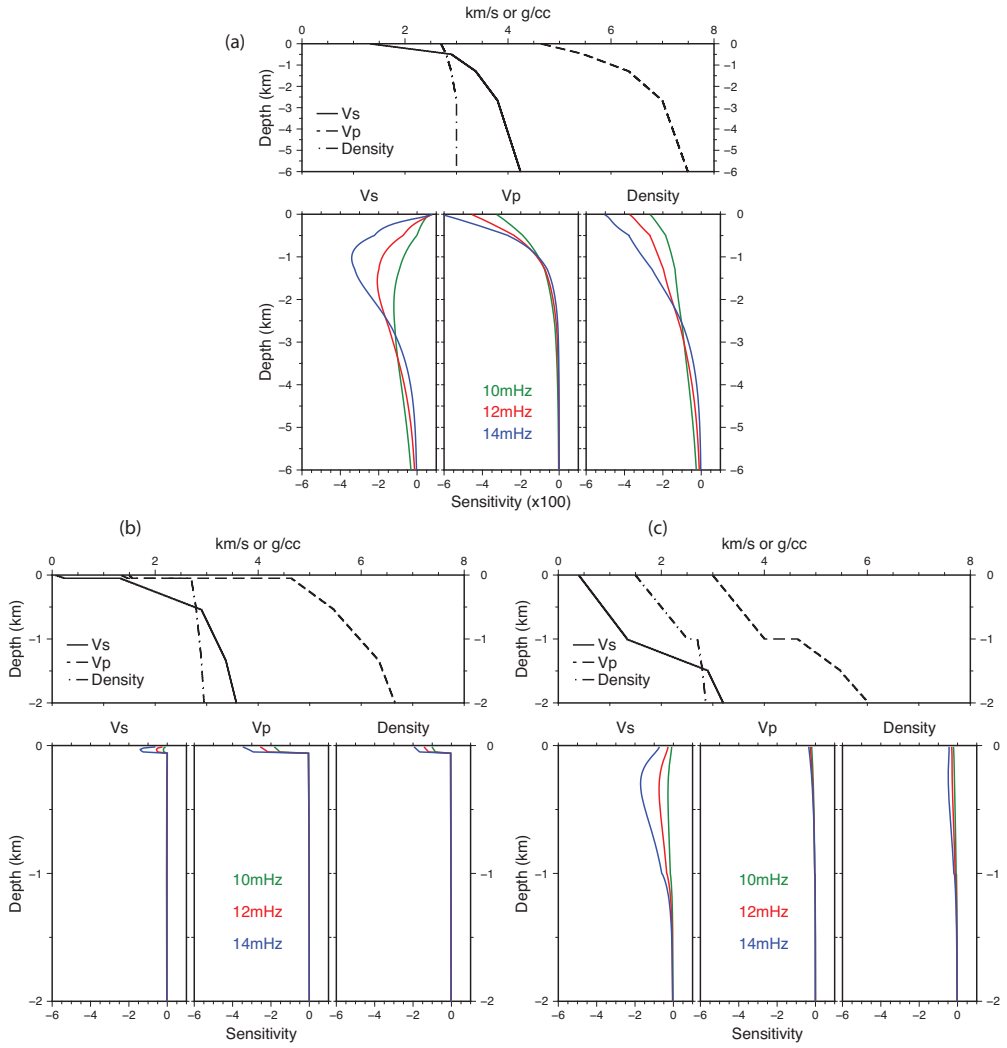

Figure 3.2: The sensitivity of the compliance function to fractional changes in model parameters. For each panel, the starting model is shown on top, while the sensitivity functions for 10, 12, and 14 mHz are shown below. The kernels are calculated assuming a water depth of $H = 5000$ meters. (a) Kernels computed for a typical oceanic crust with no overlying sediments. (b) Kernels computed for a typical crust with 100 meters of slow, pelagic sediments overlying the crust. (c) Kernels computed for a typical crust with 1000 meters of fast, volcanic sediments overlying the crust. Notice that the vertical scale only covers 2 km for the two lower sets of kernels. The sensitivities in panel (a) were multiplied by 100 to allow comparison with the sensitivities in (b) and (c).

gain of the DPGs using the technique of Zha and Webb (2016) and calibrated the long-period frequency response of the DPGs with tidal models of Egbert and Erofeeva (2002). Additional details can be found in the supplemental DPG Appendix C (see also: An et al. (2017)).

We analyzed discrete one-hour segments of 1 sps continuous data. We first removed the tilt-induced noise from the vertical acceleration data, a process which has been shown to improve the long-period ($<$ 10 s) signal by 20 dB or more (e.g., Crawford and Webb, 2000; Crawford et al., 2006) and is now regularly applied to free-fall OBS data (e.g., Dolenc et al., 2007; Taira et al., 2014). We specifically followed the method of Bell et al. (2015a), whereby the angle and direction of tilt are also found. We then calculated the pressure-acceleration transfer function and removed the instrument response. We also removed an additional acceleration term, the gravitational attraction of the water column above the station, which is induced by the changing mass of the water column. The acceleration is given by $a_w = 2\pi G\rho_w e^{-kH} h_w$, where G is the gravitational constant, ρ_w is the density of the water, H is the water depth, and h_w is the infragravity wave height, calculated directly from the pressure signal (Crawford et al., 1998; Zha et al., 2014a). The effect at PLUME sites, with water depths $\geq$4.5 km, was to increase compliance values by several percent at frequencies less than 10 mHz, with a decreasing effect as frequency increases. From the suite of resulting compliance estimates, we retained only segments with a median infragravity coherence above 0.8 and removed those within two hours of a global $M_w \geq 6$ earthquake, which often produced high coherence during the passing Rayleigh waves but obeyed a different dispersion relation and therefore could have contaminated our compliance estimates. We note that the SIO phase 2 instruments produced data that contained a long-period transient that occurred approximately every 3625 seconds and lasted for about ten minutes. While effective techniques have been developed to remove these transients (e.g., Deen et al., 2017), here we simply examined 30 minute transient-free windows for these stations, which was sufficient to observe signals with periods $<$200 seconds.

As described by Crawford et al. (1991), increasing water depth decreases the frequency

range in which the signal can be observed on the seafloor. The maximum frequency at which infragravity waves can exert significant pressure on the seafloor is given by

$$f_c = \left[\frac{g}{2\pi H n}\right]^{1/2}, \quad 0.5 < n < 2 \tag{3.4}$$

where g is the acceleration due to gravity and H is the water depth. Assuming $n = 1$ and $H = 5000$, we find $f_c \approx 17$ mHz. Increasing the water depth lowers the maximum theoretical frequency. However, the noise floor can be significantly lower at deep OBS sites compared to shallow sites (e.g., Webb and Crawford, 2010; Doran and Laske, 2017). While infragravity waves are evident to periods of 1000 seconds or longer (Aucan and Ardhuin, 2013), the low-frequency limit of our measurements was determined by the frequency rolloff in the instrument response of the seismometers and pressure gauges. We observed strong infragravity signals on the CMG-3T and T240 instruments, but we were unable to see consistent signals on the T40s due to high instrument noise at low frequencies. In practice, we typically observed sufficiently high pressure-acceleration coherence between 7 and 14 mHz, although some variation in the final frequency range was observed at each site. Figure 3.3 summarizes our calculated compliance data at 43 sites. Uncertainties were estimated from the standard deviation of the measurements for all one-hour segments at each station, for each frequency.

To address potential ambiguity resulting from the trade-offs between model parameters (primarily sediment thickness and shear velocity), we incorporated Ps converted phase delay times to provide additional constraints on sediment velocities and thickness. The high impedance contrast between the bedrock and sediments produces a strong P-S conversion at their interface. The corresponding phases are observed as a slight delay of the first arrival on the horizontal components as compared to the vertical component. The delay time δt is a function of the sediment thickness h, shear velocity, compressional velocity, and incidence angle θ, such that

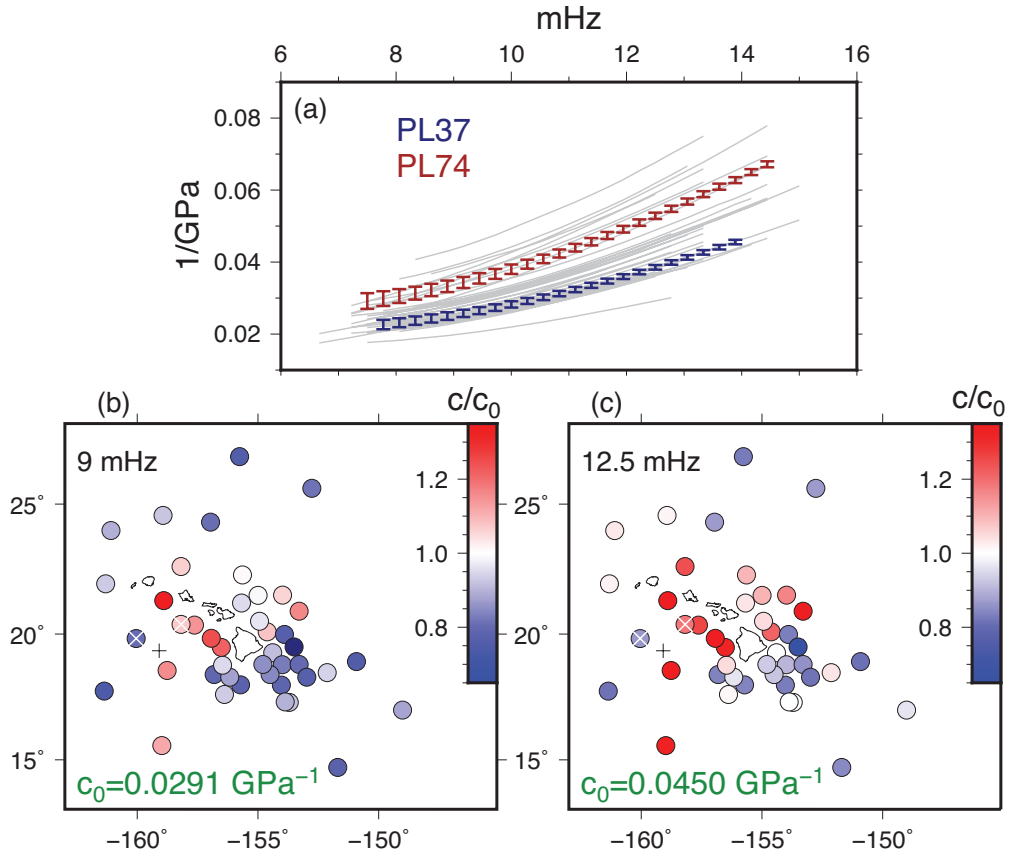

Figure 3.3: (a) Compliance as a function of frequency for all sites considered in this study. Two sites which are described in detail in this chapter, PL37 and PL74, are highlighted. (b) A map view of our compliance data at 9 mHz. The values are shown as a fraction of a reference value for each frequency. The reference values were obtained by calculating synthetic compliance values (bottom left corner) for the Hawaiian crustal model SWELL of Laske et al. (2007). The plus symbol marks the location of OSN site 843 and the white crosses identify PL37 (western site) and PL74 (eastern site). (c) The same as (b) but for 12.5 mHz.

$$\delta t = h\left(\frac{1}{V_s \cos\theta_s} - \frac{1}{V_p \cos\theta_p}\right) \tag{3.5}$$

If we assume a nearly vertical incidence caused by the high impedance contrast between the bedrock and sediments, $\cos\theta_s \approx \cos\theta_p \approx 1$. We examined all events with $6.5 \geq M \geq 4$ given by the USGS earthquake catalog within 1000 km of the array during the PLUME phase 1 and phase 2 deployments. We included events with $M \geq 3.5$ in the analysis of PLUME phase 2 stations in order to increase the number of measurements. The events are listed in Supplemental Tables S3.1 and S3.2. For each event at each station, we bandpass filtered the data between 2 and 10 Hz and manually picked the P arrival on the vertical and pressure components and the Ps converted arrival on the horizontal components. We included only events with high signal-to-noise ratios and with clear first arrivals on all three components. We rotated the horizontal components to radial and transverse orientations. The station orientations were estimated using the methods of Laske et al. (1994) and Doran and Laske (2017) (station information can be found in Supplemental Tables S3.3 and S3.4). The typical uncertainty of the orientations was on the order of 2°. In our final analysis, we used only stations with at least three Ps delay measurements. We confirmed that the measured delay time was independent of source-receiver distance for regional events (Figure S2).

Figure 3.4a shows an example of a Ps measurement at an SIO station. The first arrival on the horizontal channels trails the first arrival on the vertical and pressure channels, characteristic of the Ps converted phase. Eight measurements were made at station PL06, giving a delay time of 0.47 ± 0.04 seconds. We aligned the events on the first vertical-component arrivals and stacked the waveforms (Fig. 3.4b). We self-normalized each trace by setting the maximum amplitude of each waveform to unity in order to give equal weight to each event. The stacked waveforms improve the signal-to-noise ratio and clearly show the sedimentary Ps delay. To get a sense of the geographical patterns and inter-station consistency of the Ps delay times, Figure 3.5 summarizes the measurements at all stations. The majority of Ps delay times fall between 0.4

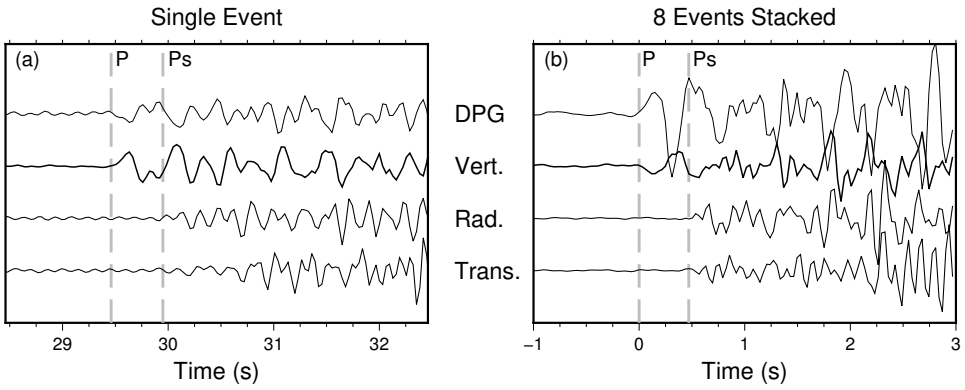

Figure 3.4: Four-component time series recorded at site PL06. The data were filtered between 2 and 10 Hz. (a) Time series following the 2005-334 M4.2 event. The time is shown as seconds since the event origin time. Each amplitude was self-normalized. Manual picks for the first arrival on the vertical and pressure trace and on the horizontal traces are shown. The measured delay for this event is 0.49 seconds (see dashed lines). (b) Stacked data from eight events measured at this site. The waveforms were aligned on the first arrival on the vertical and pressure traces. The stacked delay at this station was determined to be 0.47 $\pm$ 0.04 seconds.

and 0.6 seconds. Several sites, particularly to the immediate southwest of the islands, showed delays of up to 0.8 seconds or longer, indicating thicker or slower sediments.

3.4 Data Analysis

3.4.1 Data Modeling at PL37

We first sought to test whether existing crustal models were adequate to explain our data. We considered station PL37, located southwest of the islands, within 100 kilometers of the Ocean Seismic Network (OSN; Stephen et al., 2003b) site and on the edge of the Hawaiian Swell (Fig. 1). We used the SWELL model of Laske et al. (2007, 2011), which contained 200 meters of sediment on top of a three-layer crystalline crust. This sediment thickness is consistent with the drilling results at ODP hole 843, which found 228.8 meters of sediment at site A and 242.5 meters at site B (Fig. 3.6; Dziewonski et al. (1992a)). Our initial modeling showed that including this much sediment over-predicted the compliance data. We first adjusted only the sediment thickness, but the high and low frequencies could not be modeled simultaneously.

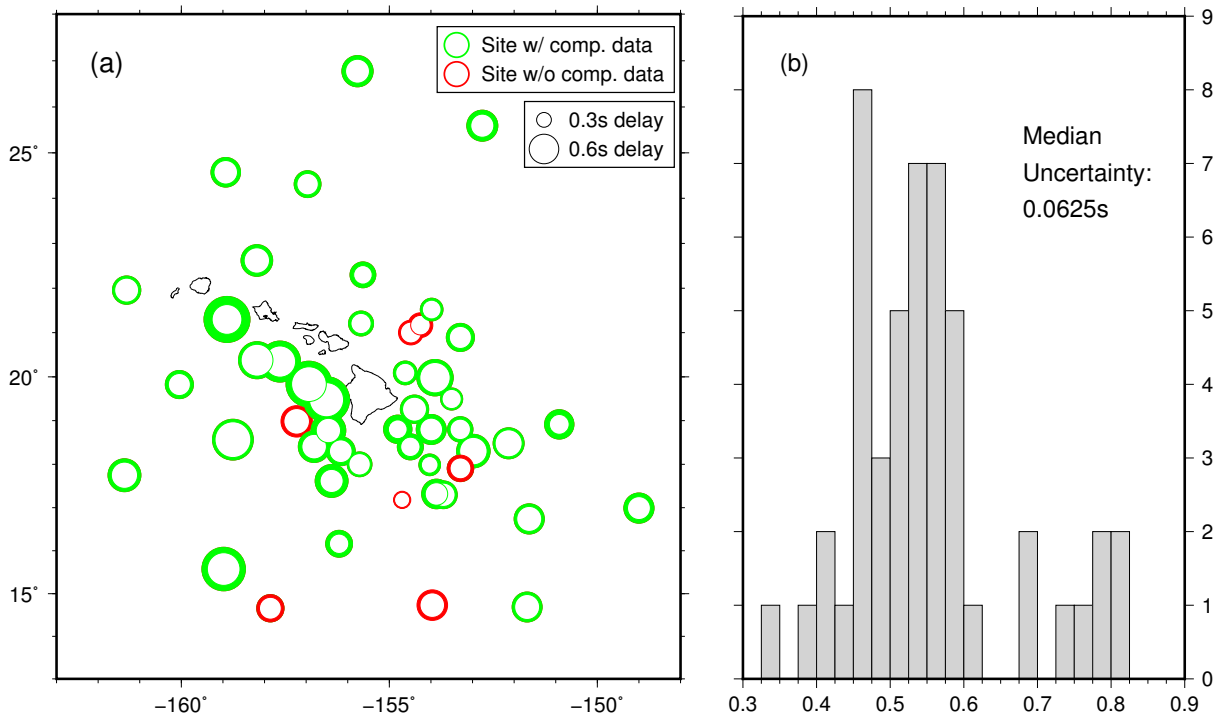

Figure 3.5: (a) A map view of sediment Ps delay times measured at each PLUME station. The circles scale with the measured time, where the line width reflects the uncertainty. (b) A histogram of the measured delay times. The majority of sites have delay times between 0.4 and 0.6 seconds. Several sites have delay times greater than 0.7 seconds, nearly all of which are located to the immediate southwest of the island chain.

Fitting the lowest frequencies required thinner sediments than fitting the highest frequencies. We also tested the detailed crustal model of Lindwall (1991), derived from reflection and refraction data within 50 km of PL37, but encountered similar problems. We were able to fit the data with 80 meters of sediment with an average Vp/Vs ratio of 27 with the SWELL crustal model (producing a synthetic Ps delay time of 1.03 seconds) and an average Vp/Vs ratio of 32 for the Lindwall crustal model (producing a synthetic Ps delay time of 1.48 seconds). In addition to being unrealistic, these values do not agree with the measured delay time of 0.51 ± 0.05 seconds at PL37, demonstrating the utility of including these data in the modeling of compliance. Using a constant Vp value of 1.5 km/s, closer to what was measured *in situ* (Fig. Dziewonski et al. (1992a)), only increased the discrepancy.

We defined a new model of one sedimentary layer overlying crustal layers 2A, 2B, 3A and 3B (Table 1). The model was created to be consistent with the measurements from ODP hole 843 and with the active seismic results of Lindwall (1991). We fixed linear gradients in the sediments of $\rho(z) = 1350 + 1.5z$ kg/m^3 and $V_p(z) = 1500 + 1.0z$ m/s, based on the borehole data shown in Figure 3.6. These gradients are very similar to those found by Hamilton (1978) for Vp and Hamilton (1976a) for density of pelagic sediments in the upper 250 meters. We set Vs at the seafloor to be 75 m/s, consistent with other studies of seafloor sediments (e.g., Hamilton, 1976b; Nolet and Dorman, 1996). Our initial Vp and Vs structure below the sediments approximated a smoothed, simplified version of the Lindwall (1991) crust. We did not include any low-velocity zones or high-velocity laminae, which have not been consistently reported in other regional investigations (e.g., Shor and Pollard, 1964; Sutton et al., 1971; Watts et al., 1985; ten Brink and Brocher, 1987). Crustal density values were chosen to be consistent with the borehole values in the upper crust (Fig. 3.6) and with the scaling relationship between Vp and ρ for porous basalts of Carlson and Raskin (1984). We set a constant Poisson's ratio of σ=0.277 (Vp/Vs=1.8) throughout layer 3, a typical value for the lower crust (e.g., Shaw, 1994). We placed a mantle half-space beneath the crust with constant values of Vp=8.2 km/s, Vs=4.6 km/s, and ρ=3.4 g/cc,

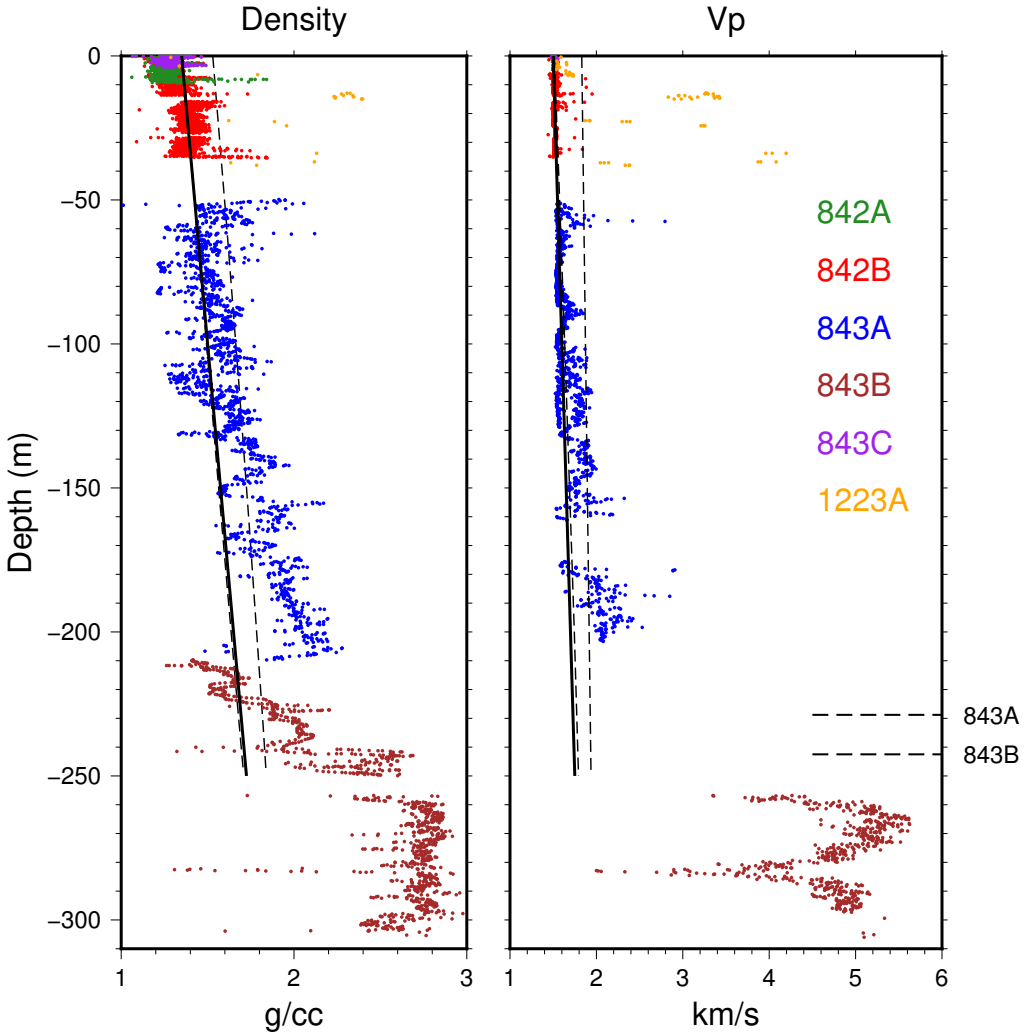

Figure 3.6: Density and compressional velocity (Vp) *in situ* drilling measurements from ODP sites 842, 843, and 1223 (Dziewonski et al., 1992a; Stephen et al., 2003a). As shown in Figure 3.1, site 1223 is located northeast of Oahu and sites 842 and 843 are southwest of Oahu. Drilling legs 842 and 843 were able to drill and measure through the sedimentary cover and through over 50 meters of basement. Sediment thicknesses of 228.8 and 242.5 meters were recorded. Two density profiles of Hamilton (1976a) are shown in dashed lines: one for pelagic sediments (with lower densities) and one for terrigenous sediments. The linear approximation used in this study is shown in the thick solid line. Two Vp profiles are shown: one from Hamilton (1978) (with lower velocities) and one from Nafe and Drake (1957). The linear approximation used in this study is again shown in the thick solid line.

consistent with Laske et al. (2011) and the Nishimura and Forsyth (1989) model for 52-110 Ma lithosphere.

Table 3.1: Initial Crustal Model

Layer[a]	Thickness (km)	Vp[b] (km/s)	Vs[b] (km/s)	ρ[b] (g/cc)
2A	0.5	4.5[c] / 5.6	1.5[c] / 3.2[c]	2.7 / 2.8
2B	0.8	5.6 / 6.3	3.2[c] / 3.5	2.8 / 2.9
3A	1.5	6.3 / 7.2	3.5 / 4.0	3.0 / 3.0
3B	3.5	7.2 / 7.2	4.0 / 4.0	3.0 / 3.0
Mantle	-	8.2	4.6	3.4

[a]Sedimentary layer not shown
[b]Values correspond to top and bottom of the layer
[c]Parameters included in joint structural inversion

We then varied individual parameters through targeted forward modeling to better understand the compliance sensitivity. We performed a grid search for the best fitting sedimentary structure (assuming a linear Vs gradient) that was consistent with the Ps measurement, yielding a thickness of 94 meters. While drastically decreasing the data misfit from our previous modeling, these parameters still produced compliance values that over-predicted the measured data at low frequencies and under-predicted the data at high frequencies. As seen in Figure 2, this suggested that the lower crust needed to be faster, the upper crust needed to be slower, or both. Because of the reduced sensitivity of compliance data to lower crustal structure, we were hesitant to increase Vs in the lower crust beyond 4.0 km/s, a value suggested by a range of oceanic crustal studies (e.g., Christensen and Salisbury, 1975; Christensen, 1996). As suggested by Lindwall (1991), the upper ≈700 meters of the oceanic crust surrounding Hawaii is poorly constrained with existing active seismic data, so we then investigated the sensitivity of compliance to changes in layer 2. Compliance data are primarily sensitive to Vp at the top of the crust, and while Lindwall (1991) reports Vp = 4.35 km/s at the top of the basement, the borehole logs (Fig 3.6) suggest higher values, potentially exceeding 5.0 km/s. Increasing Vp from 4.35 km/s at the top of the basement further reduced the misfit, though increases to Vp deeper in the crust had negligible

effect. Lowering the shear velocity at the top of the basement and at the base of layer 2A also decreased misfit, while decreasing Vs at the bottom of layer 2B increased the misfit.

To jointly invert our compliance and Ps delay data and to incorporate *a priori* information, we implemented a nonlinear joint inversion algorithm as described by Jackson and Matsu'ura (1985) and previously used with synthetic compliance data by Crawford (2004). This inversion minimizes the weighted sum of the data misfit and the deviation from the prior estimates. The algorithm requires a model vector of prior estimates m_p with an associated prior covariance matrix D. These values represent our *a priori* constraints and respective confidence in these values. We assume errors of the prior estimates are uncorrelated, and therefore D is diagonal with positive definite values. In reality, these errors are likely correlated, leading to an underestimation of model uncertainties. The method iteratively solves for a model vector that minimizes the distance from the prior estimates in model space and converges to an acceptable misfit (in our case, $\chi^2/N < 1$). For each iteration of the inversion, we linearize around a model m_k and find

$$m_{k+1} = m_k + b\left(A_k^T E^{-1} A_k + D^{-1}\right)^{-1}\left(A_k^T E^{-1} e_k + D^{-1} d_k\right) \tag{3.6}$$

where E is the weighting matrix of the data, $e_k = d_0 - F[m_k]$ is the data misfit produced by the model m_k, and $d_k = m_p - m_k$ is the distance of m_k from the prior estimates. The design matrix relating the model parameters to the data $A_{ij} = \partial f_i/\partial m_j$ is recalculated numerically during each iteration. b serves as an adjustable parameter that would equal 1 for linear problems but should be reduced for nonlinear problems to decrease the inversion step size. We used $b = 0.1$ since compliance sensitivity is highly dependent on the starting model. For each inversion, we began with m_k equal to the prior estimates.

We performed an inversion for five parameters: sediment thickness, sediment Ps delay time, Vp at the top of the basement (Vp_0), Vs at the top of the basement (Vs_0), and Vs at the bottom of layer 2A, 500 meters into the crust (Vs_1). We defined the Ps delay prior estimate

as our measured value in order to allow the modeled delay time to vary within the uncertainty range. We set the prior velocity estimates in the crust at Vp_0 = 4.5 km/s, Vs_0 at = 1.5 km/s, and Vs_1 = 3.2 km/s, consistent with the model of Lindwall (1991), with associated uncertainties of 5% for each crustal parameter. We ran 50 iterations of the nonlinear inversion, and the results of the process are shown in Figure 3.7. We found a final sediment thickness of 92 meters, Vp_0=4.9 km/s, Vs_0=1.45 km/s, and Vs_1 =2.85 km/s. The sedimentary structure accounted for the majority of the improvement in fit: adjusting the sediments alone decreased the misfit by 99.1% compared to a model with 200 meters of sediments, and including crustal structure in the inversion lowered the misfit an additional 25.1%. The preferred Vp_0 value was much closer to those measured *in situ* and still consistent with what has been typically found in older Pacific crust (e.g., White et al., 1992; Carlson, 1998). We also ran an inversion where our prior estimate of Vp_0 was 5.0 km/s, and arrived at an inverted value of 4.9 km/s. The inverted shear velocities are on the low end of what is typically observed at these depths (e.g., Purdy, 1983; Swift et al., 1998), but we still had difficulty fitting the lowest-frequency data within the uncertainties. Although lower Vs values at the top of the crust would further decrease the misfit, our prior covariance matrix inhibited the inversion from departing greatly from values that are typically observed in the oceanic crust. The method of Jackson and Matsu'ura (1985) is formulated in a Bayesian framework, and allows estimation of the posterior covariance matrix. Supplemental figure S3 plots the joint posterior probability density function (PDF) for predicted sedimentary Ps delay time and Vs at the bottom of layer 2A. A correlation between the variables shows the tradeoff between Vs at these depths, where increasing Vs in the sediments requires a lower Vs in the upper crust, and vice versa. By keeping sedimentary Vs within the limits defined by the Ps delay measurement, we forced a lower Vs in the crust. To ensure that the initial model was not biasing our results, we ran separate inversions in which we varied the starting model but kept the prior estimates constant. Following Crawford (2004), we ran 100 inversions with random starting models drawn from uniform distributions of the model parameters (Figure S4). The resulting

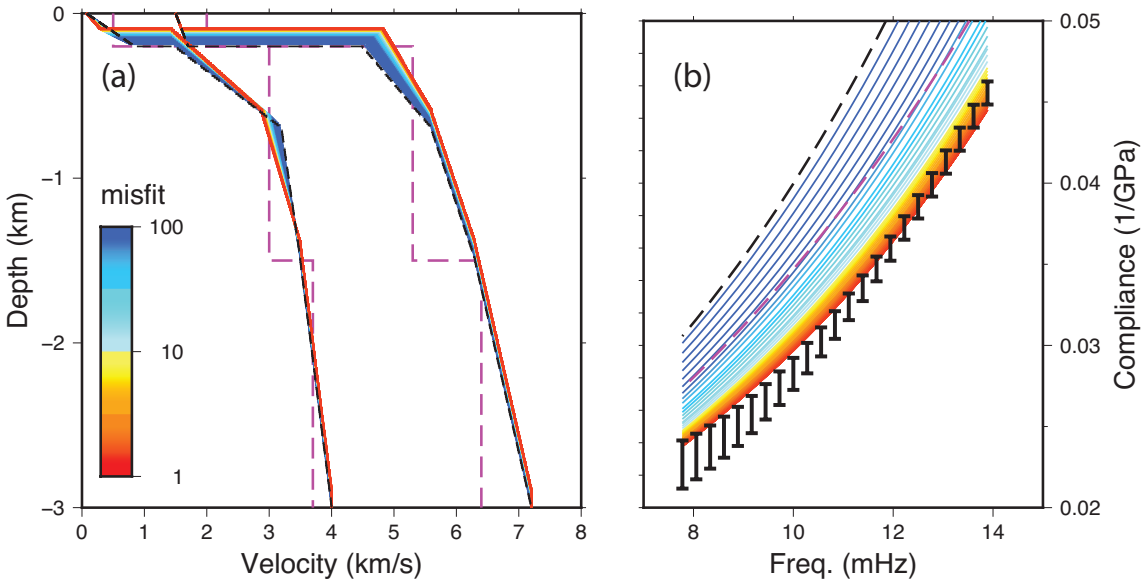

Figure 3.7: 50 iterations of our inversion at site PL37. We solved for five parameters in this inversion, as described in the text. The left panel displays the crustal model for Vp and Vs colored by χ^2/N misfit. The model from the prior estimates is shown in black dashed lines. We arrived at a final misfit of 1.49. The red dashed lines show the SWELL model of Laske et al. (2007) for reference. The model of Lindwall (1991) is not shown because it would be mostly obscured by the starting model and intermediate inversion iterations. The right panel displays the compliance data generated by the models in the left panel, also colored by misfit.

median model had 96±4 meters of sediment and shear velocities of 1.44±0.09 km/s at the top of the crystalline crust and 2.81±0.07 km/s at 500 meters into the basement, consistent with our initial results.

3.4.2 Data Modeling at PL74

We next considered site PL74, located over 100 km closer to the islands than PL37 (Fig. 1). Using the inverted crustal model of PL37, we were able to fit the compliance data to within χ^2/N=0.45 with 170 meters of sediment and Vs increasing linearly to 0.70 km/s, which agreed with the measured Ps delay time. However, previous analyses of reflection and refraction data by Brocher and ten Brink (1987) suggested between 900 and 1900 meters of sediment, significantly more that our estimate. PL74, situated just south of Oahu and east of Maui, was

adjacent to regions where massive submarine lava flows (Holcomb et al., 1988) and landslides (Moore et al., 1989, 1994) have been documented and mapped (Fig. 1). Sediments and debris from these events have been found extending hundreds of kilometers from the islands into water as deep as 5.5 km. This has been supported by active seismic experiments, where authors have found thick volcaniclastic sediments close to the islands (Rees et al., 1993; Leslie et al., 2002). As noted in a previous analysis of sedimentary Ps delay times by Davis et al. (1976), thick, fast sedimentary units can produce similar delay times data as thin, slow sedimentary units. We observed a similar phenomenon with compliance data. We defined a sedimentary profile with the approximate Vp values reported by Brocher and ten Brink (1987) (Vp at the seafloor to 3.0 km/s and a linear gradient of 1.0 [km/s]/km) and density values for terrigenous sediment from Hamilton (1976a) (ρ increasing from 1.5 to 2.0 g/cc). Although very little is known about the seismic properties of marine volcaniclastic sediments, these values are generally consistent with the few *in situ* measurements that have been made surrounding other islands in the Pacific, which showed higher Vp and ρ values than typical pelagic sediments (Carlson et al., 1980; Kenter and Ivanov, 1995). We then performed a grid search for sediment thickness and shear velocity constrained by the Ps delay data (Fig. 3.8), and found a best fit for 875 meters of sediment with Vs increasing linearly from 0.3 km/s to 2.2 km/s. We tested other values for Vs at the seafloor, but a velocity of 0.3 km/s produced the most overlap between the compliance and Ps delay time. We also tested other density profiles, but again the terrigenous profile produced the best fit. The underlying crust was kept constant, except Vs was increased to 2.3 km/s at the top of the basement for the high-velocity sediment model to avoid a low-velocity zone (LVZ). The presence of thick, high-velocity sediments inhibited our ability to interpret crustal structure beneath the sediments, as variations in both crustal Vp and Vs changed the misfit by negligible amounts. These results indicate that even with both compliance and Ps delay data, we cannot unambiguously distinguish between these sediment regimes without *a priori* information.

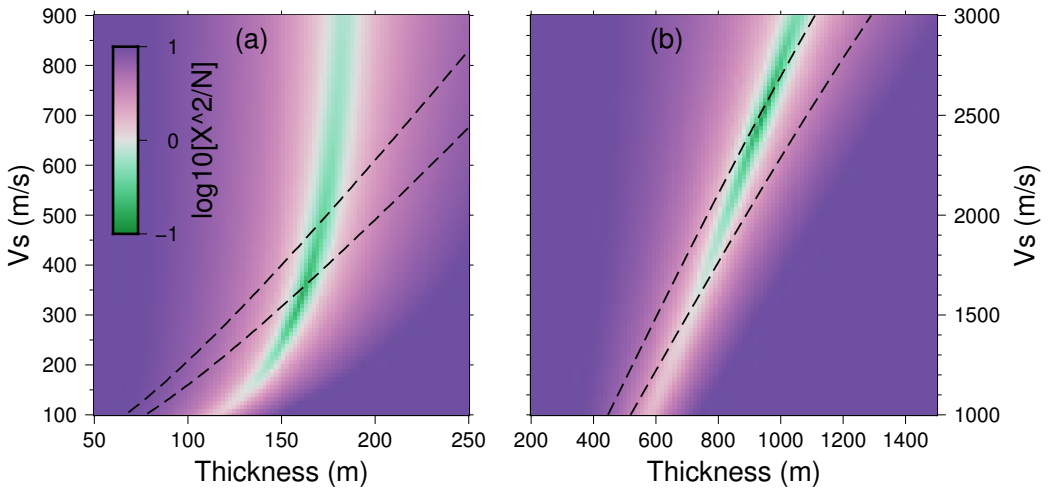

Figure 3.8: A grid search for best fitting sediment thickness and shear velocity to the compliance data at PL74. (a) shows the results for low-velocity sediments, where Vp=1.5 km/s and ρ=1.35 kg/m^3 at the seafloor, and (b) shows the results for high-velocity sediments, where Vp=3.0 km/s and ρ=1.5 kg/m^3 at the seafloor. The two lines indicate the region of acceptable values from the Ps delay time of 0.70 ± 0.053 seconds.

3.5 Results & Discussion

We inverted the remaining data for sedimentary and upper crustal structure using the five-parameter nonlinear inversion described above. We used the inverted values at PL37 as our new prior estimates for Vp at the top of the crust (4.9 km/s), Vs at the top of the crust (1.45 km/s), and Vs at 500 meters depth (2.85 km/s), and assigned an uncertainty of 0.1 km/s to each parameter. Although the thickness of the Hawaiian crust varies from 6 km to over 15 km (Leahy et al., 2010), we maintained a constant thickness of 6.3 km since compliance data in our frequency range are largely insensitive to structure beyond these depths. For the inversion at each site, we ran 50 iterations, but stopped the inversion if we reduced misfit to a value of $\chi^2/N \leq 1.0$. At sites PL02 and PL05 we computed compliance data but were unable to estimate consistent Ps delay times. Both of these sites were surrounded by sites with delay times between 0.42 and 0.47 seconds. We defined a delay time of 0.45 ± 0.05 seconds at each site and proceeded with the inversions. We were able to fit the data at all sites with $\leq$300 meters of sediment with a median misfit of $\chi^2/N = 0.98$. However, our estimated sediment thicknesses were substantially

less than found by previous studies immediately to the south of the islands (e.g., Brocher and ten Brink, 1987) and to the north of the islands (e.g., Rees et al., 1993). We therefore performed a grid search for high-velocity terrigenous, volcanic sediments at seven near-island sites: PL03, PL33, PL34, PL35, PL36, PL47, and PL74 (Fig. 1). As described previously, we used the crustal model found for PL37, only altering Vs of the uppermost crust to avoid low-velocity zones. We found best-fitting sediment thicknesses ranging between 700 and 1500 meters, with sediments thickening closer to the islands. Comparison with the seismic reflection data of Rees et al. (1993) allowed confirmation of our results. Figure 1 includes sedimentary two-way travel time (TWTT) isocontours determined from reflection profiles northwest of Oahu. At site PL47, we calculated a synthetic TWTT of 524 miliseconds using our volcanic sedimentary thickness and Vp profile. The closest isocontour of Rees et al. (1993) shows a TWTT of 500 ms, in close agreement with our value. For comparison, the slow-sediment solution at this site produced a synthetic TWTT of 234 ms. We ran the same calculation at PL03 with high-velocity sediments and found a TWTT of 419 ms, also in agreement with the estimated 400 ms from Rees et al. (1993). The results of previous analyses informed our decision to limit the high-velocity sediments to these seven sites. For example, several other sites further from the islands were also within the region analyzed by Rees et al. (1993), but the TWTT values were well fit by our low-velocity sediment results. PL48 sat just outside of the 200 ms contour, and our pelagic results led to a synthetic TWTT of 183ms. The borehole measurements from DSDP 67 (Fig. 1), outside the reflection isocontours, measured Vp between 1.5 and 1.7 km/s in the sediments (Winterer et al., 1971), further supporting our classification. To the southeast of the islands, Ewing et al. (1968) measured a sedimentary thickness of approximately 100 meters, and DSDP site 43 (Fig. 1) recovered a core comprised of silty mud (McManus et al., 1970). Furthermore, the seismic lines of Leslie et al. (2002) show the volcanic sediments tapering out before the closest PLUME sites (PL13 and PL24), and our solutions agree with the maps of Moore et al. (1989). However, as a final test, we performed a grid search for high-velocity sediments at site PL17, over 300 km east

of Hawaii and far off the Swell. We found a best-fit sediment thickness of 600 meters assuming volcanic sediments, which we found less plausible than our estimate of 135 meters of pelagic sediment. While interpretation of compliance data depends heavily on prior information, the multitude of previous work surrounding Hawaii allows us to identify sedimentary regimes.

Our final sedimentary model ranges in thickness from less than 50 meters to the south and west of Hawaii to 1500 meters within the Hawaiian Moat (Figure 3.9). This figure includes extrapolated results from eight sites with Ps delay data but without compliance estimates (see table S2). We did not invert for crustal structure at these sites but estimated the sediment thickness by examining neighboring sites with similar Ps measurements. We assumed the same sedimentary velocity structure as the nearest site and used the Ps delay time to estimate the sediments. In our modeling, we have assumed two distinct sedimentary regimes, corresponding to volcaniclastic, terrigenous sediments near the islands and pelagic sediments further away. The sites with pelagic sediments range in thickness from 50 and 300 meters, in agreement with the oceanic sediment model of Divins (2003) and the 1°x1° global sediment map of Laske and Masters (1997). Although it is generally believed that oceanic sediments thicken with increasing age of the lithosphere (e.g., Sclater, 2003; Olson et al., 2016), the sediment thicknesses show no clear correlation with crustal age within this region. Two stations south of the islands appear anomalously thick, with over 100 meters of additional sediment compared to the surrounding sites. Interestingly, these sites agree more closely with the sediment thickness found at the OSN site, immediately north of PL73, than most of the surrounding sites. We attempted to include compliance data measured at the two OSN OBS sites for comparison, but were hampered by instrument response issues (Doran and Laske, 2016). Another region of anomalously thick sediments was found to the northeast of Hawaii, and appears to lie within the Molokai Fracture Zone.

Our *in situ* point measurements also presented an opportunity to investigate lateral heterogeneity in the velocity structure of marine sediments. Studies of pelagic sediments throughout

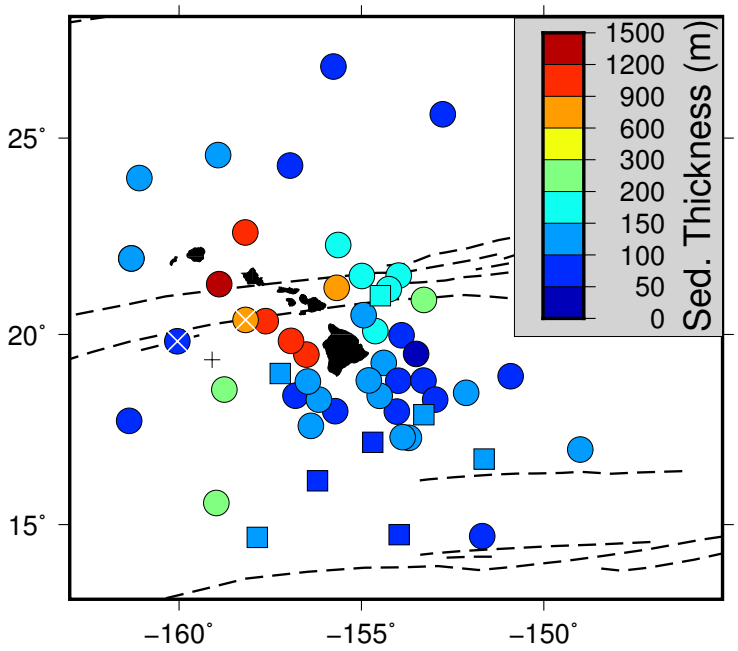

Figure 3.9: Final map of sediment thickness surrounding the Hawaiian islands. Note the nonlinear scale. Sites where the sediment thickness is estimated from Ps delay measurements only are shown with squares. In our final model we assumed fast sediment velocities at seven near-island sites, as discussed in the text. We found sediments thicker than 600 meters at each of these sites. The median uncertainty for sediment thickness at pelagic sites is 4%, while the median uncertainty at volcanic sites is 6% (See Table S2 for individual uncertainties). The fracture zones shown in Figure 1 are plotted here for reference. As in Figure 3, the plus symbol marks the location of OSN site 843 and the white crosses identify PL37 and PL74.

the deep Pacific (>2 km water depth) have yielded a wide range of shear velocity estimates (e.g., Bratt and Solomon, 1984; Bromirski et al., 1992). Figure 3.10 shows our final velocity-depth profiles in the sediments at all sites. Two velocity profiles are shown for comparison: that of Hamilton (1979b), estimated from *in situ* measurements of Vs in marine sediments, and that of Ruan et al. (2014), estimated from the transfer function between displacement and pressure in the microseism frequency band (5 - 10 seconds) using data from the Cascadia Initiative (Toomey et al., 2014). Our median depth-velocity profile for pelagic sediments is defined as Vs = $2.8z$ + 75, where z is in meters and Vs is in m/s. The profile begins with a Vp/Vs of 20 at the seafloor and decreases to 4.6 by 100 meters depth. This is similar to the profile of Hamilton (1979b), which has Vp/Vs=13 at the seafloor and Vp/Vs=4.5 at 100 meters depth. Our median shear velocity profile for volcanic sediments increases from 0.4 km/s at the seafloor to 2.2 km/s at the top of the basement, corresponding to an average Vp/Vs ratio beginning at 7.5 and decreasing to below 2.0 at the top of the bedrock. The median depth-velocity relationship is defined as Vs = $1.9z$ + 400, where z and Vs are again in meters and m/s, respectively. Sites to the northeast of the islands (e.g., PL05, PL07, PL08, seen as the high-gradient red lines in Fig. 3.10) exhibited consistently faster velocity profiles than other sites with pelagic sediments. Proximity to the Molokai Fracture Zone may influence these sedimentary velocities, as hydrothermal activity has been linked to high velocity-depth gradients at other pelagic sites in the Pacific (Essen et al., 1998) and enhanced hydrothermal circulation has been observed on some Pacific fracture zones (e.g., Hein et al., 2008). Additionally, these sites may exhibit significant interbedding between pelagic and volcaniclastic sediments. Such interbedding was also observed at nearby ODP site 1223A (Figs. 1, 3.6; Stephen et al. (2003a)). The limited scatter between the other pelagic velocity profiles may be caused by a lesser degree of volcanic interbedding, which has been found in the uppermost sediments surrounding the Hawaiian islands both on and off the Swell (Naka et al., 2000, 2002) and has been identified in sediments over 500 km from the islands (Rehm and Halbach, 1982). We assumed linear velocity-depth gradients for both types of sediments,

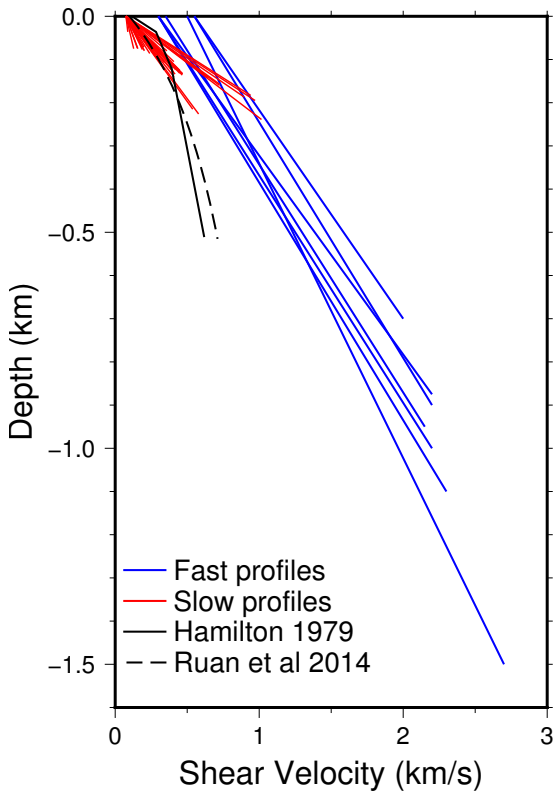

Figure 3.10: Profiles of sedimentary shear velocity as a function of depth at all PLUME sites. Solutions for fast sediments are shown in red, solutions for slow sediments are shown in blue. The velocity-depth sedimentary profiles of Hamilton (1979b) and Ruan et al. (2014) are shown for reference.

although many studies have found nonlinear concave down velocity-depth relationships (e.g., Hamilton, 1979b; Ruan et al., 2014; Bell et al., 2015b). In addition, the *in situ* measurements at ODP 843B showed a concave up trend with increasing depth (Fig. 3.6), contrary to what is typically assumed. We could not jointly fit compliance and Ps delay data at all pelagic sites with published profiles, and were wary of mapping misfit in the sediments into crustal structure given the uncertainty related to sediment properties. We therefore solved for individual linear profiles to simplify our modeling while allowing for lateral variation in Vs structure.

Our final median crustal model is shown in Figure 3.11 and detailed in Table 2. As discussed above, we did not include results beneath stations with thick, high-velocity sediments, as our sensitivity even to the top of the basement is significantly reduced. We attempted a separate

inversion in which we fixed the crustal model and solved only for sedimentary structure at each station. The two inversions produced virtually identical sediment thicknesses and velocity profiles, with the median thickness at each site differing by less than two meters. However, allowing the crust to vary between sites resulted in an average misfit 9% lower than that for the sediment-only inversion, confirming that some variation in crustal structure improves our modeling of the data. Although we inverted for variations in Vp at the top of the basement, our data are consistent with less than 0.5% variation of Vp. We found Vs anomalies on the order of $\pm 5\%$ at both the seafloor and at the bottom of layer 2A (Fig. 3.11). The anomalies do not appear to correlate with the Hawaiian Swell. Previous studies of similarly-aged Atlantic crust attributed lateral heterogeneity in Vp structure to differences in local topography or extrusive porosity (Swift and Stephen, 1989), which may affect the velocities surrounding Hawaii as well. Site PL08, to the northeast of Hawaii and potentially within the Molokai Fracture Zone, shows strong ($> 10\%$) low velocity anomalies. Fracture zones typically exhibit lower shear velocities, thinner crust, and can have systematic compositional differences and elevated temperature profiles than typical oceanic crust (White et al., 1984; Phipps Morgan and Forsyth, 1988; Behn et al., 2007), although here we can only resolve distributed low velocities throughout the upper crust. We fixed Poisson's ratio at $\sigma = 0.277$ below layer 2, but due to the low shear velocity required in the uppermost crust, our median model exhibits Poisson's ratios in excess of $\sigma = 0.35$ in the upper 500 meters of the crystalline crust. While this is higher than typically expected in the oceanic crust (Hyndman, 1979; Christensen, 1996), values of up to $\sigma = 0.40$ have been observed in old Pacific crust to depths of several hundred meters and are usually attributed to seafloor weathering or other large-scale porosity effects (Shearer, 1988; Swift et al., 1998). In our inversions for structure of the upper crust we have not scaled Vp with Vs, as is commonly done in seismic imaging (e.g., Laske and Widmer-Schnidrig, 2015). This is because the borehole measurements and Vp profiles of Lindwall (1991) have provided *a priori* constraints on density and Vp in the sediments and uppermost crust, allowing us to directly invert for Vs. We included Vp_0 in our

inversion because our initial modeling and the sensitivity kernels showed the compliance data were sensitive to this value, but our data were consistent with very little variation in Vp at the top of the crystalline crust. We attempted inversions with Vp scaled to Vs in layer 2 through a constant Poisson's ratio or through the mafic regression line of Brocher (2005), but these inversions resulted in misfit increased by a factor of two or more. We also attempted to improve the misfit by adjusting density at the top of the crust, where the data are most sensitive to this parameter, but varying the density within the expected range of values ($\pm$0.3 g/cc) affected the misfit by less than 0.5%.

Table 3.2: Median final inverted crustal model.

Layer	Thickness (km)	Vp (km/s)	Vs (km/s)	ρ (g/cc)
2A	0.5	4.9 / 5.6	1.4 / 2.8	2.7 / 2.8
2B	0.8	5.6 / 6.3	2.8 / 3.5	2.8 / 2.9
3A	1.5	6.3 / 7.2	3.5 / 4.0	2.9 / 3.0
3B	3.5	7.2 / 7.2	4.0 / 4.0	3.0 / 3.0
Mantle	-	8.2	4.6	3.4

In order to improve images of the hypothesized Hawaiian Plume, compliance results will need to be combined with data sensitive to deeper structure. The required correction to body wave arrival times are straightforward to compute from the individual sediment profiles at each station. We computed synthetic group and phase velocity curves with periods between 10 and 50 seconds using the algorithms of Haney and Tsai (2017) in order to examine the expected effect of sedimentation on dispersion measurements (Figure S5). We tested three crustal models overlying a model for 52-110 Ma oceanic lithosphere from Nishimura and Forsyth (1989): a typical oceanic crust, our median solution with 200 meters of slow sediment, and our solution with 1500 meters of fast sediment. Group velocities can differ by $>$5% at $T = 20$ seconds and $> 1\%$ at $T = 40$ seconds, demonstrating that even intermediate-period data are sensitive to very near-surface structure. These effects are the same order of magnitude as caused by perturbations in Earth structure beneath Hawaii Laske et al. (2007, 2011), and could potentially hamper high-

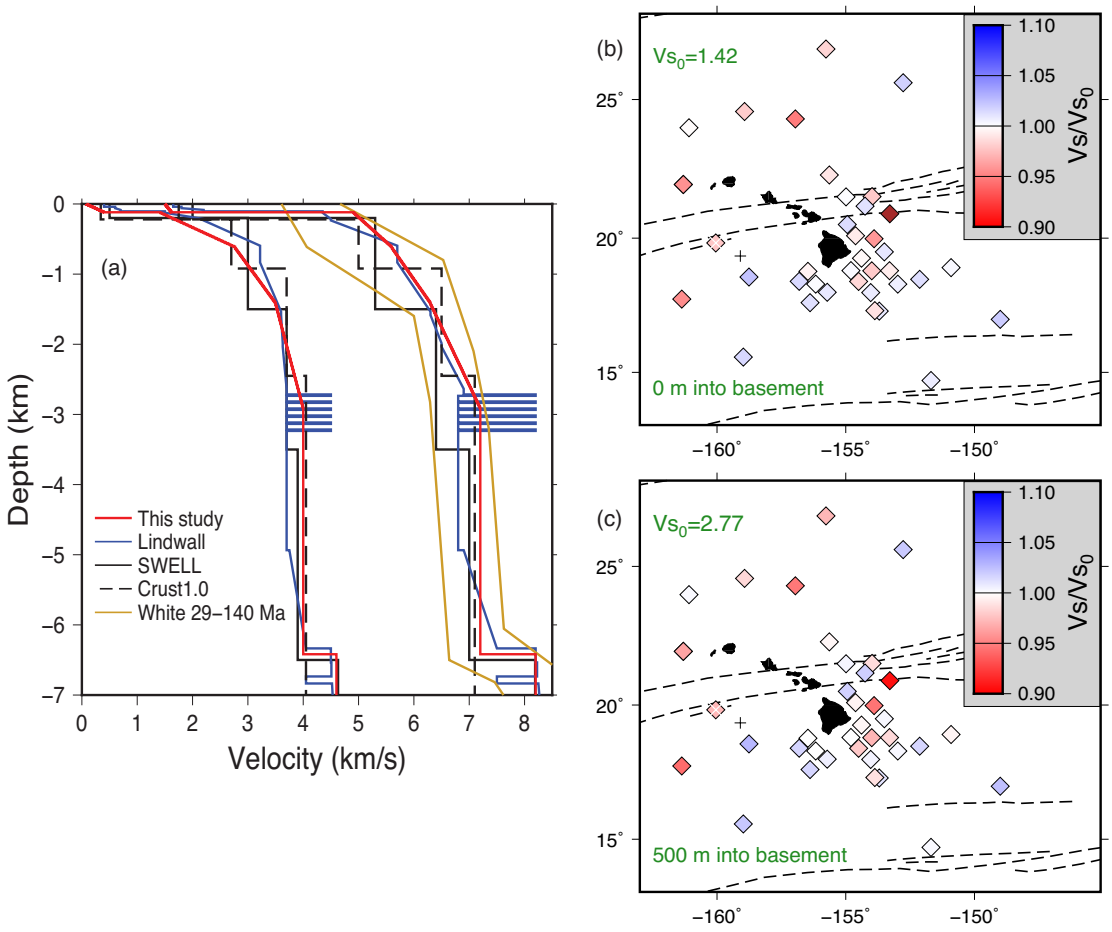

Figure 3.11: (a) The final average crustal model for Vp and Vs as a function of depth presented in this study (solid red lines). For comparison, we also show the crustal model of Lindwall (1991), the SWELL model (Laske et al., 2007, 2011), and the Crust 1.0 model calculated at the PL37 location (Laske et al., 2013). The Vp limits from White et al. (1992) for Pacific crust between 29 and 140 Ma are also shown. (b) Map view of the shear velocity anomalies as a fraction of the average value at the top of the crystalline crust. (c) Same as (b) but calculated at the bottom of layer 2A, 500 meters into the crystalline crust.

fidelity imaging of the crust and uppermost mantle. Since the body wave delays in the sediments are also the same order of magnitude as the travel times through the whole crust, we would expect that receiver functions and related estimates of Moho depth (e.g., Leahy et al., 2010) may also be affected. As erroneous assumptions about shallow structure can map into greater depth, an ideal future seismic approach would jointly invert all seismic constraints together for a sediment, crust, and mantle model.

3.6 Conclusions

We imaged the oceanic sediments and crust with point measurements surrounding the Hawaiian Islands using year-long PLUME passive seismic broadband OBS records. We found that the marine sediments range in thickness from approximately 50 to 1500 meters across the array, with the thickest sediments immediately north and south of the island chain. We identified two distinct classifications of sediments: slow, low density pelagic sediments typically less than 300 meters thick, and fast, high density volcaniclastic sediments, increasing in thickness with proximity to the islands to a maximum of 1500 meters. Even with both compliance and Ps delay data available, incorporating additional information from previous studies is necessary to unambiguously identify these sedimentary regimes. While sedimentary structure accounts for the majority of the compliance signal, our data are best fit by including lateral variations within the upper crystalline crust on the order of $\pm 5\%$ over scales of hundreds of kilometers. Fitting our data required relatively high values for Poisson's ratio throughout Layer 2A, defined here as the upper 500 meters of the crust. Our data can be explained with very little variation in Vp ($< 0.5\%$). Our analysis supports previous findings that oceanic crust approaches uniformity as it ages, but some lateral heterogeneity remains.

3.7 Acknowledgements

Waveforms and station metadata are publicly available and were accessed through the Incorporated Research Institutions for Seismology Data Management Center (IRIS-DMC; http://ds.iris.edu/ds/nodes/dmc/). The data were accessed between November 2016 and June 2017. The global earthquake catalog used for the DPG and seismometer calibrations were obtained from the International Seismological Centre (ISC; http://www. isc.ac.uk) through the Python toolbox ObsPy (Beyreuther et al., 2010; Megies et al., 2011; Krischer et al., 2015) in March 2017. The regional earthquake catalog used for the Ps delay measurements was obtained from the USGS earthquake database (https://earthquake.usgs.gov/) also through ObsPy, in October 2017. We thank Wayne Crawford for supplying the forward code (publicly available at http://www.ipgp.fr/∼crawford/), for providing guidance with the nonlinear inversion, and for helpful discussions. We thank Wayne, Spahr Webb, John Collins, Sean McPeak, Martin Rapa, Jacques Lemire, Jeff Babcock, and John Souders for very helpful discussions regarding the instrument response of the DPGs. We thank Jessie Saunders for useful discussions. We thank Martha Savage, Spahr Webb, and an anonymous reviewer for suggestions to improve the manuscript. All of the figures in this chapter were created using Generic Mapping Tools (GMT; Wessel and Smith (1991, 1998); Wessel et al. (2013)). ODP and DSDP data were accessed through the Janus Web Database (http://www-odp.tamu.edu/database/). This research was funded by NSF grants OCE-16-34440 and OCE-17-36516. This research was partially supported by the Chateaubriand Fellowship of the Office for Science & Technology of the Embassy of France in the United States.

Chapter 3, in full, is a reformatted version of material that has been accepted for publication in the Journal of Geophysical Research: Doran, A.K., and G. Laske (2019), Seismic structure of marine sediments and upper oceanic crust surrounding Hawaii. I was the primary investigator and author of this paper.

S3 Supplemental Figures & Tables

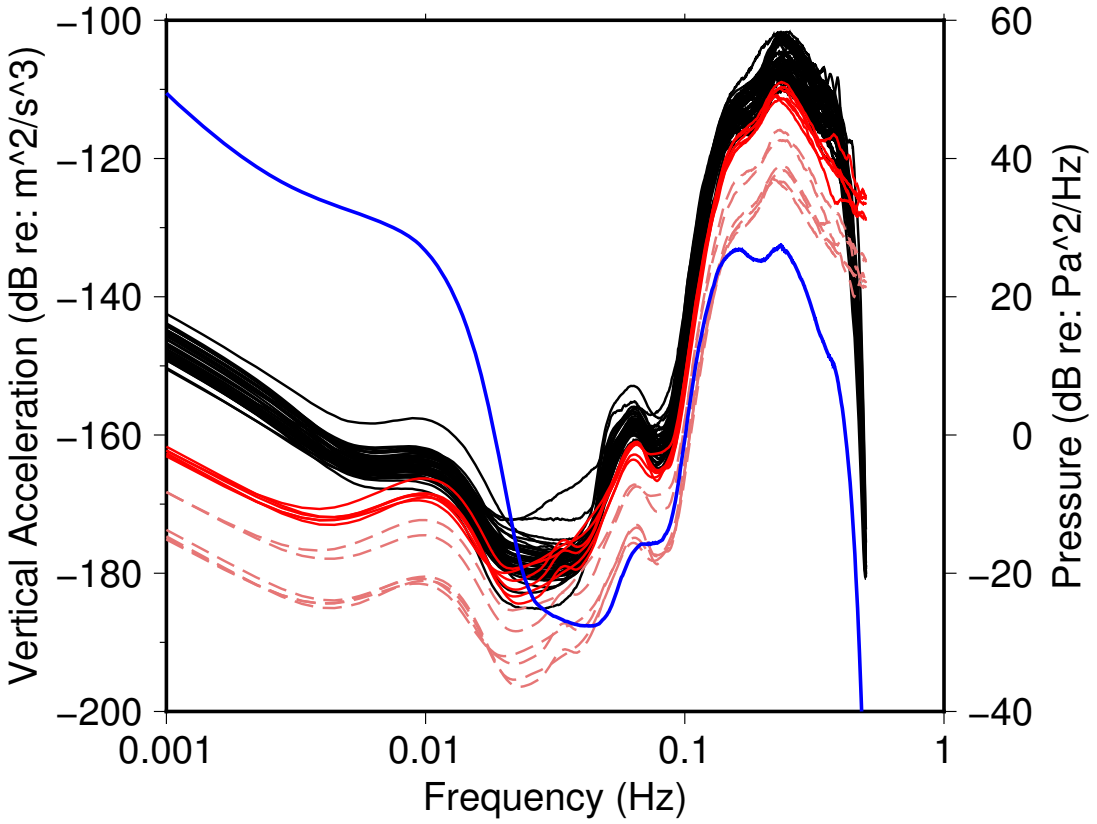

Figure S3.1: Median hourly acceleration spectra calculated at WHOI (black) stations and SIO2 (red & pink) stations. The spectra have been tilt-corrected. The dashed pink lines represent the nominal SIO T240 acceleration spectra, while the solid red lines represent the gain-corrected spectra. To compute the corrected gain, we assume the nominal gain is off by a factor of 2^n, where n is an integer value. We compute the transfer function between the median WHOI spectra and the individual SIO spectra. The nominal gain at two of the sites was off by a factor of 2, while the nominal gain at the remaining WHOI sites was off by a factor of 4. We also compute earthquake spectra following M$\geq$7 events, and see the same ratios as in the ambient spectra. The gain factor used at each SIO site is listed in Supplemental Table T1. The blue line, shown for reference, shows the median hourly pressure spectra computed from all WHOI sites. This line has been corrected for instrument response as described in the supplemental material.

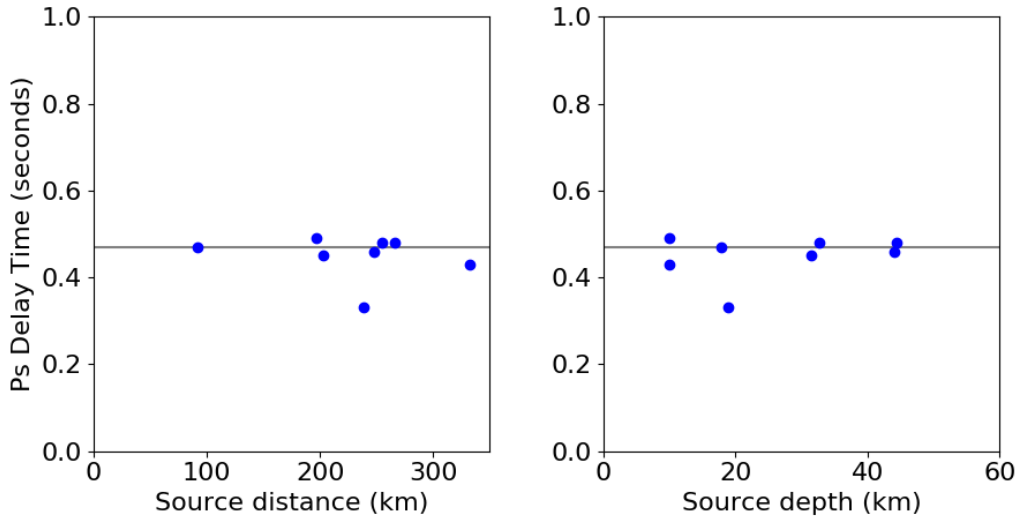

Figure S3.2: A comparison of the measured Ps delay time for eight events at PL06 as a function of source-receiver distance (left panel) and source depth (right panel). The measured delay time at this station was 0.47±0.04 seconds (shown by gray line).

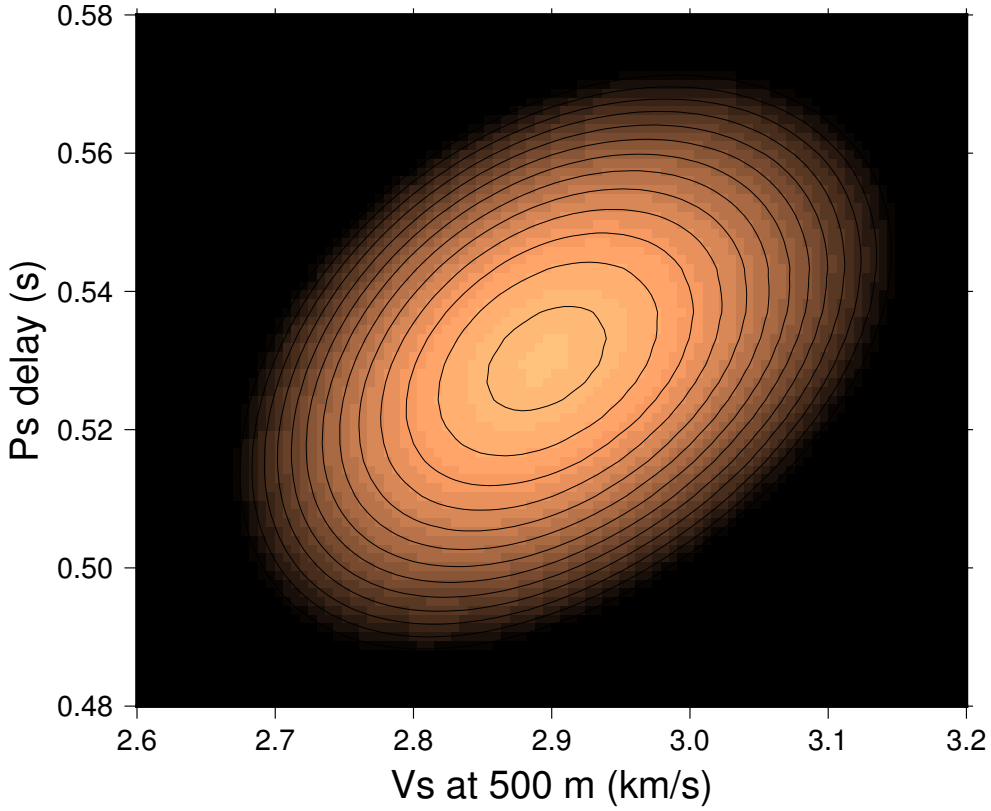

Figure S3.3: A joint posterior PDF of predicted Ps delay time in the sediments and shear velocity at 500 meters into the basement. Lighter colors represent a greater likelihood. The likelihood is also contoured for emphasis. The tradeoff between Ps delay time and shear velocity suggests that faster sediments would require a slower upper crust, and vice versa.

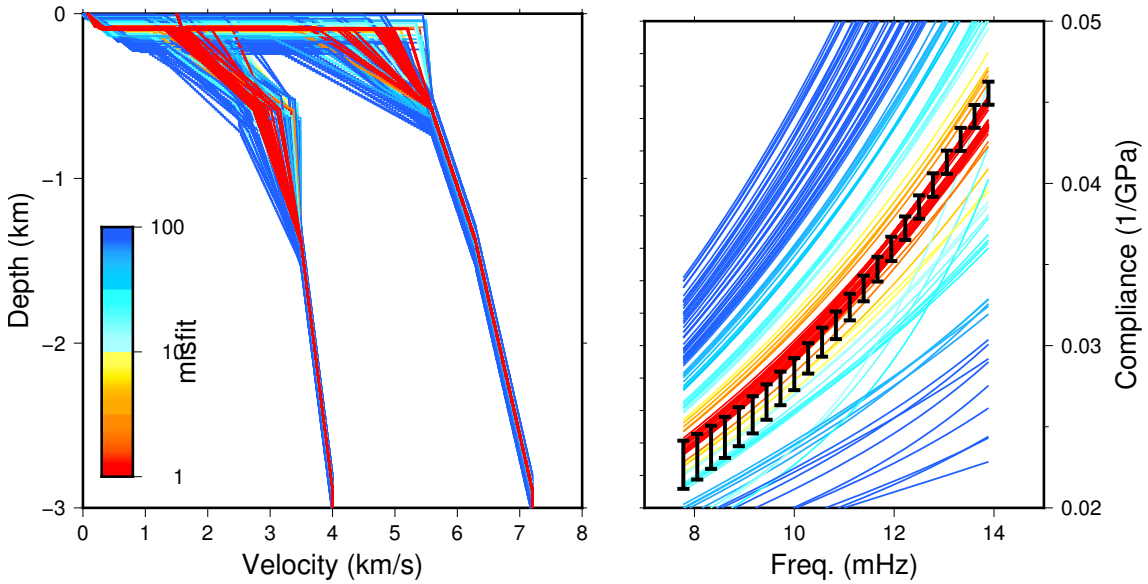

Figure S3.4: The results of 100 nonlinear inversions, each iterated 50 times or until the desired misfit was reached, at site PL37. In each inversion, the starting model was varied but the prior estimates were kept constant. Note that in this figure only the starting and final models are shown, not the intermediate iterations. Using the ensemble average and standard deviation, we find a sediment thickness of 96±4 meters, Vp at the top of the basement of 4.87±0.19 km/s, Vs at the top of the basement of 1.44±0.09 km/s, and Vs at 500 meters into the basement of 2.81±0.07 km/s.

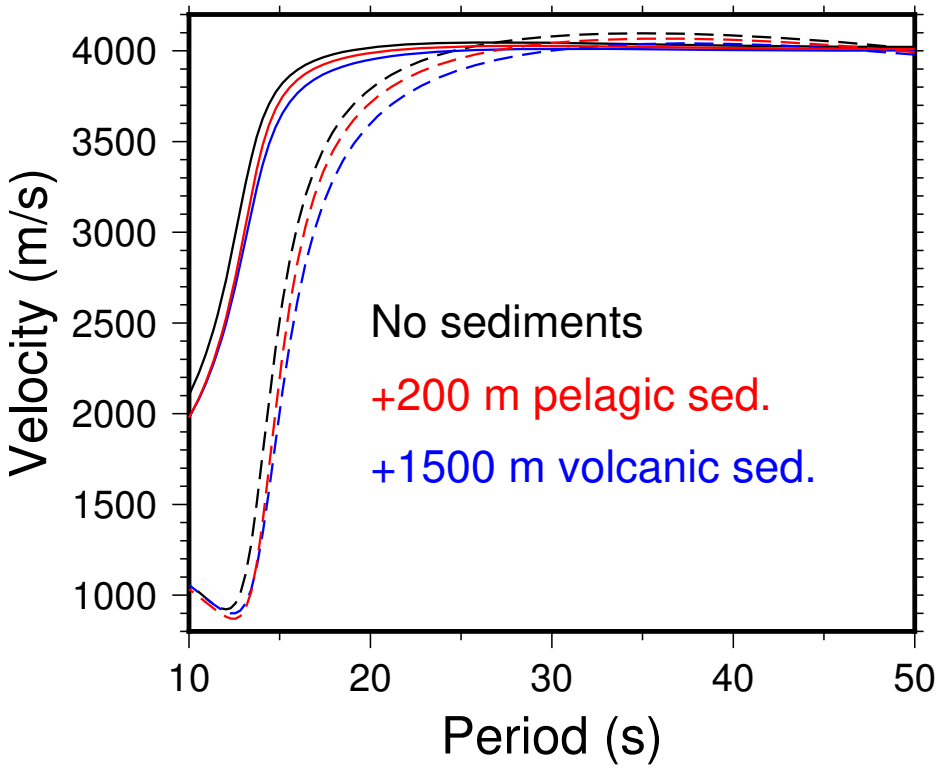

Figure S3.5: Predicted phase velocity (solid lines) and group velocity (dashed lines) computed for oceanic lithosphere age 52-110 Ma (Nishimura and Forsyth, 1989). We show the expected velocity from typical oceanic crust (black), and from our crustal model with 200 meters of pelagic sediments added (red) and 1500 meters of volcanic sediments added (blue). Forward models were run using the modeling codes of (Haney and Tsai, 2017) assuming 5000 meters of water.

Table S3.1: Earthquakes analyzed in for PLUME 1 DPG calibration and Ps delay time measurement

	Date	Time	Lat	Lon	Mag
Global	2005-11-14	21:38:50	38.047	144.879	7.0
	2005-10-08	03:50:35	34.524	73.640	7.6
	2005-09-26	01:55:37	-5.736	-76.475	7.5
	2005-09-09	07:26:42	-4.561	153.479	7.7
	2005-08-16	02:46:26	38.201	142.114	7.2
	2005-07-24	15:42:05	7.907	92.146	7.2
	2005-06-15	02:50:55	41.447	-125.585	7.2
	2005-06-13	22:44:32	-19.917	-69.216	7.8
	2005-03-28	16:09:35	2.096	97.113	8.6
	2005-03-02	10:42:09	-6.566	129.880	7.1
	2005-02-05	12:23:18	5.290	123.436	7.1
Regional	2005-12-07	11:58:08	18.873	-155.182	4.0
	2005-12-07	11:42:12	18.923	-155.175	4.7
	2005-12-07	09:02:06	18.921	-155.264	4.0
	2005-11-30	08:26:22	19.330	-155.110	4.2
	2005-10-10	09:44:59	19.498	-155.469	4.2
	2005-07-26	08:08:35	19.348	-155.327	4.2
	2005-07-17	19:15:03	18.779	-155.447	5.1
	2005-07-15	15:48:54	20.441	-155.133	5.3
	2005-05-20	15:52:07	21.671	-157.607	4.1
	2005-05-13	10:06:41	18.866	-155.202	4.6
	2005-04-23	13:01:29	18.798	-155.193	4.3
	2005-03-08	17:26:16	19.015	-155.357	4.2

Table S3.2: Earthquakes analyzed in for PLUME 2 DPG calibration and Ps delay time measurement

	Date	Time	Lat	Lon	Mag
Global	2007-04-01	20:39:56	-8.447	157.026	8.1
	2007-03-25	00:40:03	-20.567	169.346	7.1
	2007-01-21	11:27:44	1.082	126.362	7.5
	2007-01-13	04:23:23	46.231	154.503	8.1
	2006-12-26	12:26:21	21.864	120.545	7.0
	2006-11-15	11:14:14	46.681	153.211	8.3
	2006-08-20	03:41:45	-61.016	-34.285	7.0
	2006-07-17	08:19:26	-9.318	107.424	7.7
Regional	2007-05-24	20:51:36	19.382	-155.241	3.9
	2007-05-24	19:33:09	19.384	-155.238	4.1
	2007-05-24	19:13:44	19.395	-155.251	4.2
	2007-05-02	15:35:11	20.021	-155.315	3.5
	2007-04-26	15:16:15	19.356	-155.077	3.7
	2007-01-31	03:33:48	19.313	-156.299	3.6
	2006-12-05	12:54:44	19.923	-156.256	3.5
	2006-12-03	12:22:21	19.959	-155.983	4.5
	2006-11-23	19:20:10	19.890	-155.967	5.2
	2006-11-13	01:36:06	19.896	-155.864	3.7
	2006-10-17	16:57:33	19.987	-156.028	3.5
	2006-10-17	15:26:45	20.029	-155.957	3.9
	2006-10-15	20:35:21	20.085	-155.965	4.4
	2006-10-15	18:19:57	19.928	-155.922	3.7
	2006-10-15	17:29:04	19.883	-155.896	3.6
	2006-10-15	17:14:12	20.129	-155.983	6.1
	2006-09-05	03:27:39	19.842	-155.953	3.7
	2006-08-29	06:09:58	21.758	-157.483	3.6
	2006-07-27	20:03:33	20.340	-156.576	4.4

Table S3.3: PLUME 1 station parameters.

Site	Inst. Type	Long.	Lat.	Depth	HN	DPG gain	Ps Delay	Sies. Gain	Sed. Thickness
PL01	WHOI	20.088	-154.617	-5580	210.52 ± 2.52	2.093 ± 0.053	0.435 ± 0.0475	1	196 ± 7
PL02	WHOI	20.499	-154.937	-5065	306.41 ± 2.66	2.048 ± 0.035		1	142 ± 6
PL03	WHOI	21.205	-155.679	-5144	51.45 ± 1.8	2.003 ± 0.043	0.46 ± 0.05	1	700 ± 40
PL04	SIO1	22.289	-155.595	-4515					
PL05	WHOI	21.507	-154.994	-5196	207.93 ± 5.3	2.279 ± 0.114		1	158 ± 7
PL06	SIO1	21.001	-154.482	-5373	206.56 ± 1.41		0.465 ± 0.04	1	162
PL07	WHOI	21.519	-153.982	-4912	16.4 ± 2.44	1.397 ± 0.032	0.42 ± 0.04	1	184 ± 7
PL08	WHOI	20.892	-153.292	-5157	282.09 ± 2.2	1.273 ± 0.025	0.51 ± 0.06	1	240 ± 10
PL10	WHOI	19.979	-153.902	-5336	220.76 ± 2.03	1.954 ± 0.047	0.68 ± 0.0625	1	76 ± 4
PL11	WHOI	19.495	-153.503	-5181	201.59 ± 1.76	1.312 ± 0.027	0.42 ± 0.03	1	37 ± 7
PL12	SIO1	19.506	-154.017	-5385					
PL13	WHOI	19.262	-154.394	-5515	294.44 ± 4.04	2.422 ± 0.066	0.53 ± 0.045	1	125 ± 5
PL14	WHOI	18.797	-153.992	-5252	292.39 ± 3.06	1.637 ± 0.035	0.535 ± 0.075	1	98 ± 5
PL15	WHOI	18.800	-153.295	-5077	89.4 ± 30.29	1.887 ± 0.041	0.465 ± 0.05	1	88± 5
PL17	WHOI	18.481	-152.132	-5184	119.76 ± 2.65	2.243 ± 0.058	0.59 ± 0.04	1	135 ± 8
PL18	WHOI	17.906	-153.290	-4938	242.88 ± 14.04	2.041 ± 0.043	0.48 ± 0.0575	1	110
PL19	SIO1	16.711	-153.407	-5163					
PL20	WHOI	17.297	-153.700	-5120	16.44 ± 2.01	1.27 ± 0.023	0.52 ± 0.045	1	125 ± 6
PL21	SIO1	17.180	-154.691	-4993	47.15 ± 1.09		0.33 ± 0.0225	1	70
PL22	WHOI	17.988	-154.035	-5057	255.35 ± 1.84	1.234 ± 0.023	0.39 ± 0.05	1	80 ± 5
PL23	WHOI	18.401	-154.495	-5167	146.86 ± 2.52	2.084 ± 0.041	0.46 ± 0.0675	1	106 ± 4
PL24	WHOI	18.803	-154.797	-5319	326.46 ± 2.03	2.388 ± 0.049	0.48 ± 0.0975	1	106 ± 4
PL26	WHOI	17.975	-155.002	-4997					
PL27	WHOI	18.000	-155.715	-5099	33.52 ± 2.54	2.303 ± 0.047	0.47 ± 0.035	1	79 ± 5
PL28	SIO1	17.602	-156.499	-4792					
PL29	WHOI	18.404	-156.808	-4627	304.21 ± 2.27	1.345 ± 0.029	0.57 ± 0.0725	1	81 ± 6
PL30	WHOI	18.301	-156.167	-5091	114.56 ± 2.98	2.026 ± 0.042	0.525 ± 0.0625	1	114 ± 5
PL31	WHOI	18.775	-156.465	-4610	353.79 ± 3.07	1.527 ± 0.048	0.6 ± 0.105	1	140 ± 7
PL32	SIO1	18.984	-157.227	-4604	284.61 ± 1.31		0.58 ± 0.06	1	122
PL33	WHOI	19.477	-156.510	-4707	320.81 ± 1.63	1.683 ± 0.031	0.815 ± 0.12	1	1000 ± 60
PL34	WHOI	19.832	-156.932	-4748	127.23 ± 1.95	1.501 ± 0.029	0.82 ± 0.1125	1	1100 ± 65
PL35	WHOI	20.346	-157.627	-4650	145.86 ± 1.9	1.987 ± 0.041	0.735 ± 0.1	1	950 ± 60
PL36	WHOI	21.298	-158.903	-4762	184.39 ± 2.34	1.956 ± 0.02	0.77 ± 0.165	1	1500 ± 90

Table S3.4: PLUME 2 station parameters.

Site	Inst. Type	Long.	Lat.	Depth	HN	DPG gain	Ps Delay	Sies. Gain	Sed. Thickness
PL37	WHOI	19.8234	-160.0475	-4676	234.92 ± 2.46	2.157 ± 0.069	0.51 ± 0.0625	1	92 ± 4
PL38	SIO2	19.9863	-162.0256	-4897	179.37	2.2			
PL39	WHOI	21.9563	-161.3149	-4543	300.04 ± 2.02	1.366 ± 0.024	0.53 ± 0.045	1	136 ± 6
PL40	SIO2	23.9972	-161.095	-4691	168.32 ± 1	2.16 ± 0.019	0.535 ± 0.1	4	134 ± 8
PL41	WHOI	24.5738	-158.9331	-4749	48.89 ± 2.36	2.342 ± 0.034	0.54 ± 0.0625	1	133 ± 6
PL43	WHOI	26.7767	-155.7653	-5545	293.73 ± 1.16	1.297 ± 0.015	0.56 ± 0.075	1	77 ± 3
PL44	WHOI	25.5928	-152.7658	-5420	333.88 ± 1.48	1.344 ± 0.014	0.55 ± 0.08	1	87 ± 8
PL45	WHOI	24.2006	-154.812	-4686					
PL46	WHOI	24.3121	-156.9646	-4428	42.59 ± 1.44	2.048 ± 0.03	0.49 ± 0.055	1	94 ± 4
PL47	SIO2	22.6202	-158.1854	-4830	277.13 ± 1.14	3 ± 0.01	0.58 ± 0.0625	4	900 ± 55
PL48	WHOI	22.2999	-155.6362	-4528	96.94 ± 1.74	1.305 ± 0.017	0.45 ± 0.075	1	160 ± 6
PL49	SIO2	21.1687	-154.2518	-5173	290.45 ± 1.18	2.24 ± 0.1	0.45 ± 0.0525	2	188 ± 11
PL50	WHOI	22.3199	-152.7427	-5021					
PL51	WHOI	23.6843	-151.6957	-5485					
PL55	WHOI	18.3018	-152.9812	-5076		1.683 ± 0.016	0.62 ± 0.06	1	74 ± 5
PL57	WHOI	18.9142	-150.915	-5335	101.65 ± 1.56	2.087 ± 0.037	0.5 ± 0.0975	1	72 ± 4
PL59	WHOI	16.989	-149.0009	-5374	29.97 ± 2.28	2.317 ± 0.03	0.54 ± 0.075	1	108 ± 9
PL61	WHOI	16.7378	-151.6376	-5186	352.97 ± 2.18		0.56 ± 0.0525	1	117
PL62	WHOI	14.6891	-151.6866	-5765	283.31 ± 1.1	2.107 ± 0.048	0.56 ± 0.05	1	78 ± 5
PL63	SIO2	14.7313	-153.9675	-5603	70.05 ± 0.9	2.48 ± 0.03	0.56 ± 0.0625	4	75
PL65	WHOI	17.3154	-153.8682	-5115	65.47 ± 1.18	2.132 ± 0.023	0.53 ± 0.0725	1	125 ± 6
PL66	WHOI	17.6149	-156.3877	-4826	76.23 ± 1.52	1.692 ± 0.023	0.57 ± 0.1	1	129 ± 8
PL67	SIO2	16.162	-156.2066	-5112	66.15 ± 0.96		0.47 ± 0.0775	4	95
PL68	WHOI	14.6596	-157.8591	-5637	120.49 ± 0.98	0.0044 ± 0.0004	0.5 ± 0.055	1	100
PL69	WHOI	16.3484	-157.7008	-5365					
PL70	SIO2	15.574	-158.9825	-5591	144.84 ± 0.96	3.1 ± 0.03	0.775 ± 0.11	4	216 ± 13
PL71	WHOI	17.7469	-161.3676	-5601	315.15 ± 3.5	1.958 ± 0.031	0.6 ± 0.0675	1	76 ± 4
PL73	SIO2	18.5647	-158.7602	-4686		2.05 ± 0.01	0.78 ± 0.05	2	227 ± 11
PL74	WHOI	20.3778	-158.1795	-4541	181.25 ± 0.97	1.59 ± 0.029	0.7 ± 0.0525	1	875 ± 50

S3 DPG calibration for PLUME instruments

S3.1 Overview

At the time of writing (24 January 2018), the IRIS DMC listed the poles and zeros of both WHOI and SIO DPGs as:

Table S3.5: Nominal complex poles and zeros of PLUME DPGs

ZEROS (3)	0 + 0i
	0 + 0i
	-11656 + 0i
POLES (5)	-0.01.6667 + 0i
	-57.471 + 0i
	-100 + 0i
	-0.21277 + 0i
	-1655.6 + 0i

The gain constant was different between the instruments, and was listed as -8.074077e+05 for WHOI instruments and 1.121353e+06 for SIO instruments. As our compliance data are low frequency, for this study we were only concerned with the long-period poles, i.e. those below 1 sec/rad. In this document we shall refer to the pole nominally at -0.213 rad/sec as the intermediate pole and the pole nominally at -0.017 rad/sec as the low pole.

The WHOI intermediate pole has been determined as the inverse product of a 1MΩ resistor and a 4.7μF capacitor, as expected for an RC high-pass filter. However, there is disagreement regarding the correct value of the intermediate pole of the SIO instruments. Existing electronics diagrams suggest the pole should be at 0.05 rad/sec, while a contemporaneous pole/zero document described the pole at 0.2 rad/sec. The original instruments have been destroyed and direct measurement of this pole is now impossible. The low pole, relating to the relaxation time constant of the DPG, varied between instruments, but should not vary systematically between institutions. John Collins [pers. comm., Nov. 2017] has confirmed the accuracy of the WHOI

intermediate pole as the inverse product of a 1MΩ resistor and a 4.7μF capacitor, as expected for an RC high-pass filter. However, there is disagreement regarding the correct value of the intermediate pole of the SIO instruments. Spahr Webb and Wayne Crawford [pers. comm., Nov. 2017] have argued that this pole should be at 0.05 rad/sec based on existing electronics diagrams, while a contemporaneous pole/zero document describes the pole at 0.2 rad/sec [Jeff Babcock, pers. comm., Dec. 2017]. The original instruments have been destroyed and direct measurement of this pole is now impossible [Martin Rapa and Sean McPeak, pers. comm., Jan 2018]. The low pole, relating to the relaxation time constant of the DPG, varied between instruments, but should not vary systematically between institutions [John Souders and Jacques Lemire, pers. comm., Dec. 2017]. The gain of individual DPGs is known to vary by a factor of two or greater between instruments. This document details our results of calibrating the intermediate pole at SIO stations, the low pole at all sites, and the gain constant at all sites.

S3.2 WHOI Instruments

Gain correction

Ball et al. (2014a) first discussed DPG gain corrections in the context of compliance studies. As given by Filloux (1983), the relationship between seafloor pressure p_s and vertical seafloor acceleration is given by

$$p_s = \rho h \frac{d^2x}{dt^2} \tag{3.7}$$

where ρ is the density of sea water, h is the water depth, and x is the position of the seafloor at time t. This equation is assumed valid at periods much larger than the acoustic resonance period of the local water column. Ball et al. (2014b) adjusted the measured transfer function at 30 seconds to the ρH theoretical value for each OBS package deployed as part of the MOANA experiment offshore New Zealand in 2009-2010 (Yang et al., 2012). The authors

presented the mean and standard deviation of the 28 corrections (0.9 ± 0.1), and presented the results for two individual stations: NZ16, with $g_{DPG} = 1.0$ (meaning no correction necessary), and NZ06, with $g_{DPG} = 0.7 \pm 0.1$.

Starting with the equations of motion for Rayleigh waves in water, Zha and Webb (2016) derived the pressure-acceleration transfer function during transient Rayleigh waves to be

$$\left.\frac{P}{a}\right|_{z=H} = \frac{\rho \sin(rH)}{r\cos(rH)} \approx \rho H \qquad\qquad r = \omega(\alpha^{-2} - c^{-2})^{1/2} \tag{3.8}$$

where ρ is the density of sea water, H is the water depth, ω is angular frequency, α is the speed of sound in water, and c is the phase velocity of the Rayleigh wave. The authors examined all earthquakes with $M \geq 7$ during the deployment and obtained the gain factors by minimizing the difference between observed and predicted P/a ratios between 0.04 and 0.1 Hz., a slightly higher frequency range than infragravity waves.

We calculated the pressure-acceleration transfer function for a single event during a 15 minute window centered on the 25 mHz group velocity arrival time as predicted by the global dispersion maps of Ma and Masters (2014). Figure S3.6 shows the calculation for one event as station PL20. Once we performed these calculations for every $M \geq 7$ event (see Tables S3.1 and S3.2 for events considered), we analyzed the ensemble of transfer function estimates to compute the gain correction coefficient. We incorporated only events producing high-coherence data (defined as having coherence greater than 0.9 at 20 mHz, typically yielding between 5-10 usable events) and computed the median and standard deviation of the transfer function value at each frequency between 19-35 mHz. We then divided these data by theoretical transfer function, calculated using Equation 3.8. We used $\rho = 1024$ kg/m^3 and α = 1500 m/s. We used phase velocity values calculated using a PREM model overlain by an oceanic crust (Laske and Widmer-Schnidrig, 2015). We also tested using the phase velocities from Ma et al. (2014), but the difference in the theoretical transfer function was negligible. We defined the static correction factor as the weighted mean value of the transfer function at frequencies between 19-35 mHz,

given as

$$\mu_w = \sum_{i=1}^{n} \frac{d_i w_i}{w_i} \tag{3.9}$$

where d_i are the data and w_i are the weights. We define the the weights as $w_i = 1/\sigma_i^2$, where σ_i is the standard deviation of the transfer function at each frequency. The uncertainty of the weighted mean was calculated as following Taylor (1997) as:

$$\sigma_{\mu_w} = \frac{1}{\sqrt{\sum w_i}} \tag{3.10}$$

Figure S3.7 shows summary results at station PL20. High coherence was seen during nine large events. We calculated consistent transfer function estimates and a final gain correction with low uncertainty. We assumed a purely static gain correction and did not include frequency-dependent effects.

Figure S3.8 displays the range of DPG correction values calculated at the PLUME WHOI sites. Summary statistics of previous analyses are included for comparison. This gain calibration value corresponds to a factor by which the nominal gain is too large: therefore, for an instrument with a gain correction of 2, the actual gain is twice the value of the nominal gain. This means that spectral power values calculated using the nominal gain value are too high. We also ensured that we did not bias our results by not removing the tilt signal during the DPG calibration procedure. We expected that the tilt signal would not significantly impact the vertical acceleration channel because the seismic waves are over an order of magnitude larger than the tilt signal (e.g., Crawford et al., 2006). Figure S3.9 shows the final result at PL20 obtained while removing the tilt and not removing the tilt. The final gain corrections are statistically equivalent and fall within the respective error bars.

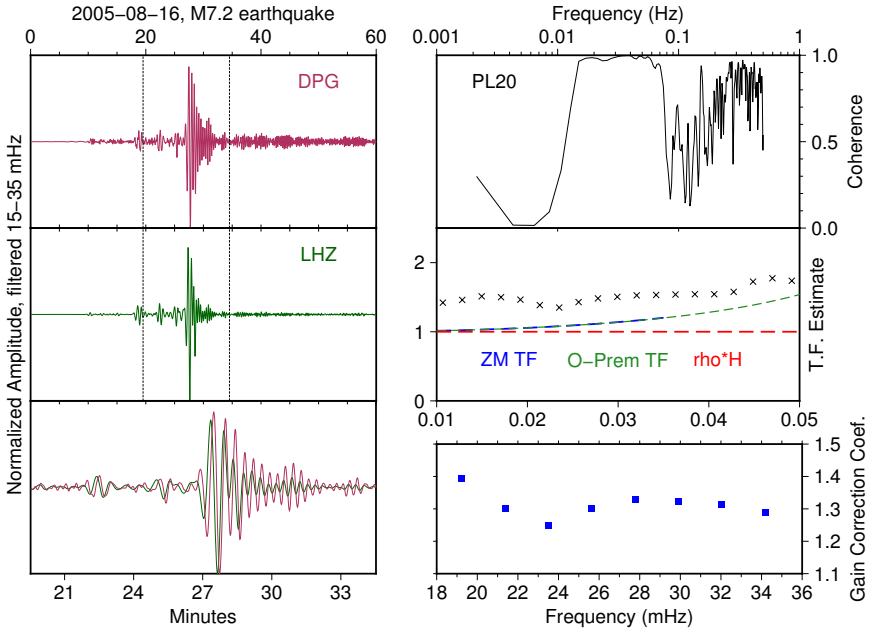

Figure S3.6: DPG gain correction results from analysis of the August 16th, 2005, M7.2 Miyagi earthquake recorded at PLUME1 WHOI site PL20. The left three panels show filtered pressure and acceleration signals, with the analysis window identified as described in the text and highlighted in the bottom left panel. The top right panel shows the coherence between the signals, and the middle right panel shows the transfer function estimate for these data. We include the hypothetical values calculated using ρH and the phase velocities of an oceanic PREM model (Laske and Widmer-Schnidrig, 2015). The correction at several frequencies is shown in the bottom right panel.

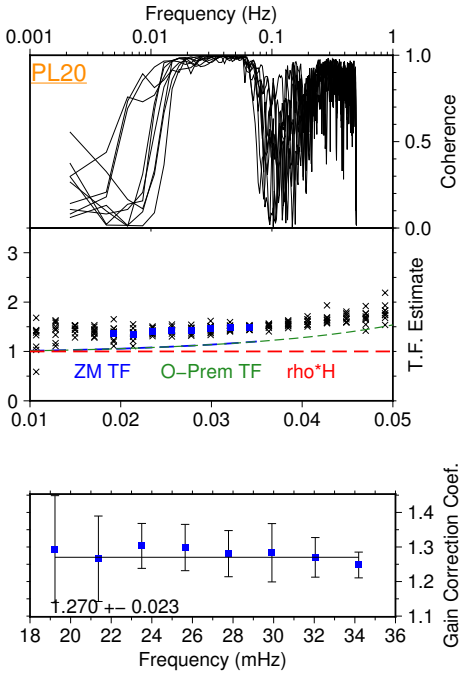

Figure S3.7: Summary of DPG calibration results at site PL20. The coherence and transfer function estimated from nine different events producing high pressure-acceleration coherence are shown. The final gain correction at this site is calculated to be 1.270±0.023.

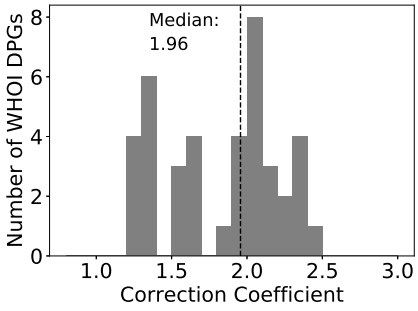

Figure S3.8: Summary of DPG calibration at PLUME WHOI sites. No distinction between PLUME 1 and 2. Not shown is the correction for station PL68, with a calculated correction factor of 0.0044. One of the WHOI DPGs analyzed by Zha and Webb (2016) also required a significantly lower correction factor, hypothesized to result from a leaky valve in the DPG. We have been unable to confirm whether or not this is the same instrument. We note than John Collins also found one highly-anomalous instrument (see text), though again we cannot confirm which instrument this is. the median calibration factor of Zha and Webb (2016) is 1.73 and the mean calibration factor of Ball et al. (2014b) is 0.9. John Collins [pers. comm., Nov. 2017] provided additional unpublished measurements for WHOI instruments, ranging from 0.725 - 1.4.

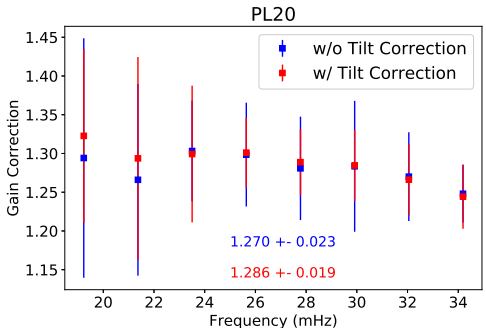

Figure S3.9: Comparison of DPG gain correction results at site PL20 after removing the tilt signal and after not removing the tilt signal. The final results for this station are statistically equivalent.

Low pole calibration

We then focused on the gain-corrected WHOI spectra and calibrated the long-period pole using tidal models. We calculated the tidal models using the OTIS tidal model (Egbert and Erofeeva, 2002) and a regional Hawaiian bathymetry map (Smith and Sandwell, 1997). We calculated synthetic tide data every 1000 seconds for the month of February and include tidal constituents M2, S2, N2, K2, K1, O1, P1, Q1, Mm, and Mf. To calculate the DPG spectra we downloaded continuous data for the month of February, removed a linear trend and applied a 10% cosine taper, filter and decimate to 100 second data, calculated the power spectrum, removed the instrument response, and then applied the gain correction.

As seen in Figure S3.10, using the nominal pole of 60 sec/rad produced higher spectral values at the tidal frequencies than predicted by the model. We verify that the model is not the issue by comparing OTIS with SPOTL and seeing similar results. In order to reach agreement between the data and the model, pole values of approximately 250 sec/rad were required. This is a significantly higher value than typically used. Previous measurements of WHOI instruments have typically found pole values between 90-100 sec/rad, but have noted very large discrepancies between predicted and actual tidal amplitudes, as seen here. John Collins [pers. comm., Nov. 2017] measured the time constants of 12 instruments, finding pole values typically between 90-

100 sec/rad, with one outlier at 120 and another at 27. As described above, John Collins noted that he recently found pole values typically between 90 - 100 for most instruments. However, he also noted that he saw "very large" discrepancies between predicted and actual tidal amplitudes, as we see here. He noted as well significant differences between individual instruments, which we also observe. We also report (from Wayne Crawford, per. comm., Nov 2017) that two instruments in use by the Institut de Physique du Globe de Paris (IPGP) had measured low pole values of 55 sec/rad and 72 sec/rad. We used a constant value of 95 rad/sec in our analysis of PLUME data. The effect on the instrument response and on the resulting spectra can be seen in Figure S3.11. By adjusting the low pole from 60 sec/rad to 95 sec/rad, we altered the compliance data by approximately 3% at the lowest frequencies (7 mHz) and by less than 0.5% at the highest frequencies (15 mHz).

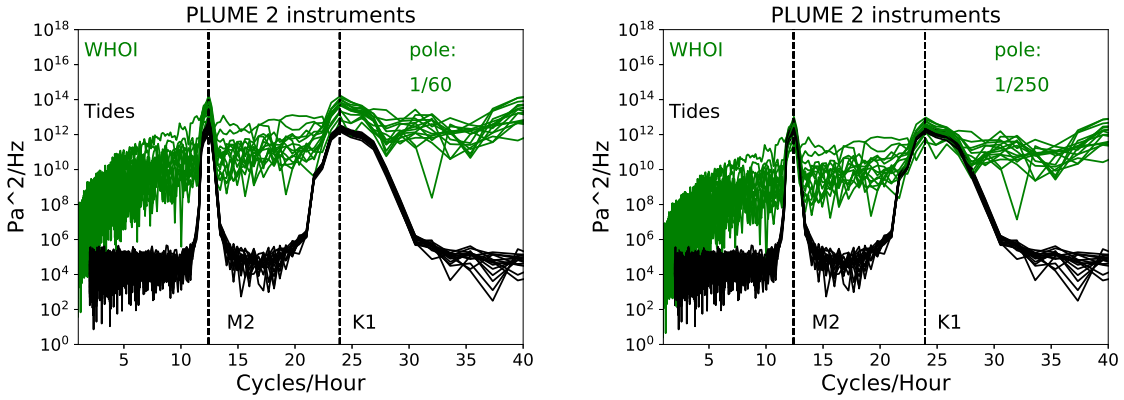

Figure S3.10: DPG spectra calculated using 28 days of data (February 2007). The spectra are compared with the predicted spectra from the tidal model OTIS. In the left panel, a value of 60 rad/sec is used for the low pole, while in the right panel, a value of 250 rad/sec is used for the low pole.

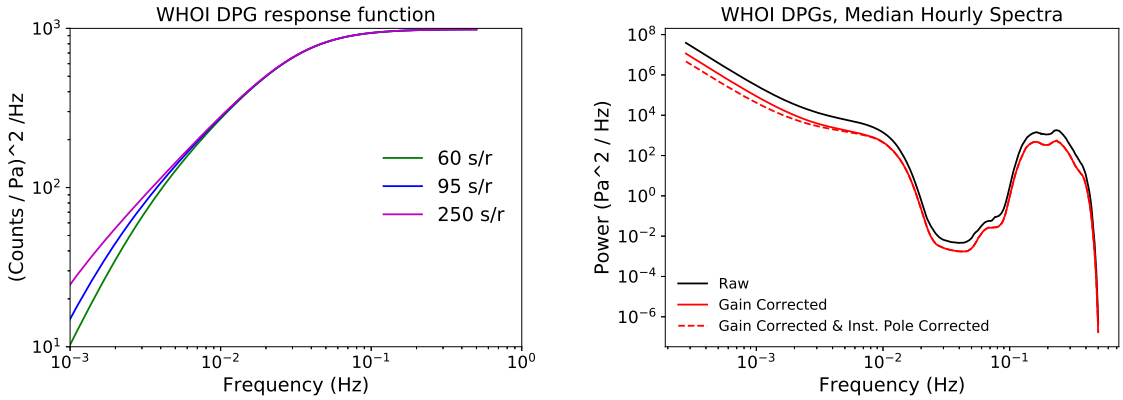

Figure S3.11: (a) The instrument response of WHOI DPGs as a function of the value of the low pole. (b) The resulting difference on the median DPG spectra. Adjusting the gain lowers the entire spectra by a fixed amount, while adjusting the low pole affects data 10 mHz and lower.

S3.3 SIO Instruments

The SIO DPG spectra were systematically different from the WHOI DPG spectra when the same nominal instrument response was used. The difference began at approximately 5-8 mHz and increased with increasing frequency. Since it was a frequency-dependent issue it could not simply be solved with a gain calibration. In addition, we knew that there should be no systematic differences between the long-period poles of the instruments. Therefore, we suspected a problem with the electronics pole.

First we tried the 1-pole response as reported for SIO instruments used in the Cascadia Initiative provided by J. Berger (pers. comm. 2014, also used as Cascadia responses). This response assumes there is no intermediate pole present on the instrument. As seen in Figure S3.12, this did not lead to the expected spectra. Conversations with S. McPeak, M. Rapa, & others confirmed that there should be an electronics pole associated with these instruments. We then placed the pole at 0.2 rad/s and 0.05 rad/s, as discussed previously. Neither pole produced spectra that were consistent with the WHOI spectra (Fig. S3.13). In addition, many of the calibration results were still unsatisfactory, i.e., the gain calibration still appeared to have a frequency dependence. We attempted a grid search to find the best pole value, but in all cases the resulting compliance values had systematic and significant differences.

We therefore constructed an empirical transfer function between the pressure spectra at WHOI and SIO instruments, assuming the WHOI spectra were correct. We examined both ambient noise spectra and earthquake spectra, which should yield consistent results. We calculated the pressure spectra of each station for the eleven events listed in Table S3.2 and divided the SIO results by the WHOI results. The spectra were calculated using 15 minutes of 1 sps data centered on the predicted 25 mHz Rayleigh wave group arrival. We calculated the uncertainty as the standard deviation of the results at each frequency. Figure S3.14 shows the median pressure spectra (uncorrected for instrument response) for WHOI and SIO stations following the M7.5 Indonesia event mentioned previously. The WHOI stations were systematically higher, and the

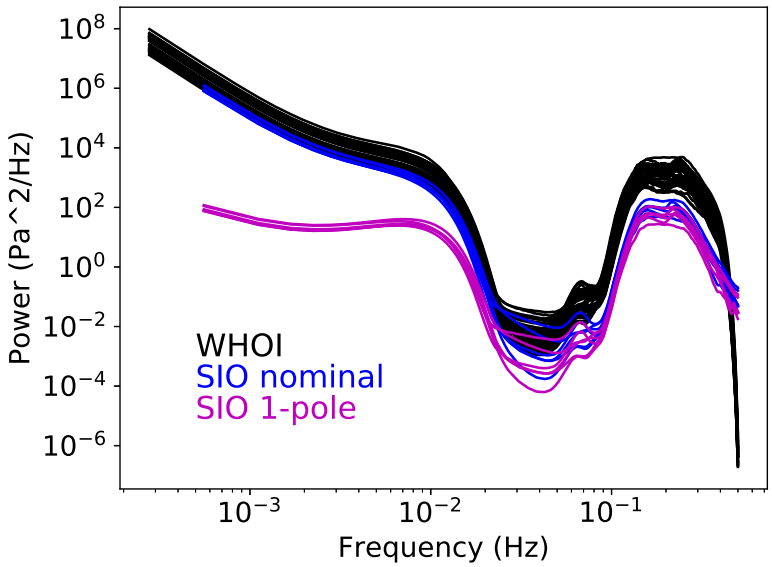

Figure S3.12: WHOI median hourly DPG spectra (uncorrected for gain calibration) compared with SIO spectra calculated using the nominal poles & zeroes and with the 1-pole response. Neither instrument response is able to reproduce the WHOI spectra to within a constant gain offset.

difference was a function of frequency. This confirmed that the instruments did not have the same frequency response. For the ambient noise spectra, we divided the median spectrum at each SIO station by the median ambient spectrum at each WHOI station, and calculated the uncertainty in the same manor. The combined results are shown in Figure S3.15. The transfer functions yielded consistent results, and we defined an empirical transfer function:

$$TF\left(\frac{SIO}{WHOI}\right) = \frac{0.85}{(1+(f/0.008)^2)^{0.3}} \tag{3.11}$$

The empirical instrument response of SIO sites is now the product of the nominal response and the empirical transfer function. Figure S3.16 shows the summary results for correction of the SIO intermediate pole. We finally calibrate the SIO DPG gain constants in the same way as the WHOI stations. We exclude events corrupted by the long-period seismometer spikes. An example of the calibration at PL40 is shown in Figure S3.17.

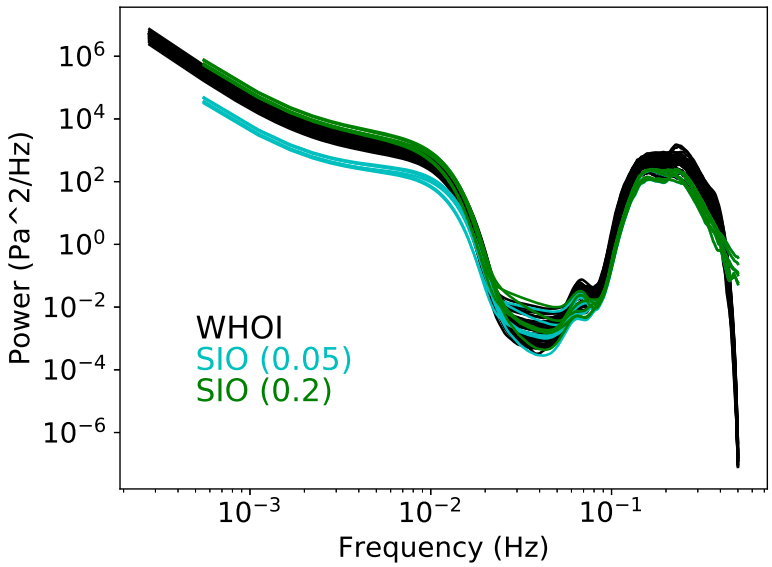

Figure S3.13: WHOI median hourly DPG spectra (now corrected for gain calibration) compared with SIO spectra calculated using the nominal poles & zeroes with only the intermediate pole altered (to 0.05 and 0.2 rad/sec). Neither instrument response is able to reproduce the WHOI spectra to within a constant gain offset. We perform a grid search for values between these extremes but are unable to reproduce the spectral shapes.

Table S3.6: Single-pole response of DPGs in modern SIO OBS packages.

Zeros	Poles
0.00 + 0.00i	-0.0126 + 0.00i

We compared compliance data between SIO and WHOI sites to ensure the empirical transfer function was adequate. PL40 (SIO) and PL41 (WHOI) both were situated several hundred kilometers north of the island of Kauai, with PL40 west of PL41. The water depth was only 58 meters greater at PL41 (4749m compared to 4961m), and the sites were in similar bathymetric settings. Figure S3.18 plots the compliance curves at these two sites. Both pairs of sites had nearly identical compliance values at frequencies greater than 10 mHz, but diverged slightly at lower frequencies. The discrepancy could have several origins. The empirical instrument response could be incorrect at low frequencies, or could differ slightly between instruments. Another possibility is that the higher values at the WHOI sites could be related to the 120 sec-

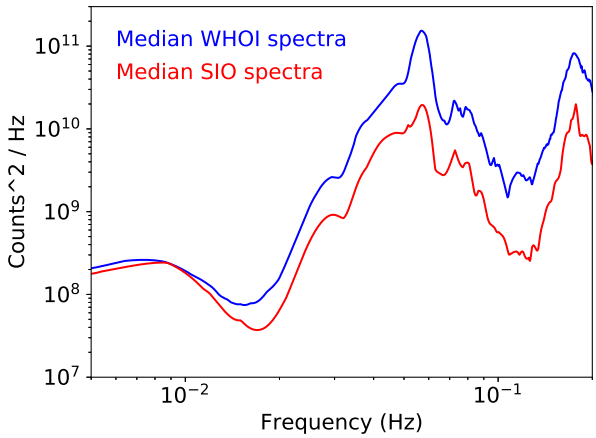

Figure S3.14: Median DPG earthquake spectra calculated at SIO and WHOI sites (uncorrected for instrument response) following the 21 January 2007 M7.5 Indonesian event. Details of the spectra calculation are found in the text. The instruments have the same nominal response, but clearly record different power levels.

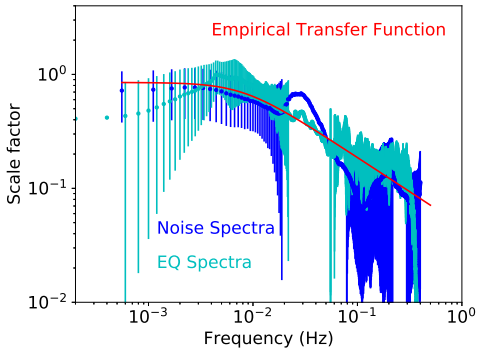

Figure S3.15: Empirical transfer function between SIO and WHOI pressure gauges. The results of both the earthquake spectra and the ambient noise spectra are shown. Equation 3.11 defines the final empirical transfer function.

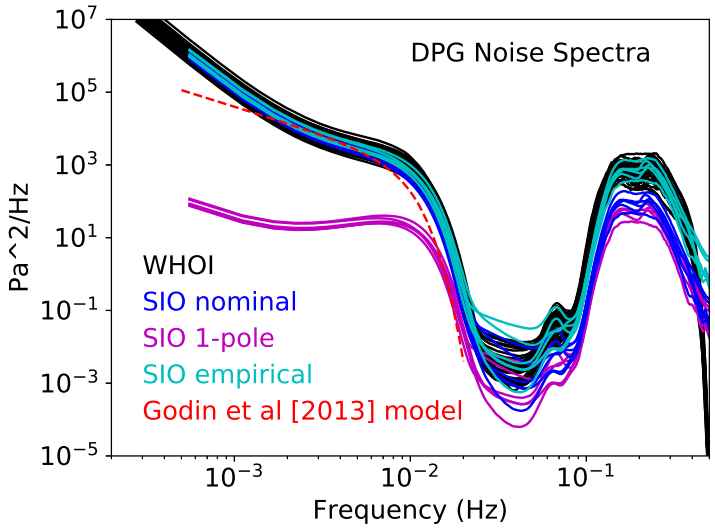

Figure S3.16: Ambient noise spectra from WHOI and SIO stations. The 'SIO nominal' spectra are calculated using the nominal instrument response. The 'SIO 1-pole' spectra are calculated using the single pole response listed in Table S3.6, while the 'SIO empirical' spectra are corrected for the empirical instrument response. The Godin et al. (2013) model for power of infragravity waves on pressures sensors is included for comparison.

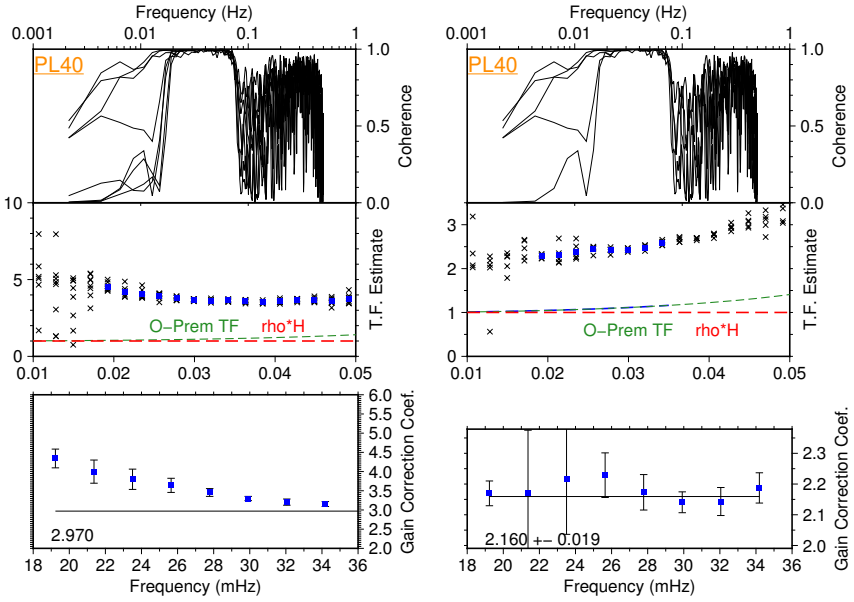

Figure S3.17: A summary plot of the DPG gain calibration at PL40 similar to Figure S3.7. (A) The calibration results using the nominal instrument response. The transfer function does not converge to the expected value at low frequencies. (B) The calibration results using the empirical transfer function. We now calculate a consistent gain correction coefficient independent of frequency.

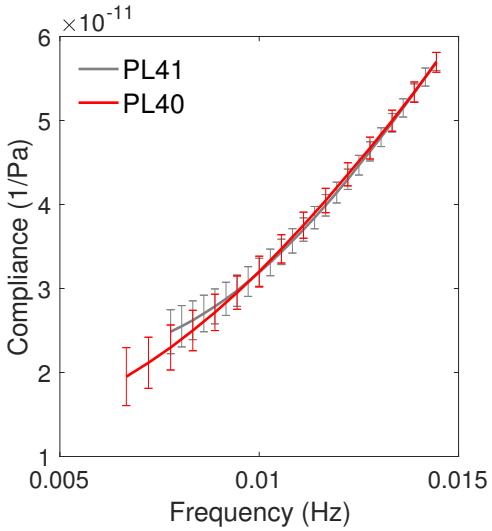

Figure S3.18: Comparison of final compliance data at PL40 and PL41, which are located in similar geologic and bathymetric settings as described in the text. The curves are very similar at high frequencies but begin to diverge at low frequencies, although the differences are within the uncertainties.

ond instrument roll-off of the Güralp CMG-3Ts; however, this effect should be accounted for through the instrument response and the signal coherence. Finally, some of the difference could be due to real structural differences, although since lower frequencies generally reflect deeper structure we find this unlikely. We conclude that the effect is probably due to an imperfect transfer function, but proceed with these results.

Table S3.7: Gain calibration constants at the eight SIO PLUME2 sites. These are calibrated using the empirical transfer function, and so cannot be compared to the WHOI calibration coefficients.

Site	g_{DPG}
PL38	Not enough data
PL40	2.16±0.02
PL47	3.00±0.01
PL49	2.24±0.1
PL63	2.48±0.03
PL67	Not enough data
PL70	3.10±0.03
PL73	2.05±0.01

S3.4 Summary

To summarize, one adjustment was necessary to the nominal poles and zeros for WHOI instruments. The lowest-frequency pole should have been -1/95 (-0.0105), instead of -1/60 (-0.0166), as listed. This made a small difference at frequencies lower than 10 mHz.

The final poles and zeros values for WHOI instruments were:

Table S3.8: Final complex poles and zeros of WHOI PLUME DPGs

ZEROS (3)	0 + 0i
	0 + 0i
	-11656 + 0i
POLES (5)	-0.00105 + 0i
	-57.471 + 0i
	-100 + 0i
	-0.21277 + 0i
	-1655.6 + 0i
CONSTANT	-807407.7

with the gain correction applied to the constant. For SIO instruments, we used this instrument response multiplied by the empirical transfer function of Equation 3.11. This empirical transfer function was determined from ambient and earthquake spectra because a satisfactory fix could not be found by only adjusting the intermediate pole. We then applied the gain constant calculated using this response. While we acknowledge that the final factor of $f^{0.6}$ is nonphysical, we feel it is sufficient for the adjustments required here. Further examination of the effects of temperature could also be warranted. Oil viscosities can vary by as much as 3% per degree, impacting the response time of the instruments. If significant temperatures differences were observed between the stations, differences in timing may also have to be considered. For another detailed look at DPG responses, see An et al. (2017).

4 Structure of the lower crust and uppermost mantle surrounding Hawaii

1 Abstract

We present models of crustal thickness and uppermost mantle velocity structure beneath the Hawaiian Swell and surrounding region. The models are derived from measurements of intermediate-period (14 - 24 seconds) Rayleigh-wave phase velocities that were obtained using seismic data collected during two year-long broadband ocean-bottom seismometer deployments for the Hawaiian Plume-Lithosphere Undersea Mantle Experiment. The phase velocity data were estimated from ambient noise correlations computed using over one year of continuous data. We inverted for phase velocity maps as a function of period, and then modeled the resulting velocities at the location of OBS stations. Our initial results demonstrate that the uppermost mantle may exhibit variations in shear velocity on the order of $\pm$ 5%. The strongest variations were found directly north and northeast of Hawaii, and may be related to the location of the Molokai Fracture Zone These low-velocity anomalies could be explained through several percent partial melt and a thermal anomaly of several hundred degrees, consistent with results from the lower lithosphere presented by Laske et al. (2011).

2 Introduction

Recent research has contributed numerous observations supporting the hypothesis that the Hawaiian hotspot is sourced from a deep-rooted mantle plume. Analyses of diverse geophysical observations have traced the plume from the base of the mantle (French and Romanowicz, 2015), through the transition zone (Ritsema and Allen, 2003; Wolfe et al., 2009, 2011), and into the lithosphere with a complex non-vertical pathways of upwelling mantle melt (e.g., Constable and Heinson, 2004; Laske et al., 2007, 2011; Rychert et al., 2013; Agius et al., 2017). However, the source of the Hawaiian hotspot remains controversial. Geodynamical models have been developed to support the plume hypothesis (Ballmer et al., 2011, 2013), but a number of models exist that can explain the observed volcanism through small-scale convection within the

upper mantle and may not require a plume at all (e.g., Anderson and Natland, 2005; Natland and Winterer, 2005; Ballmer et al., 2007; Anderson, 2011).

Any theory for the origin of the Hawaiian hotspot must explain the Hawaiian Swell, the bathymetric uplift surrounding the Hawaiian islands. In one model, the lithosphere reheats and thins over a hotspot, causing seafloor uplift ("thermal rejuvenation"; e.g., Detrick and Crough (1978)). In another, the mantle plume itself causes the entire unaltered lithosphere to rise by exerting normal stresses at the base ("dynamic support"; e.g., Olson (1990)). Existing geophysical data are seemingly inconclusive or contradictory. Using data from the Gravity Recovery and Climate Experiment (GRACE), a pair of satellites launched by NASA in 2002, Cadio et al. (2012) analyze geoid measurements and rule out thermal rejuvenation as an important mechanism, but recent tomographic studies (e.g., Li et al., 2004; Laske et al., 2007, 2011) are most consistent with a hybrid model of thermal rejuvenation and dynamic support. Other recent studies have introduced ideas of chemical buoyancy in the form of crustal underplating (Phipps Morgan et al., 1995; Leahy et al., 2010) to reconcile the observed bathymetry with heat flow measurements.

One major impediment to improved understanding of the Hawaiian hotspot is uncertainty in the elastic parameters of the crust beneath Hawaii. Around the Hawaiian islands, the oceanic crust increases from a typical thickness of approximately 6 km off the Swell to nearly 20 km beneath the island of Hawaii (e.g., Zucca et al., 1982; Watts et al., 1985; Watts and ten Brink, 1989; Leahy et al., 2010). Local variation in crustal structure has been attributed to lithospheric flexure (ten Brink and Brocher, 1987), and evidence has also been presented for systematic differences in crustal thickness across the Molokai Fracture Zone (ten Brink and Brocher, 1988). The thickness and velocity of local sediments show strong regional differences, and thickness has been observed to increase from 100 m far from the islands to over 2 km within the Hawaiian Moat (Rees et al., 1993; Leslie et al., 2002; Doran and Laske, 2019). Despite these observations, additional constraints are needed on the shear structure of the lower crust and uppermost mantle to improve the accuracy of structural inversions. The sensitivity of even long-period seismic data to

near-surface structure is well documented, as are the nonlinear effects of strong lateral variations in crustal structure (e.g., Montagner and Jobert, 1988; Marone and Romanowicz, 2007).

3 Data

Surface wave group and phase velocity measurements between two stations have often been used to constrain Earth structure (e.g., Romanowicz, 2002), and recovering group and phase velocity dispersion information from ambient noise records has progressed beyond infancy and is now a routine way of imaging lithospheric structure (e.g., Campillo and Paul, 2003; Sabra et al., 2005; Shapiro and Campillo, 2004; Lin et al., 2006; Bensen et al., 2007; Harmon et al., 2007b; Campillo and Roux, 2015). Much like the analysis of teleseismic surface waves, the analysis of ambient noise provides path-averaged dispersion curves that lead to frequency-dependent dispersion maps in 2D tomographic inversions.

PLUME consisted of two year-long deployments of wideband and broadband ocean bottom seismometers (OBS) at over 60 seafloor sites with an array aperture of over 1000 km (Laske et al., 2009). The majority of the OBSs were provided by Woods Hole Oceanographic Institute (WHOI) and contained Güralp CMG-3Ts (corner period at 120 seconds). The remaining instruments were provided by Scripps Institution of Oceanography (SIO), of which the PLUME phase 1 instruments contained Nanometrics Trillium 40 wideband seismometers (corner period at 40 s) and the PLUME phase 2 instruments contained Nanometrics Trillium 240 broadband seismometers (corner period at 240 s). All instruments contained Cox-Webb differential pressure gauges (DPGs; Cox et al. (1984)). The experiment included ten additional temporary land stations equipped with Wielandt-Streckeisen STS-2s (corner period 120 seconds) and took advantage of three GSN stations (KIP, POHA, and MAUI), all broadband instruments with responses flat to 120 seconds or longer.

In this study we examined vertical component data from all available broadband OBSs

and land stations. We calculated the ambient noise correlations closely following the method of Bensen et al. (2007). In order to pre-process each day of 1 sps data, we filter the data between 2 and 50 seconds, remove the nominal instrument response, remove the tilt signal (calculated during the compliance data analysis), and apply one-bit normalization and spectral whitening (Lecocq et al., 2014). We then compute the cross-correlation between two stations and stack each daily correlation. The correlation produces both causal and acausal signals, representing the waves traveling in both directions between the stations.

We measure group velocity also following Bensen et al. (2007), based on the FTAN method of Levshin et al. (1989). For each correlation waveform, we calculate the complex analytic signal, given as

$$S_a(t) = s(t) + iH(t) \tag{4.1}$$

where $H(t)$ is the Hilbert transform of the original signal. To examine the signal as a function of frequency, we apply a series of bandpass Gaussian filters, defined in the frequency domain as

$$G(\omega - \omega_0) = \exp\left[-a\left(\frac{\omega - \omega_0}{\omega_0}\right)^2\right] \tag{4.2}$$

where ω_0 is the center frequency of the filter and a is a tunable parameter that determines the frequency resolution. The group arrival time as a function of frequency $\tau(\omega)$ is measured from the arrival time of the maximum of the amplitude of the analytic signal (also called the envelope function). The group velocity $U(\omega)$ is defined as the inter-station distance divided by the group arrival time. During the calculations, the nominal frequency must be replaced by the instantaneous frequency, defined as the rate of change of the phase of the analytic signal: $\omega_i = |d\phi(t,\omega_0)/dt$. As noted by Bowden et al. (2016), steep topography and velocity changes can lead to additional arrivals. We therefore implemented a selection guide, based on the expected

arrival time accounting for water depth. An example calculation is shown in Figure 4.1. The uncertainty is estimated from the difference in measurement between the causal and acausal signals.

In order to measure phase velocity, we follow the method of Ekström et al. (2009), based on the formulation of Aki (1957). This allows an independent assessment of phase velocity that is not dependent on group velocity measurements. This solution removes the $\pi/2$ phase shift introduced with traditional measurements (e.g., Lin et al., 2008). In this approach, the zero-crossings of the real part of the Fourier transform of the cross-correlation waveform are associated with zeros of a Bessel function to estimate phase velocities at discrete frequencies. As described by Ekström et al. (2009), if ω_n denotes the frequency of the nth observed zero crossing and z_n denotes the nth zero of J_0, the corresponding phase velocity is determined as

$$c(\omega_n) = \frac{\omega_n r}{z_n} \tag{4.3}$$

where r is the inter-station distance and J_0 is a zeroth order Bessel function of the first kind. In order to account for noisy spectra with possible missed or extra zero crossings, a suite of solutions is calculated as

$$c_m(\omega_n) = \frac{\omega_n r}{z_{n+2m}} \tag{4.4}$$

Figure 4.1 shows an example measurement of phase velocities between PL17 and PL24. The measurement uncertainties are taken as the difference between the estimated phase velocities using the positive zero crossings (i.e., the spectrum crossing from negative to positive) and the estimates using the negative zero crossings.

We assembled a database of measurements for group velocity between 5 and 22 seconds and for phase velocity between 14 and 24 seconds. Notice in Figure 4.1 that at short periods we observe overtone arrivals, which are sensitive to deeper structure, but we do not incorporate

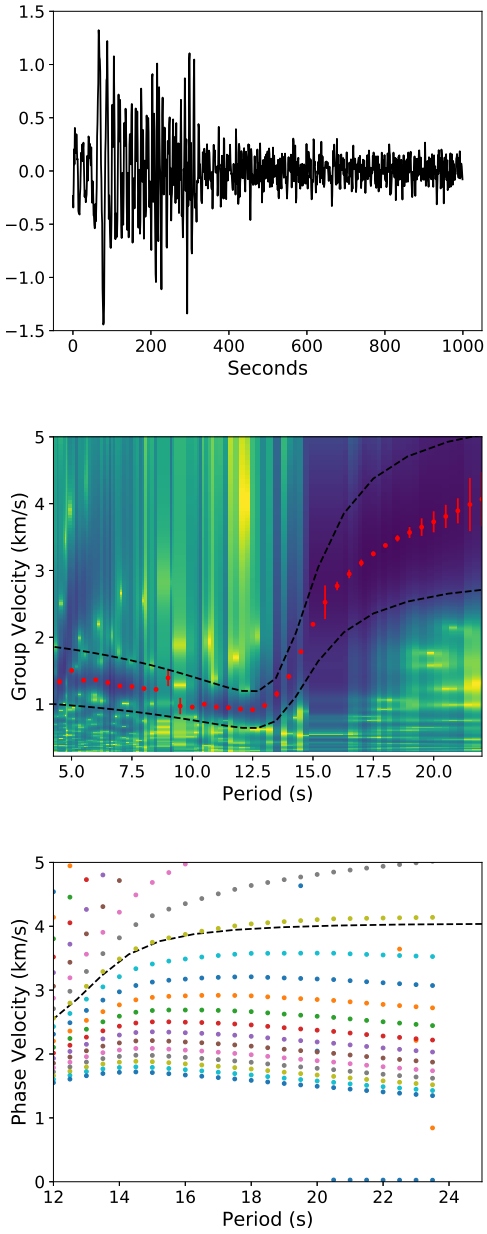

Figure 4.1: (a) The final stacked cross-correlation function between PLUME sites PL17 and PL24. This waveform is the summation of the causal and acausal signals. (b) An example of the measurement of a group velocity curve. The log of the amplitude of the envelope function squared is shown as a function of period and arrival time, converted to velocity by dividing by the inter-station difference. The group velocity corresponds to the energy maximum at each period. The black dashed lines represent the automated picking guide, which limits the range of allowed values based on predicted group velocities. (c) An example of the measurement of a phase velocity curve. The individual curves show possible phase velocities assuming missed cycles of $\pm 2n\pi$. The phase velocities which best align with expected values (shown with the black dashed line) are selected.

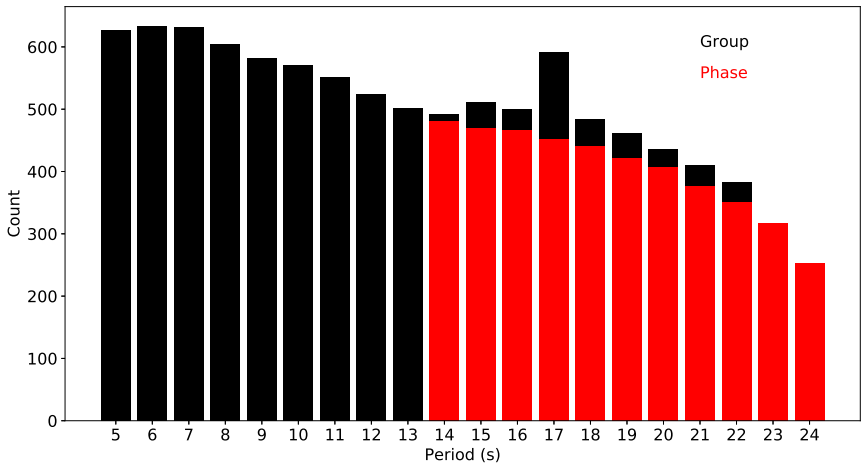

Figure 4.2: Number of group and phase velocity measurements as a function of period.

those into this study. The number of measurements as a function of period is shown in Figure 4.2. The number of usable measurements decreases with increasing period due to decreasing signal-to-noise ratio, an effect observed in other ambient noise analyses using OBS data (e.g., Zha et al., 2014b) We plot our initial two-station measurements for group velocity and phase velocity in Figures 4.3 and 4.4, respectively.

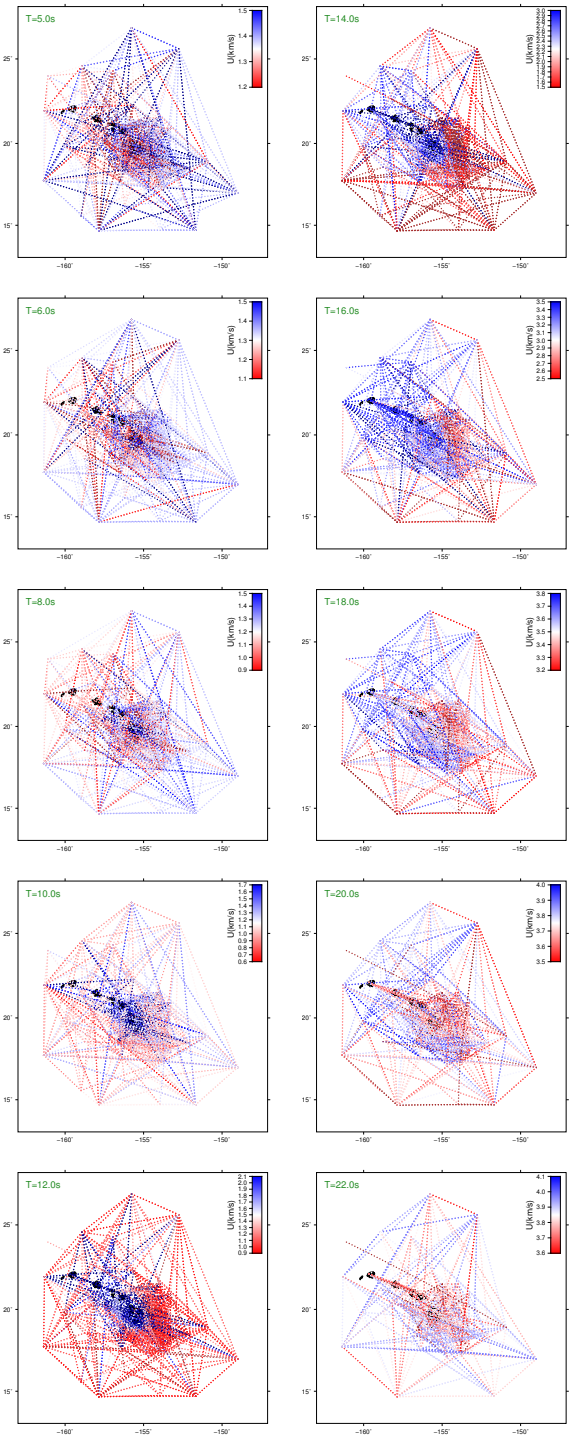

Figure 4.3: Two-station measurements of group velocity as a function of period.

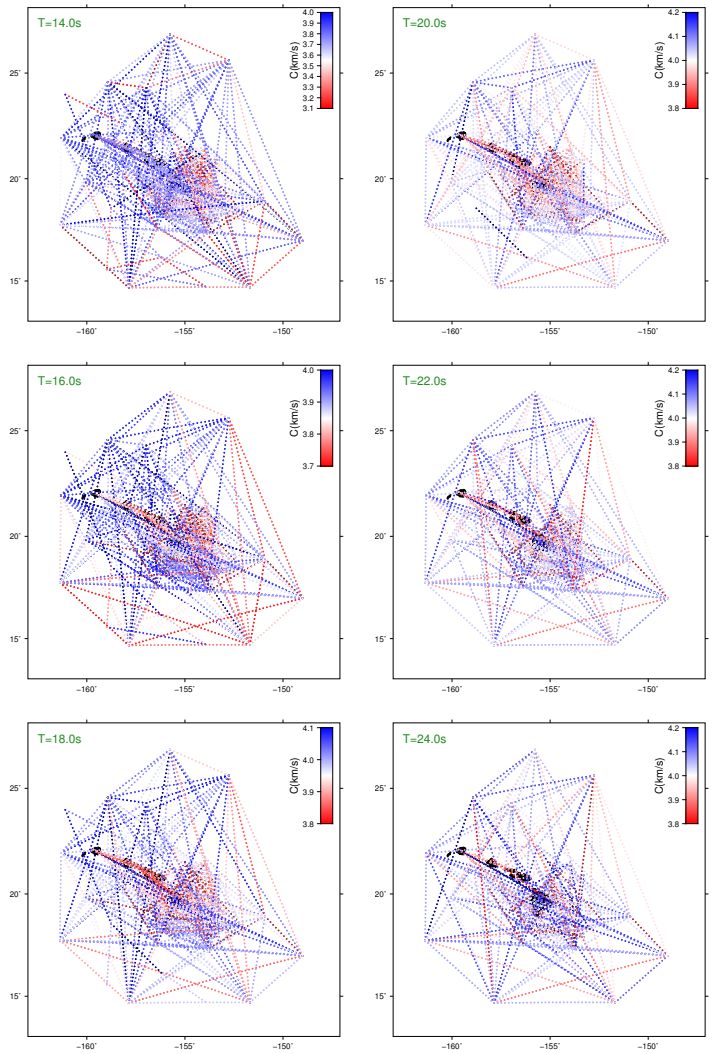

Figure 4.4: Two-station measurements of phase velocity as a function of period.

4 Sensitivity & Forward Modeling

To forward model group and phase velocity data, we used the software of Haney and Tsai (2017). We first computed sensitivity kernels to explore the sensitive of different periods to structure at depth (Fig. 4.5). We initially assumed a model for 52 - 110 Ma lithosphere from Nishimura and Forsyth (1989) and a water depth of 5000 meters. Like compliance data, analyses typically focus on sensitivity to shear structure, though all elastic parameters contribute to the observed velocities. Notice that near-surface structure can contribute to even long-period data, particularly Vp structure.

The kernels highlight the sensitivity to Earth structure, but the water depth also plays a significant role. Water depth varies between approximately 4.5 km over the Hawaiian Swell and 5.5 km in the abyssal plains. The seafloor depth decreases quickly with proximity to the islands. Figure 4.6 plots dispersion curves calculated for water depths between 4.5 and 5.5 km. Water depth affects the predicted dispersion curves at all periods, particularly between 10 and 15 seconds. This agrees with the observed variations in measured velocities (Figs. 4.3 and 4.4), which show the largest variation between these periods.

Our inversions for velocity maps and then shear structure will occur on a 13 x 13 1° grid covering Hawaii. In order to assess the potential effect of water depth at each location, we computed group and phase velocities using the median water depth of every grid cell while keeping Earth structure constant. We used the bathymetric grid of Smith and Sandwell (1997). The effects are shown in Figures 4.7 and 4.8. The effects vary between 1% and 20% for phase velocity and between 5% and 100% for group velocity, meaning that without properly accounting for water depth, our interpretations could be significantly biased. Figure 4.9 compares the water depth listed for each site to the median water depth for the grid cell that each site is situated in. The difference is greater than 1000 meters in two cases (PL35 and PL36), and greater than 400 meters in six cases. This indicates that water depth must be carefully considered, and may

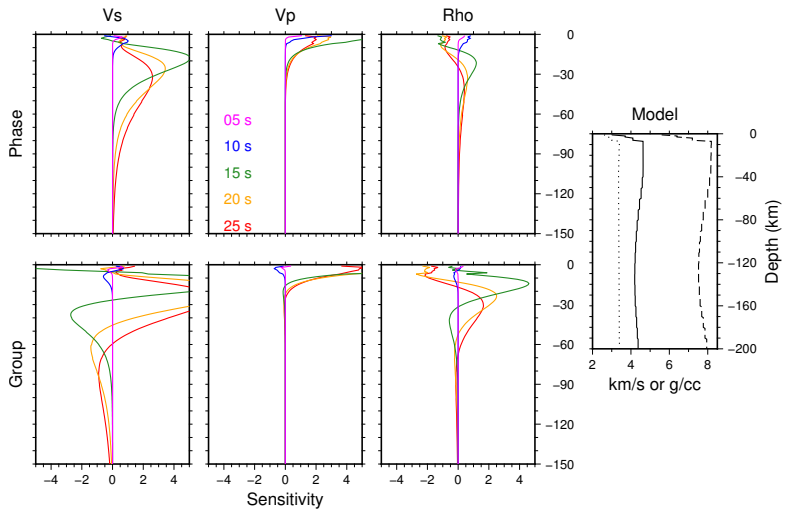

Figure 4.5: Sensitivity functions of dispersion data as a function of function of frequency. The starting model used to calculate these kernels is shown on the far right. The solid line represents Vs, the dashed line represents Vp, and the dotted line represents ρ.

need to be varied in addition to Earth structure, since even 100 meters can produce a measurable signal.

5 Inversion of phase and group velocities

The measured two-station dispersion curves were used to solve for velocity as a function of period in each of the 169 (13 x 13 1°) grid cells independently for both group and phase velocity. We used Occam's inversion (Constable et al., 1987), in which we minimized the weighted sum of the data misfit and model roughness. Formally, we minimized the function U, given by

$$U = \chi^2 + \mu|\mathbf{m}^T \partial^T \partial \mathbf{m}| \tag{4.5}$$

where χ^2 is the misfit, $\mathbf{m}$ is the model vector, μ is the smoothing parameter, and $\partial\mathbf{m}$ is the model roughness. The results are shown in Figures 4.10 and 4.11. For now we assume uncertainties on the order of 0.5%. Formal uncertainties could be estimated from inversions of the standard deviations of the path-averaged velocity curves (e.g., Laske et al., 2011). We

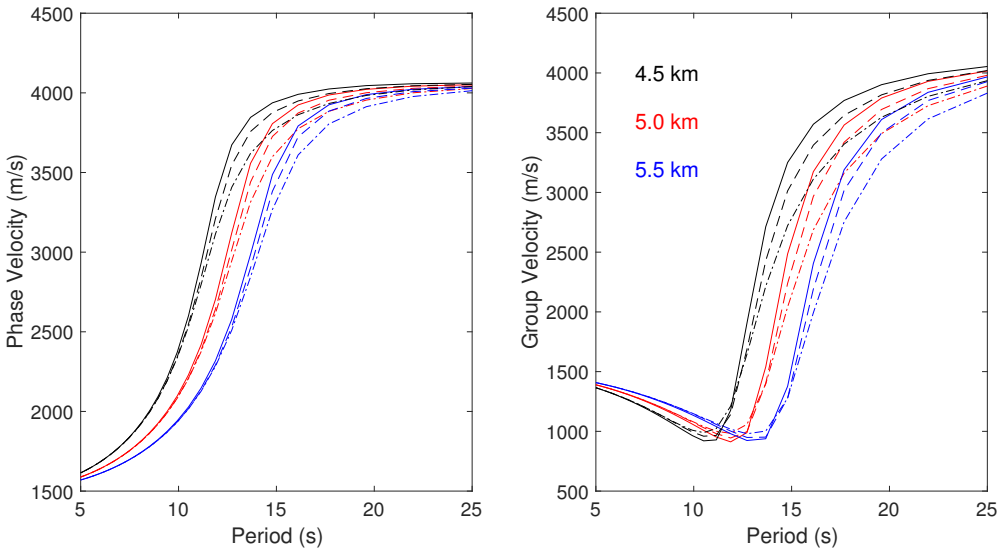

Figure 4.6: The effect of water depth and crustal thickness on group and phase velocity data. Dispersion curves were computed for water depth varying between 4.5 km and 5.5 km and for crustal thicknesses of 6 km (solid line), 12 km (dashed line), and 18 km (dot-dashed line).

chose a lower misfit than is typically used in the inversion of velocity maps (Fig. 4.12) in order to allow the significant variations across the array induced by changes in water column height, crustal thickness, and mantle velocities. We allowed greater model roughness between periods of 10 - 16 seconds, in which bathymetric effects are most pronounced.

Some overlap between our frequency range and that of Laske et al. (2011) allows a direct comparison of results. Figure 4.13 compares our results for phase velocities at 20 seconds (50 mHz). The map of Laske et al. (2011) is slightly smoothed over the grid cells. The high velocities to the southeast of Hawaii are clear in both maps, as is a broad region of low velocities to the northeast of Hawaii. In addition, a region of low velocities extends south of Hawaii in both inversions, though the region is shifted by 1 degree between the maps. A number of differences are also clear. A strip of high velocities between Hawaii and the lows of the northeast found by Laske et al. (2011) is missing from our new maps, as is a broad region of high velocities north of Oahu and Kauai.

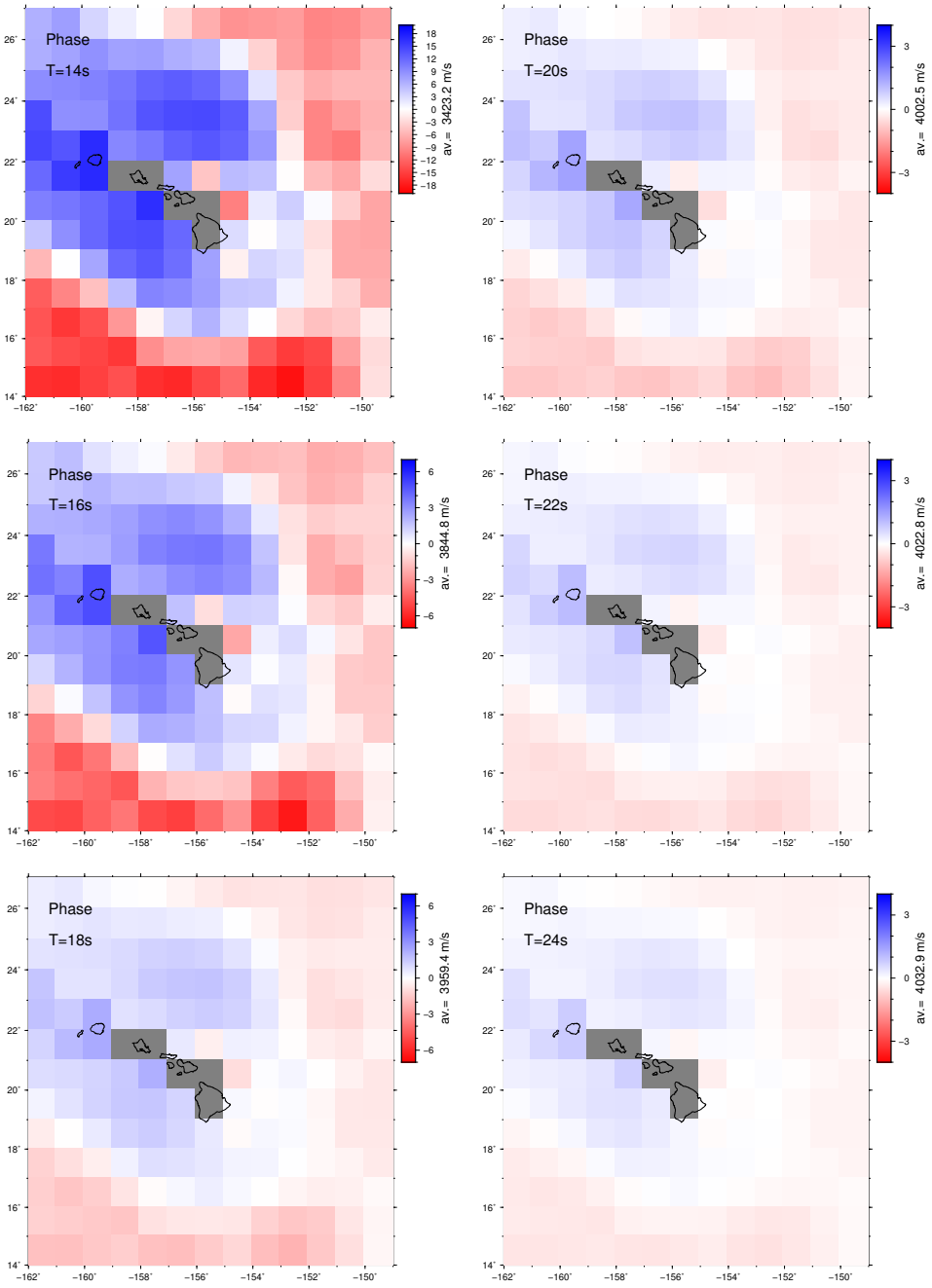

Figure 4.7: Effect of water depth on phase velocities. The mean water depth of each grid cell was calculated from the bathymetry maps of Smith and Sandwell (1997). The earth structure used in each grid cell is identical excepting the water depth.

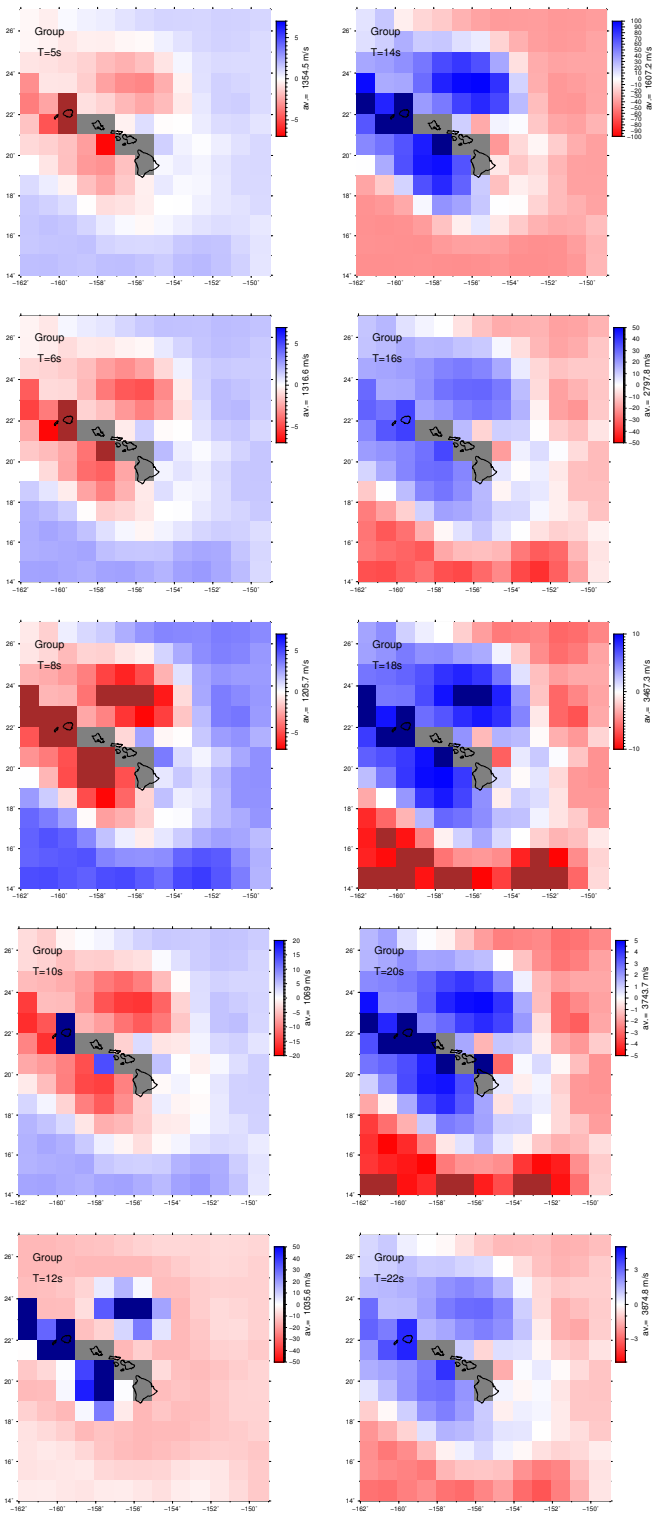

Figure 4.8: Effect of water depth on group velocities. The mean water depth of each grid cell was calculated from the bathymetry maps of Smith and Sandwell (1997). The earth structure used in each grid cell is identical excepting the water depth.

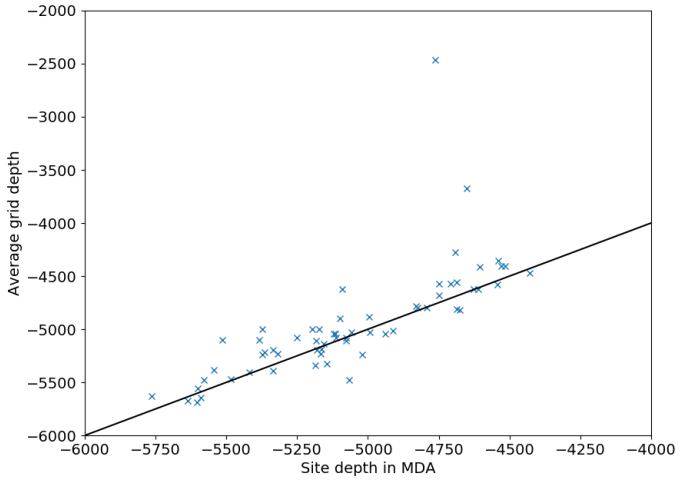

Figure 4.9: A comparison between the individual site depths listed in the IRIS Meta-data Aggregator (MDA) and the average water depth within the grid cell for each station.

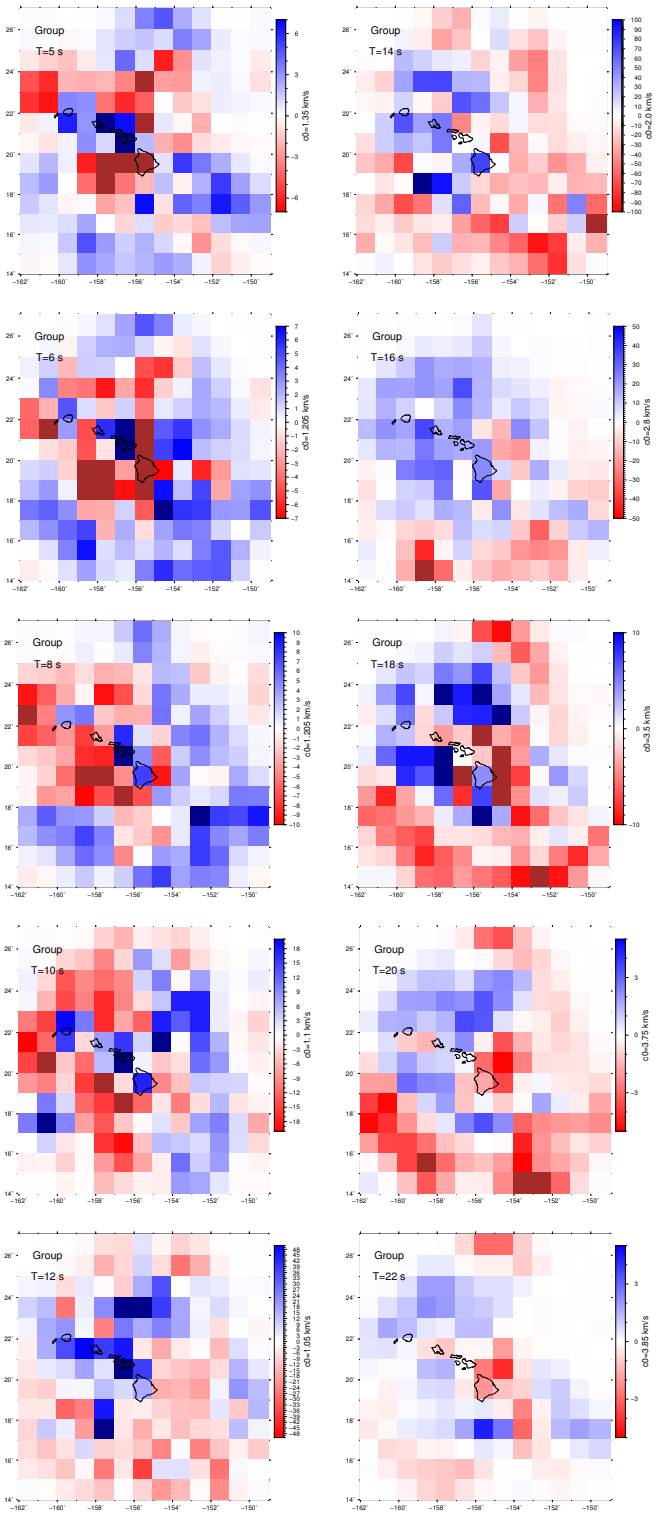

Figure 4.10: Maps of local group velocity anomaly at ten periods from inversions of path-averaged velocity data.

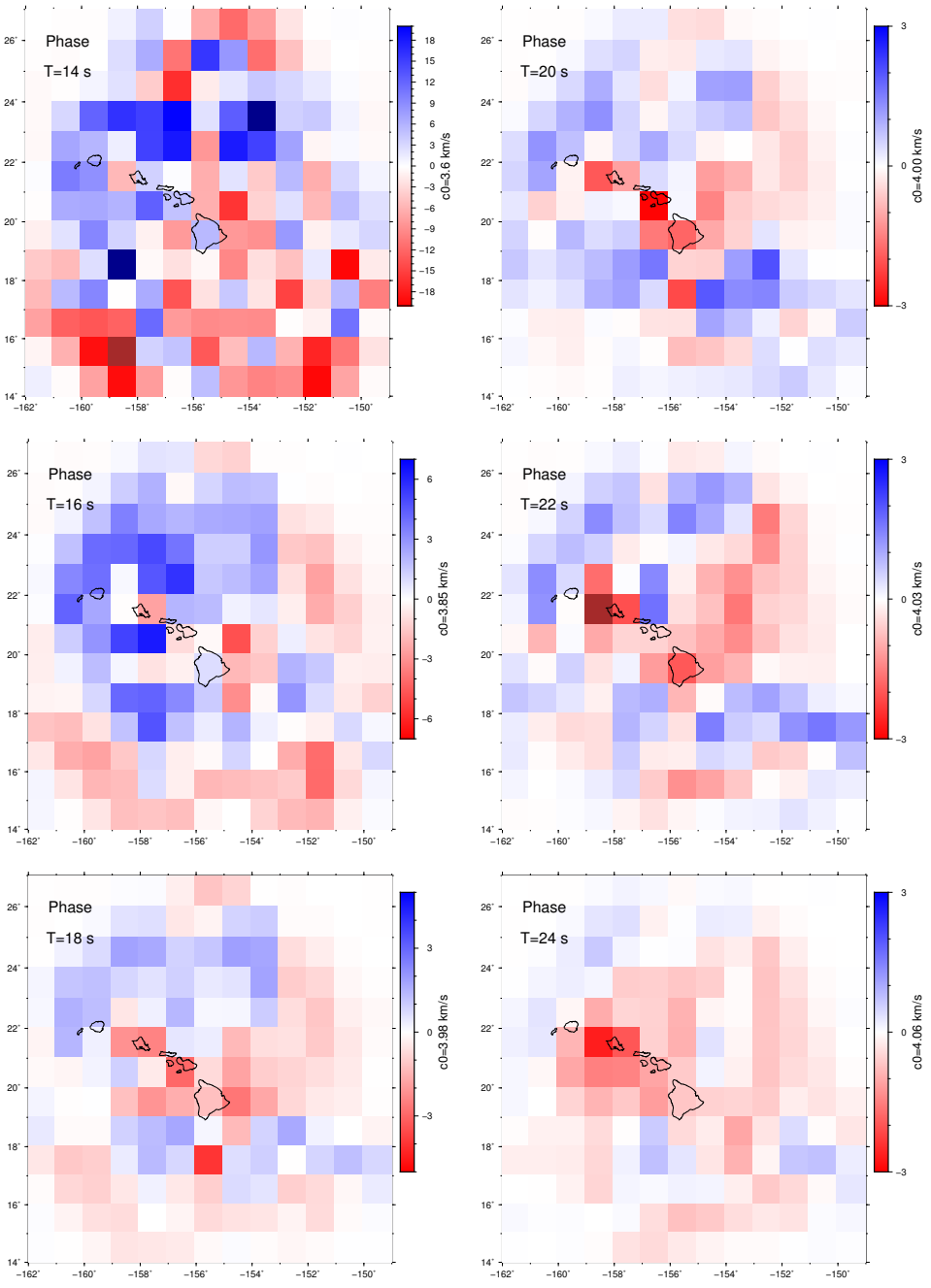

Figure 4.11: Maps of local phase velocity anomaly at six periods from inversions of path-averaged velocity data.

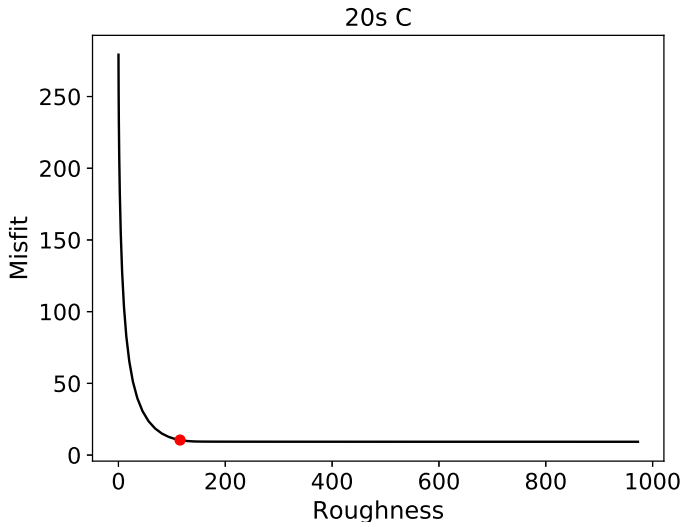

Figure 4.12: χ^2 misfit as a function of model roughness in the inversion for phase velocity at a period of 20 seconds. The final model selected is shown in the red dot.

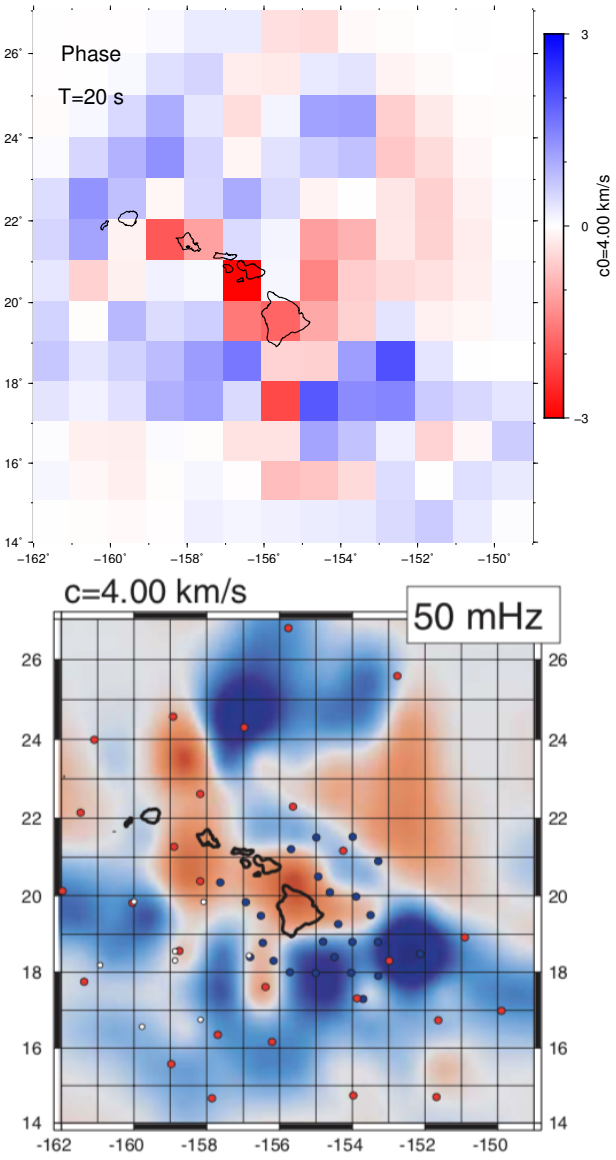

Figure 4.13: A comparison of our inverted 20 second phase velocity map (upper panel) with the inverted results at the same period from Laske et al. (2011), measured from teleseismic surface wave arrivals (lower panel). The color scales are roughly equivalent.

6 Modeling crustal structure

I began modeling phase velocities, which are most sensitive to structure between depths of 10 and 30 km for periods between 14 and 24 seconds (Fig. 4.5). In order to account for the effect of water depth, I computed the median depth in each 1° x 1° cell from the topographic map of Smith and Sandwell (1997) and fixed this value in the modeling. Some authors prefer to invert directly for water depth (e.g., Harmon et al., 2007a), but this risks mapping variations in Earth structure into the water column. In order to explore the potential bias from inaccurate water depths, I also computed the standard deviation of the bathymetry within each grid cell. Cells with large bathymetric ranges ($>$ 500 meters) will be carefully reassessed to determine best-fitting parameters. I currently limit my modeling to grid cells containing PLUME stations, with the eventual goal of jointly inverting dispersion and compliance data.

Forward modeling was done using the dispersion codes of Haney and Tsai (2017). I used the upper mantle velocity profile of Nishimura and Forsyth (1989) for 52 - 110 Ma lithosphere, which was also used as a starting model by Laske et al. (2011). For a crustal model, I used a modified version of the SWELL model (Laske et al., 2007) discretized into 500 meter layers. The uppermost 500 meters were set at 2.0 km/s, slightly higher than found in the compliance modeling of Doran and Laske (2019) but lower than assumed in SWELL. The next 500 meters were set at 3.0 km/s. The following 2 km, Layer 2B, were set to 3.7 km/s, and the lower crust was set at 4.0 km/s with a thickness of 3.5 km. The uppermost mantle was set at 4.63 km/s. In the crust, I assumed a Poisson's ratio of $\sigma = 0.30$ (Vp/Vs = 1.88), consistent with typical values found in old oceanic crust (e.g., Hyndman, 1979). Vp/Vs in the mantle was set at 1.75. Density was defined as 2.7 g/cc in Layer 2, 2.9 g/cc in the lower crust, and 3.3 g/cc in the uppermost mantle. At sites with thick sediments, as described by Doran and Laske (2019), I used average Vs values of 1.0 km/s and Vp values of 3.5 km/s.

Around the Hawaiian islands, the oceanic crust increases from a typical thickness of

approximately 6.5 km off the Swell to nearly 20 km beneath the island of Hawaii (e.g., Zucca et al., 1982; Watts et al., 1985; Watts and ten Brink, 1989; Leahy et al., 2010). In order to confirm that the inverted velocities were not solely a function of water depth, I computed a 'water-corrected' phase velocity map, in which the predicted velocities from bathymetry were subtracted from the inverted velocities (Fig. 4.14). A clear low-velocity zone is apparent over the Hawaiian Swell, indicating slower crustal or mantle velocities in this region. Initially I sought to fit the data by only increasing crustal thickness. I used Vs = 4.2 km/s for the underplated material, as described by Leahy et al. (2010). Figure 4.15 shows the data at two sites along with the modeled values assuming a crust of variable thickness. At PL44, far from the islands, the data seem to prefer a typical crustal thickness of 6.5 km, while at PL13, directly southeast of Hawaii, a thicker crust is preferred. Leahy et al. (2010) provide estimates of crustal thickness derived from receiver functions. At PL44, they found no underplating, and at PL13 they found 6 km of underplated material. However, thickening the crust does not appear to be sufficient to fit the data, since the model is still faster than the observations. We therefore additionally attempted to vary the velocity of the uppermost mantle, defined here as the mantle to 50 km depth. Increasing or decreasing the velocity by several percent can have similar effects as varying crustal thickness. Figure 4.15 also shows modeling at PL13 with the crust held constant but the velocity of the mantle varied by $\pm 3\%$. Based on these results, we cannot distinguish between a thickened crust or a slower uppermost mantle.

We quantified the trade-off between crustal and mantle structure by performing a grid search (Fig. 4.16). Notice that a thicker crust produces similar misfit as a slower mantle, as we expected. Although there is a value that produces a minimum misfit, the phase data are unable to unambiguously determine both crustal thickness and mantle shear velocity. We therefore used the crustal thickness estimates from Leahy et al. (2010) to estimate uppermost mantle shear velocity at each station. Our results for mantle velocity are shown in Figure 4.17.

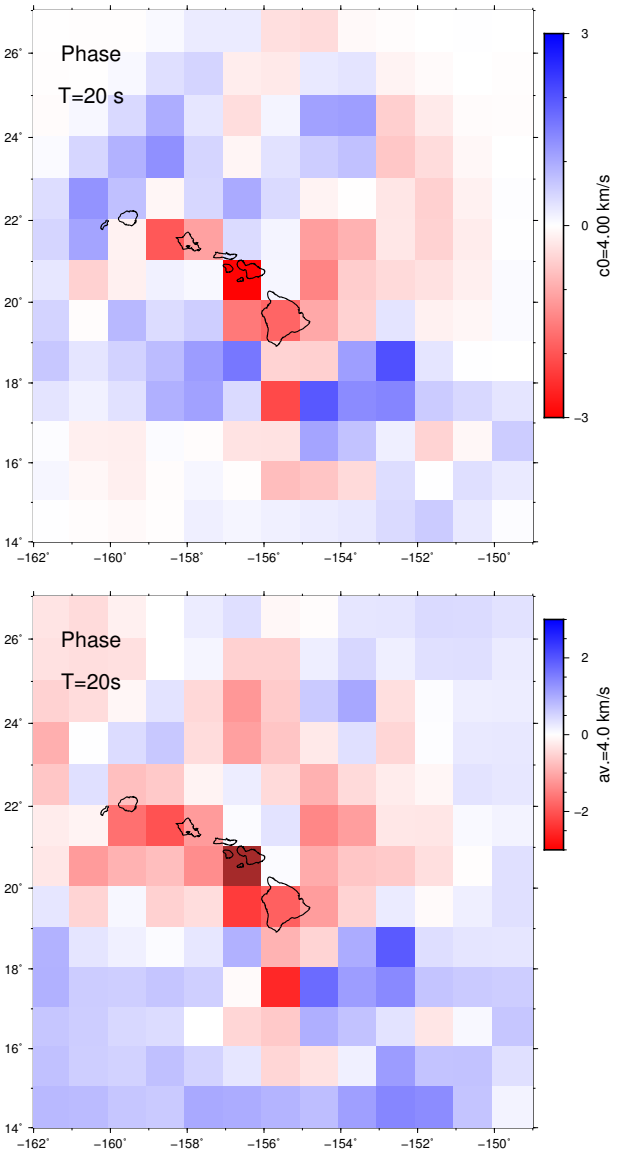

Figure 4.14: The top panel shows the inverted phase velocity map at 20 seconds. The bottom panel shows the same map 'corrected' for water depth, in which the predicted phase velocities from bathymetry alone are removed from the inverted phase velocities. This test confirms that we expect lower shear velocities on the Hawaiian Swell.

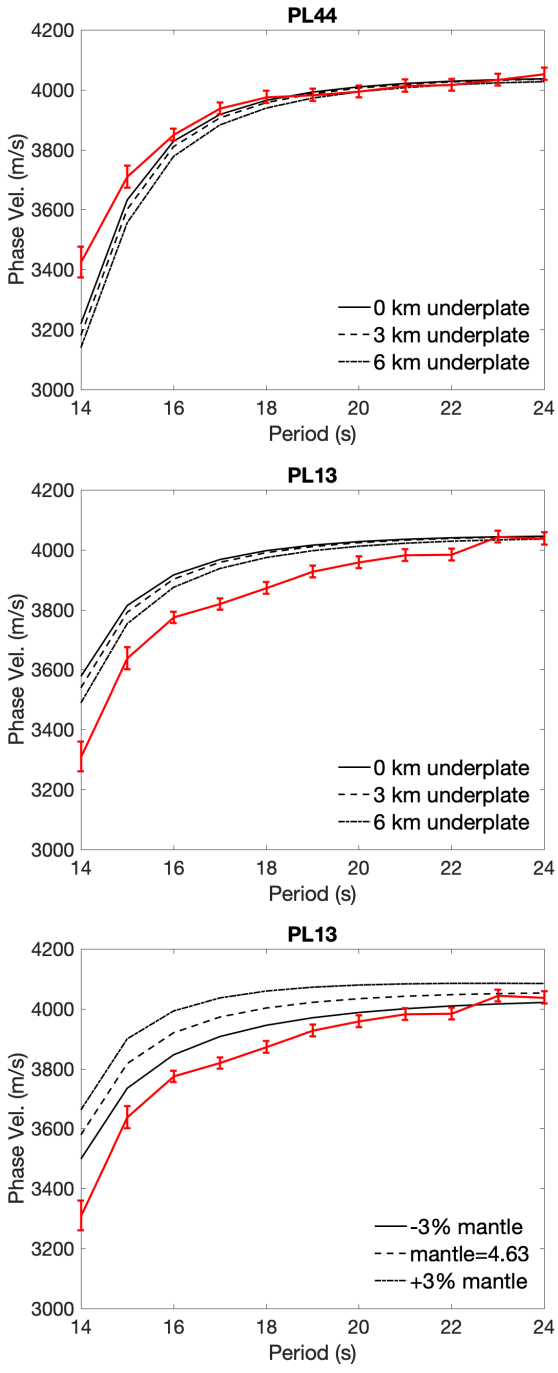

Figure 4.15: Initial modeling of phase velocity data at PL44 and PL13. In the top plots, only the thickness of the crust is varied. In the lower plot, the crust is held constant while the velocity of the uppermost mantle is varied.

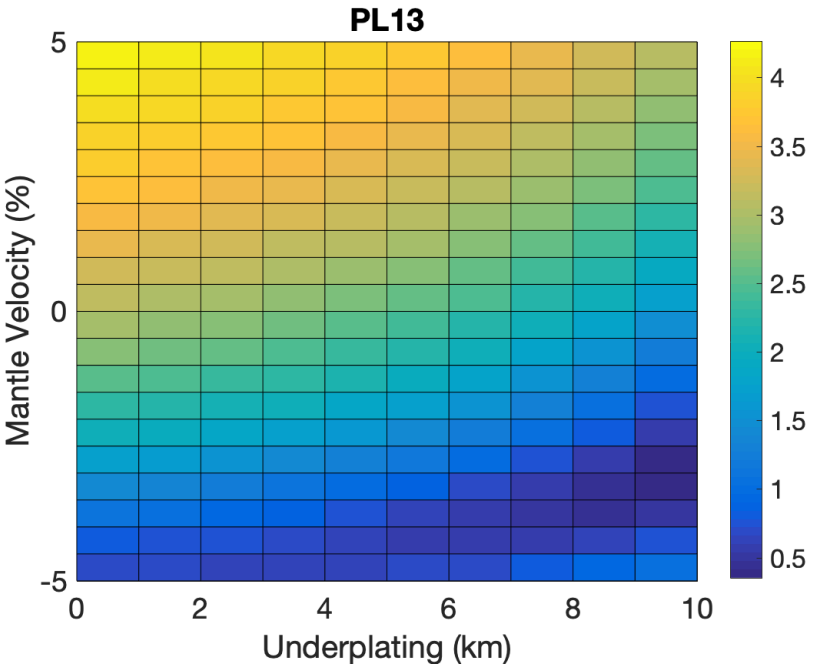

Figure 4.16: χ^2/N misfit (shown with a log scale) as a function of crustal thickness and mantle velocity using phase velocity data at PL13. The underplating thickness was added to the typical oceanic crustal thickness of 6.5 km.

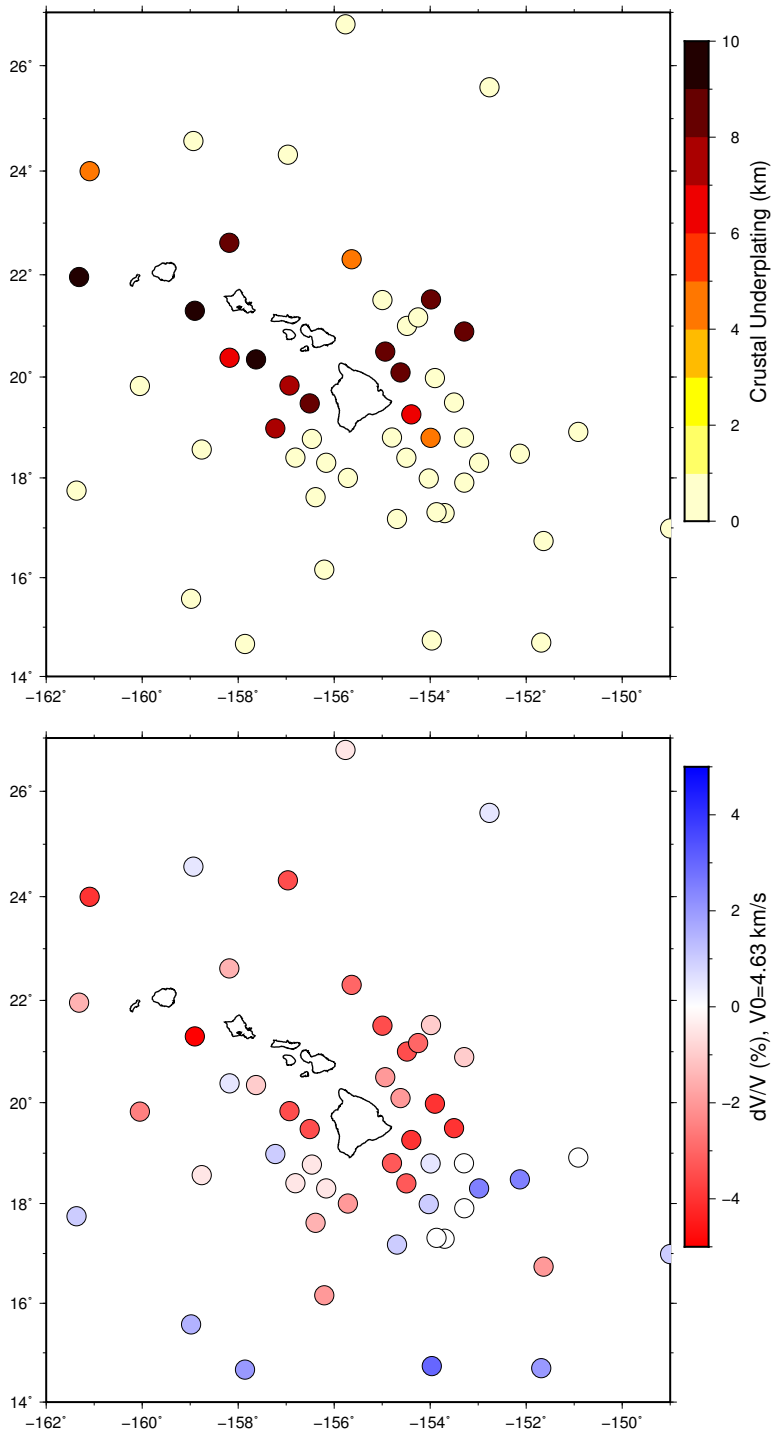

Figure 4.17: The upper plot shows a map of crustal underplating presented by Leahy et al. (2010). Only the thickness of the underplating is shown; to find the total crustal thickness at each site, the thickness of the normal oceanic crust must be added. The lower plot shows our estimates for uppermost mantle velocity using our phase velocity data and the previous crustal thickness estimates.

7 Discussion

Our measurements of Rayleigh wave phase velocities between periods of 14 to 24 seconds reveal slow velocities over the Hawaiian Swell. One initial result of our modeling is that a thickened crust, as found by numerous previous researchers, is not sufficient to explain the magnitude of the low velocities. The data can be explained by allowing the uppermost mantle to vary by $\pm 4\%$. We also attempted to fit the data using a slower lower crust instead of a slower mantle. As before, these parameters trade off. However, a grid search at using data at PL37 indicated that lower crustal velocities would need to be reduced by 20% to explain the data, as opposed to a mantle perturbation of 2%. Since pronounced low-velocity zones within the crust have not been reported by other investigators (e.g., Watts et al., 1985; Lindwall, 1991; Leahy et al., 2010), we prefer to model the phase velocities with mantle anomalies. The low mantle velocities generally coincide with the extent of the Hawaiian Swell. The largest low-velocity anomaly is found directly to the north and east of Hawaii. Another low-velocity region is present to the south of Hawaii. A high-velocity region can be seen far to the south and southeast of Hawaii. These results agree qualitatively with those presented by Laske et al. (2011) at 40 km depth.

Several sites may warrant a re-examination of the crustal thicknesses presented by Leahy et al. (2010). As seen in Figure 4.17a, two sites to the northeast of Hawaii (PL07 and PL08) have thick underplating while surrounding sites do not. The modeling at these sites (Fig. 4.18) indicated that the best-fit model contained a normal oceanic crust (6.5 km) with significantly slower mantle velocities (-3%). Proximity to the Molokai Fracture Zone may explain these results. Other sites southeast of the island (e.g., PL23 and PL24) preferred thicker crust, implying that some underplating might exist beneath these sites. Additional analysis of the measured receiver functions is required to further constrain crustal structure in these regions.

Velocity perturbations in the uppermost mantle could have a variety of sources, including temperature anomalies, partial melt, or compositional variations. Melt extraction and mantle

depletion, which may characterize the uppermost mantle beneath Hawaii, likely leads to slightly higher seismic velocities (e.g., Phipps Morgan et al., 1995). However, if eclogite is melted and extracted from the mantle, seismic velocities could decrease. Hauri (1996) estimated that upwelling mantle may be composed of up to 5% eclogite, leading to a change in velocity of 0.3% (Laske et al., 2011). We therefore look for additional factors to explain the low velocities.

We examined the effects of thermal perturbations as well as fluid content to assess end-member scenarios in which the entire velocity anomaly was explained by a single effect. The true cause is likely a combination of factors. An increase in temperature lowers the seismic velocity. Assuming thermal a thermal derivative appropriate for upper mantle of $\partial \ln V_S / \partial T = -9.1 \times 10^{-5}$ /°C (Sobolev et al., 1996), a 6.5% range of mantle velocities (-4% to +2.5%) requires a span of temperatures ΔT = 660 °C. Using an alternative relation of $\partial \ln V_S / \partial T = -1.8 \times 10^{-4}$ /°C (Goes et al., 2000) yields a temperature difference of ΔT = 340 °C.

Partial melt leads to a reduction of Vs, but the magnitude is highly dependent on the geometry of the melt inclusions (e.g., Mavko, 1980; Schmeling, 1985; Sato et al., 1989; Hammond and Humphreys, 2000; Taylor and Singh, 2002; Schmeling et al., 2012). At depths of 50 km, the derivative for $\ln V_S$ per 1% melt ranges from 0.76 $\times 10^{-2}$ to 8.5 $\times 10^{-2}$, depending on the inclusion geometry (Goes et al., 2000). The low estimate yields less than 1% high aspect-ratio melt in the uppermost crust, while the melt fraction may be as high as 7.5% melt. The higher estimate is consistent with the estimate of Constable and Heinson (2004), although this was inferred at a depth of 150 km.

The obvious next step is to analyze the group velocity measurements in order to further constrain crustal and uppermost mantle structure. Group velocities are sensitive to structure through a slightly greater depth range, and are more sensitive to changes in Vp and ρ than phase velocities (Fig. 4.5). These measurements could confirm our estimates of crustal structure and allow more confidence in the uppermost mantle results. Finally, these results should be jointly inverted with seafloor compliance data (Doran and Laske, 2019) and receiver function estimates

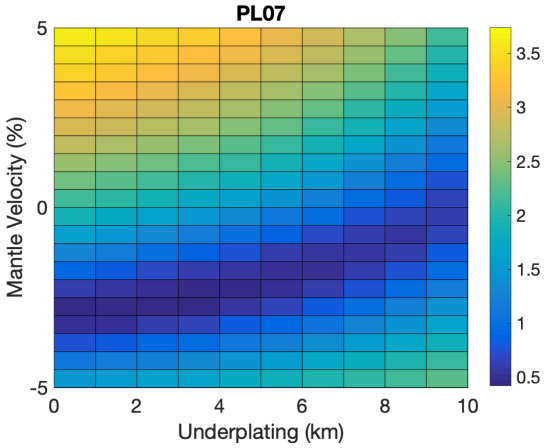

Figure 4.18: χ^2 misfit (shown with a log scale) as a function of crustal thickness and mantle velocity using phase velocity data at PL07.

(Leahy et al., 2010) for a complete picture of the upper lithosphere. This will then allow truly top-down imaging with the long-period measurements of Laske et al. (2011) that will constrain the size and shape of the upper mantle plume.

8 Conclusions

We measured group and phase velocities over the Hawaiian Swell between periods of 5 and 24 seconds. We inverted the phase velocity measurements for velocity maps at specified periods. Modeling of the resulting local phase velocities indicated that thickened crust over the Hawaiian Swell was insufficient to explain the inverted data. We proposed to explain these low velocities over the Swell through variable uppermost mantle velocities. We found that beneath the Swell, the uppermost mantle was up to 4% slower than predicted, with the most significant anomalies directly north and east of the island of Hawaii. We explored explanations for these anomalies, and found upper estimates of potential thermal anomalies above 600 °C and potential melt fractions as high as 7.5%. Including both a thermal and melt component will lower the required anomalies.

5 Infragravity waves and horizontal seafloor compliance

1 Abstract

We report the first consistent observation of horizontal seafloor compliance induced by infragravity (IG) waves. Long-period IG ocean waves manifest themselves as broad, dominant features in ocean bottom pressure and vertical deformation spectra, but signals are rarely (if ever) identified on the horizontal components of traditional ocean-bottom seismometers (OBS) due to low signal level and high current-induced tilt noise at long periods. We examine two OBS stations with shallow-buried seismometers: the Monterey Ocean Bottom Broadband (MOBB) site offshore California and the Ocean Seismic Network (OSN) pilot site OSN1B near Hawaii. We use nearby weather buoys to investigate the relationship between the presence of infragravity waves and environmental conditions. We find strong evidence that infragravity wave generation is primarily confined to the near-coastal environment. Additional IG source information is found by examining the directionality of passing IG waves as a function of frequency, which we analyze using the coherence between pressure and the two horizontal components. Finally, we evaluate the implications for a joint vertical and horizontal compliance inversion.

2 Introduction

Energy from oceanic infragravity (IG) waves dominates the long-period power spectra of broadband ocean-bottom seismometers. Infragravity waves in the deep ocean have small wave heights ($\leq$ 1cm), long wavelengths (1-20 km), long periods (30-300 s), high phase velocities ($>$ 100 m/s in 2 km water depth), and propagate great distances over the ocean while experiencing minimal attenuation (Yang et al., 2012; Webb, 1998). Observations were first made near the coast (Munk, 1949; Tucker, 1950) but infragravity energy is now routinely observed in the open ocean as well (Webb et al., 1991; Godin et al., 2013). The mechanism of infragravity wave generation remains a target of intense study. Significant correlation has been reported between infragravity waves and local short period wind and swell waves (e.g., Herbers et al., 1995a; Ardhuin et al.,

2014). Consensus is slowly building that infragravity waves are formed by nonlinear interactions of short-period ocean waves in the near-shore environment that either become trapped on the continental shelf or leak outwards into the deep ocean (e.g., Herbers et al., 1995b; Webb, 1998; Rhie and Romanowicz, 2006; Aucan and Ardhuin, 2013; Ardhuin et al., 2014; Godin et al., 2014; Crawford et al., 2015).

Infragravity energy can be observed on broadband ocean bottom seismometers (OBSs) and pressure sensors in all regions of the ocean. Infragravity studies have a wide range of applications in both seismology and oceanography. Infragravity waves play a role in sediment transport and other near-shore processes (Dolenc et al., 2005), and have been proposed as a source of the Earth's continuous free oscillations (Rhie and Romanowicz, 2006). Recent work has suggested that long period IG waves may transmit mechanical energy between the ocean and atmosphere (Godin and Fuks, 2012), and some investigators have linked open ocean IG waves with ice-shelf deformation (Bromirski et al., 2010). Seafloor compliance studies utilize the transfer function between the pressure and acceleration in the infragravity band to investigate crustal elastic structure (Crawford et al., 1991, 1998; Willoughby et al., 2008; Zha et al., 2014a). In order to lower regional and teleseismic detection thresholds on OBSs, infragravity noise can be deconvolved from the time series using concurrent seafloor pressure records (Crawford et al., 1999; Crawford and Webb, 2000; Taira et al., 2014).

Current studies involving OBSs focus on characterizing infragravity energy on vertical acceleration recordings. Low instrument self-noise on modern broadband instruments and high coherence between vertical acceleration and pressure over a broad range of frequencies allows easy association with infragravity waves. Infragravity energy and deformation occur in the horizontal plane as well as the vertical plane, but thus far high noise levels have inhibited their study (Crawford et al., 1991; Crawford and Singh, 2008). The noise is primarily caused by current-induced tilt, is significant particularly at long periods and at installations in shallow water, and can overwhelm even very strong teleseismic arrivals (Webb, 1998).

Two factors obscure the horizontal infragravity signal on OBSs: the horizontal deformation due to vertical loading is inherently smaller in magnitude than the vertical deformation (e.g., Iassonov and Crawford, 2008), and tilt noise dominates the ambient spectrum of horizontal OBS components at long periods (e.g., Webb, 1998; Duennebier and Sutton, 1995). Tilt noise is caused by seafloor currents flowing past an instrument and by the turbulence and eddies created by non-linear interactions between the fluid and the package. The lower the profile of the instrument, the less long-period noise is induced, and burial of the instrument minimizes the effects of this noise. Buried OBSs allow us for the first time to characterize infragravity waves using horizontal components. We investigate 1-month long data segments at two such sites: the Monterey Ocean Bottom Broadband (MOBB) site offshore California (Romanowicz et al., 2006), (Figure 5.1), and the Ocean Seismic Network (OSN) pilot site OSN1 near Hawaii (Dziewonski et al., 1992b), (Figure 5.2). Buried seismometers can be between 20-50 dB quieter than seafloor instruments at long periods (Duennebier and Sutton, 1995; Collins et al., 2001), and studies of both OSN1B (Crawford and Webb, 2000) and MOBB (Dolenc et al., 2007) records confirm that tilt noise at these sites is negligible.

For OSN1, we concentrate our study on the buried package OSN1B (Collins et al., 2001). Both MOBB and OSN1B are buried in the sediment such that the top of the package is at least 10 cm beneath the seafloor (Stephen et al., 2003b; Romanowicz et al., 2006). In this chapter, we briefly introduce the IG terminology and detail our analysis method. For the 1-month long data segments, we examine the feasibility and measures required to optimize observed horizontal compliance. We study the relationship between horizontally-recorded infragravity energy and local weather conditions, and try to infer whether IG waves are generated near the coast or in the deep ocean basin. We also examine the directionality of IG waves as revealed by the two orthogonal horizontal components at both OBS sites. Lastly, we discuss the potential of joint vertical and horizontal compliance studies to retrieve seismic anisotropy in marine sediments.

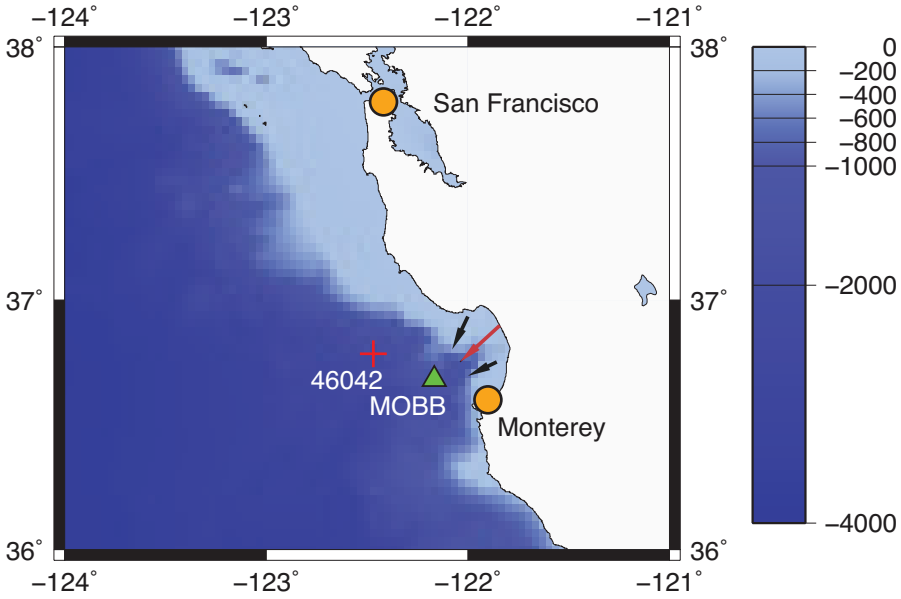

Figure 5.1: Location map for Monterey Ocean Bottom Broadband station MOBB. The water depth at the OBS site is 1036 m. Also shown is the closest NOAA buoy (46042), 24 km northwest of MOBB. The arrows depict the primary inferred source azimuths of infragravity waves as described in Section 6.3. The red arrow is the median azimuth.

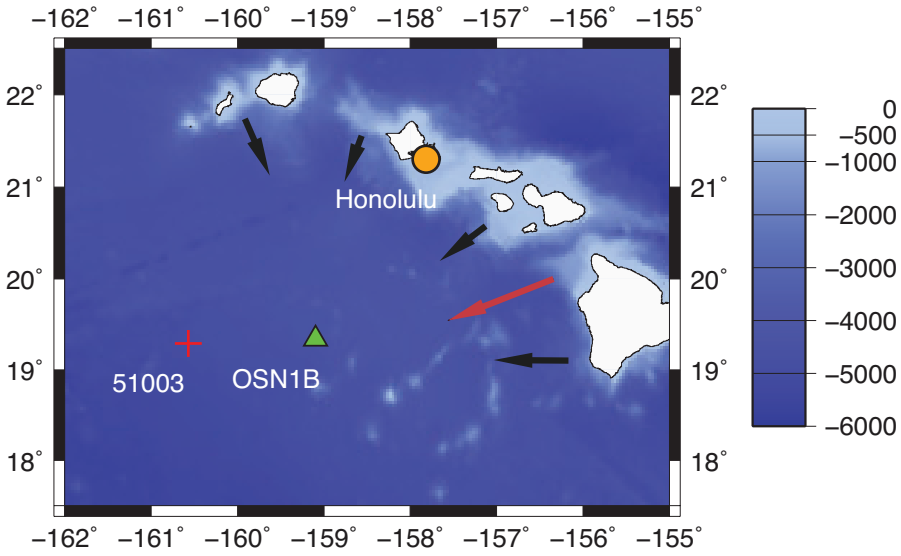

Figure 5.2: Location map for Ocean Seismic Network pilot station OSN1B near Hawaii. The water depth at the OBS site is 4150 m. Also shown is the closest NOAA buoy (51003), about 100 km west of OSN1B. The arrows depict the primary inferred source azimuths of infragravity waves as described in Section 6.3. The red arrow is the median azimuth.

3 Theory & Terminology

Infragravity waves propagate through the oceans and create a pressure signal on the seafloor; this pressure then induces ground deformation (and consequently ground acceleration). The seafloor pressure at a water depth H caused by a surface gravity wave of height ζ is given by

$$P_{bottom} = \frac{\rho g \zeta}{\cosh(kH)} \simeq P_{surface} e^{-kH} \tag{5.1}$$

where k is the wave number, ρ is the water density and g is the gravitational acceleration (e.g., Dolenc et al., 2005). Infragravity waves are freely propagating surface gravity waves (Webb et al., 1991), and the frequency and wavenumber are related through the dispersion relation (Apel, 1987)

$$\omega^2 = gk \tanh(kH) \tag{5.2}$$

where ω is the angular frequency of the wave. The ground deformation is a function of the underlying elastic structure. An analytic normalized compliance expression (the ratio of deformation to vertical stress, normalized by the wavenumber) can be derived for an elastic half-space (Crawford, 2004):

$$\eta = k\xi = k\frac{\mathbf{u}}{\tau_{zz}} = k\frac{u_x\hat{x} + u_z\hat{z}}{\tau_{zz}} = \frac{-i}{2(\lambda+\mu)}\hat{x} + \frac{\lambda+2\mu}{2\mu(\lambda+\mu)}\hat{z} \tag{5.3}$$

where $\mathbf{u}$ is the displacement, τ_{zz} is the vertical stress, and λ and μ are the Lamé parameters. Displacement is expected in both the vertical and horizontal directions, but to date no studies have focused on horizontal deformation.

The water depth controls the maximum frequency to which either horizontal or vertical coherence in the IG frequency band can be analyzed (Crawford et al., 1991). Depending on the

wave height of the infragravity waves at the sea surface, the highest frequency that waves can have to exert pressure on the seafloor are those with wavelengths between 0.5 to 2 times the water depth. With the wavenumber, k, becoming

$$k = 2\pi/(nH), \qquad 0.5 < n < 2 \tag{5.4}$$

using equation 5.2, $\omega = 2\pi f$, and with $\tanh(2\pi/n) \simeq 1, n \leq 2$, this gives a maximum frequency for IG waves that exert significant pressure on the seafloor

$$f_c = \left[\frac{g}{2\pi Hn}\right]^{1/2}, \qquad 0.5 < n < 2 \tag{5.5}$$

At OSN1B, the water depth is 4150 m, so the respective frequencies are 27 and 14 mHz (for n=0.5;2). At MOBB, the water depth is 1036 m, so the respective frequencies are 55 and 27 mHz. In principle, we should then expect that IG waves at MOBB contain higher frequencies than at OSN. To keep the comparison simple, however, we low-pass filter the data from both sites at 30 mHz. Infragravity waves continue to periods of 1000 seconds and longer (Aucan and Ardhuin, 2013), but we are limited by the instrument response of the seismometers and differential pressure gauges (Figure 5.3). We therefore restrict our analysis to frequencies between 5 and 30 mHz.

We note that the instrument responses listed in the IRIS DMC metadata files for the OSN1B instruments (the pressure gauge and all seismometer components) were grossly inconsistent with our observations. Inquiries with OSN PIs Frank Vernon and John Collins revealed that these responses are, in fact, incorrect. We obtained the correct values from John Collins [Personal communication, 2015], and incorporate those into our analysis. Details of the instrument responses can be found in Appendix A.

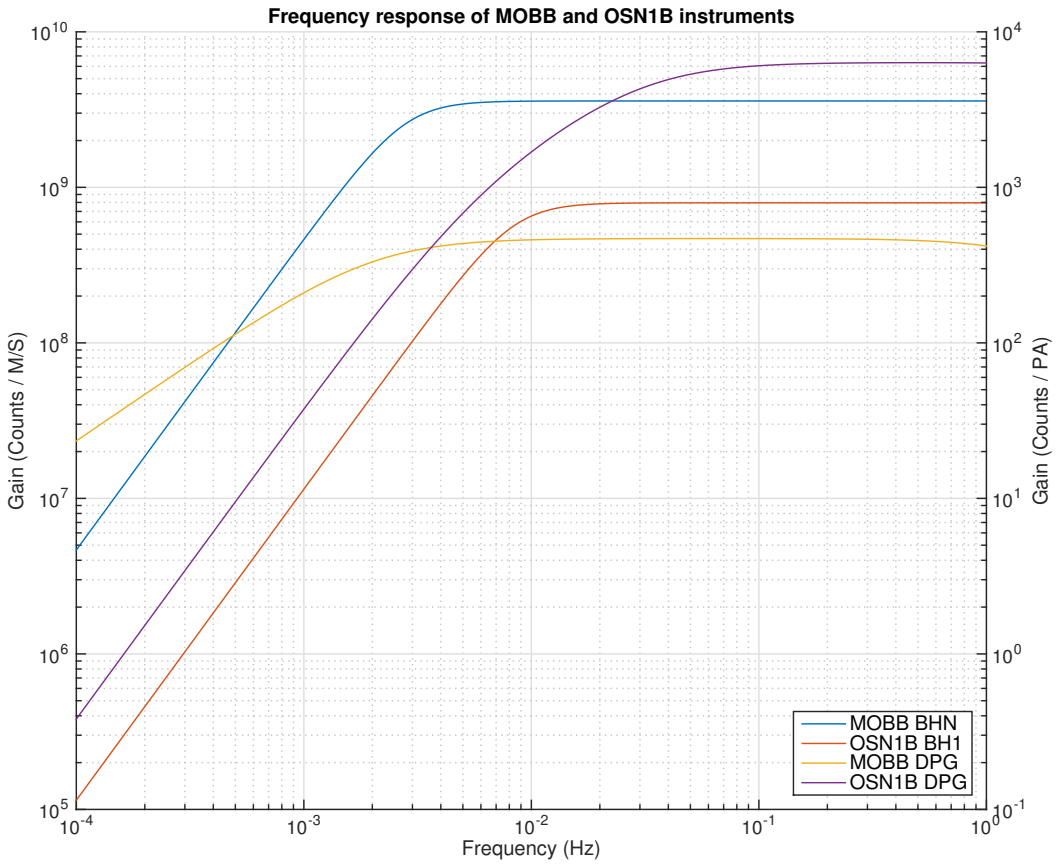

Figure 5.3: Instrument responses of the sensors used in this study, and as reported at the IRIS DMC. The seismometer at MOBB is a Guralp CMG-1T, while the seismometer at OSN1B is a Guralp CMG-3T. The pressure sensor at both MOBB and OSN1B is a Cox-Webb DPG.

4 Site Description

The 1998 Ocean Seismic Network Pilot Experiment (OSNPE) studied the feasibility of adding permanent oceanic seismic stations to the Global Seismic Network (GSN) (Stephen et al., 2003b). The site was 225 km southwest of the island of Oahu, where the seafloor is 4150 m below the sea surface. The OSNPE consisted of three instrument packages. OSN1 was a very broadband three-component Teledyne KS-54000 borehole seismometer and was installed approximately 240 meters below the seafloor in Ocean Drilling Program (ODP) Hole 843B (Dziewonski et al., 1992b). Data for this sensor are available at the Incorporated Research Institutions for Seismology (IRIS) Data Management Center (DMC) between February 3 and May 29. OSN1B was a package comprised of a broadband three-component Guralp CMG-3T seismometer and a Cox-Webb differential pressure gauge (DPG)(Cox et al., 1984). It was installed one meter below the seafloor, and data are available at the IRIS DMC between February 3 and June 14. OSN1S used identical equipment as OSN1B but was deployed directly on the seafloor. Its data are available between February 7 and June 14. The long-period horizontal signal on the borehole instrument was degraded by fluid convection in the well, but analysis of OBS1B records showed that the horizontal traces on the buried instrument were over 40 dB quieter than those of the seafloor instrument (Collins et al., 2001; Stephen et al., 2003b).

The MOBB package is a permanent ocean observatory comprised of a very broadband three-component Guralp CMG-1T broadband seismometer, along with a DPG and two orthogonal seafloor current meters that are aligned with the horizontal seismometer components (Romanowicz et al., 2006, 2009). The system was emplaced by an ROV and is routinely calibrated with a built-in leveling system. The system is located 40 km offshore Monterey Bay on the western side of the San Gregorio Fault at a water depth of 1036 meters, and is buried approximately 20 centimeters beneath the seafloor. We assume that the two horizontal components are closely aligned with N-S and E-W.

In order to explore the relationship between infragravity energy on OBSs and environmental conditions, we inspect weather buoy data. The United States National Oceanographic and Atmospheric Administration (NOAA) maintains buoys throughout the oceans that monitor wind, wave, and other environmental data. We use buoys located in the vicinity of our OBS packages. NOAA buoy 51003 is located 100 km west of OSN1, and NOAA buoy 46042 is 24 km NW of MOBB (see Figures 5.1, 5.2). Here, we use NOAA's published mean hourly wind speeds where the wind speed is averaged over an 8-minute interval every hour. Previous studies have inferred that high seas and winds lead to higher vertical infragravity power (Dolenc et al., 2005; Wang et al., 2010; Webb et al., 1991); Ardhuin et al. (2014) calculate an empirical parameter relating the height of nearshore infragravity waves with significant wave height and the square of the mean wave period. Little research has been devoted to the correlation between these conditions and horizontal infragravity deformation. We employ wind, wave, and tide data collected by the NOAA buoys in our investigation. The availability of seafloor current data at MOBB also provides us a unique opportunity to explore the effects of deep-ocean currents on observations of infragravity energy as defined in this chapter.

5 Data Processing

5.1 Coherence and Power Spectra

We use the magnitude-squared coherence between the infragravity pressure signal and horizontal deformation as a measure of horizontal infragravity energy, as it gives a quantitative evaluation of how much of the horizontal acceleration is attributed to infragravity loading. Coherence is given by the equation

$$C_{xy}(f) = \frac{|P_{xy}(f)|^2}{P_{xx}(f)P_{yy}(f)} \tag{5.6}$$

where $P_{xx}(f)$ and $P_{yy}(f)$ are the power spectral densities of the two time series and $P_{xy}(f)$ is the cross power spectral density between them. To process the data, we cut the time series into one-hour segments and apply a bandpass filter between 1 and 1000 seconds. Previous studies used data windows ranging from 1024 seconds to 4096 seconds or longer (e.g., Crawford et al., 1991; Crawford and Singh, 2008; Crawford, 2004) in order to balance frequency resolution with increased averaging. Dolenc et al. (2005) found that one-day stacks of one-hour pressure-displacement transfer functions provide a robust estimate. We adopt this strategy and process 1-h time segments.

Our spectra are computed using the package `psd` (Barbour and Parker, 2014), which is based on the Riedel-Sidorenko minimum bias multiple taper spectral estimation method (Riedel and Sidorenko, 1995). Instead of Slepian (also known as discrete prolate spheroidal sequences) tapers, the Riedel-Sidorenko method takes advantage of two families of orthonormal tapers: minimum bias tapers and sinusoidal tapers. The program uses these families to produce power spectral density estimates through an iterative refinement of the optimal number of tapers at each frequency. The number of tapers used varies according to spectral shape: where the spectrum is flat, more tapers are taken and thus higher accuracy is attained at the expense of lower frequency resolution. The reverse is applied in frequency ranges where the spectrum is relatively rough. The program applies smoothing that varies with frequency to minimize the sum of variance and bias at each point. This results in variable resolution and error as a function of frequency, but produces robust and stable spectral estimations.

We ensure that the signal is uncorrupted by other sources, including energy from passing teleseisms or instrument spikes. Before analysis, we inspect the U.S. Geological Survey National Earthquake Information Center (NEIC) earthquake catalog and exclude time segments associated with global events with magnitudes $M_w \geq 6$. In addition, we exclude time segments for events at regional and local distances (epicentral distance $<$400 km) and magnitudes $M_w \geq 4$. These segments may have high coherence between the vertical seismometer component and

pressure, but the associated signal obeys a different dispersion relation than the IG waves and would therefore contaminate our compliance estimates.

5.2 Signal Optimization by Horizontal Component Rotation

An important step in the analysis of horizontal OBS components is to point one of the components toward the direction from which the waves approach. For the sake of simplicity, we assume for now that the horizontal components are aligned with the geographic coordinate system, i.e. one component points N-S (BHN) and the other E-W (BHE). This is essentially the case for MOBB, but not for OSN1B, as we discuss in a later section. To optimize the coherence between horizontal deformation and pressure exerted by IG waves, we rotate the horizontal components until a maximum is found on one component, BS1, and a minimum on the other, BS2. Given the original seismometer components BHN (or BH1 for OSN1B) and BHE (or BH2 for OSN1B), we rotate each component clockwise by an angle α using the equation

$$\begin{bmatrix} S1 \\ S2 \end{bmatrix} = \begin{bmatrix} \cos\alpha & \sin\alpha \\ -\sin\alpha & \cos\alpha \end{bmatrix} \begin{bmatrix} NS \\ EW \end{bmatrix} \tag{5.7}$$

For each 1-hour data segment we independently find the angle that achieves the highest average coherence in the infragravity band (5 mHz $\leq f \leq$ 30 mHz). We only rotate by angles between 0 and 180 degrees, since a rotation by any angle α provides the same coherence maximum as a rotation by $\alpha + 180^\circ$. We then proceed by analyzing the relationship between various environmental factors and the average horizontal infragravity coherence, which we define as the average coherence value between the DPG and BS1 component in the infragravity band.

Figure 6.2 illustrates how important this step is. Before rotation, we note that the coherence is much higher for the BHN component than for the BHE component. This indicates that the infragravity waves approach from a northerly direction. However, rotation can further increase coherence for the BHN component (BS1), at the expense of decreasing it for the rotated

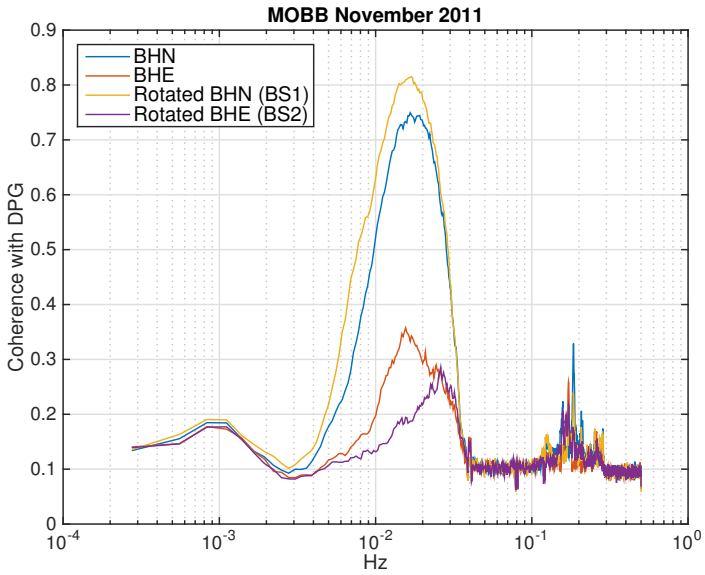

Figure 5.4: Mean coherence of unrotated BHN and BHE traces and rotated BHN (BS1) and rotated BHE (BS2) traces. Mean coherence was determined by processing 1-h time segments and subsequent averaging for the month of November 2011.

BHE component (BS2). The implications regarding the rotation angles are discussed in a later section.

6 Results

6.1 Deep-Ocean Conditions and IG Coherence

Although burial minimizes the tilt noise on OBSs, strong seafloor currents can still influence the coherence between the pressure and the resulting deformation signals. For Figure 5.5, we determine the mean hourly optimized horizontal IG coherence at station MOBB after rotating the horizontal seismometer components as described in the last section. We also determine the average hourly strength of the current along the seafloor from the two orthogonal current meters. Though the relationship between mean hourly IG coherence and current speeds along the ocean floor is rather diffuse, there is a clear overall negative trend in average coherence as

current speed increases. This implies that progressively stronger currents deteriorate the relationship between pressure from IG waves and the resulting horizontal seafloor deformation. A high coherence is rarely achieved when the seafloor current is greater than 20 cm/s, even when the seismometer is buried. We calculate the cross-correlation between the current and average coherence as a function of lag to address the question of how quickly the seismometer responds to the currents. Similar tests were previously done by Dolenc et al. (2005), Webb et al. (1991), and others between vertical coherence and sea surface conditions. The maximum correlation occurs at a lag of zero, indicating an instantaneous response of the package to the current. Ocean bottom currents can induce significant shear stress on the seafloor (Grant and Madsen, 1979; Cacchione and Drake, 1982). We infer that these current-induced horizontal stresses on the sea bed introduce additional horizontal noise and therefore lower the pressure-seafloor deformation coherence. For completeness sake, we repeated the analysis for the vertical component. Figure 5.5 clearly demonstrates that the vertical deformation caused by IG waves is much less influenced by deep-ocean currents than the horizontal deformation.

6.2 Sea Surface Conditions and IG Coherence

We proceed by investigating the relationship between our observed IG coherence and short-period ocean gravity waves (12-18 s). The underlying assumption here is that ocean gravity waves are generated locally, and wave height correlates with measured wind speeds. We should note that this is a reasonable assumption as ocean swell generated at greater distance typically has a longer period. One of the major outcomes of this analysis is that a strong correlation between horizontal IG coherence and ocean gravity waves suggests that IG waves are generated in coastal environments, in agreement with modern numerical models (Ardhuin et al., 2014). Using a different approach, previous work on MOBB data found first evidence that this is the case. Dolenc et al. (2005) computed power spectral densities (PSD) of the vertical seismometer component for 2003 and 2004. They analyzed infragravity signals during both “quiet” and

"stormy" days and investigated the marine conditions that increase the infragravity signal. Their signal was found to correlate positively with significant wave height of short-period ocean gravity waves. Thus, the authors inferred local infragravity wave generation. This supports previous discussions that IG waves have a near-coastal or a shallow-ocean continental-shelf origin (e.g., Webb, 1998).

Here, we provide an alternative approach through the analysis of horizontal IG coherence. We also provide a wider reference frame by including a test case for the deep ocean, far away from a coast, namely OSN1B. We examine average infragravity coherence and local sea state for one month of OSN1B and MOBB. For the former, we choose April 1998. This choice is controlled by the fact that complete months for OSN1B are available only for March, April and May 1998. The choice for MOBB, November 2011, is somewhat arbitrary, but this month provides a complete record of sea state data (while April 2012 does not).

We focus on wind data and sea surface gravity waves with periods between 5-25 seconds. Figure 5.6 displays average optimized horizontal IG coherence, as a function of both mean hourly wave height and hourly average wind speed observed at MOBB during November 2011. We analyze optimized coherence instead of simply spectral power in order to investigate causality and minimize the influence of incoherent noise. The horizontal IG coherence increases as wave height increases. Interestingly, as wind speed increases, wave height also has to increase to produce the same level of coherence though this may be induced intrinsically by the causal effect between local wind speed and wave height. At sustained wind speeds of 10 m/s and above, this linear dependence seems to break down and high horizontal IG coherence is reached for relatively smaller wave heights. A similar trend is observed for vertical IG coherence though much smaller wave heights and wind speeds are required to reach similar levels of coherence (Figure 5.7).

The situation seems far more complex for deep-ocean station OSN1B (Figures 5.8 and 5.9). Note that the IG coherence is significantly lower overall than that at MOBB. No relation-

ship appears to exist between horizontal IG coherence and the local sea state. We currently have no good explanation why coherence is highest for wind speeds of 8 m/s and wave heights of greater than 3 m. The IG coherence is slightly higher for the vertical component overall, but there is no obvious dependence on wind speed and wave height.

We also explore the relationship between horizontal IG coherence and the frequency content in the local sea state, at both OBS locations. Figure 5.10 confirms the relatively weak relationship at OSN1B between IG coherence and local short-period ocean waves on the one hand, but the strong relationship at MOBB on the other. Maximum coherence is achieved for periods around 15 s, which is actually the dominant period found in swell around MOBB (Dolenc et al., 2005). The situation at OSN1B is less clear.

Finally, we analyze the relationship between horizontal IG coherence and the total power in the ocean wave spectrum as expressed through the squared spectrum RMS (Figure 5.11). This figure is complementary to, and essentially confirms findings discussed for Figures 5.8 and 5.9. At MOBB, stronger local waves lead to higher horizontal IG coherences (though there exists a significant scatter), while at OSN1B no such trend can be found.

To summarize, at MOBB, we find that "stormy" conditions with great wave heights generally lead to higher IG coherence. We take this as an indication that infragravity waves are generated locally, as Dolenc et al. (2005, 2007) inferred previously. We find no such strong correlation for OSN1B and infer that the infragravity waves associated with our observations must have been generated elsewhere.

6.3 Direction of Approach of IG Waves

In this section, we examine the direction from which IG waves approach at each of the two OBS sites. To do this, we must know the orientation of the horizontal seismometer components. We are fairly confident that the components are roughly aligned with the geographic coordinate system at MOBB, but the orientation at OSN1B is unknown; however, we

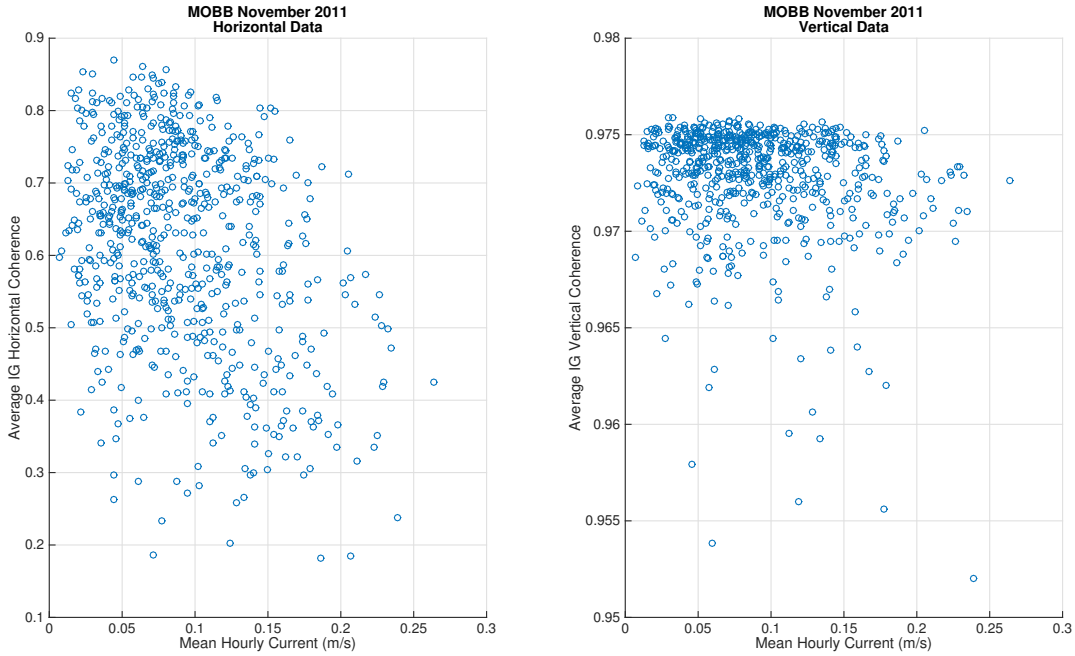

Figure 5.5: Relationship between the strength in deep-ocean currents (expressed as mean hourly current speed) and average IG coherence. Left: for the BS1 component at station MOBB; right: for the BHZ component at MOBB. Overall, horizontal coherence declines as current speed increases. At the same time, the vertical coherences is less affected. Note that the axis for horizontal coherence is highly compressed.

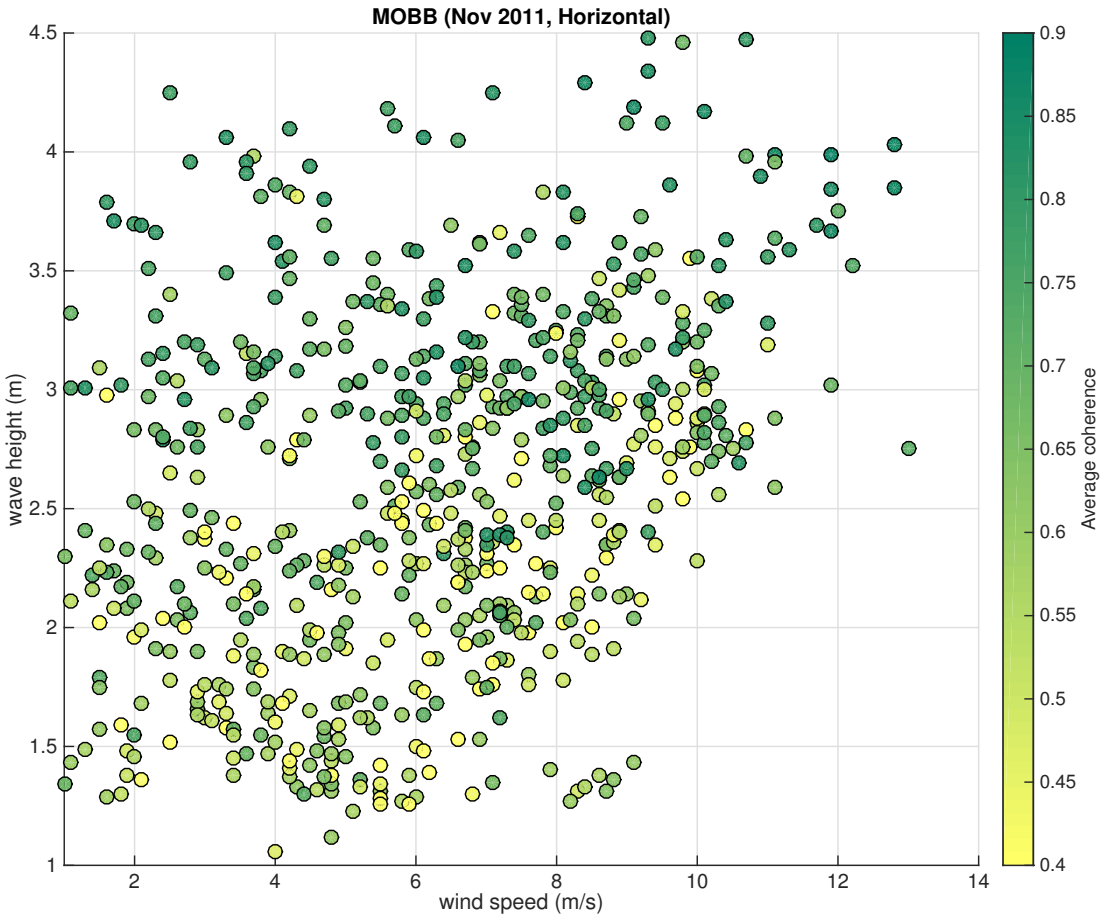

Figure 5.6: Average optimized horizontal IG coherence, as a function of hourly average wind speed and wave height, observed at MOBB and nearby NOAA buoy 46042 during November 2011. The term ”optimized” implies that the BS1 component was used.

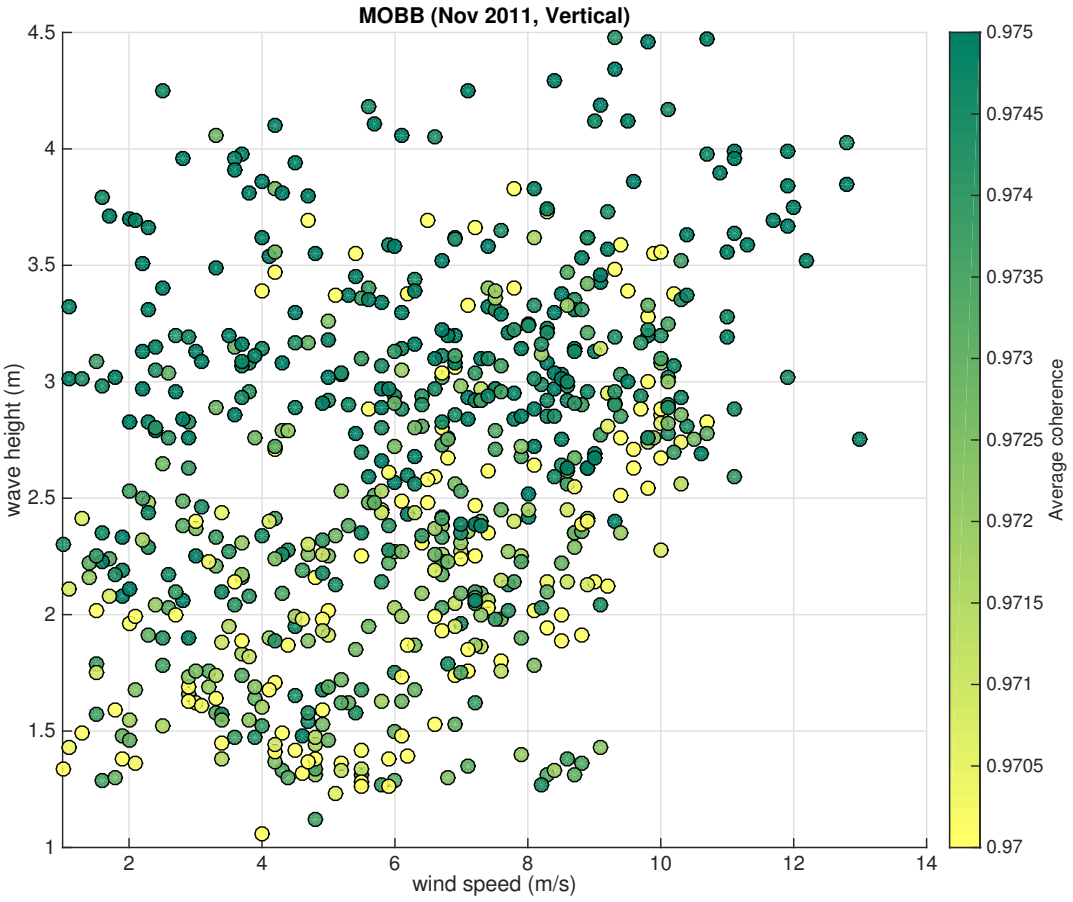

Figure 5.7: Same as Figure 5.6, but for vertical IG coherence. Note that the color scale in the previous figure is significantly compressed.

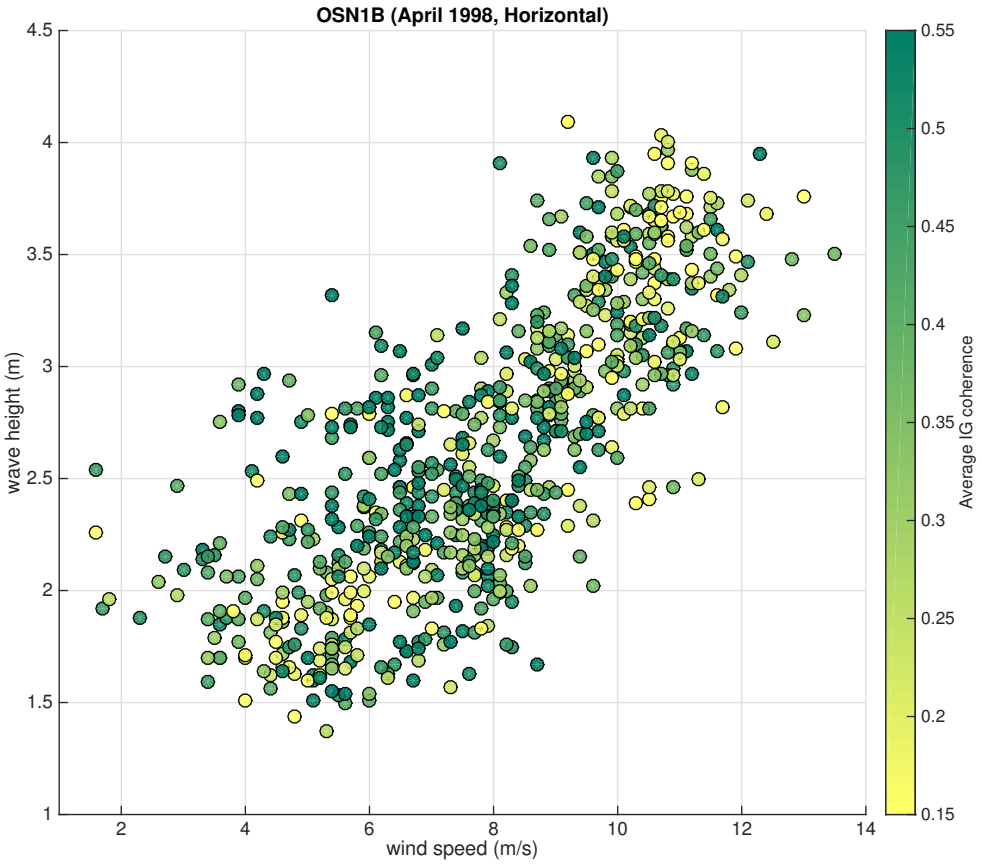

Figure 5.8: Average optimized horizontal IG coherence, as a function of hourly average wind speed and wave height, observed at OSN1B and nearby NOAA buoy 51003 during April 1998. The term ”optimized” implies that the BS1 component was used.

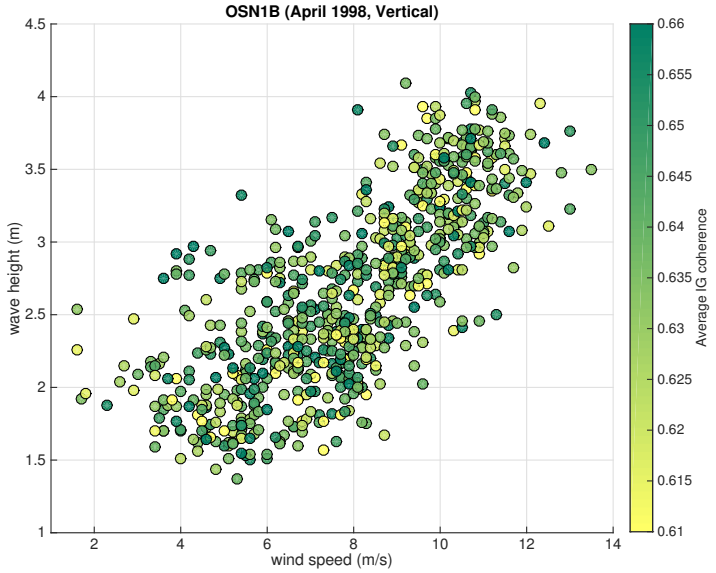

Figure 5.9: Same as Figure 5.8, but for vertical IG coherence. Note that the color scale in the previous figure is different.

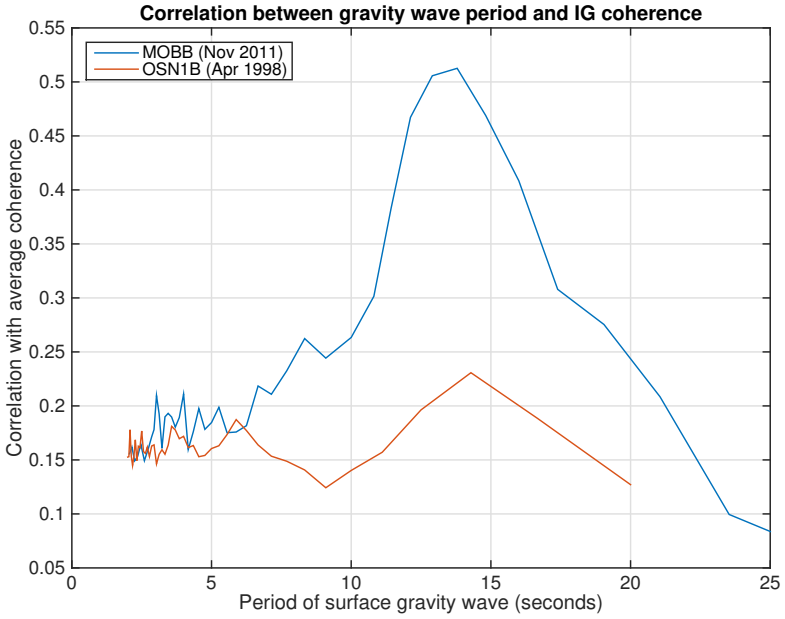

Figure 5.10: Cross-correlation between average horizontal IG coherence and period of surface gravity waves, at both OBS stations MOBB and OSN1B, averaged over the respective months noted in previous figures.

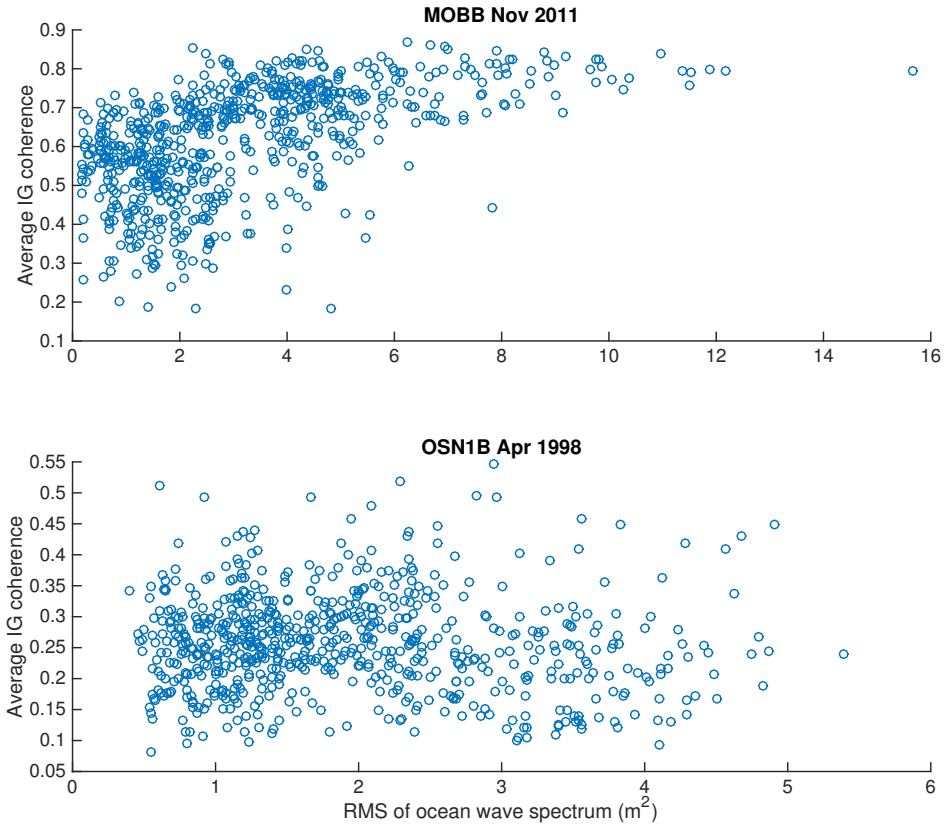

Figure 5.11: Hourly averaged horizontal IG coherence as function of power in the wave spectrum, for the months noted in previous figures. Top: MOBB; Bottom: at OSN1B.

can determine the orientation during post-processing of seismic surface waves from distant large earthquakes (e.g., Laske, 1995; Stachnik et al., 2012a). Here we determine the alignment of the horizontal components using the Rayleigh wave polarization analysis detailed by Stachnik et al. (2012a). Using 32 $M_S \geq 5.5$ global events from the entire 131 days of deployment for OSN1B, we determine the orientation of BH1 to be $148.1^\circ \pm 1.8^\circ$ clockwise from north. We also check the orientation at MOBB. We use 29 $M_S \geq 5.5$ earthquakes between September 1, 2011 and May 2, 2012. We obtain a slight misalignment with the geographic coordinate system where the orientation of BHN is $8.1^\circ \pm 3.1^\circ$. We should mention that we determine the MOBB orientation strictly for the purpose of this study. A more accurate estimate of the alignment at MOBB should include the entire timespan over which MOBB has been operational, but we feel that the associated work goes beyond the scope of this chapter.

To determine the directionality, we investigate the rotation angles that we obtain when we determined the hourly optimized horizontal IG coherence, now under consideration of the misalignment of the horizontal seismometer components as found in the teleseismic reorientation work (Figure 5.12). We take these rotation angles to be the direction of approach of the IG waves. Analysis of the corresponding horizontal seismic power spectra and particle motion plots confirms this.

We observe a fairly stable raw infragravity azimuth of $\approx 30^\circ$ clockwise from north at station MOBB. A correction for instrument misorientation would place the angle of approach at around 38°. Although the rotation analysis inherently includes a 180° ambiguity, we believe this indicates that the majority of infragravity waves are sourced from Monterey Bay and the local continental shelf where short-period surface gravity waves interfere in a nonlinear fashion. The rotation angles for OSN1B exhibit significantly higher variance, but a general azimuth of approximately 110°, corresponding to either 258° or 78° after correcting for instrument orientation (recall that BH1 is oriented 148.1° clockwise from north). 78° is approximately the azimuth between the OBS and the narrow shelf off the north coast of the island of Hawaii. It is worth

noting that there is a 2 km drop in the seafloor across the edge of the shelf. While infragravity energy observed at OSN1B may not be generated locally, it may well be generated on the Hawaiian shelf and propagate to the OBS site. The variance of the angles and the weakness of the coherence suggests that the IG energy is also approaching from many other angles as well. Figures 5.1 and 5.2 give a qualitative depiction of the infragravity wave source directions inferred at both sites.

Figure 5.12 includes a six-hour running mean for each of the angle time series. At MOBB, several periods of sustained deviation from the median rotation angle can be seen, with the strongest occurring on day 15. While we find no relationship between local weather conditions and these arrival angle excursions, the angle deviation from the median exhibits strong negative correlation with the average coherence. We interpret this to indicate that the infragravity wave field during these periods is strongly influenced by IG waves generated in a different source region, likely by a storm elsewhere in the pacific. The larger scatter in the Figure 5.12 for OSN1B may be explained by the relatively low local wave power. To investigate this, we plot the rotation angles as function of RMS of the wave spectrum (Figure 5.13). At OSN1B, rotation angles are widely scattered as a function of RMS, and no significant trends are apparent. On the other hand, at MOBB, we observe that the variance of the rotation angle decreases as the energy in the ocean wave spectrum increases. Note, however, that RMS values at ONS1B never reach those at MOBB.

We have thus far only considered the rotation angle that maximizes the average coherence in the entire infragravity band. We may gain additional insight into the internal variability of IG waves by calculating the optimal rotation angle for each frequency individually. Figure 5.14 displays a polar histogram detailing the directional distribution for two different hours at MOBB on November 1st, 2011. Note that this day is within a time span that provided fairly stable rotation angles in Figure 5.12. As is evident from both panels, the internal consistency of direction of approach can vary greatly. During hour 10, most sampled frequencies share similar

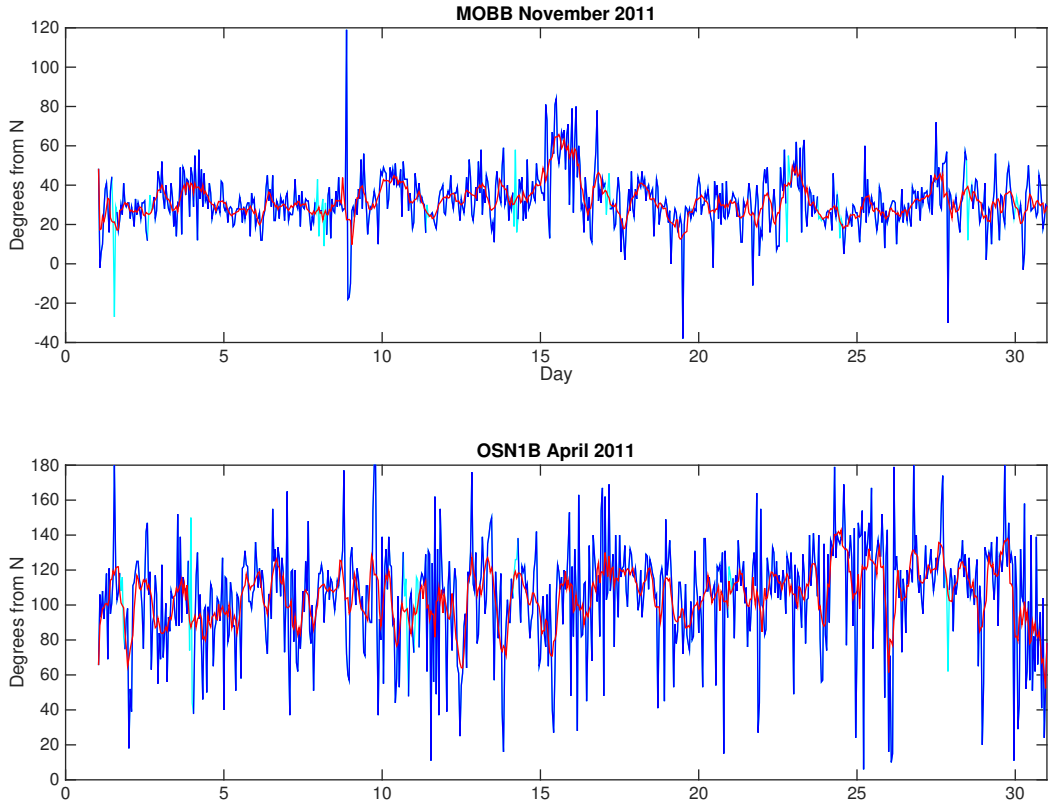

Figure 5.12: Rotation angles obtained during the optimization process for horizontal IG coherence, as a function of time, for both OBS stations used in this study. The rotation angles have not been corrected for instrument orientation. The light blue segments are rotation angles that may have been corrupted by transient seismic energy and are excluded from our analyses. The red line tracks a running mean computed using six hour intervals.

angles implying that IG waves consistently came from the same direction (roughly 40°). During hour 3, angles are much more distributed, which may indicate that waves of different periods came from different directions or that IG wave activity was generally lower, leading to less coherent wave packets. Hour 10 also coincides with a higher mean wave height (3.6 m versus 2.7 m) and higher average coherence (0.71 versus 0.49), suggesting that coherence is optimized during periods of consistent and unidirectional infragravity wave propagation. In general, hours with higher variance in the calculated angles exhibit lower average infragravity coherence.

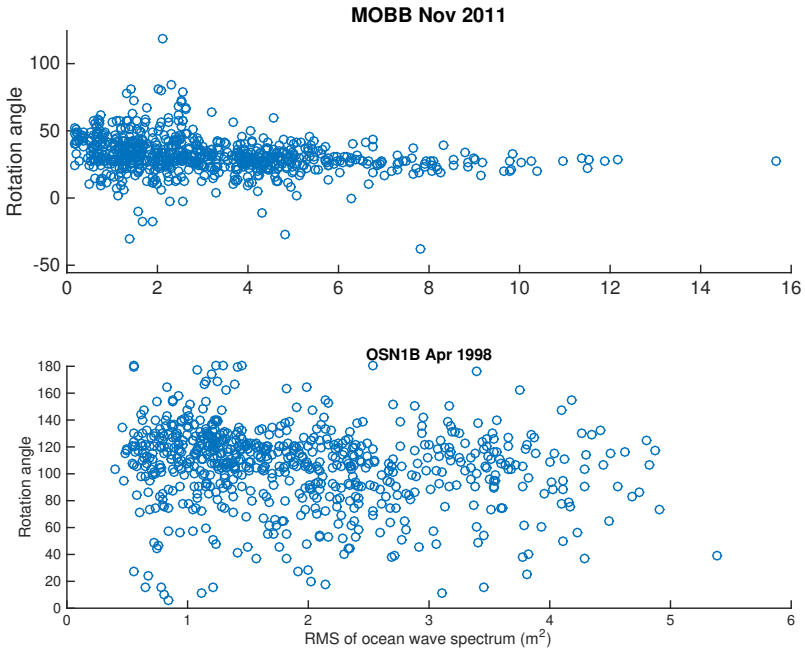

Figure 5.13: The same rotation angles in Figure 5.12, but now as a function of RMS in the local wave spectrum. Note the different scales in the x-axes.

7 Discussion

7.1 Horizontal Seafloor Compliance

Although a full analysis is beyond the scope of this chapter, our ultimate goal is the use of horizontal infragravity energy in a seafloor compliance inversion. Seafloor compliance is defined as the transfer function between displacement and pressure, and was first developed as a tool to study shallow shear structure (<10 km) in the deep oceans by (Crawford et al., 1991). Recent advances have improved compliance capabilities with regards to both modeling (e.g., Iassonov and Crawford, 2008; Zha et al., 2014a) and imaging (e.g., Willoughby et al., 2008; Crawford and Singh, 2008). High-quality coherent pressure and horizontal displacement data would allow us to perform a horizontal compliance inversion for subsurface structure.

Significant developments are necessary in horizontal compliance theory before a mean-

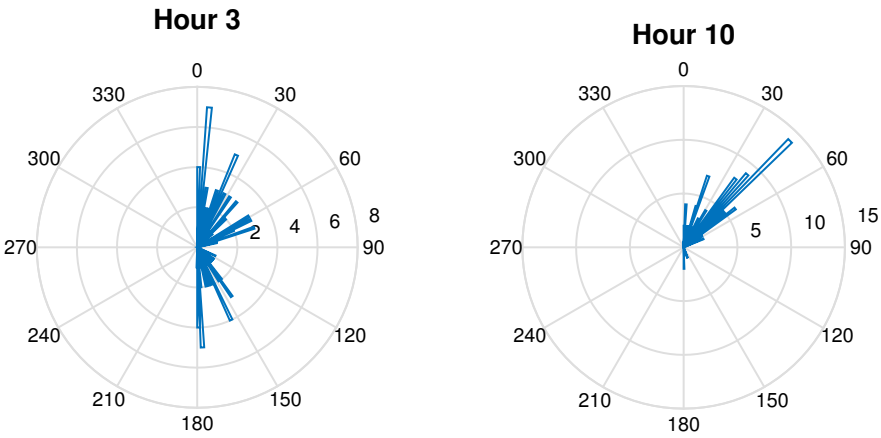

Figure 5.14: Polar representation of histograms of rotation angles (implied direction of IG wave approach) at MOBB, as a function of individual frequency, sampled at 100 frequencies between 1-30 mHz. The two panels show histograms for hours 3 and 10 on November 1, 2011 (correspond to 8pm and 3am local time). Note the different radial scales in both panels.

ingful inversion can be done. While vertical acceleration due to infragravity waves is always 180° out of phase with the pressure signal, the phase of the horizontal acceleration is dependent on frequency and Earth model (Webb, 1998); however, horizontal compliance measurements would provide significant additional constraints on local subsurface structure. A joint inversion of horizontal and vertical compliance data would provide tighter bounds on a final model and remove some of the inherent ambiguity of vertical compliance modeling. Figure 5.15a shows the results for forward modeling for two simple crustal structures with very similar vertical compliance values but horizontal compliance values that differ by a factor of three at higher frequencies. The two models represent typical oceanic crustal structure overlain by 1 km of sediment, and only the upper 500m differ in elastic parameters. Including horizontal compliance can increase the resolving power of an inversion. Additionally, as described by Crawford (2004), the ratio of vertical to horizontal compliance provides an estimate of the V_P/V_S ratio. The quasi-static 1D solution for an elastic half-space (from eq. 5.3) states:

$$\frac{\eta_Z}{\eta_H} = \frac{(\lambda+2\mu)/(2\mu(\lambda+\mu))}{1/2(\lambda+\mu)} = \frac{\lambda+2\mu}{\mu} = \frac{\alpha^2}{\beta^2}$$

From this result we expect vertical compliance to always exceed horizontal compliance, but in some realistic Earth structures this relationship may be voided. As seen in Figure 5.15b, one of the models produces expected compliance values that broadly agrees with the V_P/V_S ratios present in the starting model, while the relationship only holds at high frequencies for the other model.

The directionality measurements also suggest the possibility of detecting anisotropy from horizontal compliance measurements. Periods of sustained infragravity energy arrival angle deviation may yield different compliance curves, which could be inverted for directionally-dependent velocities. We examined several extended periods with significantly different dominant infragravity directions at both MOBB and OSN1B but were unable to identify a statistically significant azimuthal dependence for the horizontal compliance values, indicating that local

anisotropy is either negligible or beneath our limits of detection; however, this does not preclude the possibility at other locations with stronger anisotropy or more precise measurements.

Figures 5.16 and 5.17 display the horizontal and vertical compliance curves calculated at MOBB and OSN1B, respectively. The functions diverge due to distinct sensitivities to the underlying structure. While the MOBB compliance data are consistent with our expectations, the values at OSN1B appear inverted, as the horizontal signal is greater than the vertical. Araki et al. (2004) observe this phenomenon at sealed borehole seismometers offshore Japan. The authors do not report the coherence between pressure and deformation (owing to the absence of a collocated pressure gauge at the sites), but conclude that the signal is caused by compliance-induced tilting. In that location, the local geology was inferred from borehole logging, and a higher vertical compliance was expected from the starting model; this may not be the case at OSN1B. The borehole logs obtained at site OSN1 (approximately 300m from OSN1B) indicate 242 meters of soft sediment overlying crystalline basement (Dziewonski et al., 1992a). We can model an inverted signal similar to the one calculated at OSN1B using a sharp shear velocity interface between the thin sediments and the basalt. Figure 5.18 plots four possible structures, each with standard oceanic crust overlain by 250 meters of sediment. The density and compressional speed of the sediments are fixed (at 1.6 g/cc and 1.7 km/s respectively, in agreement with the ODP borehole logs), while the V_P/V_S ratio varies between 7.0 and 10.0. Sediments with velocity ratios of this magnitude are not uncommon in marine environments: Hyndman (1979) reports a 1000 meter sedimentary package with V_P/V_S ratios ranging from 2.6 at the base to 13 and greater at the seafloor. In the OSN1B environment, a higher horizontal compliance is possible. The lower relative BH1-DPG coherence at OSN1B may bias the results as well, but we believe this to be unlikely. We calculate compliance using data from all 131 days of the deployment and obtain nearly identical results as the ones presented here. The low coherence is likely due to the higher instrument response roll-off at OSN1B and to infragravity waves from different source azimuths destructively interfering. All of this leads us to have confidence that we are indeed

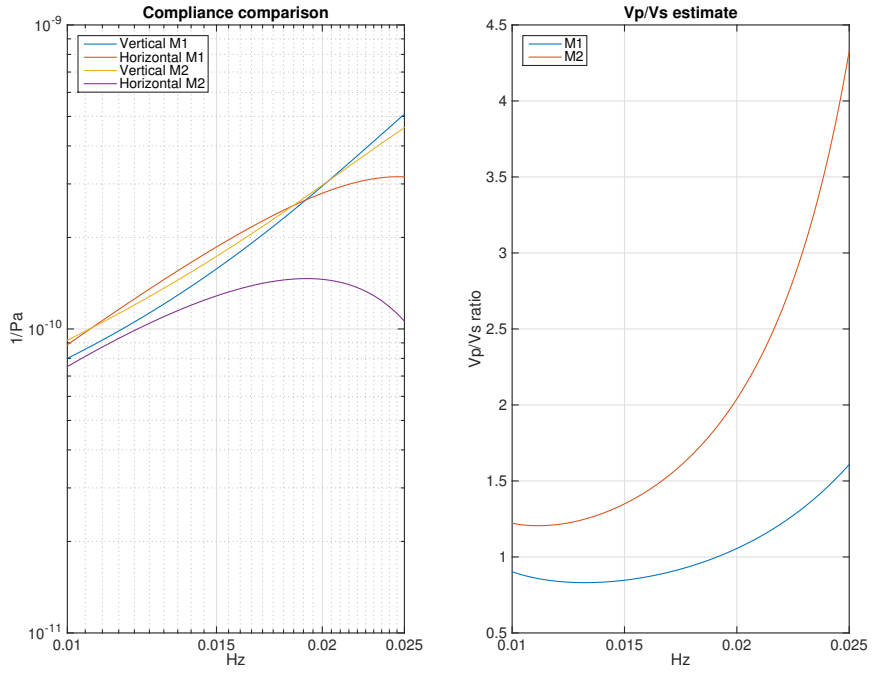

Figure 5.15: Compliance forward modeling of two structures with similar vertical compliance values but differing horizontal values. The left panel (a) compares the different compliance values obtained, while the right panel (b) plots the ratio of vertical to horizontal compliance, which may give an estimate of the V_P/V_S ratio.

observing horizontal compliance at both MOBB and OSN1B.

7.2 Removing long-period noise to lower earthquake detection thresholds

The primary use of OBS recordings is earthquake detection and waveform analysis. The detection threshold of teleseismic events has been reported as consistently higher on OBSs than on land instruments (e.g., Webb, 1998), especially when analyses rely on the horizontal seismometer components. The problem is particularly acute in the infragravity band, where noise sources are entirely absent on most land stations (though clearly visible on some island stations (Rhie et al., 2008)). A reduction of the long-periods infragravity signal on vertical OBS components has been done successfully through deconvolution of the pressure signal from the ground acceleration (Crawford and Webb, 2000; Crawford et al., 2006; Taira et al., 2014). This process

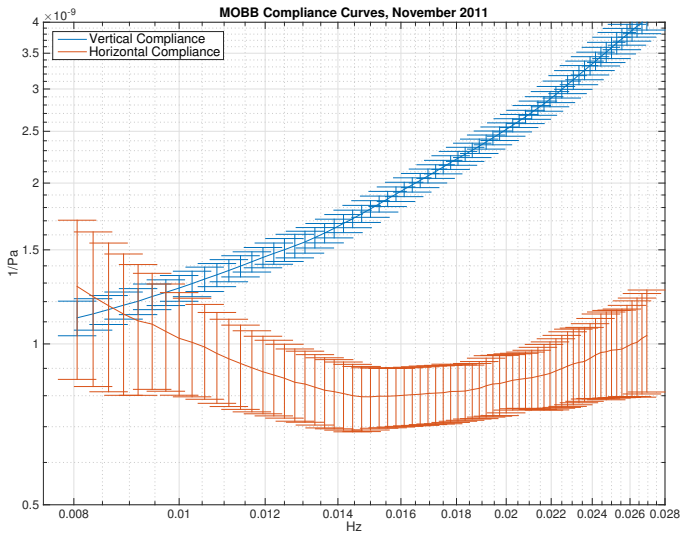

Figure 5.16: Calculated MOBB compliance curves for November 2011

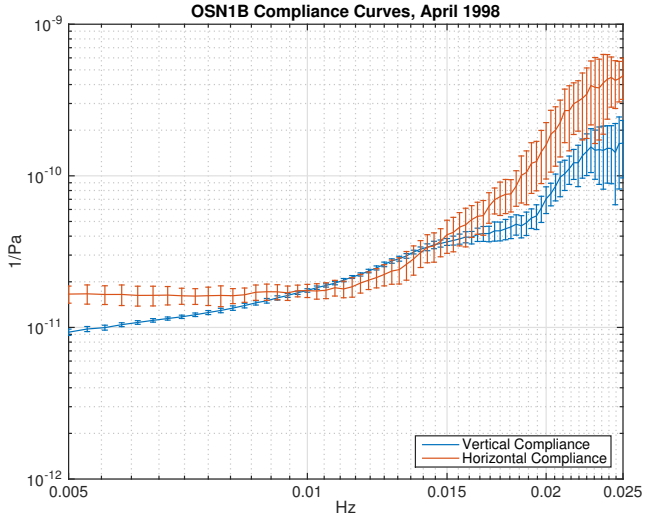

Figure 5.17: Calculated OSN1B compliance curves for April 1998

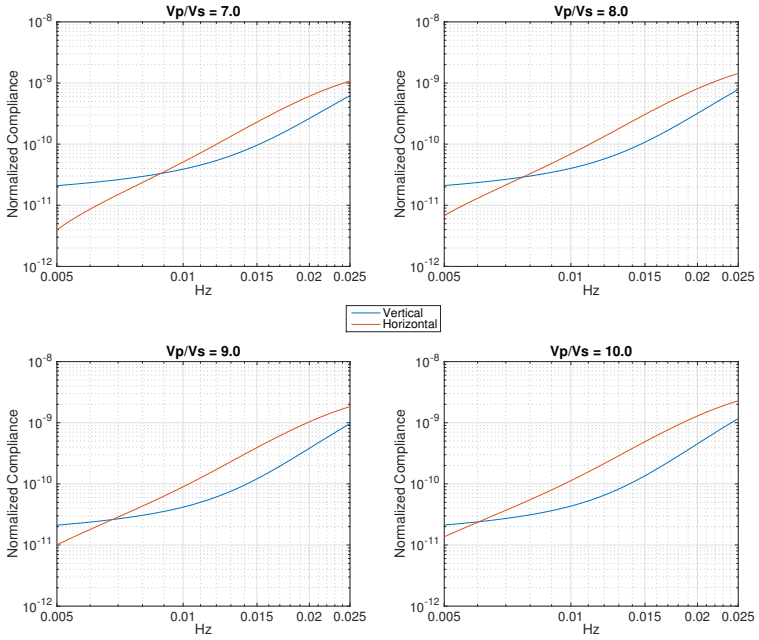

Figure 5.18: Forward modeling of OSN1B compliance. All models have fixed structure typical of oceanic crust and are overlain by 250 meters of sediment. Only the sedimentary shear velocity varies. A sharp contrast between sediment and bedrock V_P/V_S ratios can produce a higher expected horizontal compliance signal than vertical.

has started to become a routine part of pre-processing OBS vertical components (Dolenc et al., 2007; Taira et al., 2014), particularly for the waveforms gathered for the recent community OBS deployment in Cascadia. With a coherent horizontal signal, we hope to eventually apply similar procedures to horizontal components, at least on buried OBSs.

7.3 Other Buried OBS Sites

While the two OBS deployments discussed in this chapter are the only ones that we analyzed, they are not the only ones with buried seismometers. The French borehole experiment OFM conducted in 1992 provides promising seismic data, but lacked a DPG (Montagner et al., 1994). We therefore cannot conduct a corresponding study for that deployment. We note that although some vertical infragravity energy is visible on their published spectra, the horizontal components appear to be too noisy for our purposes. A "corehole" seismic experiment run in 1996 and 1997 in Monterey Bay produced very low-noise records (Stakes et al., 1998), but the limited bandwidth of the deployed sensors does not seem to allow a study as ours since the instrument response of that seismometer seems to imply high-quality data only at frequencies above 0.1 Hz. The H2O experiment halfway between Hawaii and the U.S. west coast between 1999 and 2003 was comprised of a three-component seismometer and a pressure-sensing hydrophone buried in 0.4 meters of seafloor, but high long-period noise rendered infragravity energy, both vertical and horizontal, difficult or impossible to measure (Duennebier et al., 2002).

The NEREID deployment mentioned previously (Araki et al., 2004) consisted of four borehole observatories installed offshore Japan. The three-component seismometers were cemented in the borehole to maximize coupling and to avoid flow effects that influenced long-period data of previous borehole deployments (Collins et al., 2001). The authors report clear infragravity wave energy on both the horizontal and vertical components, but lack a collocated differential pressure gauge. The goal of the study was to minimize infragravity noise in order to maximize the effectiveness of event analysis, and the authors find that the strongest infragravity

signal is found on instruments in the sediment.

8 Summary

We observe consistent infragravity energy on the horizontal components of two buried OBS stations: MOBB and OSN1B. These two sites are in vastly different ocean settings: MOBB is located in a near-shore environment at 1000m depth, while OSN1B was deployed in the deep open ocean far away from any continental coast. Infragravity waves are not routinely observed on the horizontal components of traditional seafloor OBSs because current-related tilt noise overpowers the signal; sensor burial is necessary for our observations. We choose to measure infragravity energy using the coherence between the pressure signal exerted by infragravity waves on the seafloor (as measured by a broadband pressure sensor) and horizontal seafloor deformation (as measured by a broadband seismometer). Collocating both types of sensors ensures that the horizontal deformations we observe can be attributed to passing infragravity waves. The coherence between the signals also gives us a reliable quantitative measurement of the signal-to-noise ratio of our observations.

The positive correlation between horizontal infragravity wave measurements and short-period ocean gravity waves can provide evidence for a near-shore origin where non-linear constructive interference of the local swell leads to the generation of long-period infragravity waves. The strong correlation between infragravity energy observed at MOBB, as opposed to the weak correlation seen at OSN1B, argues for such a generating mechanism. Our analysis of rotation angles obtained through the optimization process for horizontal IG energy also provides strong evidence that infragravity waves can be generated by near coastal swell.

We plan to use the observations discussed in this chapter in a forthcoming inversion of vertical and horizontal compliance. The horizontal compliance method is not identical to vertical compliance and additional theoretical development is necessary, but the combined results should

provide more robust constraints on sedimentary and crustal structure. In case of disagreement, we hope to investigate near-surface anisotropy (transverse isotropy). The results of our IG source directionality analysis imply that horizontal compliance may be best characterized in regions of unidirectional IG propagation where destructive interference is avoided and high DPG-BH1 coherence can be achieved.

Another promising avenue for horizontal compliance studies are long-term traditional OBS deployments. The PLUME experiment (Laske et al., 2009; Wolfe et al., 2009) consisted of 74 marine instruments, each deployed for approximately 12 months between 2005-2007. These are seafloor instruments that suffer from the high tilt-induced long-period horizontal noise that buried instruments lack, but the long duration of the deployments allows us to stack thousands of transfer functions, thus possibly revealing a coherent horizontal compliance signal. Initial results show that with twelve months of continuous data, enough transfer functions can be obtained to give an estimate of horizontal compliance with reasonable uncertainties.

Ruan et al. (2014) recently introduced a method of crustal imaging using the vertical displacement-pressure transfer function in the microseism frequency range (0.1 - 0.2 Hz). While using similar techniques as seafloor compliance, the displacement is caused by microseism-generated Rayleigh waves rather than water wave forcing. The microseism spectrum at any location depends on local and distant ocean wave spectra, as well as the directional spectrum of the ocean waves (Webb, 1992). Like infragravity compliance, the method depends on high coherence between the displacement and pressure spectra. While common using vertical traces, high coherence is rarely attained from horizontal recordings. We attempt to improve coherence between the pressure and the horizontal spectra using similar weather conditions and a rotation analysis as previously described, but are unable to achieve significant signal coherence. This may have implications for microseism propagation and generation, as well as intermediate-period horizontal noise.

9 Acknowledgements

This research was supported by NSF grants EAR-11-13075 and EAR-14-15763. We wish to thank the operators of the Monterey Ocean-Bottom Broadband Seismometer (MOBB), whose waveform data and metadata are accessible through the Northern California Earthquake Data Center (NCEDC). The facilities of IRIS Data Services, and specifically the IRIS Data Management Center, were used for access to Ocean Seismic Network (OSN) waveforms and related metadata used in this study. We thank John Collins for providing instrument responses and related codes. Figures 1 and 2 were generated using Generic Mapping Tools 4.5 (Wessel and Smith, 1991; Wessel et al., 2013). We thank Wayne Crawford for compliance forward modeling codes. We also thank Dr. Crawford, Michael Walter, and an anonymous reviewer for constructive comments that led to significant manuscript improvement.

Chapter 5, in full, is a reformatted version of a publication in Journal of Geophysical Research: Doran, A.K., and G. Laske (2016), Infragravity waves and horizontal seafloor compliance, J. Geophys. Res. 121, 260-278, DOI: 10.1002/2015JB012511. I was the primary investigator and author of this paper, which describes our attempts to measure and analyze horizontal seafloor compliance data.

10 Appendix

10.1 OSN1B Instrument Responses

Instrument responses for modern seismic instrumentation are traditionally presented in a poles and zeros format, satisfying the following transfer function in the frequency domain:

$$T(\omega) = k\frac{(i\omega - z_1)(i\omega - z_2)(i\omega - z_3)...}{(i\omega - p_1)(i\omega - p_2)(i\omega - p_3)...} \tag{5.8}$$

where z_n are the zeros, p_n are the poles, and k is a combined normalization factor that

includes the polynomials for the numerator and denominator as well as the data logger response. The parameter values are listed in Tables A5.1 through A5.4.

Table 5.1: Response parameters used for OSN1B DPG

Zeros	Poles	Sensitivity
0.00 + 0.00i	-3.00e-02 + 0.00i	-1.02e+06
0.00 + 0.0i	-5.75e01 + 0.0i	
-1.03e04 + 0.0i	-1.0e02 + 0.0i	
	-2.0e-01 + 0.0i	
	-2.87e02 + 0.0i	

Table 5.2: Response parameters used for OSN1B BHZ

Zeros	Poles	Sensitivity
0.00 + 0.00i	-5.90e-03 - 5.90e-03i	-3.65e+10
0.00 + 0.0i	-5.90e-03 + 5.90e-03i	
1.47e02 + 0.0i	-7.32e01 + 3.76e01i	
0.00 + 0.00i	-7.32e01 - 3.76e01i	

Table 5.3: Response parameters used for OSN1B BH1

Zeros	Poles	Sensitivity
0.00 + 0.00i	-5.90e-03 - 5.90e-03i	-3.67e+10
0.00 + 0.0i	-5.90e-03 + 5.90e-03i	
1.47e02 + 0.0i	-7.32e01 + 3.76e01i	
0.00 + 0.00i	-7.32e01 - 3.76e01i	

Table 5.4: Response parameters used for OSN1B BH2

Zeros	Poles	Sensitivity
0.00 + 0.00i	-5.90e-03 - 5.90e-03i	-3.66e+10
0.00 + 0.0i	-5.90e-03 + 5.90e-03i	
1.47e02 + 0.0i	-7.32e01 + 3.76e01i	
0.00 + 0.00i	-7.32e01 - 3.76e01i	

6 Melt evolution beneath Axial Volcano imaged with Seafloor Compliance data

1 Abstract

We present the first continuous observations of the evolution of the magmatic melt system beneath Axial Volcano. We analyzed data from December 2014 through May 2018 from two cabled broadband ocean-bottom seismometers with collocated absolute pressure sensors to estimate seafloor compliance as a function of both frequency and time. The April 2015 submarine eruption induced dramatic changes in shear structure that were primarily concentrated in the lower crust (deeper than 2.5 km). We propose that the nearly 20% drop in shear velocities in the lower crust following the eruption is not due to a significant change in melt fraction, but due to reorganization of melt within the lower crust. The absence of a signal on the eastern flank of the caldera indicates that the lower crustal melt pathway is relatively narrow in cross section ($<$1.2 km2) compared to the overlying melt chamber ($>$42 km2). The lower crustal melt must also be concentrated beneath the center or to the west of the surface caldera. We find that the melt chamber and the lower crust contain minimum melt fractions of 14% and 4%, respectively, though the true melt fractions may be significantly higher. Our images demonstrate the promise of using continuous data to understand submarine volcanism and crustal accretion processes.

2 Introduction

Axial Volcano is one of the most active submarine volcanoes in the world, with an eruption recurrence interval of 11-19 years over the past 470 years and three eruptions within the past twenty years (e.g., Clague et al., 2013, 2017). The recent installation of permanent cabled instruments on the volcano, combined with repeated campaign surveys, have led to tremendous advances in our understanding of volcanic and crustal accretion processes (e.g., Kelley et al., 2014; Wilcock et al., 2018). High-precision pressure and seafloor deformation measurements have provided constraints on the inflation of the system, successfully forecast the 2015 eruption, and should help to predict future eruptions (e.g., Nooner and Chadwick, 2009, 2016; Sasagawa

et al., 2016).

Recent experiments have produced detailed images of the internal compressional velocity (Vp) structure of the volcano and provided constraints on the melt content and distribution within a relatively large melt reservoir (West et al., 2001; Arnulf et al., 2014b, 2018). Improved mapping of shear velocities (Vs), which are highly sensitive to fluids and other low-velocity zones (LVZs), is required to further constrain the three-dimensional extent of the plumbing system. In addition, the role of the lower crust, proposed to extend to 11 km beneath the volcano summit (West et al., 2003), remains the focus of intense debate. Evidence is emerging that a substantial fraction of melt crystallization beneath ridge axes occurs in the lower crust (Wanless and Shaw, 2012), and melt sills have now been imaged beneath the primary melt chamber of several spreading centers (e.g., Nedimovic et al., 2005; Canales et al., 2009; Becel et al., 2015). To date, the lower crust beneath Axial has proven difficult to image, and our knowledge of the temporal evolution of the volcano has been limited to occasional campaign measurements.

3 Data

In this study, we present new observations of continuously-evolving melt structure in the melt chamber and lower crust. The Ocean Observatories Initiative (OOI) Cabled Array includes two sites with a broadband seismometer and a collocated pressure sensor (Fig 6.1). The sites are separated by 3.2 kilometers, and both contain Güralp CMG-1T broadband seismometers with a nominal roll-off at 360 seconds and an ocean-bottom absolute pressure recorder (NANO-BPR). Here we present results from the analysis of 42 months of continuous 1 sps data between December 1st, 2014 and May 1st, 2018.

Normalized seafloor compliance is defined as the transfer function between seafloor displacement and pressure, multiplied by the wavelength of the infragravity forcing wave (Crawford et al., 1991). Infragravity waves propagate through the deep oceans with periods longer than 30

seconds and amplitudes on the order of centimeters. These waves are the dominant source of energy recorded by ocean-bottom seismometers and pressure sensors between microseism and tidal frequencies (e.g., Webb, 1998). We computed compliance data using discrete three-hour continuous data segments beginning 01 December 2014 through 01 May 2018. To enhance our compliance signal, we first removed the estimated tidal signal from the absolute pressure gauges using the UTide package (Codiga, 2011). We also considered the effects of instrument tilt, which can cause high long-period noise on the vertical component (e.g., Crawford and Webb, 2000). We did not expect significant tilt at either site, as the sensors were installed on top of the basalt flows. Coupling to the bedrock in the form of several large sandbags surrounding the frame should provide a similar effect as burying sensors in sediment, which has been shown to significantly reduce tilt noise (Romanowicz et al., 2006; Duennebier and Sutton, 2007; Doran and Laske, 2016). Tilt noise is typically identified by high coherence between the vertical and horizontal components. While the overall effect from tilt is minimal, we observed a small signal on the north component of AXCC1, especially during the summer months. We removed tilt induced by this component, which improved the pressure - vertical acceleration (P - Z) coherence and increased the number of high-quality data segments by approximately 8%. We confirmed the orientation of the horizontal components of the two stations as North and East using the algorithm of Doran and Laske (2017), indicating that the tilt is primarily in the N/S direction. Following the method Filloux (1983) and Zha and Webb (2016), we also checked to ensure that the gain of the pressure sensors was accurate. The ratio of pressure to acceleration at long periods during passing Rayleigh waves should be equal to ρH, where H is the water depth and ρ is the density of the water. At both Axial sites this relationship holds for periods longer than approximately 20 seconds. We found correction coefficients of 0.92 ± 0.09 at AXCC1 and 0.95 ± 0.05 at AXEC2, indicating that the nominal gain is accurate to within the uncertainties.

To estimate our final compliance data as a function of frequency and time, we first selected all segments with a coherence in the infragravity band $\gamma^2 \geq 0.8$. This cutoff ensures

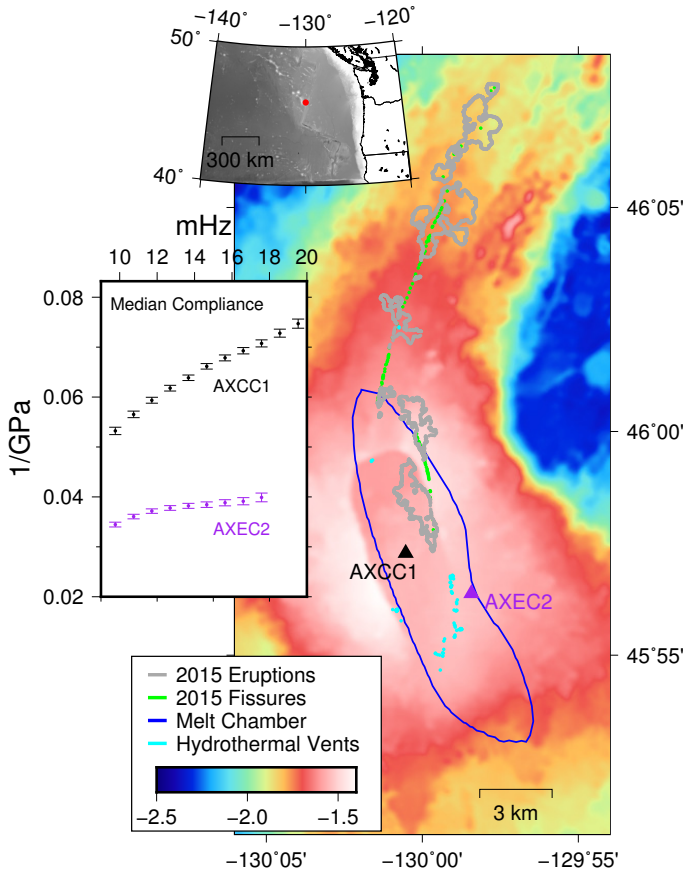

Figure 6.1: Bathymetric map of Axial seamount showing locations of the two broadband seismometers with collocated pressure gauges used to estimate compliance data in this study. Bathymetry data, the outline of the melt chamber (Arnulf et al., 2014b, 2018), and the coordinates of the 2015 fissures and mapped eruptions (Clague et al., 2017) can all be accessed at the Marine Geoscience Data Center: `http://www.marine-geo.org/`. The top inset map shows the study region with respect to North America. The inset plot shows the average compliance curves at both sites.

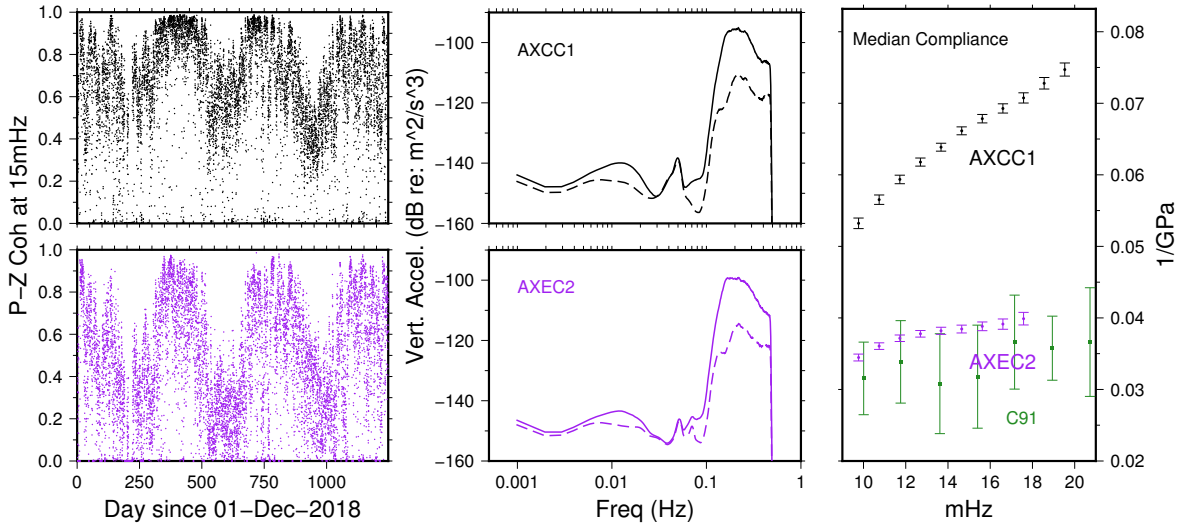

Figure 6.2: Coherence, spectra, and compliance at both AXCC1 (black) and AXEC2 (purple). Left panels: The raw coherence between the pressure and vertical acceleration signals at 15 mHz. Strong seasonal variations in the strength of infragravity waves causes the coherence between the signals to drastically decrease during the summer months. Weekly and bi-weekly variations are also clear, likely relating to ocean tides. Center panels: Median power spectra for vertical acceleration data. The solid line was computed for the winter of 2017 and the dashed line was computed for the summer of 2016. Strong seasonal variations are clear, especially in the infragravity and secondary microseism bands. Right panel: Median seafloor compliance computed using the entire data set. The green data show early compliance results from the west flank of Axial volcano presented by Crawford et al. (1991) for comparison.

that the signal is caused by infragravity waves, and has been shown to be a reliable limit to estimate compliance data without bias (Crawford and Singh, 2008; Zha and Webb, 2016). We also removed a small number of segments with high P - Z coherence in the noise notch (15 - 30 seconds). These segments are likely affected by earthquakes or other sources that obey different dispersion relationships than infragravity waves, and so could potentially corrupt our signal. We observed high P - Z coherence between 9 - 20 mHz at AXCC1 and between 9 - 18 mHz at AXEC2, consistent with the expected frequency range expected at 1500 meters depth (Crawford et al., 1991). Both sites lost between 50-100 3-hour segments due to data gaps. More significantly, the compliance signal was drastically diminished during the summer. Figure 6.2 shows the seasonal variation in P - Z coherence. While the effect was visible at both sites, it was stronger at AXEC2. Infragravity waves are considerably more energetic in the winter months in the northern hemisphere, and the northeast Pacific experiences the strongest season trends in infragravity power the world (Aucan and Ardhuin, 2013; Ardhuin et al., 2014). Without strong forcing waves, the compliance signal was no longer dominant for much of the summer months. Figure 6.2 also plots median spectra computed for Summer 2016 and Winter 2017. As expected, the infragravity power was nearly 10 dB lower in the summer. The secondary microseism, related to local storms, was also significantly diminished, while the primary microseism, related to distant storms (Webb et al., 1991), remained largely unaffected. The median compliance values calculated at both sites for the entire 41 month time period are also shown in Figure 6.2.

We estimated our compliance time series by computing one-week running medians of the individual measurements (Fig 6.3). We excluded any two-week intervals with less than 8 high-quality data segments (corresponding to 24 hours of recording). The uncertainty of each measurement at each frequency was taken as the 2σ uncertainty of the median. This yielded typical uncertainties of approximately 1% at both sites, but with typical fluctuations between 0.5% and 2.5% as a function of time and frequency. Uncertainties were lowest in the middle of the infragravity spectrum and highest at the lowest and highest frequencies, approaching max-

imums of 3% during certain time periods. Overall, the median uncertainty at AXEC2 (1.2%) was slightly higher than at AXCC1 (0.9%). Crawford and Singh (2008) demonstrated that an incorrect assumption regarding the source of the noise, originating from either the pressure or acceleration data, can bias the data. By directly estimating the uncertainty from the variance of the measurements, we avoid assuming one primary source of noise. At AXCC1, the compliance data were relatively stable before the eruption, and then rapidly increased following the eruption in April 2015. The compliance values stayed elevated for several weeks, and then slowly decreased, though not at a uniform rate. The changes in compliance were also dependent on frequency, with lower frequencies showing a significantly larger change. By the end of the time series considered, all frequencies were lower than before the eruption. At AXEC2, we observed far less variation in compliance values following the eruption, although some of the effect could have been missed by the significant data gaps. The overall variation in compliance was much smaller, and the frequency dependence of the changes was also diminished. The strong seasonality of the signal affected both sites, although the effect appeared stronger at AXEC2. Both time series also show some short-scale variations on the order of weeks, primarily at high frequencies.

4 Results

4.1 Occam Inversion

We began by attempting to model the median compliance curves. We used a layered one-dimensional code that assumes infinitely-long layers and uses the minor propagator vector method to forward model the data (Gomberg and Masters, 1988; Crawford et al., 1991). This technique has been found to bias results towards weaker velocity anomalies (meaning higher Vs values) in the presence of 2D or 3D structure (e.g., Latychev and Edwards, 2003; Iassonov and Crawford, 2008; Zha et al., 2014a), but remains the preferred way to analyze local structure due to the speed and simplicity of the algorithm. We will later discuss our attempts to quantify the

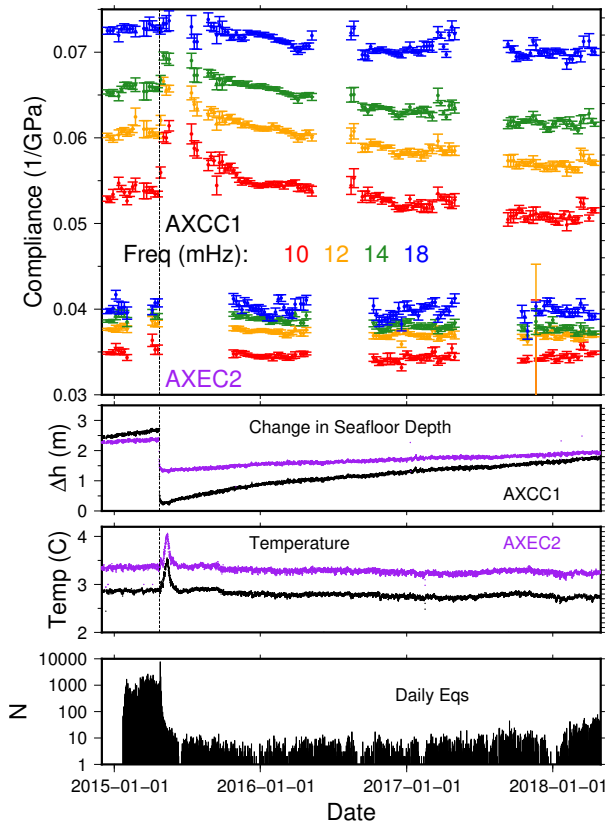

Figure 6.3: Compliance data at discrete frequencies as a function of time at both AXCC1 and AXEC2. The lower panels show the seafloor height and temperature recorded at each site, along with the daily number of recorded earthquakes. The vertical dotted line indicates the time of the April 2015 eruption.

effects of lateral structure.

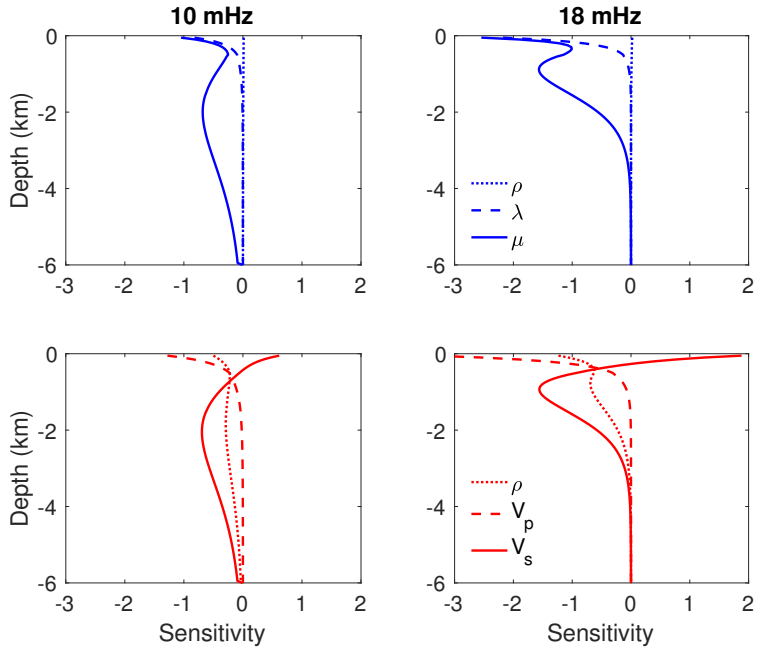

Figure 6.4: Sensitivity functions for compliance data at two frequencies. The top two panels show the sensitivity of the data to changes in density (ρ) and the two Lame parameters (λ and μ). The bottom two panels show the sensitivity of the data to changes in ρ and the two seismic velocities, Vp and Vs. In both cases, lower frequencies are sensitive to deeper structure. The starting model had a constant Vs of 2.0 km/s and the Vp profile shown in Figure 6.5.

Compliance data are primarily sensitive to crustal shear structure, although density and Vp can play a significant role in the uppermost crust (Fig. 6.4). Lower frequencies are sensitive to deeper structure, and our data are generally insensitive to structure below 6 km. We assumed no low-velocity pelagic sediments, which should be valid for spreading centers and simplifies the compliance modeling greatly, as uncertainties in the sediment layer often introduce significant ambiguity in compliance data (e.g., Doran and Laske, 2018). We first attempted an Occam minimum-structure inversion to investigate the requirements of the data in the absence of any *a priori* information (Constable et al., 1987). Instead of examining Vs, we instead inverted directly for shear modulus μ, which simplified the sensitivity of compliance data by essentially removing

the sensitivity to density (Crawford (2004); Fig. 6.4). We formulate the Occam inversion as seeking to minimize the functional

$$U = ||\partial^2 \mathbf{m}||^2 + \mu^{-1} \left(||\mathbf{Wd} - \mathbf{WF[m]}||^2 - \chi_*^2 \right) \tag{6.1}$$

where **m** is the model vector, **d** is the data vector, **W** is the data weighting matrix, **F[m]** is the forward functional, and ∂^2 is a smoothing matrix. The first term describes the roughness of the model and the second term describes the misfit, and the parameter μ controls the tradeoff between them. χ_*^2 is a target misfit that attempts to avoid overfitting the data. We defined a starting model with constant 50 meter layers. We set λ increasing from 0 to 93 GPa (roughly corresponding to a Vp profile increasing from 3.0 to 7.0 km/s) , and μ beginning at a constant value of 16.25 GPa. (Fig 6.5). We used the median compliance values and uncertainties derived from our compliance time series.

At AXCC1, an LVZ was not strictly required when regularizing with either the first or second derivative of the model roughness. A model with shear modulus increasing from 10 GPa at the surface to 35 GPa in the lower crust was sufficient to fit the data. However, median uncertainties calculated from two-week data segments potentially underestimate the uncertainty of the entire deployment. To continue exploring the model space, we again performed an Occam's inversion but with uncertainties reduced by a factor of three. In this instance, an LVZ was required beginning at 1.5 kilometers depth and with $\mu = 10$ GPa. Assuming a constant density of 2.6 g/cc, this yields a shear velocity of 1.96 km/s, in line with melt chambers imaged at other spreading centers using seafloor compliance data (e.g., Crawford and Webb, 2002). These depths are also consistent with studies of the melt chamber beneath Axial volcano (West et al., 2001; Arnulf et al., 2014b). At AXEC2, the median data similarly did not require a LVZ until the uncertainties are reduced by a factor of 2.5. In this case, a melt chamber began at 1.5 km depth with μ of 15 GPa. These data required higher μ throughout the crust than at AXCC1, particularly in the uppermost 1.5 km. This corresponds to significantly higher shear velocities in the chamber of

2.40 km/s, assuming the same density. In both cases, the top of the LVZ was identified by the Occam inversion, but the bottom may be smeared out over a wide depth range. Previous tests of synthetic data have also demonstrated this effect (Crawford, 2004).

We then generated a simplified forward model based on the results of the Occam inversions (Figure 6.6). The median Vp profiles presented by Arnulf et al. (2018) for inside and outside the region containing the melt chamber are shown for comparison. As observed in the Occam inversion, we required a faster upper crust at AXEC2 to fit the compliance data, but we assumed identical structure as the AXCC1 at depths greater than 1.5km. We included a discontinuity under the melt chamber since a bottom reflector was identified in the active study of Arnulf et al. (2018). We attempted to introduce a thin, low-velocity melt lens of 50 meters in the model, but found that compliance data are insensitive to very thin layers, even those with very low shear velocity, a conclusion shared by previous investigations (e.g., Zha et al., 2014a). Since a thin, ultra-low velocity lens was not presented by Arnulf et al. (2018) or required by our data, we did not include one in our 1D profile. We also tested if the existence of a second low shear velocity zone was compatible with our data, as presented at other spreading centers (e.g., Crawford and Webb, 2002). Because of the inherent tradeoffs between the thickness and velocity of a layer, the magnitude and location of a deep LVZ could not be uniquely determined. We therefore decided to solve for a mean velocity of the entire lower crust beneath the melt chamber, acknowledging that this may hide small-scale variations. We set the total crustal thickness to be 11 km, as found by Arnulf et al. (2018). However, compliance data cannot resolve structure this deep, and thus cannot constrain changes in crustal thickness. It is worth reiterating here that 1D compliance inversions have been found to bias results towards lower anomalies, meaning higher shear velocities. This implies that our results should be interpreted as upper estimates, and the melt chamber and lower crust may have individual layers or an entire average Vs that is lower than we present here.

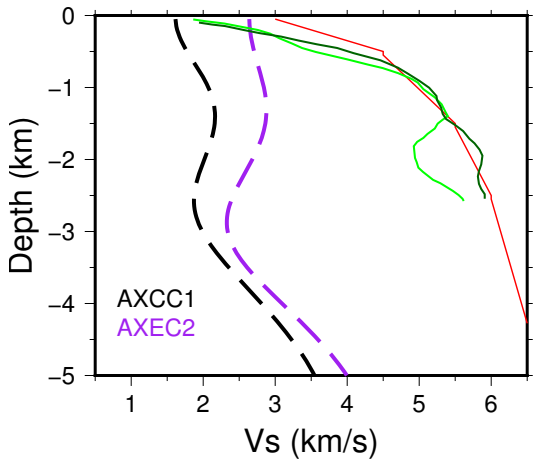

Figure 6.5: Results of an Occam minimum-structure inversion using median data at both sites. The starting model for Vp is shown in red, and the starting Vs profile was constant at 2.0 km/s. The median Vp profiles for inside and outside the region containing the melt chamber from Arnulf et al. (2018) are shown for reference.

4.2 Bayes Inversion

We used our preferred 1D models at both sites (shown in Figure 6.6) to investigate the changes in crustal structure through time required by the compliance data. We set up a constrained minimization inversion following the method of Jackson and Matsu'ura (1985) and Crawford (2004). In this formulation, we minimize the functional:

$$U = ||\mathbf{W}_m\mathbf{m} - \mathbf{W}_m\mathbf{m}_{a\ priori}||^2 + \mu^{-1}\left(||\mathbf{Wd} - \mathbf{WF[m]}||^2 - \chi_*^2\right) \tag{6.2}$$

where $\mathbf{m}_{a\ priori}$ and $\mathbf{W}_m$ are the *a priori* parameter estimates and *a priori* uncertainties, respectively. As before, the right term is a measure of the model misfit, whereas the left term is a measure of deviation from the *a priori* information. This nonlinear inversion is iterative, and proceeds until the desired misfit is achieved. We stopped the inversion after 10 iterations if the misfit failed to converge to 1.0.

We inverted weekly medians of the compliance data. For the first week of data, we set the prior estimates to correspond with our preferred 1D starting model. The inversion then finds the model with acceptable misfit with the minimum deviation from this model. For each

subsequent week, we redefined the prior model as the resulting model from the week before. In this way the inversion only adopts changes to crustal structure required by the new data, and acts as a sort of damping factor. We allowed only two parameters to vary in our model: Vs in the melt chamber and Vs in the lower crust. We defined the melt chamber as the region of high melt fraction between 1.5 and 2.5 km, and the lower crust to be all structure deeper than 2.5 km. Examination of the sensitivity functions of the Bayesian inversion demonstrate that changes to the melt chamber affect all frequencies, with the largest effects at middle frequencies, while changes to the lower crust affect the lowest frequencies the most and have very little influence on the highest frequencies. We did not expect the size of the melt chamber to change significantly, as the volume of erupted melt in 2015 has been estimated to be on the order of 1% of the melt stored in the system (Nooner and Chadwick, 2016). We also did not expect the depth of the melt chamber to drastically change, as the depth of the chamber is thought to be controlled by the local freezing depth of melt (e.g., Phipps Morgan and Chen, 1993). Forward modeling confirmed that our compliance data are insensitive to small changes in the size of these layers.

The results for AXCC1 are shown in Figure 6.6. We see systematic changes in the shear velocity of both the lower crust and the melt chamber. The most dramatic changes occurred in the lower crust. This confirmed our initial impressions, as the largest changes to the compliance data were at the lowest frequencies. Before the eruption, shear velocity was relatively constant at approximately 2.95 km/s, and then rapidly dropped to 2.45 km/s over the course of several weeks following the eruption. Shear velocity in the lower crust eventually recovered to pre-eruption values by May 2018. The variations in the melt chamber had smaller amplitude than the lower crust, and also show a different trend. The velocities were constant at 1.6 km/s before the eruption, slightly dipped immediately following the eruption, and then began to gradually increase. The shear velocity ended at 1.8 km/s, 12.5% higher than the pre-eruption value. The primary source of misfit came from unmodeled fluctuations at the highest frequencies ($f \geq$16mHz). We attempted an inversion with higher *a priori* uncertainties, but observed no

decrease in misfit. Variations in the uppermost crust could relate to the extensive hydrothermal venting has been mapped around Axial seamount (e.g., Butterfield et al., 1990; Embly et al., 1990; Chadwick et al., 2001, 2013). Hydrothermal circulation has been observed to cause significant localized impact on the velocity structure of the uppermost crust up to depths of 1000 meters and deeper in very young crust (Marjanovic et al., 2017), and it has been proposed that interaction with the axial melt lens (or a convecting lower crust) is a primary driver of hydrothermal venting (Singh et al., 2006; Fontaine et al., 2017). In a separate inversion, we allowed the uppermost crustal velocities to vary. Almost no difference was observed in the shear velocities of the melt chamber and lower crust, but the velocity of the uppermost crust varied on the order of 5%. The velocities were greatest following the eruption, remaining approximately 4% above the starting value for 60 weeks, but fluctuations on the order of 1% occurred throughout the time series. This decreased the misfit such that 85% of the data segments were fit within a misfit of 1.0. There is a tradeoff between the thickness and strength of the variations, but nonetheless this suggests that hydrothermal circulation may play a continuous role in the velocities of the uppermost crust

We observed very different trends at AXEC2 (Fig 6.6). Before the eruption, the melt chamber shear velocity was 2.25 km/s, while the shear velocity in the lower crust is 3.0 km/s. In May 2018, shear velocity in the lower crust was 3.1 km/s and shear velocity in the melt chamber was 2.28 km/s. There is some evidence that the velocities in the lower crust increased slightly following the eruption, and that the velocities in the melt chamber slightly decreased following the eruption. Vs in the melt chamber then appears to have risen by approximately 8% over the remainder of the time period considered. These would be an opposite trend from AXCC2, but we are hesitant to infer significant temporal trends in either layer at this site due to the higher scatter compared to the potential trend. We used a starting model with higher Vp and Vs in the uppermost crust, as required in the Occam inversion. We attempted starting models with a slower upper crust, similar to that presented by Arnulf et al. (2018), but were unable to to adequately

fit the data. We also attempted starting models without a low-velocity zone, but it made no statistical difference in the resulting models. We are therefore confident that the melt chamber is present under this site, although with lower melt amounts, as represented by the higher shear velocity and will be discussed later. When we tried another inversion with the uppermost crust allowed to vary, again the resulting shear velocities in the crust were very similar. However, the inversion preferred consistently higher near-surface velocities. Since we are already assuming faster velocities than found by Arnulf et al. (2018), we maintained our inversion at AXEC2 without variations in the uppermost crust.

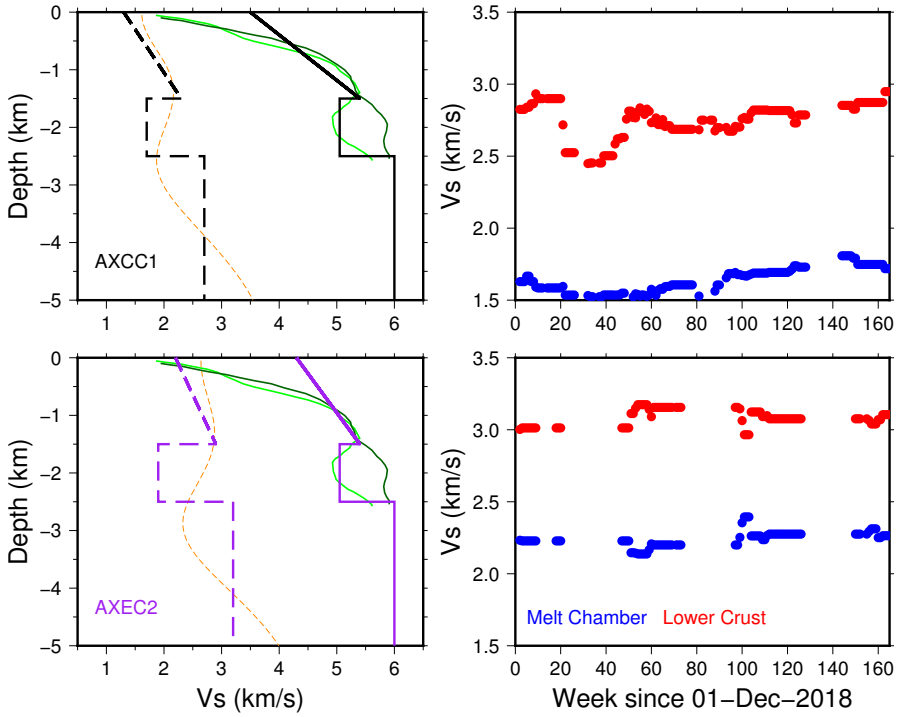

Figure 6.6: Results from the Bayesian inversion for shear velocity in the melt chamber and lower crust at AXCC1 and AXEC2. The left panels show the starting 1D velocity models used in the inversions. Solid lines represent Vp and dashed lines represent Vs. The orange lines show the result from the Occam inversion for shear velocity with depth at each site (see text for details). The green lines represent the mean Vp models inside the melt chamber (light green) and outside the melt chamber (dark green) presented by Arnulf et al. (2018). The right panels show the inverted shear velocity for each week of data in both the melt chamber and lower crust.

5 Discussion

5.1 Constraints on 2D geometry

Even with significant *a priori* information, 1D interpretations of seafloor compliance data may lead to smaller anomalies (meaning higher velocities) than those required by strong 2D or 3D structure (e.g., Iassonov and Crawford, 2008). In order to investigate and quantify the effects of laterally variable structure on compliance data, we used the semi-analytic 2D solution of Hulme et al. (2005). The method considers a cylinder with constant density, Vp, and Vs, buried at a depth z_c with radius r_c. The cylinder is buried in an infinite half-space, also with constant ρ, Vp, and Vs. The algorithm computes compliance as a function of frequency and geographic offset.

In our first test, we approximated the melt chamber as a cylinder with a radius of 500 meters centered at a depth of 1500 meters below the seafloor. We used a background half-space with basalt properties listed in Table 6.1, and chamber properties of Vp = 5.0, Vs = 1.6, and ρ = 2.6. We reran the model with the chamber velocity increased to 1.8 km/s, as modeled by our 1D code, and examined the change in compliance as a function of frequency and horizontal offset (Fig. 6.7a). As expected, both high and low frequencies are affected by changes in Vs in the melt chamber. Notice that the amplitude of the changes are small (on the order of 1-2%), but these may be minimum estimates, as the true crustal structure cannot be modeled with this simple model. The tests also show that changes in the melt chamber will affect only local (within 2-3 km) compliance data. It is possible that the changes sensed at AXCC1 are independent of those at AXEC2, although if the structural changes occurred between the sites, we would expect them to be visible at both stations. We also investigated the response to changes in the lower crust. We used the same background half-space model, but used lower crustal properties of Vp = 6.0, Vs = 2.35, and ρ = 2.6. We centered the anomaly at 3500 meters depth and assumed a radius of 500 meters (Fig. 6.7b). As expected, the changes are primarily visible at lower

frequencies. However, the effects are sensed to a much larger offset, particularly for the lowest frequency data. Figure 6.7c plots a map view of the 10 mHz curve of Figure 6.7b. The changes are centered approximately one kilometer southwest of AXCC1, in the same location as the preferred point source deformation location of Nooner and Chadwick (2016).

Table 6.1: Material properties used in modeling of melt fractions and geometry for two-phase medium. Basalt properties from Johnston and Christensen (1997), basaltic melt properties from Mainprice (1997).

Material	ρ (kg/m^3)	Vp (m/s)	Vs (m/s)
Basalt	2971	6400	3500
Basaltic Melt	2700	2350	0

5.2 Melt Constraints

In our modeling of melt we assumed a two phase medium with properties listed in Table 6.1. These values were chosen to be consistent with the modeling of Arnulf et al. (2018) and allow a direct comparison of melt results. The shear velocities throughout the crust are relatively constant at AXCC1 in the six months before the eruption. Using the relationship between porosity and shear velocity given by Dvorkin (2008) and the parameters listed in Table 6.1, we estimate 29% melt in the upper melt chamber (corresponding to Vs=1.62) and 8-9% melt in the lower crust (corresponding to Vs=2.85) before the eruption. These values are consistent with the average melt fractions presented by Arnulf et al. (2018). At AXEC2, we estimate melt fractions of 13-14% in the melt chamber (corresponding to Vs=2.24) and 0.6 - 0.7% in the lower crust (corresponding to Vs=3.15).

We then used the formulation of Schmeling et al. (2012) to investigate the amount of allowable melt as a function of melt geometry. We computed the apparent shear velocity due to spheroidal inclusions with aspect ratios between 1:1 and 1:100. We considered two end-member cases, where the melt pockets were either completely isolated or completely connected. The

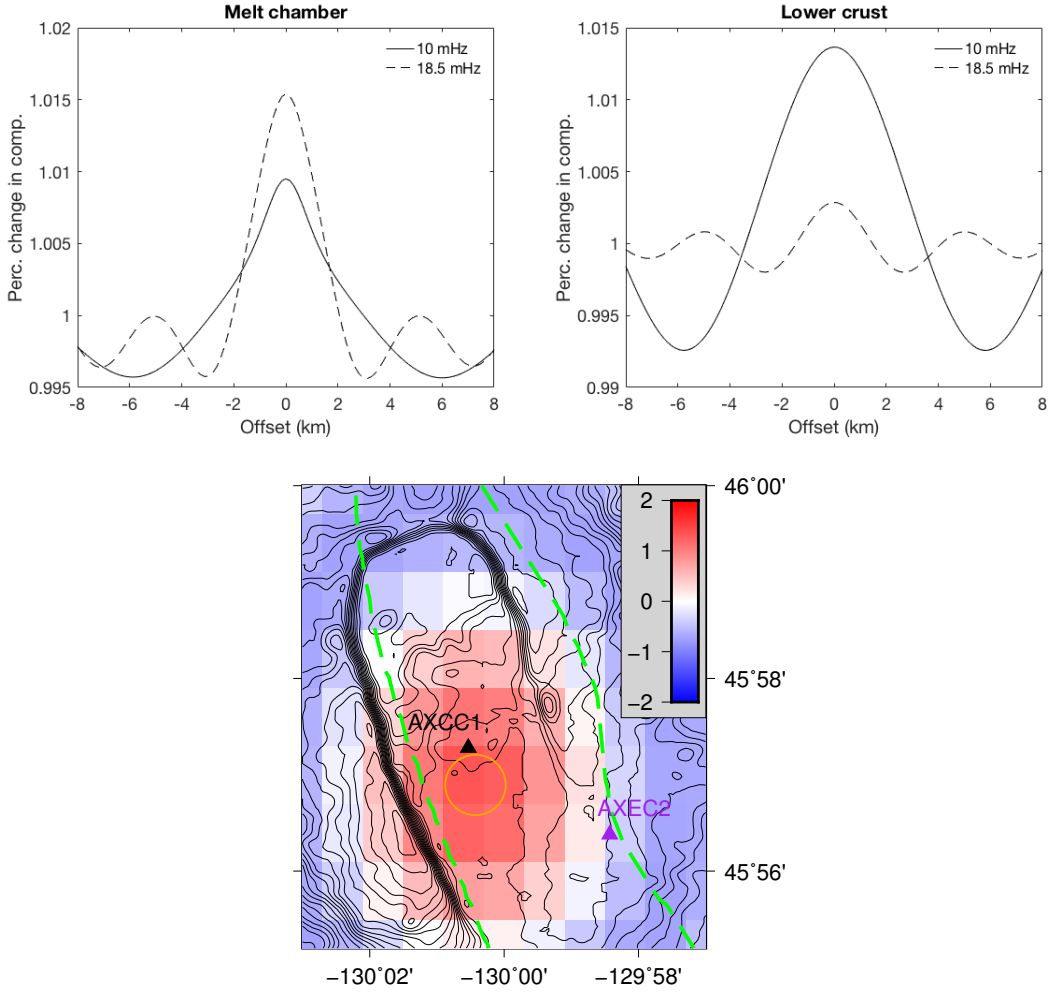

Figure 6.7: Two-dimensional effects of the inferred changes in the melt chamber and the lower crust computed using the semi-analytic solution of Hulme et al. (2005). The top left panel shows the change in compliance data as a function of frequency and horizontal offset for a change in the melt chamber, simulated by a cylinder of radius 500 meters buried at a depth of 2000 meters. Velocity and density values are discussed in the text. The top right panel shows the change in compliance data as a function of frequency and horizontal offset for a change in the the lower crust, simulated by a cylinder of radius 500 meters buried at a depth of 3500 meters. The bottom panel shows a map view of the expected lateral affects on the compliance data (plotted as a percent change) from the structural change described in the top right panel at 10 mHz. We center the effect just southwest of AXCC1, approximately the same location as the preferred point source deformation location from Nooner and Chadwick (2016).

results are shown in Figure 6.8. Using pre-eruption Vs values of 1.6 km/s in the melt chamber and 2.85 km/s in the lower crust at AXCC1, we see that the melt fraction in the melt chamber can be as high as 46% if the melt is concentrated in isolated, spherical inclusions. Increasing the aspect ratio or the connectivity of the melt reduces the amount of melt allowable in the system. The maximum allowable melt in the lower crust is 30%. At AXEC2, assuming shear velocities of 2.25 and 3.15 in the melt chamber and lower crust, respectively, yields maximum melt percentages of 35% and 11%. This may reflect lower melt fractions on at the edge of the melt chamber, or could reflect lateral changes in melt geometry.

The Vp results of Arnulf et al. (2018) allow us to put additional constraints on the geometry and amount of melt. We performed a grid search to find the melt fraction and geometry that fits our pre-eruption velocities (we assume Vp=5.0 km/s in the melt chamber and Vp=6.0 in the lower crust; see Fig 6.6). At AXCC1, this yields a preferred geometry of 14% melt of connected inclusions with average aspect ratios of approximately 1:10 in the melt chamber. This is a significantly lower melt fraction than inferred by studies of compressional velocity alone (Arnulf et al., 2014b, 2018). However, as discussed previously, our compliance data put an upper bound on shear velocity, and therefore may underestimate the amount of melt in the system. This may also reflect strong lateral heterogeneities in the amount of crustal melt. Additional measurements would be needed to constrain the shear velocity of the entire chamber. In the lower crust, the best fit geometry yields of approximately 4% with isolated inclusions with aspect ratios of 1:50. This number is in agreement with the estimate presented by Arnulf et al. (2018), and suggests that the melt geometry of the lower crust may be significantly different than the melt chamber.

5.3 Evolution of the Crust

Our results at first appear counter-intuitive. As the lower crust replenishes between eruptions and the chamber inflates following the model of Nooner and Chadwick (2016), melt fraction should increase and Vs should decrease. However, we see the opposite signal. Vs imme-

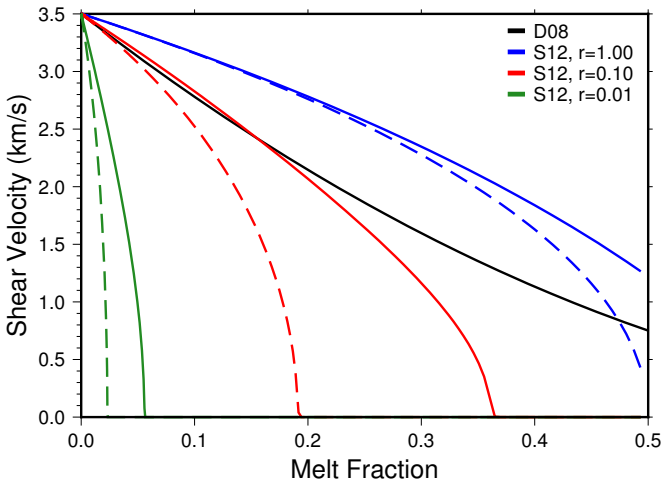

Figure 6.8: Apparent shear velocity as a function of melt fraction and geometry. D08 refers to the relationship of Dvorkin (2008), which relates porosity to velocity without accounting for melt geometry. The three colored lines, calculated using the equations of Schmeling et al. (2012), assume spheroidal inclusions with aspect ratios of 1:1, 1:10, and 1:100. The solid lines represent the effect of completely isolated melt inclusions, while the dashed lines represent completely connected melt inclusions.

diately drops after the eruption, and then increases over time, indicating that melt is leaving the system. We therefore cannot model the changes in shear velocity as simply due to changes in melt fraction. Elevated temperatures likely contributed ≈10% of the observed signal. The maximum temperature of the chamber or lower crust is determined by the liquidus temperature, $T_L = 19.1$ MgO% + 1054 C (Sinton and Detrick, 1992). Chadwick et al. (2016) measured MgO concentrations of approximately 8.0% in eruptions above the caldera, leading to a maximum temperature of 1207 K (Chadwick et al. (2016) calculate eruption temperatures between 1178 - 1201 C using the relationship of Sugawara (2000)). We assumed temperature gradients of $\partial \ln V_s / \partial T$ between -0.78 and -2.07 %/100K (Sobolev et al., 1996). Chen and Lin (2004) presented numerical results for the thermal structure of an intermediate spreading center with elevated mantle temperatures influenced by a local hot-spot, which approximates the geologic context at Axial very well (e.g., Hooft and Detrick, 1995). Considering a similar thermal structure as presented by Figure 4(c) of Chen and Lin (2004), we calculate negligible change in Vs due to thermal effects in the melt chamber and find that no more than 10% of the Vs drop in the

lower crust can plausibly be explained by a temperature increase.

We propose that the drop in Vs reflects the emplacement of melt sills in the lower crust (Fig. 6.9). The addition of only 1-2% of highly-connected melt in high aspect-ratio (100:1 or greater) geometries is sufficient to explain the decrease in Vs. Sudden drops and subsequent recovery of Vs have been observed following a number of large earthquakes (e.g., Brenguier et al., 2008; Wu et al., 2016) and eruptions (e.g., Brenguier et al., 2016) in continental crust. As argued by Schaff and Beroza (2004), transient stresses can open fluid-saturated cracks, leading to temporary or permanent reductions in Vp and / or Vs. Cannata (2012) invoked a similar mechanism to explain sudden decreases in Vs following the eruption of a subaerial volcano. However, the strength of the signal reported here is an order of magnitude greater than most previous observations.

We attribute the subsequent rise in Vs following sill emplacement to melt freezing. Vs in the lower crust returned to pre-eruption values after three years, allowing an estimation of an average cooling rate in the lower crust. As given by Turcotte and Schubert (2002), the time for a dike to solidify from both sides as

$$t_s = \frac{b^2}{4\kappa\lambda_2^2} \tag{6.3}$$

where b is the dike thickness, κ is the thermal diffusivity of basalt, and λ_2 is a function of the specific heat of basalt, the latent heat of fusion, and the temperature difference between the melt and the ambient country rock. We find that assuming $\kappa = 1$ mm^2/s, L=400 kJ / kg, c = 1 kJ / kg K, and an ambient temperature difference of 50 C, a sill of 1.1 m thickness would completely freeze after three years. Increasing the temperature difference allows for thicker sill formation. If the sills formed with an aspect ratio of 100:1, a central melt pathway of 300 - 400 meters would be consistent with our observations. Higher aspect-ratios would generate larger Vs differences and thus require less total melt to produce our observations. A denser sampling of compliance data would allow more refined estimates on the total volume of melt emplaced in

the lower crust following surficial eruptions. Delayed peaks in the Vs progression, for example in early 2016, may indicate sill emplacement between eruptions.

The absence of a signal on the eastern flank of the caldera places strict constraints on the spatial scale of lower crustal activity. Compliance data at low frequencies (10 mHz) sample structure within several kilometers of the site (Fig. 6.7c). The entire region of deformation, including the emplaced sills, is therefore likely no larger than 600 meters. A central melt pathway as narrow as 300 - 400 meters thick, as suggested by Nooner and Chadwick (2016), would explain the signal so long as it is concentrated in the center or to the west of the caldera. However, we cannot rule out a more complex, non-vertical pathway for the melt plumbing system beneath the melt chamber. We are hesitant to infer melt content outside of the caldera, although the Vs inferred at AXEC2 suggest 2% or more melt given the same geometries. This may reflect the influence of large off-axis melt sills, as imaged beneath the Juan de Fuca ridge by Canales et al. (2009). Additional compliance sites would be able to more precisely constrain the lateral extent of the lower crustal deformation.

The fluctuations in Vs within the melt chamber suggest a different response than inferred in the lower crust. Vs in the melt chamber appears to peak between eruptions, potentially indicating an inflection point in the eruptive cycle. The immediate response of the melt chamber to the eruption is more subdued than the lower crust, which may be expected for a melt system with vastly more material than erupted in any individual event. The sampling radius of the highest frequencies suggests that the effects are diffuse and may take place on the scale of several kilometers. Changes beneath the central caldera would be unable to induce the signal observed under the eastern flank, and we therefore infer that changes in melt geometry are distributed throughout the melt chamber.

The distribution of stations prevents us from quantifying lateral movement of melt if the flow is primarily in the north-south direction. Since the most recent eruption propagated northward (Chadwick et al., 2016), it is possible that we are observing the replenishing of the

northern segment of the melt chamber sourced from the center of the caldera. If the entire signal were due to the northward movement of melt and no changes in geometry, we would infer a cross-sectional flux velocity of 0.04 km2 / yr for a total leading to a 3 - 5% drop in melt fraction. As this would sum to less than the 0.148 km3 of material erupted in 2015 (Chadwick et al., 2016), lateral melt movement may comprise a significant portion of the observed signal. In this case, the decrease in Vs observed at the end of the time series may be indicative of melt re-entering the melt chamber from the central conduit in the lower crust.

6 Preliminary Conclusions

In this study, we analyzed seafloor compliance data to image the evolution of the melt structure at Axial Volcano. The melt chamber and the lower crust show dramatically different responses following the April 2015 eruption. Our data show the lower crust responded instantly following the 2015 eruption. We are able to place lower bounds on the fraction of melt in the melt chamber and lower crust at 14% and 4%, respectively. Our inverted results for Vs as a function of time are consistent with the introduction of high-aspect ratio pure melt sills into the lower crust following the eruption, and then a subsequent freezing of melt. We found that the lower crustal melt system must be concentrated in a relatively thin region directly beneath or to the west of the caldera. We have demonstrated that continuous broadband measurements are capable of characterizing melt evolution throughout the crust.

7 Acknowledgements

We use a Python implementation of the UTides program written by Wesley Bowman, accessible at `https://github.com/wesleybowman/UTide`. The seismic data used in this study are publicly available and were accessed from IRIS DMC using the ObsPy library (Krischer

et al., 2015). Seafloor pressure and temperature data are available from the OOI data portal. Figures in this chapter were created using Generic Mapping Tools (GMT; Wessel et al. (2013)). We thank Bill Chadwick for providing locations of mapped hydrothermal vents. We thank Tom Hulme for providing 2D analytic software. We thank Javier Escartń, Paul Johnson, Jean-Arthur Olive, Donna Blackman, Yuri Fialko, and Alistair Harding for stimulating conversations. We thank Adrien Arnulf for providing data and helpful ideas. We thank Matt J. Cook for assistance throughout this project. A.K.D. was partially supported by the Chateaubriand Fellowship.

I was the primary investigator and author of Chapter 6, which is currently in preparation for journal submission. This work was undertaken in collaboration with Wayne Crawford at IPGP.

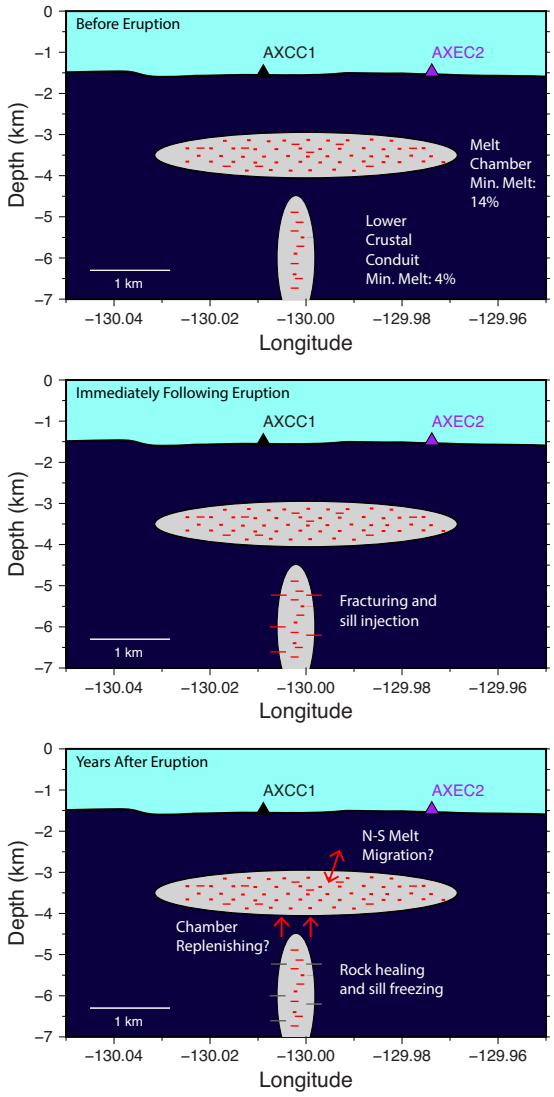

Figure 6.9: Schematic of melt evolution in the melt chamber and lower crust. (a) Before the eruption, we identify a melt chamber between 1.5 and 2.5 km beneath the seafloor with a minimum melt fraction of 14% and a lower crustal chamber with a minimum melt fraction of 4%. (b) Immediately following the eruption, we observe the injection of small (1 meter thick, 100+ meters long) melt sills in the lower crust that drastically lower Vs in this region. (c) After several years, the melts sills in the lower crust have frozen. Changes in the melt chamber suggest that replenishment from the lower crust could be ongoing or north - south migration of melt may have occurred.

7 Conclusions & Future Directions

1 Conclusion

Throughout this thesis, I have used broadband ocean-bottom seismic data to study the structure and heterogeneity of the oceanic crust. I have focused on several regions of the Pacific, namely the Hawaiian Swell and offshore of the west coast of North America. The primary tool I used to accomplish this was seafloor compliance data, although other observations were incorporated as well.

In order to address uncertainty related to the geographic orientation of ocean-bottom seismometers, I developed an automated algorithm to measure surface wave arrival angles and statistically analyze the results of many earthquakes to determine the orientation of the horizontal seismometer components. The results compared favorably with other measurement techniques, including the manual, high-accuracy method of Laske et al. (1994). I used the method to compute the orientations of the 200+ instruments deployed during the Cascadia Initiative. An important by-product of the results was the ability to compare data quality as a function of water depth and instrument design. Deep-water, shielded SIO instruments appeared to produce higher signal-to-noise ratio data than other designs. This software package is now available online, and has been used by numerous researchers to efficiently calculate the instrument orientations.

I then used seafloor compliance data and sedimentary converted phase information to characterize the seismic structure of the sediments and uppermost oceanic crust surrounding the Hawaiian islands using data from PLUME (Laske et al., 2009). I produced maps of sedimentary thickness and shear velocity as a function of depth. Thick ($\geq$1500 meters), high-velocity (Vs$\geq$2000 m/s), volcanic sediments are present immediately adjacent to the islands, which taper out to pelagic sediments approximately 100 meters thick far from the islands. I also showed that the uppermost crystalline crust may vary on the order of $\pm$5% in the abyssal plains. These results will be useful for improving the accuracy of deeper images aiming to investigate the source and scale of the Hawaiian plume.

I analyzed Rayleigh wave dispersion data between 5 and 24 seconds measured from ambient noise correlations in order to extend these results into the lower crust and uppermost mantle. Initial results indicate that the uppermost mantle may exhibit variations in shear velocity on the order of several percent. The most concentrated region of low velocities is immediately to the north and east of Hawaii. I interpreted these results in the context of thermal anomalies and the presence of partial melt. Our results are broadly consistent with those of Laske et al. (2011), who inferred several percent melt in the lithosphere and temperature anomalies of approximately 200 °C.

I then explored seafloor compliance at buried seafloor sites. These sites produced significantly quieter data than typical ocean-bottom seismometer deployments, and allowed the investigation of horizontal seafloor compliance. These data measure the horizontal deformation of the seafloor induced by infragravity waves (as opposed to vertical motion, which is typically studied in seafloor compliance analyses). I demonstrated that combining vertical and horizontal seafloor compliance can improve constraints on sedimentary and crustal structure, but I was inhibited from implementing these techniques due to issues with instrument response and data availability. However, the technique holds promise for future low-noise seafloor installations.

Finally, I used a unique cabled array to investigate changes in crustal structure over time beneath Axial Volcano on the Juan de Fuca Ridge. Analyzing 3+ years of continuous data that spanned a submarine eruption, I was able to show that the lower crust reacted instantly to the eruption, and that the ensuing drop and slow recovery of shear velocities are opposite the expected signal from the replenishment of melt observed by other researchers. I constrained the two dimensional size of the lower crustal melt chamber and provided minimum constraints on the amount of melt in the entire system.

2 Prospects for future study

A number of the projects begun during this thesis present clear opportunities for continued research. The most obvious topic would be to continue probing the Hawaiian hotspot. With new constraints on sedimentary and crustal structure of the Hawaiian Swell, data sensitive to deeper structure could be reanalyzed. Ideally, dispersion data (including short-, intermediate-, and long-period measurements), receiver functions, and body waves could be jointly inverted to identify the path of the plume through the mantle. Heat-flow, gravity, and electromagnetic data sensitive to deep structure could also be combined into one analysis. Such research could also shed light on the mechanism generating the Hawaiian Swell, which remains fiercely debated.

Another possibility will be to examine heterogeneity of the sediments and crust at a larger scale. I have made preliminary calculations of seafloor compliance using OBS data from ALBACORE (Kohler et al., 2010, 2011), Cascadia (Toomey et al., 2014), and NoMelt (Lin et al., 2016), in addition to PLUME. The experiments span deep abyssal plains as well as the continental shelf. Strong variations in compliance values are observed (Fig. 7.1), indicative of lateral structural variations. This work could be expanded to include projects in the Atlantic ocean (e.g., ENAM; Van Avendonk et al. (2014)) or Indian ocean (e.g., Rhum-Rum; Barruol and Sigloch (2013)) to investigate global differences in sedimentary structure.

The research at Axial Volcano provides another promising avenue. The instruments, deployed as part of the Ocean Observatories Initiative, are still collecting data, and should continue to do so through the next eruption, predicted to occur in approximately 2021. Compliance data could capture the full cycle of the eruption, and investigate how the lower crust contributes to crustal accretion. As OBS deployments increase in quantity and duration, compliance data promise to be a useful way to investigate changes in structure through time.

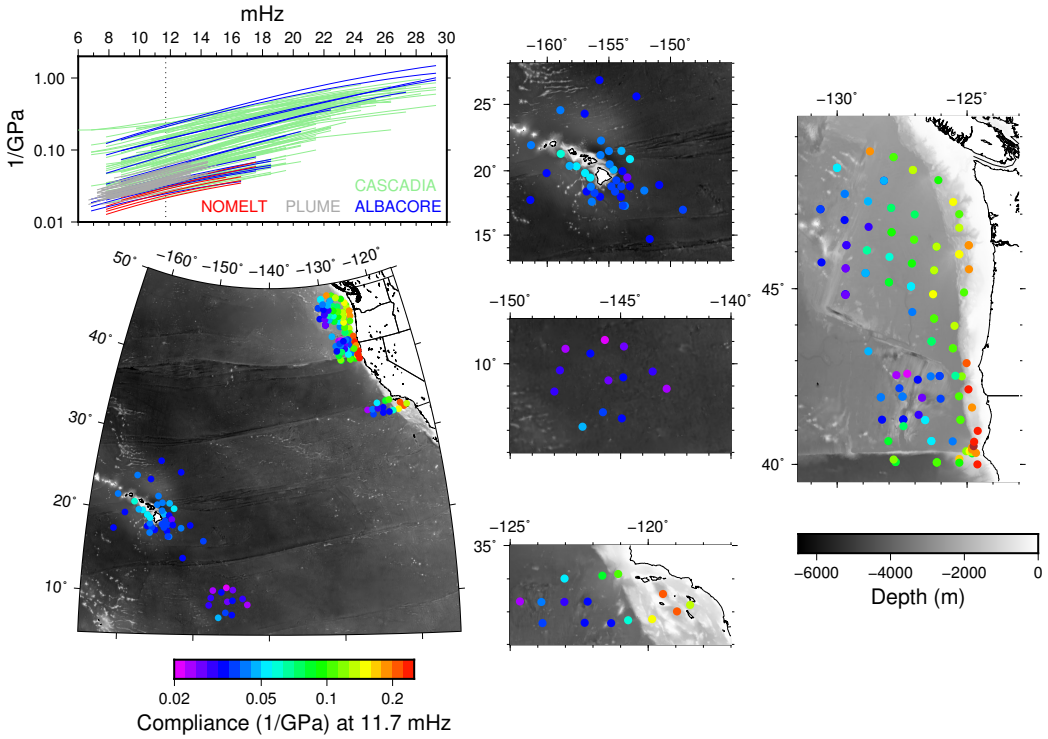

Figure 7.1: A map of compliance data using OBS data collected across the central and eastern Pacific.

A Experiments in the California Borderland

1 Background

The California Borderland is a complex geologic regime characterized by a series of submarine peaks and troughs that stretches several hundred kilometers to the west offshore southern California (Fig. A.1). The environment is currently thought to be a transpressional regime, but significant evidence exists to suggest the area was once a subduction zone in which the Farallon plate subducted under southern North America (Legg et al., 2015; Reeves et al., 2015). Although recent OBS deployments (e.g., Kohler et al., 2010, 2011) have allowed improved large-scale imaging of the region (e.g., Bowden et al., 2016), significant uncertainty remains regarding recent tectonic activity. Seismicity maps and seismic velocity profiles compiled by the Southern California Earthquake Center (SCEC) are generally limited in the Borderland and very poorly constrained in the outer Borderland and the abyssal plain west of the Patton Escarpment (e.g., Astiz and Shearer, 2000), in large part due to limited instrumentation.

During initial investigations of OBS data collected from the abyssal plains west of the California Borderland as part of the ADDOSS deployments (Berger et al., 2016), we noted inconsistencies between estimates of sediment properties from borehole measurements (Yeats and Others, 1989) and preliminary modeling of seafloor compliance measurements. We therefore successfully competed for ship time in 2015 and conducted an experiment in order to detect local seismicity and improve constraints on near-surface structure. We repeated the experiment in 2018, with the additional goal of improving the calibration of the instrument response of the differential pressure gauges (DPGs) included in the OBS packages. Seafloor compliance data rely on accurate response information, and DPGs are known to vary on an individual basis from the nominal response in both the gain and frequency roll-off. The location of all instruments can be found in Tables A.1 and A.2 and in Figure A.1.

2 Cruise & Instrumentation Details

Our first experiment consisted of five sites in the abyssal plain immediately west of the Patton Escarpment, a steep shelf which marks the end of the California Borderland. The three-day deployment occurred in August 2015 and the three-day recovery occurred in November 2015, with both cruises aboard the R/V R. G. Sproul. In addition to UC Ship Funds, we received funding from the Paul. G. Silver Young Scholar Research Enhancement Award, UCSD, and the ADDOSS project. We deployed five instruments, with details in Table A.1. Our second experiment consisted of five broadband seismometers deployed in the San Clemente Basin. The two-day deployment occurred in June 2018 and the two-day recovery occurred in October 2018, also aboard the R/V R. G. Sproul. The instruments are listed in Table A.2. Initial assessments indicated that these are rich datasets with a number of interesting phenomena recorded, including earthquakes at all scales (teleseismic, regional, local, and many not in any catalogs).

Table A.1: Patton Escarpment station info & instrumentation specifications. Note that the seismometer at site AKD1 and the hydrophone at site AKD 3 produced only noise.

Site	AKD 1	AKD 2	AKD 3	AKD 4	AKD 5
Latitude (°N)	32.5125	32.4585	32.5442	32.5976	32.5336
Longitude (°W)	120.5891	120.4737	120.4141	120.5254	120.4998
Depth (m)	3828	3821	3834	3813	3817
Seismometer	T-240	T-240	4x4 Flip	4x4 Flip	T-240 (ADDOSS)
Pressure sensor	DPG	DPG	Hydrophone	Hydrophone	DPG
Sampling rate (SPS)	50	50	200	200	50

Table A.2: San Clemente Basin station info & instrumentation specifications. Several experimentally determined parameters are also listed (see Section 6 for details).

Site	SCB 1	SCB 2	SCB 3	SCB 4	SCB 5
Latitude (°N)	32.5041	32.5362	32.5412	32.5216	32.5104
Longitude (°W)	118.1417	118.1164	118.1464	118.1615	118.1222
Depth (m)	1886	1904	1850	1704	1626
Seismometer	T-240	T-240	T-240	T-240	T-240
Pressure sensor	DPG	DPG	DPG	DPG	DPG
Sampling rate (SPS)	100	100	100	100	100
DPG Drop?	Yes	Yes	Yes	No	No
DPG gain	0.76	N/A	1.16	1.43	1.01
HN Orientation		N/A			
Epirical DPG pole	26.49	116.76	130.99	62.34	116.04

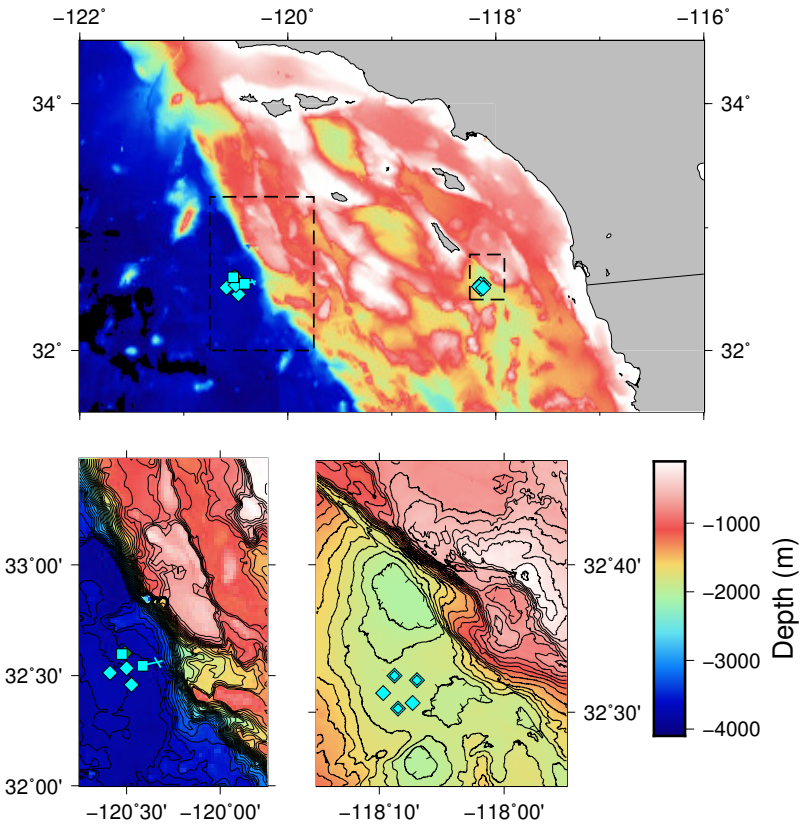

Figure A.1: Locations of OBSs deployed in the California Borderland during the AKD (western sites) and SCB (eastern sites) projects. The diamonds represent sites long-period (T-240) seismometers and DPGs, while sites with short-period (4.5 Hz) sensors and hydrophones. The SCB sites with double outlines indicate instruments. Site ADS3B, collected during an earlier deployment, is shown with a green diamond, and is almost collocated with the northernmost AKD site.

3 Modeling sedimentary structure

We computed preliminary compliance data at sites ADS3B and AKD2 (Fig A.2). The sites were situated in 3800 meters of water west of the Patton Escarpment within 15 km of each other. These data have not been corrected for additional acceleration terms (see Chapter 4) or for errors in the DPG instrument response, and therefore the final compliance values may differ slightly. Since instrument response issues can be specific to individual instruments, this may explain some of the discrepancy between the estimates at frequencies lower than approximately 9 mHz.

We began modeling the data from ADS3B by performing a simple grid search for best-fitting sediment thickness and shear velocity. We used a sedimentary layer with $\alpha = 2.0$ km/s and $\rho = 1.9$ g/cc placed above a half-space with typical oceanic crustal values of $\rho = 2.8$ g/cc, α=7.0 km/s, and β=4.0 km/s. Since sedimentary structure most strongly affects compliance at the highest frequencies, we at first only considered $0.015 < f < 0.02$ Hz. The minimum misfit occurred at a sediment thickness of 496 meters and $\bar{V}_S$=475 m/s, but a range of models fit the data within the errors. As observed with the Hawaiian PLUME data (see Chapter 4), a thinner, slower sedimentary layer can provide a similar fit to a thicker but faster layer. DSDP drill site 469 was drilled very close to site ADS3B and borehole logs detected 390 meters of sediment. This thickness would correspond with an average sedimentary shear velocity of $\approx$ 300 m/s. To resolve the ambiguity resulting from the tradeoff between velocity and thickness, we can include sedimentary Ps converted phases as done before. Figure A.3 shows the Ps delay time measured at AKD4, within 10 km of ADS3B. With a measured delay time of 1.4 and again assuming sediment thickness of 390 meters, we calculate $\bar{V}_S = 260$ m/s. While early results are promising, additional work remains to characterize the velocity structure of the sediments in the abyssal plains west of the Patton Escarpment.

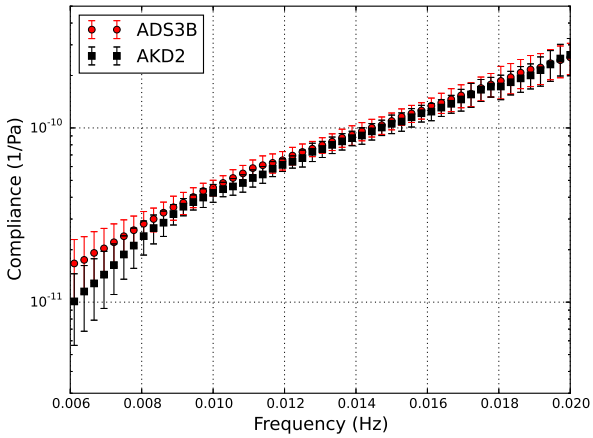

Figure A.2: Compliance values calculated for sites ADS3B and AKD2. Both sites lie in the abyssal plains west of the Patton Escarpment in 3800 meters of water, and are situated approximately 15 kilometers apart.

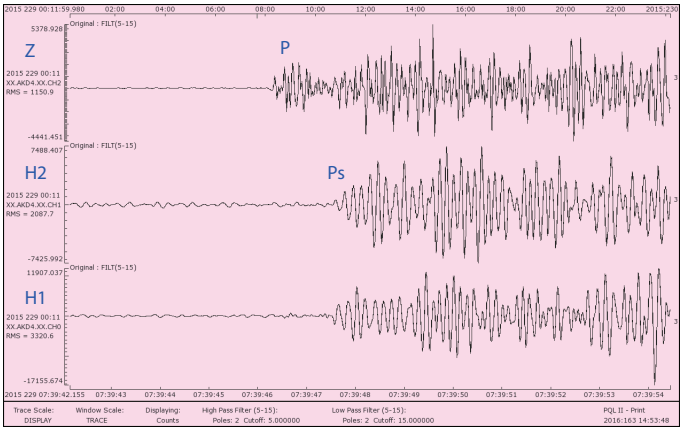

Figure A.3: Traces from AKD4 showing the $\approx$ 1.4 second delay. The top trace is the vertical component. The recorded event was M3.8 and occurred 270 kilometers away at 10 km depth (USGS event ID 37228879). The P arrival was chosen by visual inspection and is consistent with $V_p \approx 7.3$ km/s. The delayed arrival on H1 and H2 is theorized to be a Ps conversion at the sediment-bedrock interface.

4 Knudsen experiments

In order to provide an additional constraint on sedimentary properties, we utilized the Knudsen echosounder mounted on the hull of the R/V R. G. Sproul. Use of the Knudsen was unavailable during the SCB cruise due to instrument malfunction and unavailable during the recovery of the AKD instruments due to timing and inclement weather. Nevertheless, we collected useful data when possible. We attempted both the 3.5 kHz mode and the 12 kHz mode. Typically, lower frequency chirps are able to penetrate deeper into the sediments.

We were unable to resolve the sediment-bedrock interface in the region of the AKD OBS sites. However, we transited over several unusual seamounts, and we were able to see limited internal structure. Figures A.4 & A.4 show the returns while crossing a submarine seamount that appeared to be an active mud volcano (Fig. A.1). We have yet to interpret these data further, but internal structure is visible in both pairs of images and may highlight unexpected geologic formations at the transition between the Borderland and the abyssal plains.

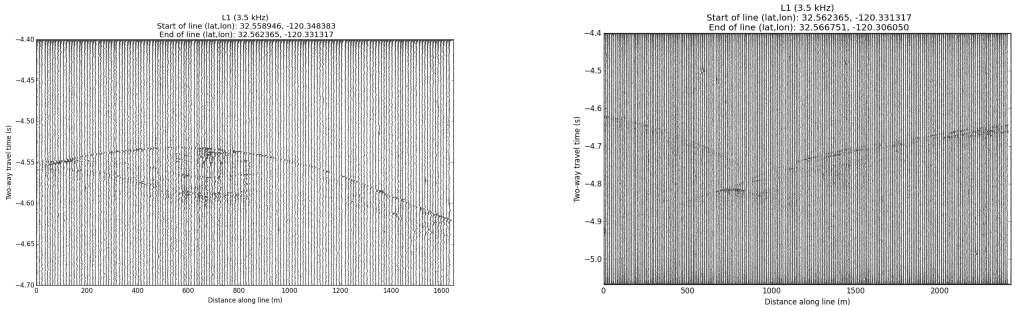

Figure A.4: A Knudsen line recorded with the 3.5 kHz transponder.

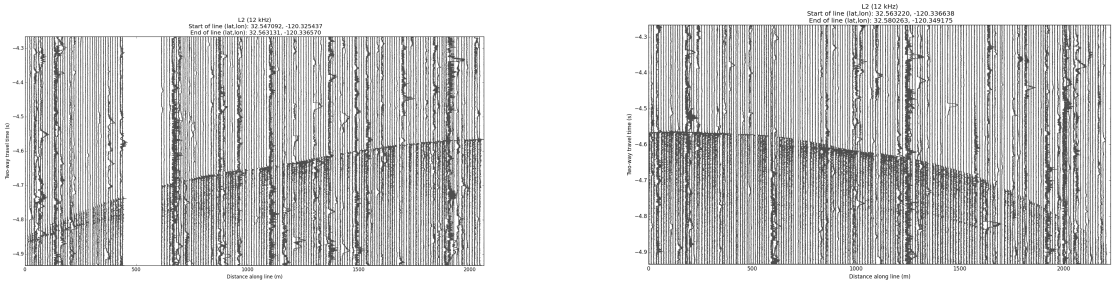

Figure A.5: A Knudsen line recorded with the 12 kHz transponder.

5 Whales

A surprising discovery within our data set was the recording of a great many whale calls. Marine mammals are now recognized to be one of the primary contributors to acoustic energy at frequencies above 10 Hz in the oceans (e.g., Wilcock et al., 2014). Identifying and tracking whales with seafloor pressure and seismic sensors is now relatively routine (e.g., Dunn and Hernandez, 2009; Wilcock, 2012; Soule and Wilcock, 2013), and offers a promising way to monitor these elusive creatures (Davis et al., 2017).

Following the references above, I attempted to identify species of whale and other mammals. I was able to positively identify blue and fin whales, which seem to produce the lowest frequency sounds and which our instruments (with sampling rates between 50 and 200 sps) can record. Figures A.6 and A.7 show some of these initial results. Additional research and instrumentation could provide a reliable means of tracking and monitoring these magnificent animals.

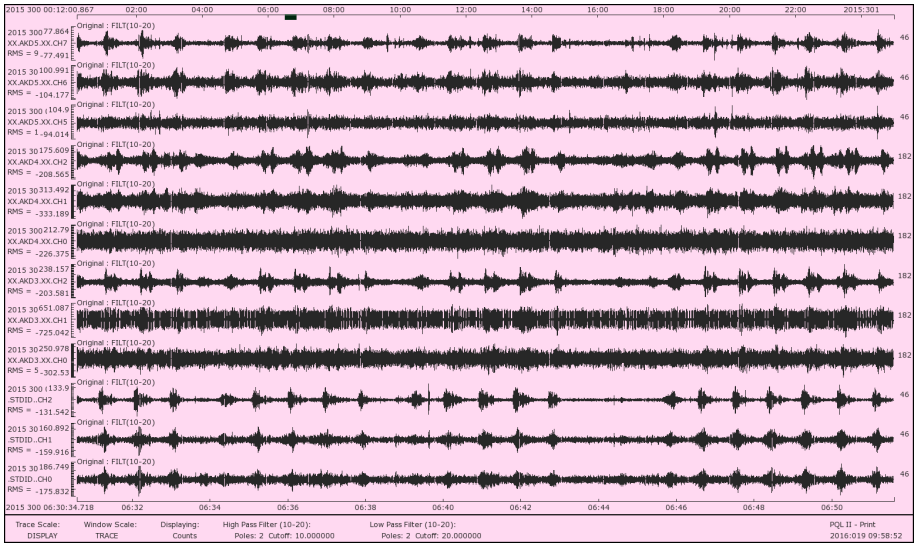

Figure A.6: Time series seismic data from four instruments during the AKD deployment. These data have been filtered between 10 and 20 Hz. The repeating whale calls can be seen approximately once per minute and were recorded on all working channels. Whales can typically be identified by the differing frequency content of the signals.

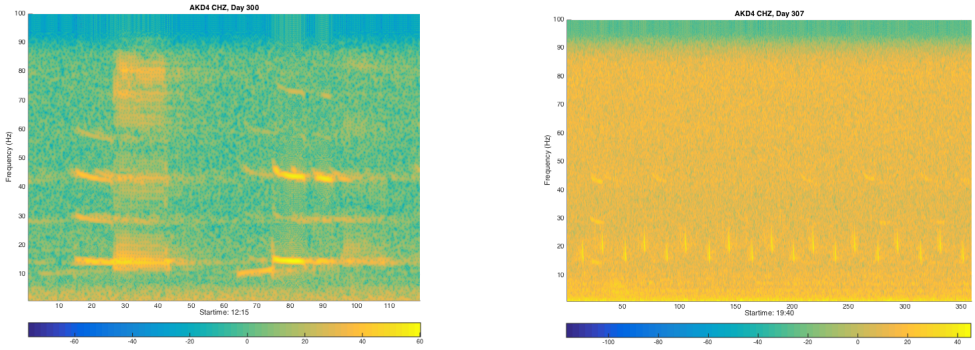

Figure A.7: High-frequency spectrograms showing the frequency content as a function of time of typical blue whale calls (left panel) and fin whale calls (right panel).

6 DPG experiment

Differential pressure gauges (DPGs) are commonly included in OBS instrument packages and provide useful measurements of seafloor pressure fluctuations that complement seismic studies. The limitation of these instruments at low frequencies is defined by the unknown thermal expansion in the confined oil (Cox et al., 1984). Modern SIO DPGs are typically characterized by the simple response listed in Table A.3, which is primarily defined by the instrument gain and the location of one pole near 79.57 seconds / radian. However, uncertainties in the long-period instrument response of DPGs have been a persistent impediment to analysis of these data. Individual instruments have been known to deviate from the nominal response in both gain and frequency roll-off.

As part of the SCB deployment, the OBS engineer Martin Rapa designed a device to drop the DPG by a pre-defined distance (3 inches, equivalent to 747.25 Pa of pressure in 4°C ocean water) several days after recording had begun on the seafloor. Photos of the design are shown in Figure A.8. Three instruments were equipped with the drop device (see Table A.2), and all performed as expected. The drop recorded at each site are shown in Figure A.9.

Zeros:	0 + 0i
Poles:	-0.012568 + 0i
Constant:	1144.440

Table A.3: Nominal poles and zeros for SIO DPGs

In this analysis I aimed to use tidal prediction models to correct the long-period response of DPGs, and then to compare these results with those obtained through the DPG drop calibration. As seen in Table A.3, only two variables can be adjusted in the DPG response function: the gain and the location of the pole. To individually calibrate the gains of the instruments, I followed the algorithm of Zha and Webb (2016), who analyze the transfer function between the DPG and the vertical seismometer component during Rayleigh waves (see the appendix of

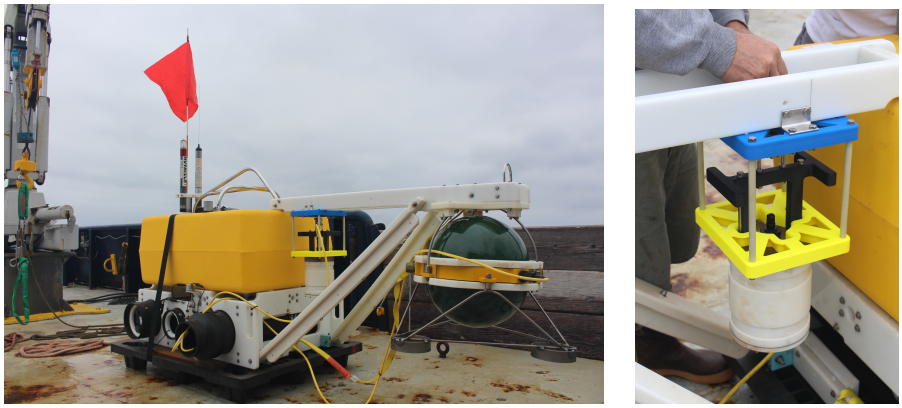

Figure A.8: Photos of the DPG drop mechanism. The left photo shows the location of the DPG drop on the OBS package, and the right photo shows a close up of the DPG during deployment, before the release..

Chapter 3 for more details). The results are shown in Table A.2. During this process, I noticed that the procedure did not produce the expected final spectrum for SCB3. I computed the acceleration spectra, and noticed that the seismometer gain at SCB3 was off by a factor of 2 (Fig. A.10)). I could not compute the calibration coefficient for SCB2 because the vertical component was not functional (Fig. A.11).

I computed two different spectral estimates for each site using data from the entire 3.5 month deployment in order to examine different parts of the spectrum. I computed mean hourly power spectra using data decimated to 1 sps, and I computed total spectra using all data decimated to 1/900 sps. These spectra, corrected for gain and nominal instrument response, are shown in Figure A.12a. In order to provide a reference for the expected spectral power at long periods, I used the OTPS software of Egbert and Erofeeva (2002) to calculate the predicted tidal amplitudes in the center of the array (118.1417 °W, 32.5041 °N). I included tidal constituents M2, S2, N2, K2, K1, O1, P1, Q1, Mm, and Mf. The resulting power spectra are included in Figure A.12a.

I performed a grid search to determine the pole value that produced the spectral values that best fit with the M2 tidal peak at approximately 12 hours. The results for this procedure, and the corrected spectra, are shown in Figure A.12b. Each instrument required a different

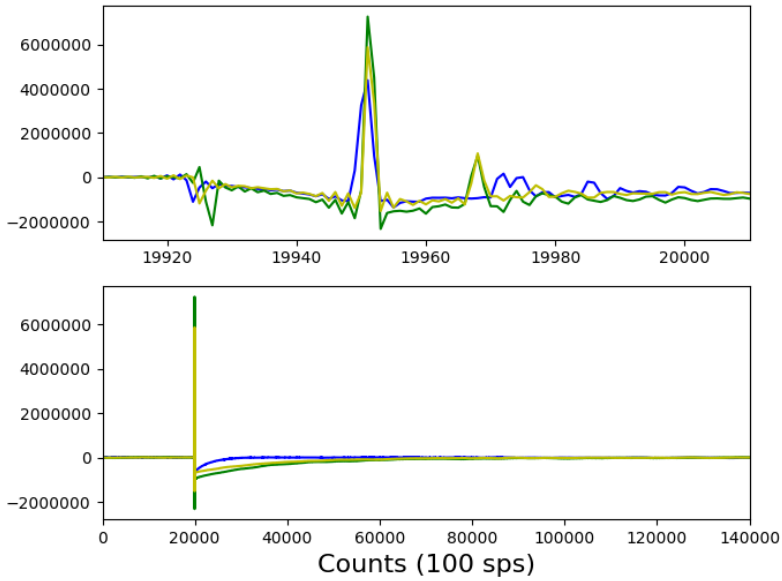

Figure A.9: Time series seismic data from DPGs with a drop mechanism (SCB1 in blue, SCB2 in yellow, SCB3 in green) aligned on the beginning of the drop data. The top panel is a zoomed in view of the bottom panel. The x-axis is labeled in counts. These instruments recorded at 100 sps, meaning that every 100 counts is equivalent to one second.

calibration factor, as expected. For most instruments, the values ranged between 60 and 130 seconds / radian. One instrument (SCB1) required a drastically lower pole value, and produced noisier spectra than all other instruments. For reference, John Collins measured the time constant of several instruments (personal communication, 2017). He found values of 100, 95, 95, 95, 95, 95, 90, 95, 27, 100, 90, and 120, and speculated that the 27 might come from a different-sized capillary. The SCB1 value of 26.5 may have a similar issue. For additional reference, Wayne Crawford at IPGP (personal communication, 2017) measured time constants on his OBSs of 55 and 72. Our measured values generally fall within these ranges, though demonstrate the variability possible between instruments.

I then examined the data produced during and after the DPG drop. Three instruments (SCB1, SCB2, SCB3) were equipped with a device that dropped the DPGs 3 inches (equivalent to 747.25 Pa of pressure in 4°C ocean water) during the deployment. The drops occurred ap-

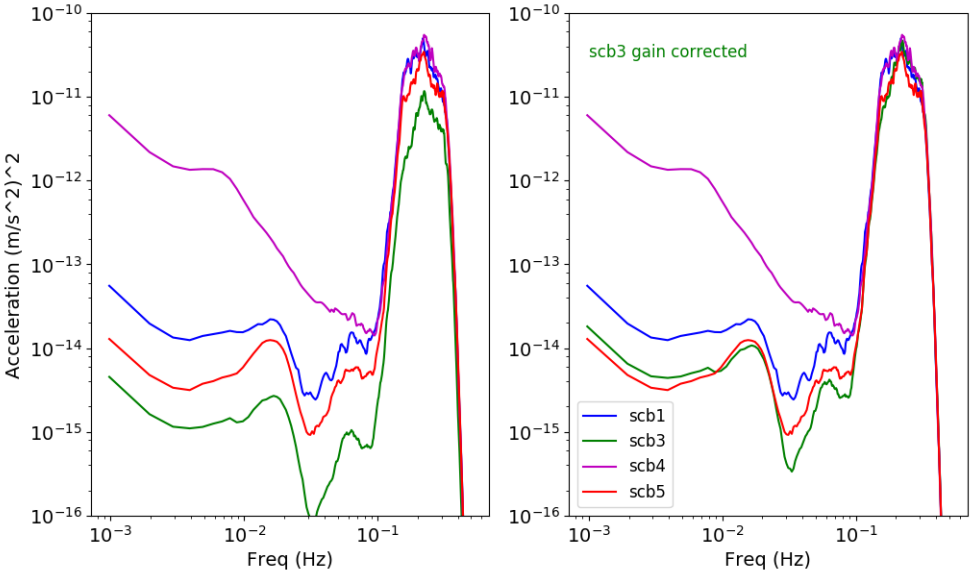

Figure A.10: Ambient vertical acceleration spectra at SCB sites (average hourly values). The raw data have been corrected for instrument response but not other effects including tilt. The original gain of the SCB3 seismometer appears to be off by a factor of 2.

proximately three days into the experiment. The experiments produced similar drop signals (Fig. A.9). However, the signal was opposite of the expected sign. After conferring with engineers Martin Rapa and Sean McPeak, we confirmed that the DPG polarity was opposite what we initially assumed. The system is set up so that an increase in pressure, corresponding to downward motion, is a negative signal. Examination of the signal produced when the instrument hit the seafloor and during the recording of a teleseismic earthquake provided further confirmation.

Assuming a linear time invariant system, the output of the system $y(t)$ is the convolution of the input $x(t)$ with the instrument response. Working in the frequency domain, we have

$$Y(\omega) = H(\omega) \cdot X(\omega) \tag{A.1}$$

where $H(\omega)$ is the complex Fourier transform of the instrument response. I modeled the drop as a step function, dropping 747.25 Pa instantly (subsequent modeling with a step function that occurred over one second did not appreciably change the results). I then convolved

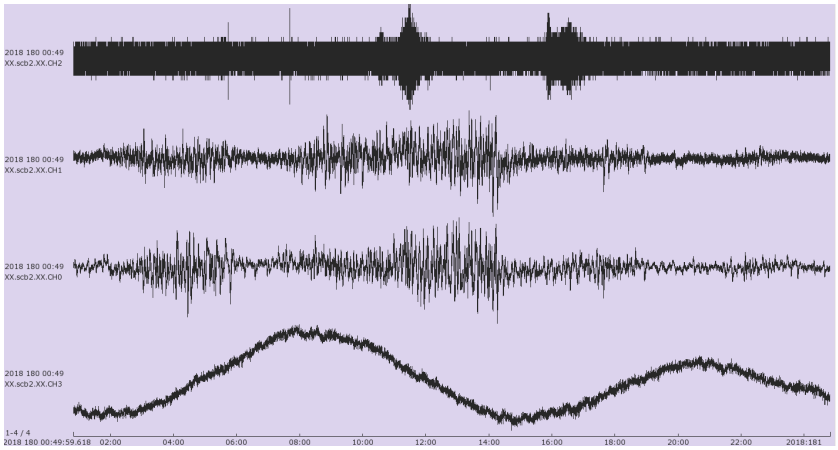

Figure A.11: Time series seismic data from SCB2 on 2018 day 180. The top trace shows vertical motion, the middle two traces show horizontal, and the bottom trace shows pressure.

the input with the nominal instrument response to obtain a predicted signal (Fig. A.13). In each case, the pole value found through the tidal modeling better fits the observed data than the nominal response. At SCB3, the drop indicates that the pole should be even lower, with better fits potentially obtained using pole values between 160 and 170 rad/sec. A zoomed in look at the drop (Fig. A.14) shows that there is still significant unmodeled signal. However, the drop appears to have largely verified the tidal calculations.

7 Acknowledgements

Appendix A contains details from two student-led cruises occurring in 2015 and 2018. I was the chief scientist on these cruises. This work was done in collaboration with Gabi Laske, Martin Rapa, and Jeff Babcock.

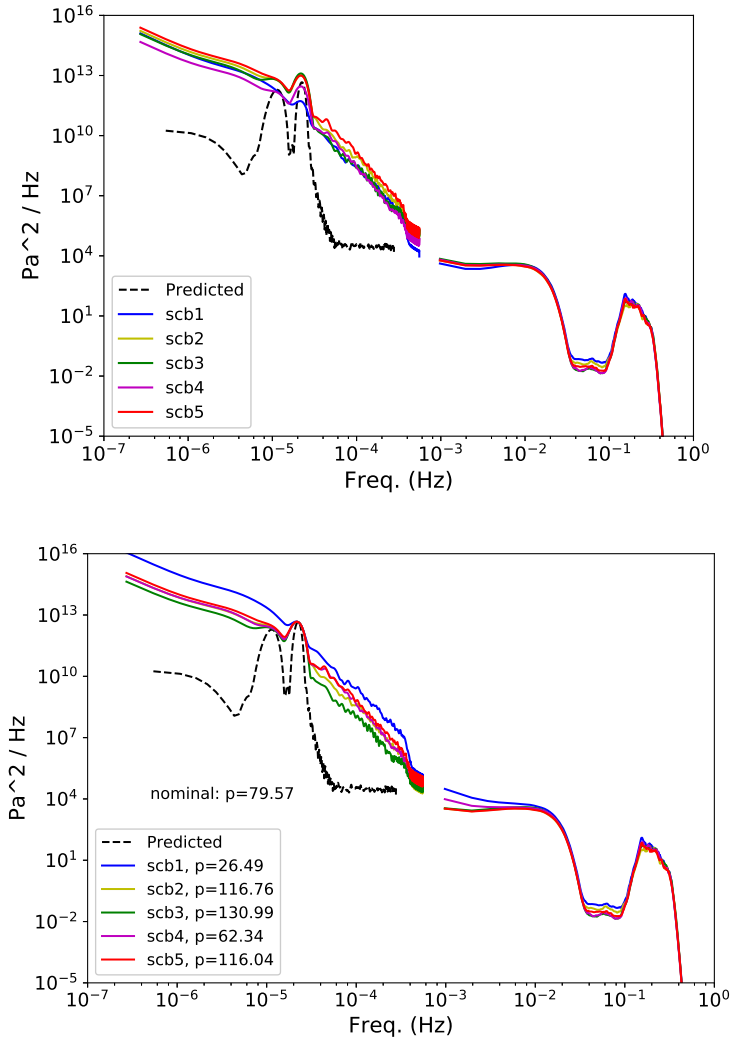

Figure A.12: Ambient pressure spectra at SCB sites. The prediction of Egbert and Erofeeva (2002) is included as the black dashed line. The data have been corrected for DPG gain and the nominal instrument response in the top panel, while the data have been corrected for DPG gain and variable pole values in the bottom panel.

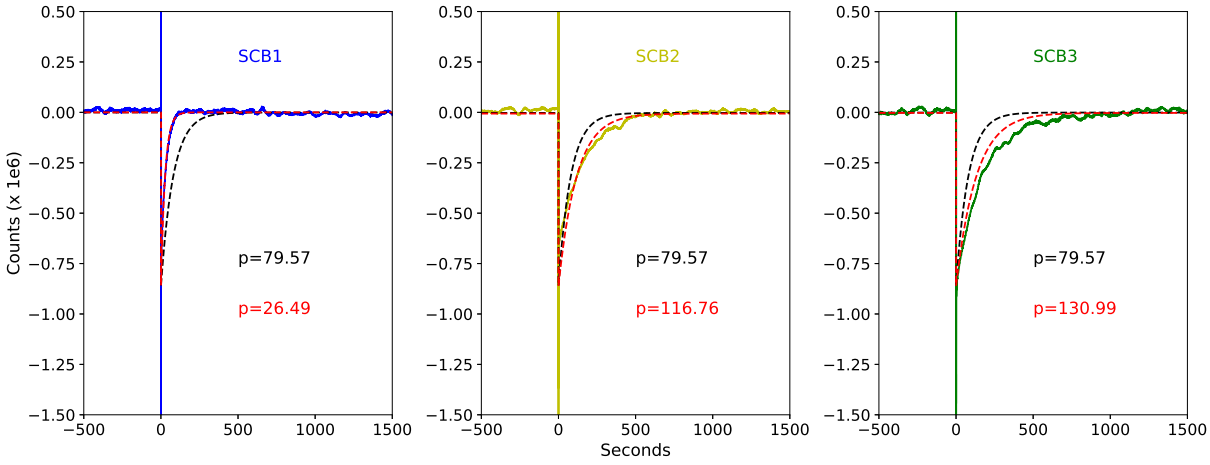

Figure A.13: The drop data from each DPG modeled as the response to a step function. The predicted responses from a step function using the nominal response and the tidal-corrected response are also shown.

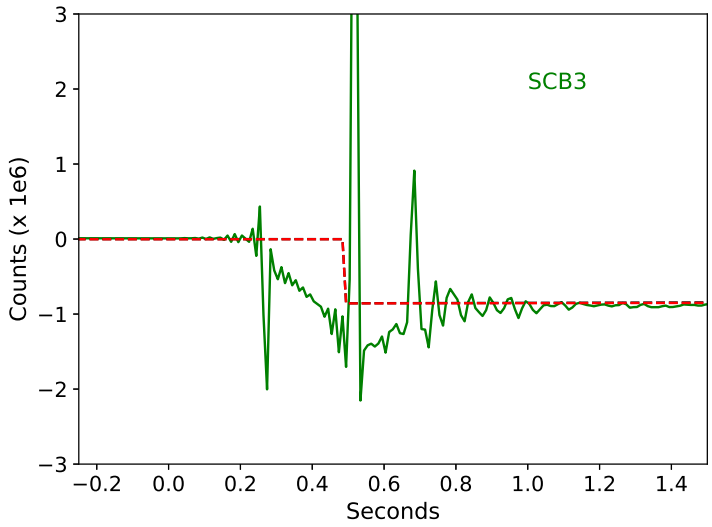

Figure A.14: Same as Figure A.13 but zoomed in to the 1.8 seconds surrounding the drop.

B Modeling Rayleigh wave azimuthal anisotropy on Glacier de la Plaine Morte, Switzerland

1 Overview

In 2016, a collaboration between IGPP / SIO and ETH Zurich began studying if 'ice-quakes', events caused by glacial fracturing or other processes that send seismic energy through a glacier, could be used to study the structure of an alpine glacier. The target glacier was Glacier de la Plaine Morte, situated in the Swiss Alps at approximately 2700 meters of elevation in the Valais region of southwestern Switzerland. This glacier was chosen because it is one of the largest in Europe and because the subglacial lake drains at the end of each summer, potentially flooding the towns below. It was hoped that seismic observations of the glacier itself and of the interactions between the ice and the glacial lakes could provide insight into the mechanics of this glacier.

I received funding from the Paul G. Silver Young Scholar Research Enhancement Award in order to help with the field campaign in the summer of 2016. Subsequently, I spent time modeling phase velocity data acquired from the glacial arrays. I first sought to understand the sensitivity of Rayleigh wave phase velocities at high frequencies (10-30 Hz) with elastic structure typical of an alpine glacier by calculating sensitivity functions for Vs, Vp, and ρ using the routines of Haney and Tsai (2017). I first tested a glacial half-space (Fig. B.1). As expected, phase velocities are most sensitive to Vs, though Vp and density (ρ) also play a role, particularly at shallow depths. 30 Hz data are insensitive to structure beneath 80 meters, while 10 Hz data are sensitive to structure down to 200 meters. I then included a basement layer at depths ranging from 50 to 100 meters. Phase velocity data are very sensitive to glacial thickness in this range, and sensitivity to ice and bedrock parameters are affected by the starting model. Notice that for 50 meters of ice, the 10 Hz data become primarily sensitive to basement structure.

I then attempted to model the measured phase velocity data with a formal inversion. At each site, we analyzed the fast and slow curves independently in order to explore the observed azimuthal anisotropy. One of the sites (A1) exhibited anisotropy primarily at high frequencies,

implying a shallow source, while the other (S2) showed anisotropy primarily at low frequencies, implying a deeper source. For formal inversions, I used the Dinver tool included in the Geopsy package (Sambridge, 1999a,b; Wathelet et al., 2008). This tool uses the Neighbourhood Algorithm to search the model space within a defined set of boundaries to produce a suite of models that fit the data to within a specified tolerance.

Beginning with data from A1, I sought a two-layer model consisting of unaltered ice and bedrock. An ice thickness of 100 meters was determined independently, and this was used as an initial constraint. Despite the sensitivities to Vp and density, I fixed these in the inversion to simplify the problem. I found that an average shear velocity of 1752 m/s produced the best fit to the data (Fig. B.2a). The best-fitting basement velocity was 2582 m/s, but was not well constrained since a wide range of velocity values produced similar data mifits. I then used this model as the starting model to fit the slow phase velocity but allowed a second ice layer on top. I set up a new inversion to vary this top layer Vs and thickness (Fig. B.2b). The best fitting model had a 40 meter thick ice layer with Vs=1620 m/s, corresponding to 7.8% anisotropy. Notice that a thinner, more anisotropic layer could also fit the data. Additional high-frequency information could better constrain this value. This top layer was inferred to correspond to crevasses in the glacier that were aligned with the direction of anisotropy. This was the first time that phase velocity values were used to map directionally-dependent structural features within a glacier.

The situation at A2 was more complicated since the anisotropy of deeper structure had no obvious physical mechanism. Note that the phase velocities at high frequencies were similar to the fast velocities at A1, indicating that the top of the glacier may have similar properties. In the inversion, I started with the fast A1 Vs model as the slow Vs model at A2. I kept the ice thickness fixed at 70 meters, again as indicated from an independent survey. The best-fit solution from the inversion indicated a slightly slower basement velocity of 2430 m/s. Repeated inversions with different parameter values returned similar values, indicating this velocity was in fact well constrained. To model the anisotropy, I allowed a lower, faster ice layer to vary in

Vs and thickness. The best fitting model had a 25 meter thick lower ice layer with Vs=2170 m/s, corresponding to 23.8% anisotropy. This value is potentially unrealistically fast for a lower ice layer, and so targeted forward modeling was explored to find alternative solutions to the data. While other solutions were found, a significantly faster lower layer was always required. The physical mechanism for this lower anisotropy remains a point of discussion.

Although the data are fit with the models presented here (Figure B.3), some discrepancies remained. First, although ice thickness was independently estimated from orthophotography, the data are better fit by a thinner glacier, between 90 and 100 meters thick at A1 and between 60 and 70 meters thick at A2. Utilizing a thinner glacier at A2 led to a smaller, more realistic set of fast layer values. Future analyses should include additional data, such as converted phases or H/V ratio information, to better constrain ice thickness and crevasse depth.

The resulting publication (Lindner et al., 2018) is included for reference.

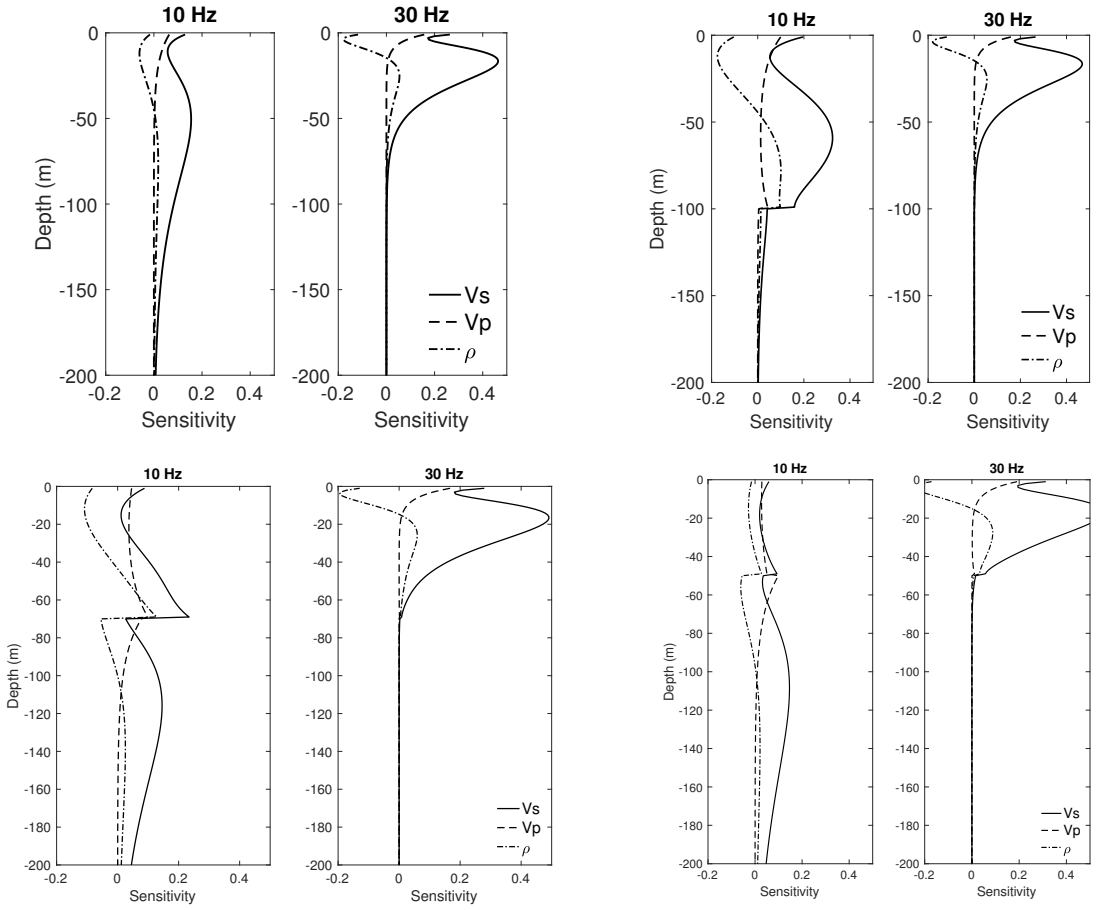

Figure B.1: Sensitivity kernels for Rayleigh wave phase velocity at 10 and 30 Hz. The starting model used in panel (a) consists of a half-space of ice, while the kernels shown in panels (b), (c), and (d) consist of ice over a half-space of karstic bedrock. The ice thicknesses shown are 100, 70, and 50 meters, respectively. The parameters for this model are summarized in Table 1 of Lindner et al. (2018).

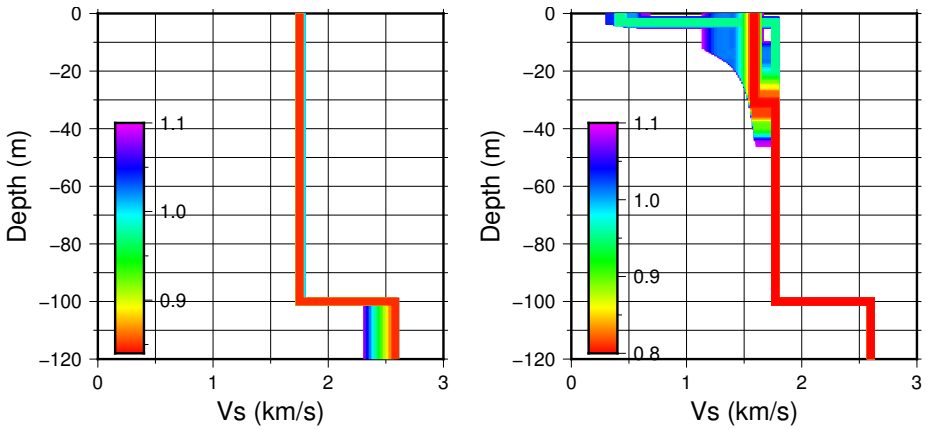

Figure B.2: (a) Inversion results for the fast curve at A1. The resulting models are colored by data misfit. Only Vs in the ice and in the basement were allowed to vary. (b) Inversion results for the slow curve at A1. The result for the fast curve at A1 was used as an input model. Only the thickness and shear velocity of a surface layer were allowed to vary.

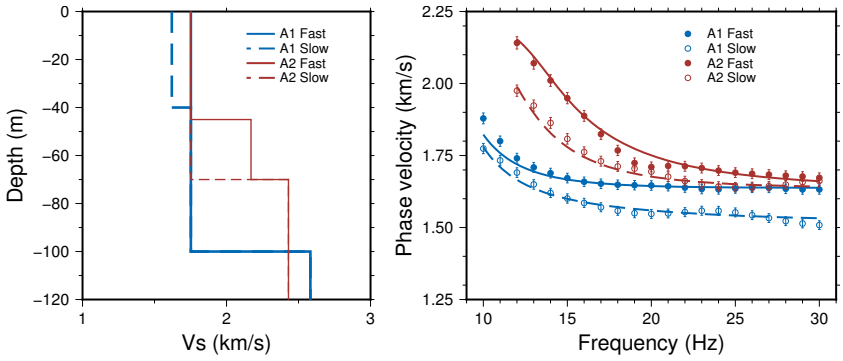

Figure B.3: Final models for arrays A1 and A2.

2 Publication

Annals of Glaciology (2018), Page 1 of 16 doi: 10.1017/aog.2018.25

Crevasse-induced Rayleigh-wave azimuthal anisotropy on Glacier de la Plaine Morte, Switzerland

Fabian LINDNER,[1] Gabi LASKE,[2] Fabian WALTER,[1] Adrian K. DORAN[2]

[1]*Laboratory of Hydraulics, Hydrology and Glaciology (VAW), ETH Zürich, Zürich, Switzerland*
E-mail: lindner@vaw.baug.ethz.ch
[2]*Institute of Geophysics and Planetary Physics, Scripps Institution of Oceanography, UC San Diego, La Jolla, USA*

ABSTRACT. Crevasses and englacial fracture networks route meltwater from a glacier's surface to the subglacial drainage system and thus influence glacial hydraulics. However, rapid fracture growth may also lead to sudden and potentially hazardous structural failure of unstable glaciers and ice dams, rifting of ice shelves, or iceberg calving. Here, we use passive seismic recordings to investigate the englacial fracture network on Glacier de la Plaine Morte, Switzerland. Glacier dynamics and the drainage of an ice-marginal lake give rise to numerous icequakes, the majority of which generate dispersed, high-frequency Rayleigh waves. A wide distribution of events allows us to study azimuthal anisotropy between 10 and 30 Hz in order to extract englacial seismic velocities in regions of preferentially oriented crevasses. Beamforming applied to a 100-m-aperture array reveals azimuthal anisotropy of Rayleigh-wave phase velocities reaching a strength of 8% at high frequencies. In addition, we find that the fast direction of wave propagation coincides with the observed surface strike of the narrow crevasses. Forward modeling and inversion of dispersion curves suggest that the azimuthal anisotropy is induced by a 40-m-thick crevassed layer at the surface of the glacier with 8% anisotropy in shear-wave velocity.

KEYWORDS: anisotropic ice, crevasses, ice thickness measurements, seismology

INTRODUCTION

Crevasses are commonly observed on ice bodies and have far-reaching implications for glacier dynamics. Given temperate conditions, fracture networks in the ice route surficial meltwater to the glacier base or store it englacially (e.g., Fountain and Walder, 1998). At the bottom of a glacier, basal crevasses can extend the subglacial drainage system some tens of meters into the ice (Harper and others, 2010). The process of crevassing affects glacial hydrology which, in turn, is crucial for ice flow dynamics (e.g., Iken and Bindschadler, 1986; Flowers and Clarke, 2002). In addition, by providing water pathways, crevasses promote cryohydraulic warming, thus softening the ice and influencing ice flow (Phillips and others, 2010). Apart from its implications for ice flow, fracturing increases the ice damage state (Pralong and Funk, 2005) and may lead to structural failure of the ice. This may be observed for example, as ice avalanching (e.g., Röthlisberger, 1977), rapid drainage of ice-dammed lakes (e.g., Das and others, 2008), or iceberg calving (Benn and others, 2007). Colgan and others (2016) provide a comprehensive discussion on the role of crevasses.

Surface crevasses can be remotely mapped and monitored using visual imagery (Krimmel and Meier, 1975) or radar imagery (Fahnestock and others, 1993). However, coarse resolution and snow cover complicate this analysis. Additionally, limited radar penetration depth prohibits the detection of englacial fractures. To investigate the latter, various geophysical methods such as borehole analysis (e.g., Harper and others, 2010), ground penetrating radar (e.g., Jezek and Bentley, 1979) and active-source seismics (e.g., Navarro and others, 2005) have been employed. Bradford and others (2013) investigated basal crevasses by means of anisotropy in electromagnetic and seismic wave velocities caused by the preferential alignment of the crevasses. Vertical fractures in an otherwise homogeneous ice body lead to a transversely isotropic medium with a horizontal axis of symmetry (or horizontal transversely isotropic) which is subject to azimuthal anisotropy in seismic wave propagation (Crampin and others, 1980; Bakulin and others, 2000). Apart from azimuthal anisotropy, the presence of crevasses may lead to band gaps in elastic wave propagation (Freed-Brown and others, 2012).

Recently, passive seismology has complemented other geophysical methods in the cryospheric sciences (Podolskiy and Walter, 2016; Aster and Winberry, 2017). Passive seismology is mainly used to investigate processes within a medium such as englacial fracturing (Neave and Savage, 1970; Walter and others, 2010), subglacial water flow (Bartholomaus and others, 2015; Gimbert and others, 2016), or stick-slip ice motion (Weaver and Malone, 1979; Winberry and others, 2011) by analyzing the seismic waves emitted by these processes. Apart from source studies, passive seismology also allows to characterize the physical properties of the medium (Zhan and others, 2013; Diez and others, 2016). This is also done using active-source seismics. Compared with active-source seismics, passive seismology is less laborious and allows the recording of long and continuous time series at the same time. Continuous recording modes, in turn, allow for monitoring the time evolution of seismic activity and changes in the medium properties.

In this study, we use the signal from naturally occurring icequakes on Glacier de la Plaine Morte, Switzerland (Fig. 1a), to investigate the variation of seismic wave velocity as a function of propagation direction. In particular, we study Rayleigh-wave azimuthal anisotropy in regions with preferential alignment of crevasses and establish a relationship between the two. In the following sections, we first describe

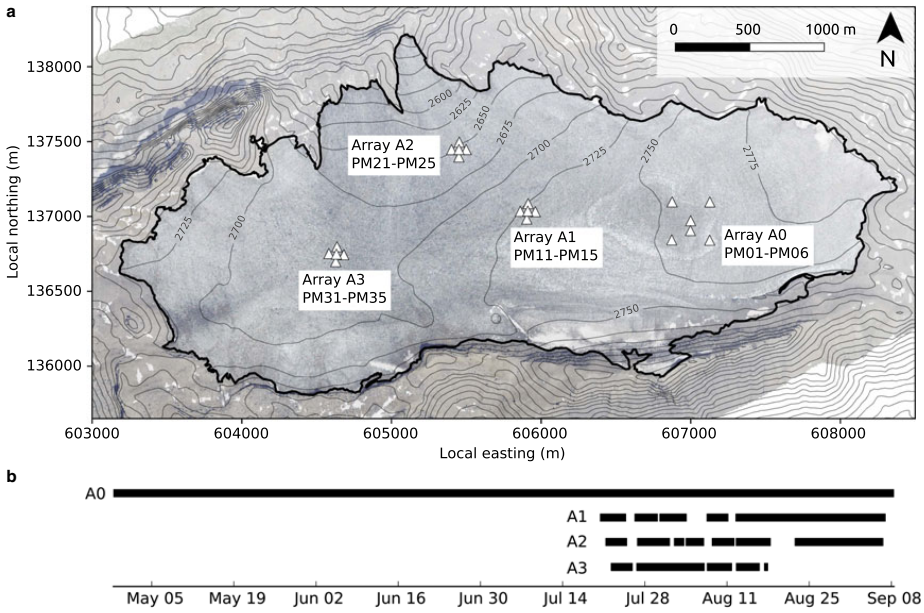

Fig. 1. (a) Map with surface topography of Glacier de la Plaine Morte. The thick black line indicates the glacier extent and the white triangles show the locations of the seismic stations. In the background, an orthophotograph is shown. Aperture of array A0 with stations PM01-PM06 is 360 m, apertures of arrays A1 (PM11-PM15), A2 (PM21-PM25) and A3 (PM31-PM35) are 100 m. Stations are numbered for each array counterclockwise from 1 (North; Northeast for A0) to 5 (center station). Station PM06 (lower center station of A0) was added late, that is, in August. Coordinates of the Swiss Grid are shown. (b) Data availability of the stations in 2016. Black bars indicate times when all stations of an array were operational (station PM06 not considered for this illustration). Only times where at least two arrays were fully operational are considered in this study.

our 2016 field campaign and the data collected. This is followed by our processing scheme to locate icequakes, and to determine the frequency-dependent Rayleigh-wave phase velocities using beamforming. We find significant azimuthal anisotropy and discuss their causes.

FIELD SITE

With an extent of ~7.5 km^2, Glacier de la Plaine Morte in Switzerland (Fig. 1a) is the largest plateau glacier in the European Alps. More than 90% of its surface occupies the narrow elevation range between 2650 and 2800 m.a.s.l. (Huss and others, 2013). This distribution of ice surface elevation implies the following two glacier characteristics: (i) due to the weak topographic gradients, ice flow is negligible and measured summer surface velocities are smaller than 1 cm d^{-1}. (ii) In most years, the equilibrium line altitude in the study region is either above or below the plateau elevation, that is, Glacier de la Plaine Morte is either completely snow free in summer, or completely snow covered year round. A separation in accumulation and ablation area is not applicable. For this reason, the glacier is extremely sensitive to small changes in the climatic forcing (Huss and others, 2013). Furthermore, the annual filling and subglacial drainage of an ice-marginal lake at the southeastern rim of the glacier was observed in recent years. This drainage increases the risk of flooding the Simme Valley to the north. In 2016, the lake reached a volume of $\sim 2 \times 10^6$ m^3 which was released within 5 days at the end of August.

For this paper, the main objective is the study of crevasse-induced azimuthal anisotropy. We chose Glacier de la Plaine Morte for our study because of the following glacier characteristics. (i) Due to the insignificant ice flow, crevasses are narrow and sparse, resulting in a comparatively homogeneous ice body with minor vertical, coherent cracks, which is expected to result in uniform azimuthal anisotropy of seismic velocities. (ii) Due to the slow ice flow, ice straining is negligible. For this reason, seismic array geometries can be considered constant during the field campaign. (iii) Glacier de la Plaine Morte is easily accessible via cable car. This simplifies the logistics of regular station visits required by high-melt conditions prevalent on most glaciers in the European Alps.

2016 FIELD CAMPAIGN AND INSTRUMENTATION

Our field campaign lasted from April to early September 2016, with a total of 21 seismic stations deployed on Glacier de la Plaine Morte (Fig. 1a). Starting the campaign in late April, we deployed six Lennartz LE-3D/BH borehole seismometers (array A0, PM01 – PM06) in shallow boreholes in the ice (~1 m deep) with an aperture of ~360 m. The 1 Hz corner-frequency sensors collected data continuously for more than 4 months (PM06 for one month, only). The data were digitized and recorded by Nanometrics Centaurs (PM06 used an Omnirecs DATA-CUBE3) at 500 samples per second. Station PM06 operated at 200 samples per second, but we resampled the data from this station to 500 samples per second. Three months later, in late July, 15 stations were grouped into three 100 m-aperture arrays, arrays

A1 (PM11 – PM15), A2 (PM21 – PM25), and A3 (PM31 – PM35), and deployed on different parts of the glacier. Each of these stations was equipped with a 4.5 Hz three-component geophone (PE-6/B manufactured by SENSOR Nederland), while data were logged continuously at 400 samples per second using an Omnirecs DATA-CUBE3 datalogger. These instruments operated for up to 7 weeks (Fig. 1b).

The ice thickness distribution of Glacier de la Plaine Morte is known from helicopter-borne ground-penetrating radar (GPR) surveys (Langhammer and others, 2018). These investigations yielded ice thicknesses beneath arrays A0, A2 and A3 of ~150, 80 and 180 m, respectively. In the region of array A1, GPR coverage is coarse. However, GPR profiles in some few hundred meters distance suggest ice thicknesses ranging between ~105 and 120 m (L. Langhammer, pers. communication 2018). The bedrock beneath the ice is characterized by a karst environment (Finger and others, 2013).

Arrays A1 and A2 were placed in regions where surface crevasses were identified from orthophotographs, while array A3 was placed on ice without discernible crevasses for comparison. Array A0 was deployed without considering the ice structure since it was not specifically installed for this project. At the time of the installation of arrays A1, A2 and A3, the glacier was covered with more than 2 m of snow. For this reason, we installed the geophones on granite tiles in snow pits. On these granite tiles, we placed the sensors with a base plate on tripods (see Apendix E in Walter (2009)), built a cavity around the sensors using metal grids covered with anti-ablation fleece, and re-filled the pits with snow. To retain GPS capability, the digitizers stayed at the surface, wrapped in plastic bags. Snow melt required us to re-dig the pits twice. Furthermore, array A3 had to be dismantled on 23 August because a thick slush layer of water-soaked snow at the site did not allow further operation of the geophones. Stations of array A2 were re-installed directly on ice (again with sensors sitting on granite tiles) on 30 August because of diminishing snow-cover.

METHODS AND THEORY

In this study, we use icequakes to investigate Rayleigh-wave azimuthal anisotropy. Rayleigh waves travel along the surface of a medium as a superposition of P-waves and vertically polarized S-waves. The resulting particle motion in a homogeneous, isotropic medium is confined to the plane spanned by the wave propagation direction and the vertical. In the presence of a velocity gradient in the subsurface, Rayleigh waves are dispersive, that is, their velocity is frequency dependent since the depth-penetration of Rayleigh waves is controlled by the wavelength. Inversion of the dispersion curve, therefore, allows the retrieval of subsurface parameters (e.g. Wathelet and others, 2004). On glaciers, Rayleigh waves are produced by shallow ice cracking, which results in relatively small overtone/body wave arrivals. This allows for clear and unbiased surface wave dispersion measurements (e.g., Walter and others, 2015). Since icequakes are abundant (hundreds to thousands per day, e.g. Roux and others, 2010) and the vast majority of these events is of shallow type emitting dominant Rayleigh waves, they provide an effective passive source for the investigation of azimuthal anisotropy in crevasse fields. Figure 2a shows an example of such an icequake recorded by all 21 stations on Glacier de la Plaine Morte. For this study, we apply an array processing scheme to determine dispersion in each array, thus, our dispersion curves constrain 'in situ' average structure beneath each array. Azimuthal coverage of icequakes allows the study of azimuthal anisotropy and, since we are using Rayleigh waves, its variations with depth (Savage, 1999). Surface crevasse icequakes produce signal in a broad frequency range (~10–50 Hz, Podolskiy and Walter, 2016). On Glacier de la Plaine Morte, we typically observe high signal levels between 10 and 30 Hz (Fig. 2b).

The first step of our processing is the detection and location of icequakes. Accurate location is crucial to later assign measured Rayleigh–wave dispersion at an array with the corresponding source back azimuth. In the following, we describe the beamforming technique which we use both to locate icequakes and to determine phase velocity dispersion curves. Subsequently, we briefly discuss azimuthal variations in Rayleigh wave phase velocities as introduced by Smith and Dahlen (1973).

Beamforming

Beamforming is a processing technique which uses the differential travel times of a seismic signal across an array of receivers to estimate its propagation direction (back azimuth) and slowness (inverse of velocity). The basic idea of beamforming is to shift the signals from all stations using a specific back azimuth-slowness combination and sum the traces. For a coherent signal, the traces will sum constructively if the true back azimuth and slowness are used (Rost and Thomas, 2002). For this study, we use a standard frequency-domain beamforming formulation which was previously used in several other studies (e.g. Gerstoft and Tanimoto, 2007; Alvizuri and Tanimoto, 2011; Diez and others, 2016).

From the vertical ground motion recordings from N stations of an array, the Fourier transforms are computed at angular frequency ω and their (complex) values are arranged to form a column vector $\mathbf{d}(\omega)$ of length N. Using this, the cross-spectral density matrix is computed as

$$\mathbf{C}(\omega) = \mathbf{d}(\omega)\,\mathbf{d}^{\dagger}(\omega), \tag{1}$$

where † denotes the complex conjugate transpose operation. Element $C_{mn}(\omega)$ with $m, n = 1, \ldots, N$ is the frequency-domain equivalent to the time-domain crosscorrelation of stations m and n, and yields the average phase delay at frequency ω between these two stations. Considering incident plane waves associated with slowness s and back azimuth Ψ, the modeled response for the same array at ω is given by

$$\tilde{\mathbf{d}}(\omega, s, \Psi) = \exp(i\omega s(\,\mathbf{r}\cdot\mathbf{e})), \tag{2}$$

where i is the imaginary unit, $\mathbf{r}$ is a $N \times 2$ matrix containing the $(x,\ y)$-coordinates of the stations and $\mathbf{e} = (\cos\Psi,\ \sin\Psi)^T$ (T is the transpose). Finally, the beam, or beam power, for a given frequency, slowness, and back azimuth is

$$b(\omega, s, \Psi) = |\,\tilde{\mathbf{d}}^{\dagger}(\omega, s, \Psi)\,\mathbf{C}(\omega)\tilde{\mathbf{d}}(\omega, s, \Psi)\,|\,. \tag{3}$$

For calculating the beam, we take the norm of the cross-spectral density matrix and the modeled array response $\tilde{\mathbf{d}}$. In this case, the beam power is normalized, that is, it is one in case the

signal is coherent across the array and the true slowness and back azimuth are chosen and smaller otherwise. In order to stabilize the results, the beams from several successive discrete frequencies may be averaged (assuming that slowness and back azimuth are close to constant in the considered frequency band).

Azimuthal anisotropy

Weak seismic anisotropy can generally be described by a trigonometric polynomial of degree 4 in azimuth Ψ (Backus, 1965). We follow Smith and Dahlen (1973) who derived a similar formulism for surface waves. In particular, they showed that the phase velocity of surface waves in an arbitrarily stratified and weakly anisotropic medium varies as

$$c(\omega,\Psi) = a_0(\omega) + a_1(\omega)\cos 2\Psi + a_2(\omega)\sin 2\Psi + a_3(\omega)\cos 4\Psi + a_4(\omega)\sin 4\Psi, \quad (4)$$

where the five coefficients a_0, a_1, a_2, a_3 and a_4 are dependent on the 21 independent elastic parameters of the elasticity tensor describing the anisotropic medium and are frequency-dependent integral functionals of depth. a_0 describes the 'isotropic', azimuthally averaged phase velocity, which can be different from the average phase velocity dispersion curve as determined in the next section, if azimuthal data coverage is insufficient. Forward modeling as well as observations suggest that Rayleigh wave azimuthal anisotropy in realistic physical media is dominated by 2Ψ variations (e.g., Smith and Dahlen, 1973; Montagner and Nataf, 1986; Montagner and Anderson, 1989).

PROCESSING AND RESULTS

Icequake locations

Triangulation

To locate icequakes, we use the four arrays as 'single summary' stations to then triangulate to the icequake. For each array, we scan the continuous, bandpass filtered (10–20 Hz for arrays A1–A3; 7–15 Hz for array A0) data of all array stations using a classical short-term average/long-term average (STA/LTA) trigger (e.g. Allen, 1978). As length for the STA and LTA windows, we use 150 samples (0.3 s for A0 stations and 0.375 s for A1, A2 and A3 stations) and 1800-sample windows (3.6 and 4.5 s), respectively, and set a trigger threshold for the STA/LTA ratio of 8. For the three seconds of data trailing a detected event, the trigger is disabled to avoid overlapping events. In order to consider a triggered signal an event, we require at least three stations to trigger concurrently. For each triggered event, we then automatically apply beamforming by averaging the beams obtained at discrete frequencies from 10 to 20 Hz (7 to 15 Hz for array A0 due to the larger aperture) in 0.2 Hz steps. We chose this frequency band since most shallow icequakes peak in amplitude in this range (Fig. 2b). We apply a grid search over back azimuth (in two-degree steps) and slowness. Since we are interested in Rayleigh waves, we use a coarse grid of slowness values associated with the minimum and maximum phase velocities of 1.25 and 2.25 km s^{-1}, which covers the typical range expected for Rayleigh waves on glaciers (Walter and others, 2015). As the final back azimuth and slowness, we chose the back azimuth-slowness combination which yields the maximum beam power. Figure 3a illustrates the results of this processing applied to the icequake shown in Fig. 2. To gain a robust result, we only use icequakes in our further analysis where the maximum beam power is larger than 0.75. This threshold effectively rejects events for which the plane wave assumption is violated or which exhibit a weak coherence across the array. In total, our processing scheme allows the detection of 71 113, 29 555, 9023 and 1052 events on arrays A0, A1, A2 and A3, respectively, of which 39 058, 28 134, 8791 and 977 events yield a beam power >0.75. The differences in events detected on different arrays indicate that many icequakes are too weak to be recorded on all arrays. In particular, array A3 encounters little seismicity compared with the other arrays (in terms of events per recording time unit).

In the final step to triangulate to each icequake and thereby determine its location, we associate events triggered on different arrays. In case an event was triggered concurrently on different arrays (and accounting for the travel-time difference between different arrays), we use the back azimuth values determined in the previous step from these arrays and estimate the event epicenter by triangulation in the horizontal plane assuming a flat glacier surface. An example is shown in Fig. 3b for the icequake shown in Fig. 2. In 15 138 cases, we can associate the waveforms recorded concurrently on different arrays with the same event. However, since many icequakes were too small in magnitude to be detected on all arrays, we locate many icequakes using two, or three arrays, only. For those events which were detected on two arrays only (11 928 icequakes), we estimate the icequakes' epicenter as the point of intersection of two beams. In the case that three or four arrays detected an event concurrently (3210 icequakes), we determine its epicenter as the average of all beam pair intersections in x (East-West) and y-direction (North-South). Since accurate icequake locations are crucial for the investigation of azimuthal anisotropy (see also next section), we set the following thresholds for location uncertainty. For events located using two arrays, we require the angle of intersection of the beams to be in the range $90° \pm 45°$. For instance, we discard icequakes which were located by two arrays with similar back azimuth estimates since these locations are very sensitive to inaccuracies in the back azimuth measurements. In the most extreme case, two arrays might yield the same back azimuth which prohibits an epicenter determination. For events located using at least three arrays, we require the uncertainties in x- and y-direction to be smaller than 100 m. We estimate the uncertainties as the standard deviation of the beam-intersection points in x- and y-direction. Applying these criteria results in 9089 events for further analysis.

Secondary vetting of icequakes

From the 9089 events associated with the high-certainty location, we select only a subset for the investigation of azimuthal anisotropy. In particular, we only select events which fulfill the following conditions. First, we require the events to be at least 500 m away from the center of the considered array. This condition is necessary because we determine the phase velocity dispersion curves by plane-wave beamforming. Closer events would require a more complex

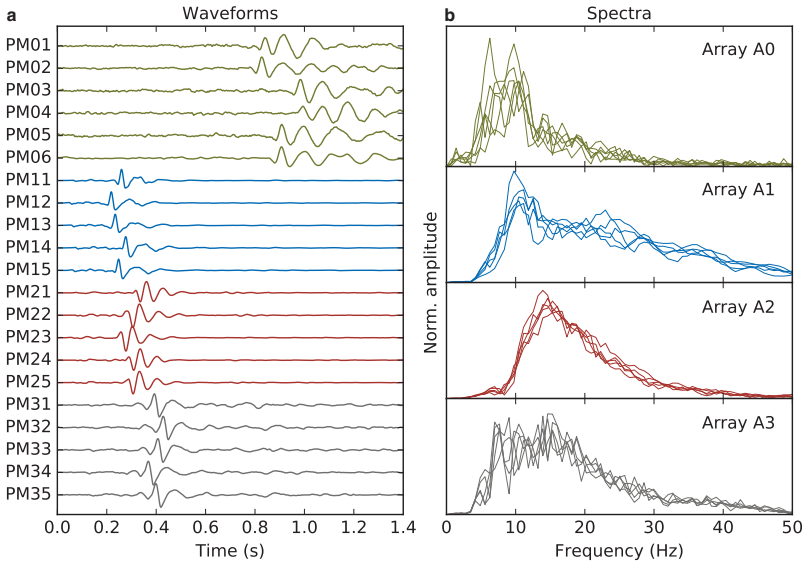

Fig. 2. (a) Vertical-component waveforms of an icequake which occurred on 13 August 2016 and was recorded on all stations. Amplitudes are normalized. (b) Amplitude spectra associated with the waveforms shown in (a).

wavefront, such as that of a spherical wave. In addition, such nearby events may be subject to near-field effects. For the lowest considered frequency of around 10 Hz and a Rayleigh wave velocity of 1.65 km s^{-1} (Walter and others, 2015), the minimum distance of 500 m corresponds approximately to three times the maximum wavelength; a plane wave assumption is therefore reasonable. Second, from the events which pass this criterion, that is, are at least 500 m away from the array, we finally select only those which exhibit a dominant Rayleigh wave. By means of visual inspection, we discard all events which show strong body waves, unidentifiable phases, noisy records, or instrumental glitches. The latter was a frequent problem for records at array A3. We apply this selection procedure to the event data bases of arrays A1, A2 and A3, but not for array A0 and omit this array in the further analysis. The reasons are as follows: (i) due to the larger array aperture, array A0 has a different array response function compared with the other arrays (Fig. 3a). For the same reason, we encountered spatial aliasing for frequencies of 19 Hz and higher. Hence, the different array characteristics complicate the comparison of the arrays. (ii) Array A0 consists of borehole sensors whose azimuthal orientation is unknown. This implies that visual inspection of the particle motion in the Rayleigh polarization plane in order to identify Rayleigh phases (as done for arrays A1, A2 and A3) is not possible.

After the event vetting process, we are left with 1370 events of which 709, 570 and 211 events were recorded at arrays A1, A2 and A3, respectively. Their spatial and azimuthal distributions are shown in Figs 4a and 4b. Initially, many more events were available, however, we think that our restrictions are important to ensure robust azimuthal anisotropy results.

Phase velocity measurements

Our last processing step involves the calculation of the Rayleigh wave dispersion curves. For each array and event shown in Fig. 4a, we cut a narrow window containing the Rayleigh waves of all array stations and apply plane-wave beamforming. For each event, we fix the back azimuth to the value determined previously and perform a fine grid search on phase velocities only (1–4 km s^{-1} in 0.005 km s^{-1} steps). In the initial beamforming step to locate the icequakes, we kept the slowness grid intentionally coarse in order to save computation time. For the same reason, we determined a single phase velocity value for the frequency range 10–20 Hz (7–15 Hz for array A0), only. By contrast, we now determine the phase velocity as a function of frequency, in 1 Hz steps, to obtain a dispersion curve instead of a single value. In order to obtain a smooth dispersion curve, we use a 4 Hz wide sliding window with 75% overlap resulting in phase velocity measurements at all integer frequencies from 8 to 30 Hz. Within the sliding window, we average the beams obtained at discrete frequencies in 0.2 Hz steps and associate the slowness value which maximizes the beam power with the center frequency of the 4 Hz wide window.

Overall, the final dispersion curves at each array are consistent and cluster within a few percent around the average dispersion curves, as shown in Fig. 4c. With phase velocities between ~2.2 km s^{-1} at 8 Hz (array A2) and 1.6 km s^{-1} at 30 Hz (all arrays), the dispersion curves are similar to curves observed previously on glaciers (e.g., Walter and others, 2015). A decrease in phase velocity with increasing frequency is consistent with a seismically slower medium (such as glacial ice) over a faster bedrock medium. At low frequencies, phase velocities are lowest at array A3 which has the thickest ice cover, and highest at A2 which has the thinnest ice cover. All these observations are consistent with a two-layer ice/bedrock model that shows lateral variations as described. Note here, however, that the average dispersion is the statistical average of our measurements. In the presence of lateral heterogeneity and/or azimuthal anisotropy, this average does not necessarily reflect the true average, isotropic phase velocity a_0 in Eqn 4.

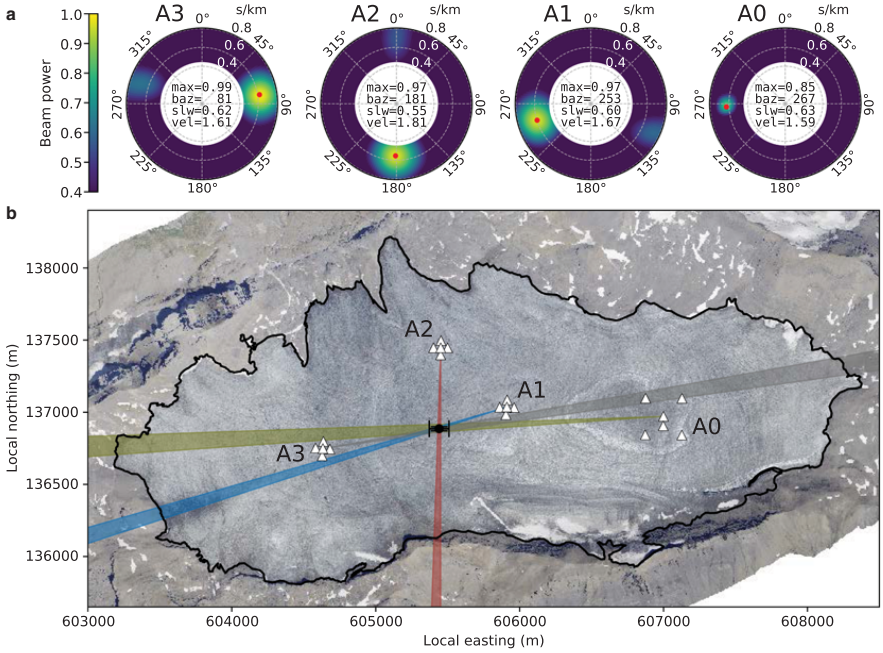

Fig. 3. (a) Beamforming applied to the icequake shown in Fig. 2. Shown is the beam power as a function of back azimuth (angular axis) and slowness (inverse of velocity, radial axis). The red dots indicate the maximum beam power. Its value (max) and the corresponding back azimuth (baz), slowness (slw) and phase velocity (vel) values are given in the centers of the polar plots. (b) Epicenter determination by triangulation for the icequake shown in Fig. 2. Shown are the back azimuths (colored cones) estimated for this icequake. The cone angle of ±1° accounts for the discrete grid search in 2° steps. The epicenter (black dot) is calculated as the average coordinates of all beam intersections and its error is estimated as the standard deviation thereof.

Azimuthal anisotropy

It becomes apparent, that the azimuthal distribution of the events is different for each array (Fig. 4b). Array A1 exhibits the best azimuthal distribution of events, followed by A2 which has many events distributed in the back azimuth range of 90–210°, thus populating a range well above a quadrant. By contrast, A3 has a poor azimuthal distribution. Since the majority of events is found at azimuths between 60° and 90°, the data coverage does not justify further in-depth study of azimuthal anisotropy. We, therefore, focus on arrays A1 and A2 in the following.

To investigate azimuthal anisotropy, at each frequency considered, we sort the measured phase velocities as a function of back azimuth Ψ. To smooth the data somewhat, we calculate the average phase velocity and its standard deviation in 10° bins where at least six measurements are available. Through these data points, we perform least-squares fits to obtain the coefficients a_0, a_1, a_2, a_3, a_4 in Eqn 4. We do not weight the data with their errors. As stated earlier, Rayleigh wave azimuthal anisotropy is dominated by 2Ψ variations (e.g., Smith and Dahlen, 1973; Montagner and Nataf, 1986; Montagner and Anderson, 1989). We adopt this idea and perform a least-squares fit for a_0, a_1 and a_2 only to determine the final azimuthal anisotropy. Though, a fit for all 5 coefficients is an useful consistency check, as a_3 and a_4 should be negligible. We then assign the difference between the two fits as error bars to our final results. Figure 5 summarizes the results of the least-squares fits for arrays A1 and A2 at six discrete frequencies. The least-squares fits after Smith and Dahlen (1973) for all integer frequencies are shown in Figs S1 and S2 in the supplementary material.

Array A1

For array A1, the phase velocities at 12 Hz scatter and a systematic pattern is not discernible (Fig. 5). Consequently, the resulting fits for 3 and 5 coefficients lead to different predictions (solid and dashed lines). At 15 and 27 Hz, the three-parameter fit and the five-parameter fit lead to almost identical predictions, implying that the 4Ψ terms are small. For the intermediate frequencies (18, 21, 24 Hz), the five-parameter fit shows moderate deviation from the three-parameter fit (peak-to-peak amplitude of the 4Ψ contribution, that is, $2\sqrt{a_3^2 + a_4^2}$, is 42, 50, 46 m s^{-1}, respectively). In the next step, we log the strength of anisotropy and the fast direction, very much in analogy to determine anisotropy-induced shear-wave splitting (Savage, 1999) parameters. The determined strength of the frequency-dependent azimuthal anisotropy is the peak-to-peak amplitude of the 2Ψ variation divided by the estimated isotropic phase velocity a_0, that is, $2\sqrt{a_1^2 + a_2^2}/a_0$. The error is estimated as the difference between the peak-to-peak amplitude of the three-parameter fit and the peak-to-peak amplitude of the five-parameter fit divided by the isotropic phase velocity. As the second anisotropy parameter, we quantify the fast direction as the peak of the three-parameter fit (in the 0°–180° range) and its error as

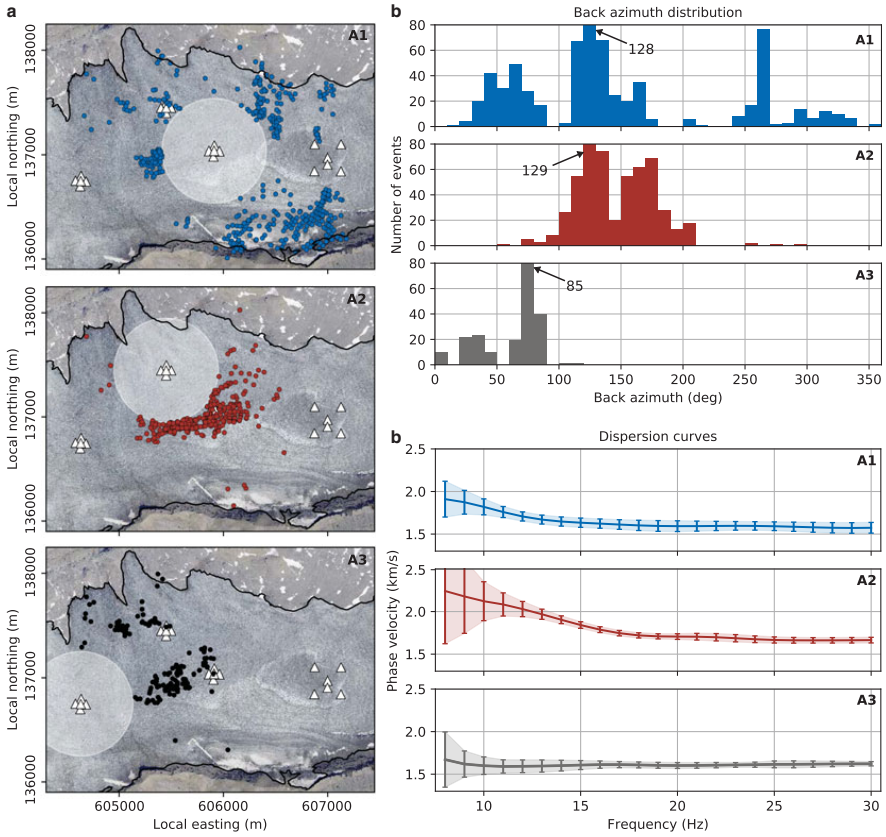

Fig. 4. (a) Located icequakes selected for the investigation of azimuthal anisotropy at arrays A1 (blue), A2 (red) and A3 (black). The selected events are at least 500 m away from the array center (outside the white shaded area), their epicenters are associated with small uncertainties, and they exhibit a dominant Rayleigh wave (for details see text). (b) Azimuthal distribution of the icequakes shown in (a). The arrows with numbers indicate the height of the clipped bars. (c) Average Rayleigh wave dispersion curves (solid lines) calculated from the events shown in (a). The errorbars indicate one standard deviation.

the deviation of the peaks of the three-parameter fit to the five-parameter fit.

The results are shown in Figs 6b and 6c. As discussed earlier, scatter in the data is considerable for low frequencies and an anisotropy pattern does not emerge. For frequencies of 14 Hz and higher, azimuthal anisotropy is present and its strength increases from ~4% at 14 Hz to ~8% at 30 Hz, although results at intermediate frequencies (17–24 Hz) have large error bars (Fig. 6b). The fast direction changes somewhat with frequency but largely stays around 55° (Fig. 6c).

Array A2

Azimuthal anisotropy at this array is assessed in the same way as for array A1. From Figs 5 and S2, we see that even though scatter in the phase velocity measurements is considerable, there is evidence for azimuthal anisotropy at low frequencies. At frequencies of ~15 Hz our data reveals azimuthal anisotropy with a strength of ~7% and a fast direction of ~55° (Figs 6b and 6c). At higher frequencies, azimuthal anisotropy is barely discernible. To summarize, we find azimuthal anisotropy for low frequencies (~15 Hz) but not at higher frequencies. This is indicative of an anisotropic layer at depth, and not near the top.

MODELING OF DISPERSION CURVES

Basic forward modeling and inversions described in the following allow a rough first-order estimate on the underlying ice properties with depth. For this purpose, we use the Geopsy package (geopsy.org; Wathelet and others, 2008). We use a two-track approach where we perform forward modeling to explore specific targets in the model space (e.g. layer thickness) but also apply a more modern approach involving a formal inversion. We start with the forward modeling because we want to gain improved insight into which parts of the model are better constrained than others, and which parts resulting from the inversion may not be required to fit the data. Another reason why we follow both tracks has to do with the sensitivity of Rayleigh wave phase velocity to structure with depth. Rayleigh waves are sensitive to both shear and compressional wave velocity, Vs and Vp, as well as density (Fig. 7). Of the three, sensitivity to Vs is greatest, but sensitivity to shallow Vp and density can be significant. Note that sensitivity to Vp is typically enhanced where sensitivity to Vs is decreased. Sensitivity to Vp and density is often ignored and inversions are performed only for Vs in order to keep an inversion well-conditioned. In our tomographic inversions for deeper Earth structure, we prefer to account for sensitivity to Vp and density by scaling the respective

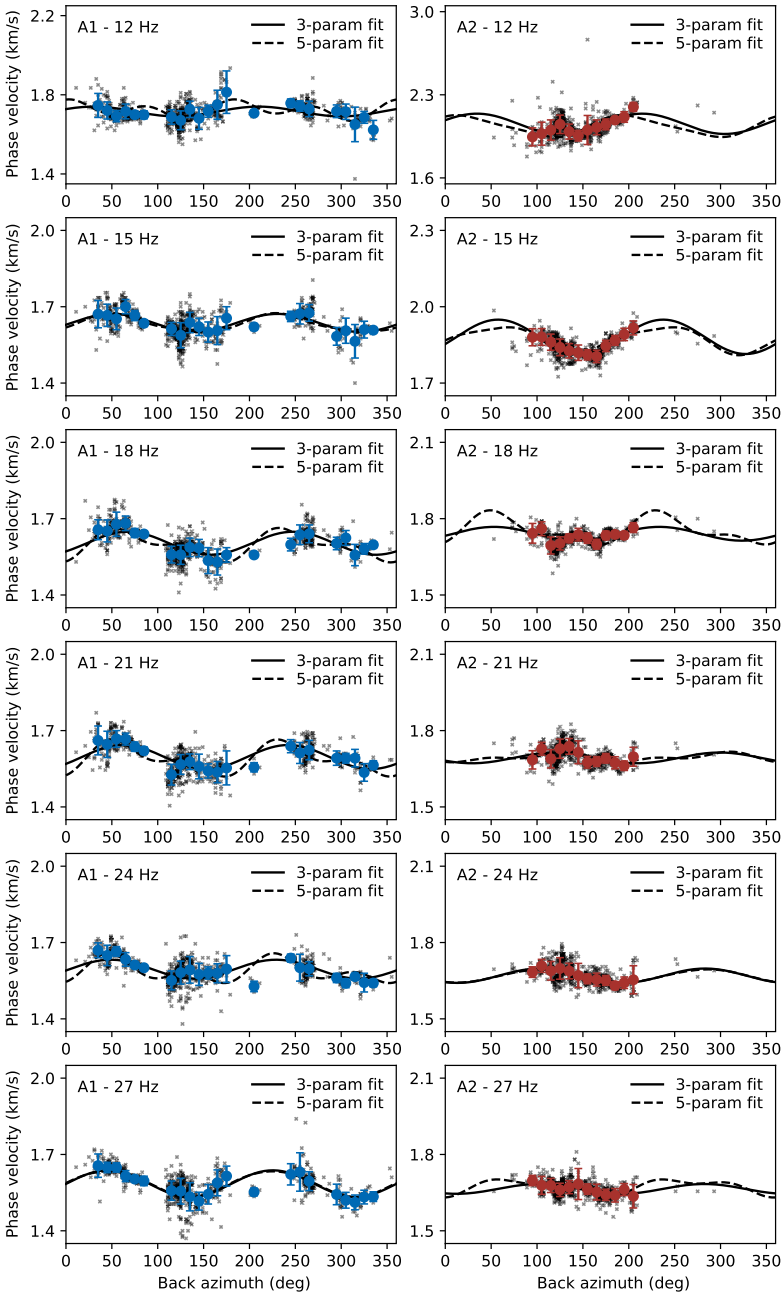

Fig. 5. Phase velocity measurements as a function of back azimuth for array A1 (left column, blue) and array A2 (right column, red). Gray crosses are the measurements from single icequakes, blue and red dots are bin averaged values in 10° bins containing at least six measurements (error bars are one standard deviation). The dashed line is the five-parameter model fit after Smith and Dahlen (1973) (Eqn 4) through the bin-averaged values. The solid line is the three-parameter fit omitting the 4Ψ terms.

kernels to that of Vs, using known scaling relationships for Earth materials, and then perform inversions for Vs. To assess the impact of ignoring sensitivity to Vp and density, we scale the kernels during forward modeling but keep Vp and density fixed to a starting model in the inversions.

Our starting model uses the values of Walter and others (2009), found for the Gorner Glacier at the nearby Monte Rosa Massif. For the basement, we use typical limestone values reported by Assefa and others (2003), since the geology beneath Glacier de la Plaine Morte is characterized

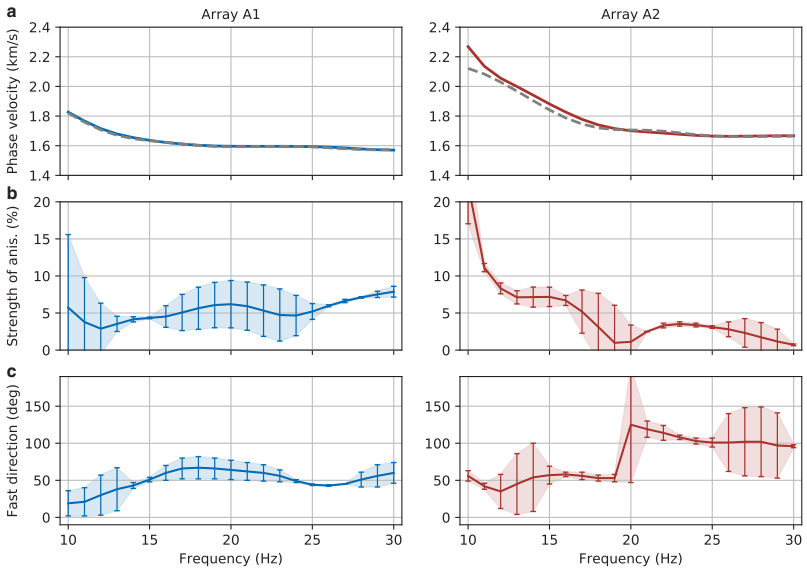

Fig. 6. (a) Isotropic phase velocities (a_0 parameters from three-parameter fits) for array A1 (blue) and array A2 (red). The gray dashed line is the average dispersion curve obtained from beamforming shown in Fig. 4c. (b) Strength of anisotropy, that is, peak-to-peak amplitude of the three-parameter fit divided by the isotropic velocity in percent. (c) Fast direction of wave propagation determined as the maximum of the three-parameter fit in the 0° to 180° degree range. The errorbars in (b) and (c) are estimated from the deviation of the three-parameter and the five-parameter fit (see text for details).

by a karst environment formed by this rock type (Finger and others, 2013). Table 1 summarizes the model, which we subsequently call the Gorner-Karst (GK) model.

At array A1, we fix the ice-basement boundary at 100 m. The sensitivity kernels computed for this array (Fig. 7) indicate that phase velocities in the frequency range considered here (10–30 Hz) are most sensitive to the structure at a depth <100 m, with only frequencies near 10 Hz or less having a rather low sensitivity to Vs below the ice-basement boundary. Because sensitivity is high just above the boundary, our dataset is actually sensitive to the depth of the boundary. To stress this point, kernels computed for an ice thickness of 70 m, as assumed for A2 (Fig. S3), confirm that our data can indeed depend on structural changes well below a depth of 100 m. Sensitivity to these depths may be suppressed as error bars increase with decreasing frequency (Figs 4c and 6).

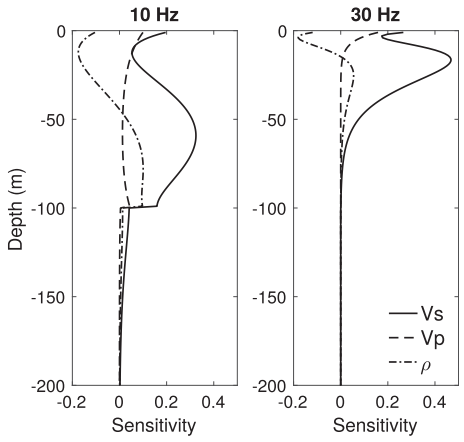

Fig. 7. Sensitivity kernels for Rayleigh wave phase velocity at 10 and 30 Hz as suitable for modeling at array A1. The underlying two-layer model consists of 100 m of ice over a half-space of karstic bedrock. The parameters for this model are summarized in Table 1. The kernels were computed using the MATLAB code of Haney and Tsai (2017).

A first step is to model the average phase velocities at arrays A1 and A2 (Fig. 6a). We seek the simplest two-layer ice-basement model that fits the data reasonably well. Targeted forward modeling for array A1 confirms that an interface near 100 m explains a slow increase in phase velocity with declining frequency below 15 Hz (Fig. S4). The shear wave velocity in the ice has to be 4% less than in the GK model to match phase velocities at high frequencies. We cannot find a simple 2-layer model that fits phase velocities at frequencies below 13 Hz. A 3-layer model with two ice layers, where the bottom 30 m have 5% higher values than in the ice layer above slightly improves the fit to the data between 10 and 13 Hz. Our data are not sensitive to small changes (8% or less) in basement Vs and Vp. However, a deeper interface near 120 m, as suggested as a deeper limit by the helicopter-borne GPR data, is inconsistent with our observations. This is confirmed by both targeted

Table 1. Gorner-karst (GK) model used as the starting model in this study

Medium	Vp (m s^{-1})	Vs (m s^{-1})	ρ (kg m^{-3})
Ice	3630	1760	910
Basement	4500	2500	2500

forward modeling as well as inversions. For array A2, a shallower interface near 70 m or slightly shallower is needed to explain the increase starting at 20 Hz (Fig. S5), and ice parameters are elevated by 1% compared with the GK model. For both A1 and A2, inversions in which the interface is a free parameter (for details on the inversions see next section) tend to return slightly shallower interfaces (90 and 60 m, respectively).

MODELING OF AZIMUTHAL ANISOTROPY

In anisotropic media, the wave speed changes with direction. In transversely isotropic media with vertical symmetry axis, the description of compressional and shear wave velocities, Vp and Vs separate into vertical and horizontal velocities, that is, Vp_v, Vp_h, Vs_v and Vs_h. Here, the sensitivity of Rayleigh wave phase velocity to Vs_v and density is essentially the same as in the isotropic case while sensitivity to Vs_h is negligible. Sensitivity to Vp is increased at depth compared with the isotropic case but still much smaller than the sensitivity to Vs. Montagner and Nataf (1986) discuss such depth sensitivities to derive anisotropy as a function of depth. In the conceptually simplest case, Rayleigh wave azimuthal anisotropy occurs when a transversely isotropic medium is tilted. Assuming that the fast and slow phase velocities can be modeled independently, the resulting Vs models allow an initial assessment of the degree of anisotropy with depth. This assumption may not be valid for media with general anisotropy, but our approach may be an acceptable starting point, particularly for media whose main symmetry axis is horizontal. For the purpose of exploring the model space, and possible inconsistencies, we follow two different strategies in the forward modeling and in the inversions. For the latter, we attempt to fit the fast and slow dispersion curves shown in Fig. 8 independently and estimate anisotropy from the resulting Vs models. In the forward modeling, we try to fit both average phase velocities and strength of anisotropy as displayed in Fig. 6 by varying the shear wave velocity and the thickness of the anisotropic layer.

At array A1, the degree of azimuthal anisotropy increases with frequency, providing evidence for a shallow anisotropic layer rather than a deep one. We use the GK model as starting model to predict the average dispersion and mimic anisotropy by allowing an upper ice layer with reduced velocities. During iterative, targeted forward modeling, we vary Vs in the ice as well as the thickness and strength of anisotropy in the top ice layer (Fig. 9). In the final set of runs, Vs in the lower ice layer was set to 3% higher than in the GK model. The top ice layer had the same Vs in the fast direction and 10% reduced Vs in the slow direction (hence the negative velocity change in the right panel). We conclude that a 30–40 m thick upper ice layer with 10% Vs anisotropy explains both the frequency-dependent average phase velocity as well as the strength of anisotropy. The thickness of the top layer trades off with the degree of anisotropy in such a way that a 20–30 m thick layer with 15% anisotropy is also consistent with our data.

For formal inversions, we use the Dinver tool included in the Geopsy package. The embedded neighborhood algorithm (Sambridge, 1999a,b) allows the estimation of model uncertainties. To balance out the weight of the data in the inversions and to avoid the dominance of data with perhaps unrealistically small error bars, we set the minimum error threshold to 1%. We first seek a model with one ice layer that fits the fast phase velocity (Fig. 10). We then use this model as the starting model to fit the slow phase velocity but now allowing a second ice layer on top, with varying Vs and thickness. The resulting best-fitting models are summarized in Fig. 11 and Table 2. As noted in the section on forward modeling, basement Vs is not well constrained by our data but the best-fitting model has a basement Vs of 2582 m s^{-1} (3% higher than in the GK model). Raising the basement Vp to 4500 m s^{-1} as in the GK model leads to higher Vs (2711 m s^{-1}) where the Vp/Vs ratio of 1.8 as typically found for limestone (Assefa and others, 2003) is no longer preserved. We stress once again that basement velocities at A1 are not well constrained. Shear wave velocities in the lower ice layer cluster around our best-fitting value of 1752 m s^{-1}. As far as the top, anisotropic ice layer is concerned, the best-fitting model has a 40-m-thick ice layer with 7.8% anisotropy in Vs. A slightly thinner, more anisotropic layer fits our data nearly equally well. This is in agreement with results from our targeted forward modeling.

The situation at array A2 is different as azimuthal anisotropy is very weak at high frequencies but increases in strength with decreasing frequency (Figs 6b and 8). This is indicative of a deep anisotropic layer. Also, note that phase velocities at high frequencies match those for the fast velocities at array A1. This means that upper ice velocities likely match those at A1. In the inversion, we start with the fast A1 Vs model as slow Vs model at A2. We keep the ice thickness fixed at 70 m. After inversions, results for basement Vs cluster around 2430 m s^{-1} and so are slightly lower than at A1 (Table 3). Repeat inversions using 4500 m s^{-1} as Vp yields the same Vs, so it seems that basement Vs is well-constrained at A2. For modeling anisotropy, we allow a lower, faster ice layer to vary in Vs and thickness. The best-fitting model has a 25-m-thick lower ice layer with 23.8% anisotropy in Vs (Table 3). Realizing that this inversion yields perhaps unrealistically high Vs for the ice, we explore other options through targeted forward modeling. We notice that phase velocity undulates somewhat around an 'average' trend as frequency increases, with a slight dip between 17 and 21 Hz (Figs 6a and 8). We suspect internal data inconsistency because no simple 2-layer ice-basement model appears to be able to fit the data between 12 and 14 Hz and above 21 Hz on one hand and those between 15 and 20 Hz on the other equally well. Forward modeling yields a 20–30 m thick anisotropic layer at the bottom of the ice where the slow phase velocities can be matched quite well with the GK model. The fast phase velocities require a Vs in the bottom layer that is at least 10% higher. At 1936 m s^{-1}, this higher Vs remains well below the Vs obtained in the inversion (see case 1 in Fig. S6). A thinner, 20 m layer requires a higher Vs of 2024 m s^{-1} in the lower ice layer or a higher basement Vs of 2625 m s^{-1}. The elevated basement Vs has no impact on the fit to the slow phase velocities and is still a reasonable value found for limestone (Assefa and others, 2003). The option of the higher basement Vs (by 8% compared with that in Table 3) is not found in the formal inversion, possibly as a result of the internal inconsistency of the data.

SURFACE CREVASSE DETECTION FROM IMAGERY

Forward modeling and inversion of dispersion curves reveal, that the observed anisotropy beneath array A1 is associated

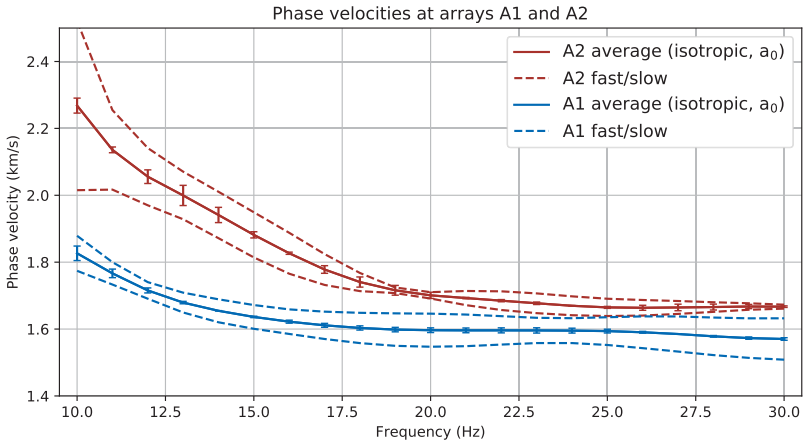

Fig. 8. Average (isotropic) phase velocities (solid lines with error bars) and fast and slow phase velocities (dashed lines) as obtained from the 2Ψ-coefficients. The error bars of the average dispersion curve represent the difference of the a_0 coefficients between the three-parameter fit and the five-parameter fit.

with the shallow ice. To test our hypothesis of crevasse-induced anisotropy, we determine the surface strike of the crevasses (direction parallel to the crevasses) at the A1 field site and compare the result with the observed fast direction of wave propagation.

To obtain the orientation of the crevasses, we apply the Canny edge detector (Canny, 1986) to orthophotographs (by swisstopo, SWISSIMAGE) of the glacier surface taken in 2015. Because the ice flow of Glacier de la Plaine Morte is negligible, we do not expect a change in crevasse pattern from the time of image acquisition in 2015 to our field campaign in 2016. Orthophotographs from 2016 are not usable because the snow cover did not vanish completely. Nevertheless, comparison of 2015 and 2016 images confirm that major features stay unmodified. We choose a 200 m × 200 m snippet from the 2015 images centered on the central station of array A1 (Fig. 12a) and load it as gray-scale image preserving the intensity information. First, we smooth the image using a two-dimensional Gaussian filter with a standard deviation of the Gaussian kernel of 3 in both directions. Second, we calculate the intensity gradients $\mathbf{G}_x$ and $\mathbf{G}_y$ of the image in x- (Fig. 12b) and y-direction (Fig. 12c) using Sobel kernels (e.g. Jähne and others, 1999). Since the crevasses on the orthophotograph appear as dark lines on the otherwise bright ice, the differentiation with respect to intensity reveals the crevasses as shown in Figs 12a–c. Ultimately, the orientation (or back azimuth) of the crevasses is obtained by the arctangent of the intensity-derivative ratio calculated for each pixel, that is, $\tan \Psi_k = G_{y,k}/G_{x,k}$ for the k-th pixel.

As can be seen from Figs. 12b and 12c, the crevasses are the dominant features detected by calculating the intensity gradients. In addition, a histogram calculated from all pixel orientations (Fig. 12d) yields a dominant orientation of approximately 55° (and 235°, i.e. 55° + 180°), which is in agreement with the surface strike of the crevasses as determined by visual inspection. Furthermore, comparing this with the average anisotropy fits in the frequency range 14–30 Hz (the frequency range where observed anisotropy is strongest; Fig. 6), we find that the Rayleigh waves propagate fastest in the direction of the crevasse surface strike (Fig. 12d).

At field site A2, azimuthal anisotropy is found at depth, and we should not expect to find that surface crevasses can explain our observations. Nevertheless, we find that the fast

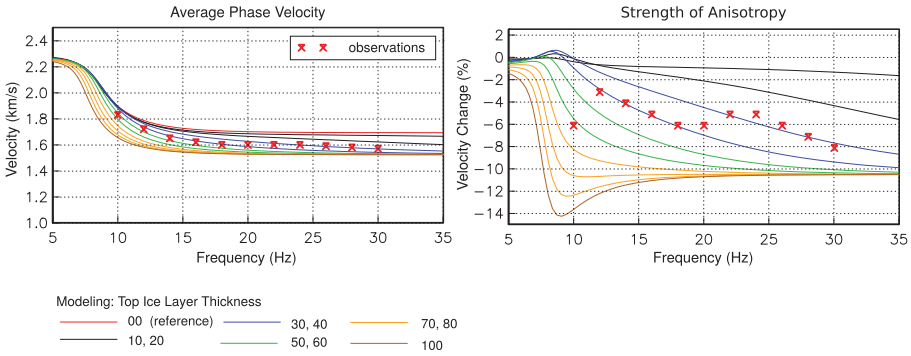

Fig. 9. Results from the final set of targeted forward modeling at array A1. The underlying model has two ice layers with an isotropic lower layer, and an anisotropic upper layer with varying thickness (marked by different colors) and 10% anisotropy. The total ice thickness was fixed at 100 m. See text for details.

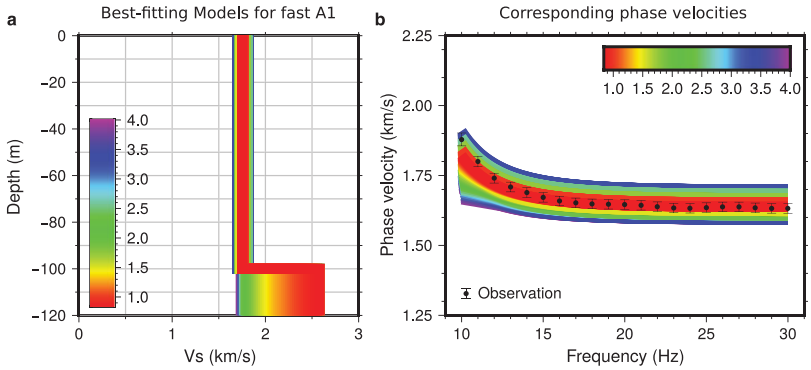

Fig. 10. (a) Best-fitting models for the fast phase velocities at array A1. (b) Corresponding predictions, different colors denote the misfit. Well-fitting models should have a misfit near 1 or less.

direction of wave propagation for low frequencies is parallel to the surface crevasses. This is shown in Fig. 13d by comparing the fast direction to the surface strike of the narrow crevasses as determined by means of visual inspection (brown dashed line in Figs. 13c and 13d). In this case, our image processing does not pick up the crevasses as dominant features. Reasons for this are (i) the crevasses at this field site are narrower (centimeter to decimeter scale) compared with array A1 and (ii) several supraglacial streams following the approximate topographic gradient are present. Consistent with visual inspection, the image processing yields the dominant direction of these supraglacial streams (blue dashed line in Figs. 13b and 13d). Even though the streams are surficial, water might also flow englacially in the shallow (~2 m), porous weathering crust (Irvine-Fynn and others, 2011; Cook and others, 2016). Since the water flow is in a preferred direction, structural anisotropy might be present in this layer. However, the weathering crust is formed by solar radiative heating (Fountain and Walder, 1998), thereby forming in a planar fashion, allowing the water to also distribute laterally away from the streams. Additionally, meltwater also penetrates the weathering crust directly where it is produced without draining in a supraglacial river. For this reason and due to the thinness of this layer, we do not expect that the weathering crust introduces strong anisotropy for seismic wave propagation.

DISCUSSION

In the case of crevasse-induced azimuthal anisotropy, we expect that the fast direction of Rayleigh-wave propagation is parallel to the crevasse alignment (Crampin, 1978). For array A1, we showed that such a correlation exists. Comparison of the fast direction at high frequencies (14–30 Hz) with the surface strike of crevasses (Fig. 12d) revealed that Rayleigh waves travel the fastest parallel to the crevasses. In addition, the estimated thickness of the crevassed, anisotropic layer of 30–40 m is within the theoretical and observed penetration depths of crevasses (Van Der Veen, 1998). Even though a maximum penetration depth of ~30 m is often stated for air-filled crevasses (e.g. Irvine-Fynn and others, 2011), deeper crevasses of this type have been reported (Colgan and others, 2016, and references therein). In the presence of water, crevasses can penetrate even substantially deeper (Van Der Veen, 1998).

Apart from preferentially aligned crevasses, crystal orientation fabric (COF) can introduce seismic anisotropy in glacial ice (e.g. Diez and others, 2014). In particular, a (thick) girdle fabric which is characterized by c-axis orientations of the single ice crystals in a vertical plane but with various angles relative to the horizontal represents a transversely isotropic medium with horizontal symmetry axis exhibiting azimuthal anisotropy (Diez and Eisen, 2015). Vs, and thus the most sensitive parameter for Rayleigh waves,

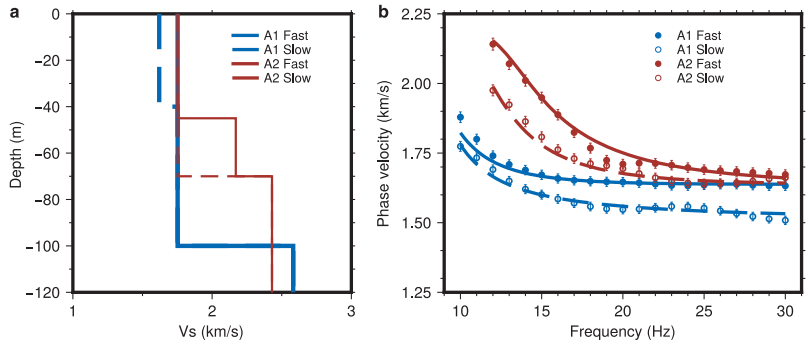

Fig. 11. (a) Summary plot showing both the fast (solid line) and slow (dashed line) Vs models at arrays A1 (blue) and A2 (red). (b) Data (circles) and model predictions (solid and dashed lines) for the Vs models on the left.

Table 2. Best-fitting models for Array A1

Layer thickness (m)	Vp (m s^{-1})	Vs (m s^{-1})	ρ (kg m^{-3})
fast model			
100	3630	1752	910
∞	4250	2582	2500
slow model			
40	3630	1620	910
60	3630	1752	910
∞	4250	2582	2500

can vary by more than 10% in such a medium (Maurel and others, 2015). However, in most (alpine) valley glaciers and on another plateau glacier in the same mountain range, multiple-maximum fabrics which contradict azimuthal anisotropy are found (Tison and Hubbard, 2000; Hudleston, 2015). For this reason – and given the correlation of fast direction with crevasse surface strike together with a reasonable thickness of the anisotropic layer – we interpret the observed azimuthal anisotropy beneath array A1 as crevasse-induced.

Compared with other cases of crack-induced anisotropy, the observed strength of up to 8% is an intermediate value. Bradford and others (2013) report only slightly more than 3% variation in p-wave velocity due to basal crevasses and Crampin (1994) reports 1.5–4.5% shear-wave velocity anisotropy due to cracks in the Earth's crust. For heavily cracked rocks close to the Earth's surface, 10% or more are found (Crampin, 1994). Two observations of anisotropy caused by crystal fabric orientation in glacial ice cover the range 3–5% shear-wave velocity (Picotti and others, 2015; Smith and others, 2017). Note, however, that these values are associated with shear-wave splitting in contrast to azimuthal variations of Vs_v as reported in this study. Incorporation of Vs_h-velocity measurements would allow us to study shear-wave splitting and thus crack density (Hudson, 1981; Crampin, 1981) but this is beyond the scope of this work.

In contrast to array A1, inversions for array A2 suggest that azimuthal anisotropy can be best explained by a 25-m-thick anisotropic layer at the base of the glacier with a shear velocity of 2170 m s^{-1} along the fast direction (Table 3). Targeted forward modeling revealed that the shear velocity in the lower ice layer trades off with its thickness as well as the basement velocity. Allowing a thicker ice layer or a higher basement velocity keeps the velocity in the lower ice layer below 2000 m s^{-1}. In the region of array A2, ice flow, even though small (smaller than 1 cm d^{-1} as measured during the field campaign), might provide stresses for ice crystal alignment (Cuffey and Paterson, 2010). However, recrystallization in temperate ice often counteracts the formation of COF favorable for azimuthal anisotropy (Cuffey and Paterson, 2010; Hudleston, 2015). In addition, even for a single ice crystal, neither the broad Vs-range from 1750 m s^{-1} to 2200 m s^{-1}, nor the high Vs of 2200 m s^{-1} as suggested by our inversions can be explained (Maurel and others, 2015). By contrast, slower shear velocities of 1950 m s^{-1} as found by our forward modeling seem more consistent with predictions for temperate ice with preferred ice crystal alignment (Kohnen, 1974; Diez and Eisen, 2015). Basal crevasses as found on Bench Glacier (Bradford and others, 2013), would require a low-velocity layer and can therefore not explain our inversion and modeling results.

Table 3. Best-fitting models for Array A2

Layer thickness (m)	Vp (m s^{-1})	Vs (m s^{-1})	ρ (kg m^{-3})
fast model			
45	3630	1752	910
25	3630	2170	910
∞	4250	2430	2500
slow model			
70	3630	1752	910
∞	4250	2430	2500

Because of the aforementioned issues in data coverage and quality, we are hesitant to draw definitive conclusions on the cause of the azimuthal anisotropy at array A2. In particular, insufficient coverage of icequakes may lead to overfitting of the data set (e.g. Burnham and Anderson, 2003). Additionally, our forward modeling and inversion approach of slow and fast dispersion curves might not be well-suited for this array since (i) (in contrast to array A1) only a narrow frequency band (around 15 Hz) shows clear azimuthal anisotropy and (ii) azimuthal data coverage is incomplete. Another issue at this array is the observation of surface crevasses which do not seem to induce azimuthal anisotropy at high frequencies. We, therefore, speculate that these surface cracks might be either too shallow or too narrow and sparse in order to result in measurable azimuthal anisotropy of the high-frequency Rayleigh waves. Another explanation would be that the infiltration of water into the ice along the surface streams results in a shallow anisotropic layer. In turn, since the streams strike approximately perpendicular to the crevasses, azimuthal anisotropy associated with this layer could potentially cancel the crevasses' signature at high frequencies.

At this point, it remains unclear why the measured dispersion curves at arrays A1 and A2 both suggest a thinner glacier compared with the helicopter-borne GPR survey. Regarding the latter, ice thickness values beneath the arrays are obtained by an interpolation of the values along the flight profiles. Inaccuracies introduced thereby, which are expected bigger for A1 than for A2 due to coarser data coverage, explain some though unlikely all of the disagreement. Additionally, errors in the ice thickness estimates from dispersion curve inversions might arise from 3-D-topography effects at the ice/bedrock interface which our horizontally-stratified model does not account for.

SUMMARY AND CONCLUSION

In this study, we used naturally occurring icequakes to investigate azimuthal anisotropy of Rayleigh waves on Glacier de la Plaine Morte, Switzerland. In a first step, we automated the task of locating icequakes using beamforming and triangulation from up to four arrays. Using the located events, we then examined the phase velocity of Rayleigh waves as a function of back azimuth of wave propagation and frequency. For array A1, we find azimuthal anisotropy for high frequencies (~15–30 Hz) and, by means of forward modeling as well as inversion of dispersion curves, we showed that the corresponding depth range is the shallow ice (upper 40 m). Furthermore, by analysis of the surface strike of crevasses, we conclude that the observed anisotropy is caused by the

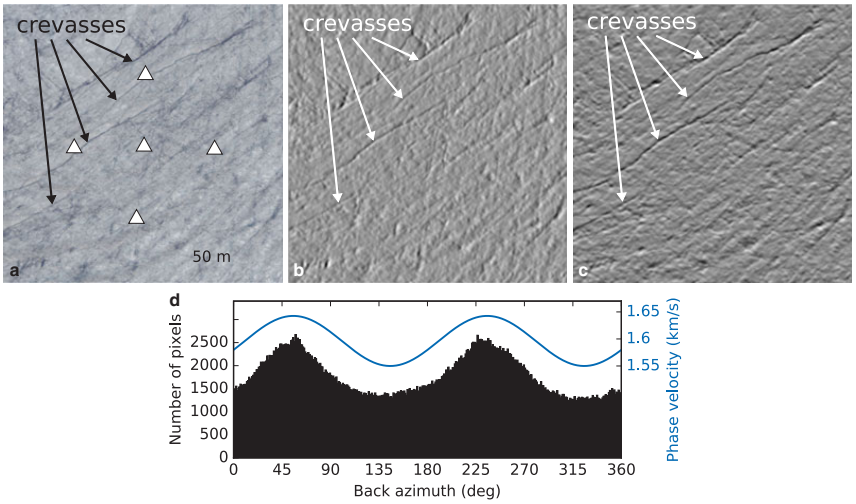

Fig. 12. Orientation of surface crevasses. (a) 200 m × 200 m orthophotograph of the glacier surface surrounding array A1 (white triangles). Some but not all crevasses are highlighted by arrows. Easting and Northing (in Swiss Grid coordinates) of the lower left corner are 605811 m and 136936 m, respectively. (b) Intensity-derivative in *x*-direction of a grayscale image version of (a) using Sobel kernels. (c) Same as (b) in *y*-direction. (d) Orientation (back azimuth) of surface structures evaluated for each pixel from intensity ratios of image in (c) and (b) (black histogram; see text for details). The blue curve is the frequency-averaged azimuthal anisotropy at array A1 for the frequency range 14–30 Hz.

preferential alignment of (near to vertical) surface crevasses. For array A2, we find evidence for azimuthal anisotropy at low frequencies, which most likely is caused by an anisotropic ice layer at the base of the glacier. Even though we are less confident in the results of this array due to poorer data quality and azimuthal distribution of icequakes compared with array A1, we argue that COF could be the cause for azimuthal anisotropy at this field site. Observed surface crevasses at array A2, though narrower compared with those at the array A1 and potentially less deep, do not seem to introduce measurable azimuthal anisotropy. This is potentially due to shallow, aligned water flow perpendicular to the crevasse strike counteracting the crevasse signal.

As determined from the orthophotographs, the biggest crevasses are approximately half a meter wide, but typical fractures observed on the glacier are on the centimeter to decimeter scale. These crevasses and fractures are found to cause anisotropy of up to ~8%. Considering that compared

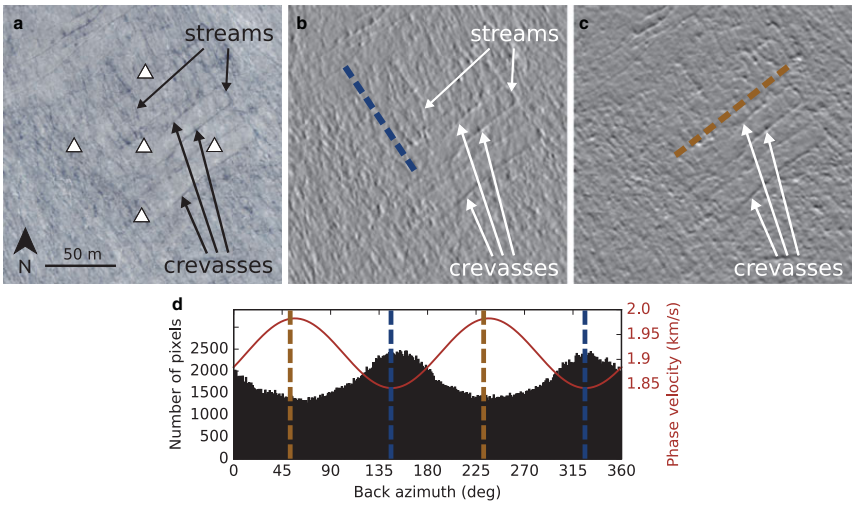

Fig. 13. Same as Fig. 12 but for array A2. (a) Easting and Northing (in Swiss Grid coordinates) of the lower left corner are 605351 m and 137346 m, respectively. In (b) and (c), the approximate surface strike of supraglacial meltwater streams and crevasses are indicated by the dashed blue and brown lines, respectively. The back azimuth of these lines are also shown in (d). The red line in (d) shows the average azimuthal anisotropy found in the frequency range 12–16 Hz. Note that our image processing picks up the orientation of the streams and not the orientation of the crevasses.

with other more dynamic glaciers, crevasses on Glacier de la Plaine Morte are sparse and narrow, we expect that wave propagation at other field sites with heavily fractured ice is influenced even more in terms of anisotropy.

Our study shows that, apart from active-source methods, passive seismological measurements can be considered for the investigation of azimuthal anisotropy and the englacial fracture state of ice bodies in the future. By continuously collecting data, the passive method is especially promising for monitoring the englacial fracture state.

SUPPLEMENTARY MATERIAL

The supplementary material for this article can be found at https://doi.org/10.1017/aog.2018.25.

ACKNOWLEDGMENTS

We gratefully acknowledge support from the National Swiss Science Foundation under project Glacial Hazard Monitoring with Seismology (GlaHMSeis, PP00P2 157551). The geophones and DataCubes for 15 stations were provided by the Geophysical Instrument Pool Potsdam (GIPP) under project AnICEotropy. The field campaign was partially financed by the Cecil and Ida Green Foundation and UC San Diego grant RP074S-LASKE. The modeling of azimuthal anisotropy was supported by U.S. National Science Foundation Grant EAR-14-46978. This article is based upon work from COST Action ES1401-TIDES, supported by COST (European Cooperation in Science and Technology). We are indebted to our technicians Pascal Graf, Christian Scherrer and Thomas Wyder and to Andreas Bauder, Loris Compagno, Florent Gimbert, Stephan Kammerer, Johannes Kobel, Giulia Mazzotti, Lukas Preiswerk, Julien Seguinot and Cornelius Senn for their support in the field and for fruitful discussions. We appreciate the constructive comments and suggestions of the scientific editor Douglas MacAyeal, one anonymous reviewer and Anja Diez which helped to improve this article. We used Python and the ObsPy package (Beyreuther and others, 2010) for data processing. The figures were created using the Matplotlib plotting library for Python (Hunter, 2007) and the Generic Mapping Tools (Wessel and others, 2013).

REFERENCES

Allen RV (1978) Automatic earthquake recognition and timing from single traces. *Bull. Seismol. Soc. Am.*, **68**(5), 1521–1532.

Alvizuri C and Tanimoto T (2011) Azimuthal anisotropy from array analysis of Rayleigh waves in Southern California. *Geophys. J. Int.*, **186**(3), 1135–1151 (doi: 10.1111/j.1365-246X.2011.05093.x)

Assefa S, McCann C and Sothcott J (2003) Velocities of compressional and shear waves in limestones. *Geophys. Prospect.*, **51** (1), 1–13 (doi: 10.1046/j.1365-2478.2003.00349.x)

Aster R and Winberry P (2017) Glacial seismology. *Rep. Prog. Phys.*, **80**, 0–74 (doi: 10.1088/1361-6633/aa8473)

Bakulin A, Grechka V and Tsvankin I (2000) Estimation of fracture parameters from reflection seismic data–Part I: HTI model due to a single fracture set. *Geophys.*, **65**(6), 1788 (doi: 10.1190/1.1444863)

Backus GE (1965) Possible forms of seismic anisotropy of the uppermost mantle under oceans. *J. Geophys. Res.*, **70**(14), 3429–3439 (doi: 10.1029/JZ070i014p03429)

Bartholomaus TC and 5 others (2015) Subglacial discharge at tidewater glaciers revealed by seismic tremor. *Geophys. Res. Lett.*, **42**, 2–9 (doi: 10.1002/2015GL064590.Received)

Benn DI, Warren CR and Mottram RH (2007) Calving processes and the dynamics of calving glaciers. *Earth-Sci. Rev.*, **82**, 143–179.

Beyreuther M and 5 others (2010) ObsPy: a Python toolbox for seismology. *Seismol. Res. Lett.*, **81**(3), 530–533.

Bradford JH, Nichols J, Harper JT and Meierbachtol T (2013) Compressional and em wave velocity anisotropy in a temperate glacier due to basal crevasses, and implications for water content estimation. *Ann. Glaciol.*, **54**(64), 168–178 (doi: 10.3189/2013AoG64A206)

Burnham KP and Anderson DR (2003) *Model Selection and Multi-Model Inference: A Practical Information-Theoretic Approach*. Springer Science & Business Media, New York, USA (doi: 10.1016/j.ecolmodel.2003.11.004)

Canny J (1986) A computational approach to edge detection. *IEEE Trans. Pattern Anal. Mach. Intell.*, **PAMI-8**(6), 679–698 (doi: 10.1109/TPAMI.1986.4767851)

Colgan W and 6 others (2016) Glacier crevasses: observations, models, and mass balance implications. *Rev. Geophys.*, 1–31 (doi: 10.1002/2014RG000468)

Cook JM, Hodson AJ and Irvine-Fynn TDL (2016) Supraglacial weathering crust dynamics inferred from cryoconite hole hydrology. *Hydrol. Process.*, **30**(3), 433–446 (doi: 10.1002/hyp.10602)

Crampin S (1978) Seismic-wave propagation through a cracked solid: polarization as a possible dilatancy diagnostic. *Geophys. J. R. Astron. Soc.*, **53**(3), 467–496 (doi: 10.1111/j.1365-246X.1978.tb03754.x)

Crampin S (1981) A review of wave motion in anisotropic and cracked elastic-media. *Wave. Motion.*, **3**(4), 343–391 (doi: 10.1016/0165-2125(81)90026-3)

Crampin S (1994) The fracture criticality of crustal rocks. *Geophys. J. Int.*, **118**, 428–438

Crampin S, McGonigle R and Bamford D (1980) Estimating crack parameters from observations of *P*-wave velocity anisotropy. *Geophys.*, **45**(3), 345–360 (doi: 10.1190/1.1441086)

Cuffey K and Paterson W (2010) *The physics of glaciers*. Academic Press, Oxford, UK

Das SB and 6 others (2008) Fracture propagation to the base of the Greenland Ice Sheet during supraglacial lake drainage. *Science*, **1**(May), 778–781 (doi: 10.1017/CBO9781107415324.004)

Diez A and Eisen O (2015) Seismic wave propagation in anisotropic ice – Part 1: elasticity tensor and derived quantities from ice-core properties. *Cryosphere*, **9**(1), 367–384 (doi: 10.5194/tc-9-367-2015)

Diez A and 7 others (2014) Influence of ice crystal anisotropy on seismic velocity analysis. *Ann. Glaciol.*, **55**(67), 97–106 (doi: 10.3189/2014AoG67A002)

Diez A and 8 others (2016) Ice shelf structure derived from dispersion curve analysis of ambient seismic noise, Ross Ice Shelf, Antarctica. *Geophys. J. Int.*, **205**(2), 785–795 (doi: 10.1093/gji/ggw036)

Fahnestock M, Bindschadler R, Kwok R and Jezek K (1993) Greenland Ice Sheet surface properties and Ice Dynamics from ERS-1 SAR imagery. *Science*, **262**(5139), 1530–1534 (doi: 10.1126/science.262.5139.1530)

Finger D and 13 others (2013) Identification of glacial meltwater runoff in a karstic environment and its implication for present and future water availability. *Hydrol. Earth Syst. Sci.*, **17**(8), 3261–3277 (doi: 10.5194/hess-17-3261-2013)

Flowers GE and Clarke GKC (2002) A multicomponent coupled model of glacier hydrology 1. Theory and synthetic examples. *J. Geophys. Res. Solid. Earth.*, **107**(B11), ECV 9–1–ECV 9–17 (doi: 10.1029/2001JB001122)

Fountain AG and Walder JS (1998) Water flow through temperate glaciers. *Rev. Geophys.*, **36**(97), 299

Freed-Brown J, Amundson JM, MacAyeal DR and Zhang WW (2012) Blocking a wave: frequency band gaps in ice shelves with periodic crevasses. *Ann. Glaciol.*, **53**(60), 85–89 (doi: 10.3189/2012AoG60A120)

Gerstoft P and Tanimoto T (2007) A year of microseisms in southern California. *Geophys. Res. Lett.*, **34**(20), L20304 (doi: 10.1029/2007GL031091)

Gimbert AF, Tsai VC, Bartholomaus TC, Jason M and Walter JI (2016) Sub-seasonal pressure, geometry and sediment transport changes observed in subglacial channels. *Geophys. Res. Lett.*, **43**, 3786–3794 (doi: 10.1002/2016GL068337)

Haney MM and Tsai VC (2017) Perturbational and nonperturbational inversion of Rayleigh-wave velocities. *Geophys.*, **82**(3), F15–F28 (doi: 10.1190/geo2016-0397.1)

Harper JT, Bradford JH, Humphrey NF and Meierbachtol TW (2010) Vertical extension of the subglacial drainage system into basal crevasses. *Nature*, **467**(7315), 579–582 (doi: 10.1038/nature09398)

Hudleston PJ (2015) Structures and fabrics in glacial ice: a review. *J. Struct. Geol.*, **81**, 1–27 (doi: 10.1016/j.jsg.2015.09.003)

Hudson JA (1981) Wave speeds and attenuation of elastic waves in material containing cracks. *Geophys. J. R. Astron. Soc.*, **64**, 133–150 (doi: 10.1111/j.1365-246X.1981.tb02662.x)

Hunter JD (2007) Matplotlib: A 2D graphics environment. *Comput. Sci. Eng.*, **9**(3), 90–95.

Huss M, Voinesco A and Hoelzle M (2013) Implications of climate change on Glacier de la Plaine Morte, Switzerland. *Geogr. Helv.*, **68**(4), 227–237 (doi: 10.5194/gh-68-227-2013)

Iken A and Bindschadler RA (1986) Combined measurements of subglacial water pressure and surface velocity of Findelengletscher, Switzerland: conclusions about drainage system and sliding mechanism. *J. Glaciol.*, **32**(110), 101–119

Irvine-Fynn TDL, Hodson AJ, Moorman BJ, Vatne G and Hubbard AL (2011) Polythermal glacier hydrology: a review. *Rev. Geophys.*, **49**(2010), 1–37 (doi: 10.1029/2010RG000350)

Jähne B and Haussecker H and Geissler P (1999) *Handbook of Computer Vision and Applications*. 2nd Edn. Citeseer, San Diego, USA

Jezek K and Bentley C (1979) Electromagnetic sounding of bottom crevasses on the Ross Ice Shelf, Antarctica. *J. Glaciol.*, **24**(90), 321–330

Kohnen H (1974) The temperature dependence of seismic waves. *J. Glaciol.*, **13**(67), 144–147.

Krimmel RM and Meier MF (1975) Glacier applications of ERTS images. *J. Glaciol.*, **15**, 391–402.

Langhammer L and 6 others (2018) Glacier bed surveying with helicopter-borne dual-polarization ground-penetrating radar. *J. Glaciol.*, in press

Maurel A, Lund F and Montagnat M (2015) Propagation of elastic waves through textured polycrystals: application to ice. *Proc. Royal Soc. A: Math. Phys. Eng. Sci.*, **471**(2177), 20140988–20140988 (doi: 10.1098/rspa.2014.0988)

Montagner JP and Anderson DL (1989) Petrological constraints on seismic anisotropy. *Phys. Earth. Planet. Inter.*, **54**(1–2), 82–105 (doi: 10.1016/0031-9201(89)90189-1)

Montagner JP and Nataf HC (1986) A simple method for inverting the azimuthal anisotropy of surface waves. *J. Geophys. Res.*, **91**, 511–520.

Navarro FJ, Macheret YY and Benjumea B (2005) Application of radar and seismic methods for the investigation of temperate glaciers. *J. Appl. Geophy.*, **57**(3), 193–211 (doi: 10.1016/j.jappgeo.2004.11.002)

Neave KG and Savage JC (1970) Icequakes on the Athabasca Glacier. *J. Geophys. Res.*, **75**(8), 1351 (doi: 10.1029/JB075i008p01351)

Phillips T, Rajaram H and and Steffen K (2010) Cryo-hydrologic warming: a potential mechanism for rapid thermal response of ice sheets. *Geophys. Res. Lett.*, **37**(20), L20503 (doi: 10.1029/2010GL044397)

Picotti S, Vuan A, Carcione JM, Horgan HJ and Anandakrishnan S (2015) Anisotropy and crystalline fabric of Whillans Ice Stream (West Antarctica) inferred from multicomponent seismic data. *J. Geophys. Res. B: Solid. Earth.*, **63**, 4237–4262 (doi: 10.1002/2014JB011591)

Podolskiy EA and Walter F (2016) Cryoseismology. *Rev. Geophys.*, **54**, 119–161. (doi: 10.1002/2015RG000504.Received)

Pralong A and Funk M (2005) Dynamic damage model of crevasse opening and application to glacier calving. *J. Geophys. Res. B: Solid. Earth.*, **110**(1), 1–12 (doi: 10.1029/2004JB003104)

Rost S and Thomas C (2002) Array seismology: methods and applications. *Rev. Geophys.*, **40**(3), 1008 (doi: 10.1029/2000RG000100)

Röthlisberger H (1977) Ice avalanches. *J. Glaciol.*, **19**(81), 669–671.

Roux PF, Walter F, Riesen P, Sugiyama S and Funk M (2010) Observation of surface seismic activity changes of an Alpine glacier during a glacier-dammed lake outburst. *J. Geophys. Res. Earth. Surf.*, **115**(3), 1–13, ISSN 21699011 (doi: 10.1029/2009JF001535)

Sambridge M (1999a) Geophysical inversion with a neighbourhood algorithm-II. Appraising the ensemble. *Geophys. J. Int.*, **138**, 727–746 (doi: 10.1046/j.1365-246x.1999.00900.x)

Sambridge M (1999b) Geophysical inversion with a neighbourhood algorithm-I. Searching a parameter space. *Geophys. J. Int.*, **138** (May), 479–494 (doi: 10.1046/j.1365-246x.1999.00900.x)

Savage MK (1999) Seismic anisotropy and mantle deformation: what have we learnt from shear wave splitting?. *Rev. Geophys.*, **37**(1), 65–106 (doi: 10.1029/98RG02075)

Smith ML and Dahlen Fa (1973) The azimuthal dependence of Love and Rayleigh wave propagation in a slightly anisotropic medium. *J. Geophys. Res.*, **78**(17), 3321 (doi: 10.1029/JB078i017p03321)

Smith EC and 6 others (2017) Ice fabric in an Antarctic ice stream interpreted from seismic anisotropy. *Geophys. Res. Lett.*, **44**(8), 3710–3718 (doi: 10.1002/2016GL072093)

Tison JL and Hubbard B (2000) Ice crystallographic evolution at a temperate glacier: Glacier de Tsanfleuron, Switzerland. *Geol. Soc. London.*, Special Publications, **176**(1), 23–38 (doi: 10.1144/GSL.SP.2000.176.01.03)

Van Der Veen CJ (1998) Fracture mechanics approach to penetration of surface crevasses on glaciers. *Cold. Reg. Sci. Technol.*, **27**(1), 31–47 (doi: 10.1016/S0165-232X(97)00022-0)

Walter F (2009) *Seismic activity on Gornergletscher during Gornersee Outburst Floods*. Ph.D. thesis

Walter F and 5 others (2009) Moment tensor inversions of icequakes on Gornergletscher, Switzerland. *Bull. Seismol. Soc. Am.*, **99** (212), 3–33 (doi: 10.1785/0120080110)

Walter F, Dreger DS, Clinton JF, Deichmann N and Funk M (2010) Evidence for near-horizontal tensile faulting at the base of Gornergletscher, Switzerland. *Bull. Seismol. Soc. Am.*, **100**(2), 458–472 (doi: 10.1785/0120090083)

Walter F and 5 others (2015) Using glacier seismicity for phase velocity measurements and Green's function retrieval. *Geophys. J. Int.*, **201**(3), 1722–1737 (doi: 10.1093/gji/ggv069)

Wathelet M, Jongmans D and Ohrnberger M (2004) Surface wave inversion using a direct search algorithm and its application to ambient vibration measurements. *Near Surf. Geophys.*, **2**, 211–221

Wathelet M, Jongmans D, Ohrnberger M and Bonnefoy-Claudet S (2008) Array performances for ambient vibrations on a shallow structure and consequences over Vs inversion. *J. Seismol.*, **12** (1), 1–19 (doi: 10.1007/s10950-007-9067-x)

Weaver CS and Malone SD (1979) Seismic evidence for discrete glacier motion at the rock-ice interface. *J. Glaciol.*, **23**(89), 171–184 (doi: 10.1017/S0022143000029816)

Wessel P, Smith WHF, Scharroo R, Luis J and Wobbe F (2013) Generic mapping tools: improved version released. *Eos, Trans. Am. Geophys. Union.*, **94**(45), 409–410.

Winberry JP, Anandakrishnan S, Wiens DA, Alley RB and Christianson K (2011) Dynamics of stick-slip motion, Whillans Ice Stream, Antarctica. *Earth. Planet. Sci. Lett.*, **305**(3-4), 283–289 (doi: 10.1016/j.epsl.2011.02.052)

Zhan Z, Tsai VC, Jackson JM and Helmberger D (2013) Ambient noise correlation on the Amery Ice Shelf, East Antarctica. *Geophys. J. Int.*, **196**, 1–7 (doi: 10.1093/gji/ggt488)

3 Acknowledgements

Appendix B contains details of modeling I performed as part of an experiment analyzing high-frequency surface wave phase velocities measured on an alpine glacier. The appendix also includes a reformatted version of the resulting publication in the Annals of Glaciology: Lindner, F., and Laske, G., and Walter, F., and A.K. Doran (2018), Crevasse-induced Rayleigh wave azimuthal anistropy on Glacier de la Plaine Morte, Swizterland, Ann. Glaciol., DOI: 10.1017/aog.2018.25.

C Research Notes

1 Scaling relations between elastic parameters in the oceanic crust

In this section is a compilation of scaling relationships between elastic parameters in the oceanic crust. These relationships were culled from literature reviews while studying the Hawaiian crust. I found it very useful to have this information in one location.

1.1 Sediments

Table C.1: Equations relating α to depth. ${}^{*}\alpha$ indicates that α is in km/s and z is in km, while ${}^{+}\alpha$ indicates that α is in m/s and z is in m.

$\alpha(z)$	Source	Additional Info
${}^{*}\alpha = 1.511 + 1.304z - 0.417z^2 + 0.257z^3$	Hamilton (1979b,c)	Valid for silt clays, turbidites, and mudstones, $z <$ 1km.
${}^{+}\alpha = 1806z^{0.015}$	Hamilton (1979b,c)	Valid for sands, $z <$20m.
${}^{*}\alpha = 0.43z + 1.83$	Nafe and Drake (1957)	Valid for sediments in deep water ($z >$ 1500 fathoms, or 2740 m).

Table C.2: Equations relating β to depth. $^{*}\beta$ indicates that β is in km/s and z is in km, while $^{+}\beta$ indicates that β is in m/s and z is in m.

$\beta(z)$	Source	Additional Info
$^{+}\beta(z) = 116 + 4.65z$	Hamilton (1976b, 1979b)	Valid for silt clays and turbidites, $0 < z < 36$m
$^{+}\beta(z) = 237 + 1.28z$	Hamilton (1976b, 1979b)	Valid for silt clays and turbidites, $36 < z < 120$m
$^{+}\beta(z) = 322 + 0.58z$	Hamilton (1976b, 1979b)	Valid for silt clays and turbidites, $120 < z < 650$m
$^{+}\beta(z) = 128z^{0.28}$	Hamilton (1976b, 1979b)	Valid for sands, $z < 20$m
$^{*}\beta(z) = (0.02z^2 + 1.27z + 0.048)/(z + 0.48)$	Ruan et al. (2014)	Study performed in Cascadia
$^{*}\beta(z) = (0.156z^2 + 1.22z + 0.049)/(z + 0.495)$	Bell et al. (2015b)	Study performed in Cascadia

Table C.3: Equations relating ρ to depth. In all equations, ρ is in g/cm^3 and z is in km.

$\rho(z)$	Source	Additional Info
$\rho(z) = 1.512 + 1.631z - 1.373z^2$	Hamilton (1976a)	Valid for deep-sea calcareous sediment, $z \leq 0.5$km
$\rho(z) = 1.172 + 0.021z - 4.697z^2$	Hamilton (1976a)	Valid for deep-sea radiolarian ooze, $z \leq 0.25$km
$\rho(z) = 1.357 + 1.338z - 0.284z^2$	Hamilton (1976a)	Valid for deep-sea pelagic clay, $z \leq 0.3$km
$\rho(z) = 1.240 + 0.757z - 0.685z^2$	Hamilton (1976a)	Valid for deep-sea diatomaceous ooze, $z \leq 0.5$km
$\rho(z) = 1.530 + 1.395z - 0.617z^2$	Hamilton (1976a)	Valid for deep-sea terrigenous sediment, $z \leq 1.0$km

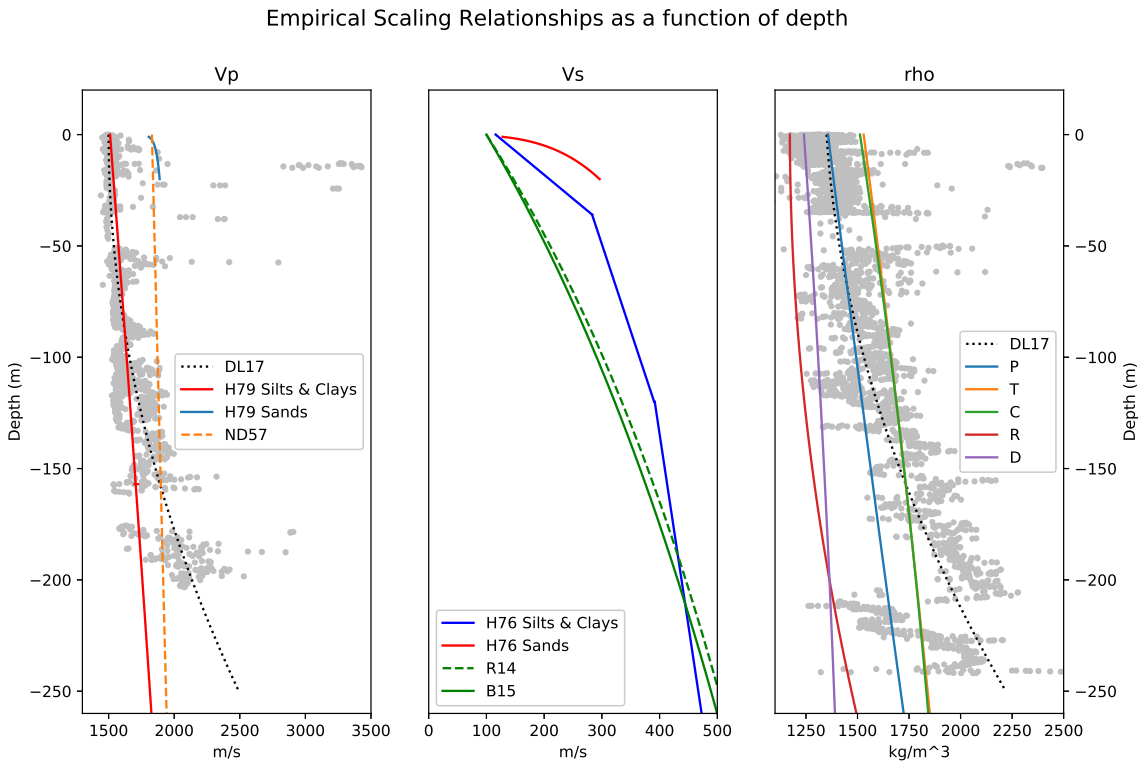

Figure C.1: Scaling relations as a function of depth for marine sediments. The gray dots represent combined well data collected from ODP sites 1223, 1215, 843A, 843B, 843C, 842A, and 842B . Only α and ρ data are available from these sites. All model equations are shown in the accompanying tables. (A) Models and data for $\alpha(z)$. The models are: H79 Silts and clays (Hamilton, 1979b,c), H79 Sands (Hamilton, 1979b,c), and ND57 (Nafe and Drake, 1957). None of the published models appear to fit the well data, each performing better at different depth ranges, so we introduce a new polynomial equation to model $\alpha(z)$. (B) Models for $\beta(z)$. No well measurements of β are available from the drill logs in this area. The models are: H76 Silts and clays (Hamilton, 1976b, 1979b), H76 Sands (Hamilton, 1976b, 1979b), R14 (Ruan et al., 2014), and B15 (Bell et al., 2015b). R14 and B15 are taken from studies of sediments around Cascadia. (C) Models and data for $\rho(z)$. All models are from Hamilton (1979c), with the letters corresponding to: P (pelagic), R (radiolarian ooze), C (calcareous), T (terrigenous), and D (diatomaceous ooze). As with the published $\alpha(z)$ models, none of the density profiles appear to fit the data. Here we again propose a new polynomial fit.

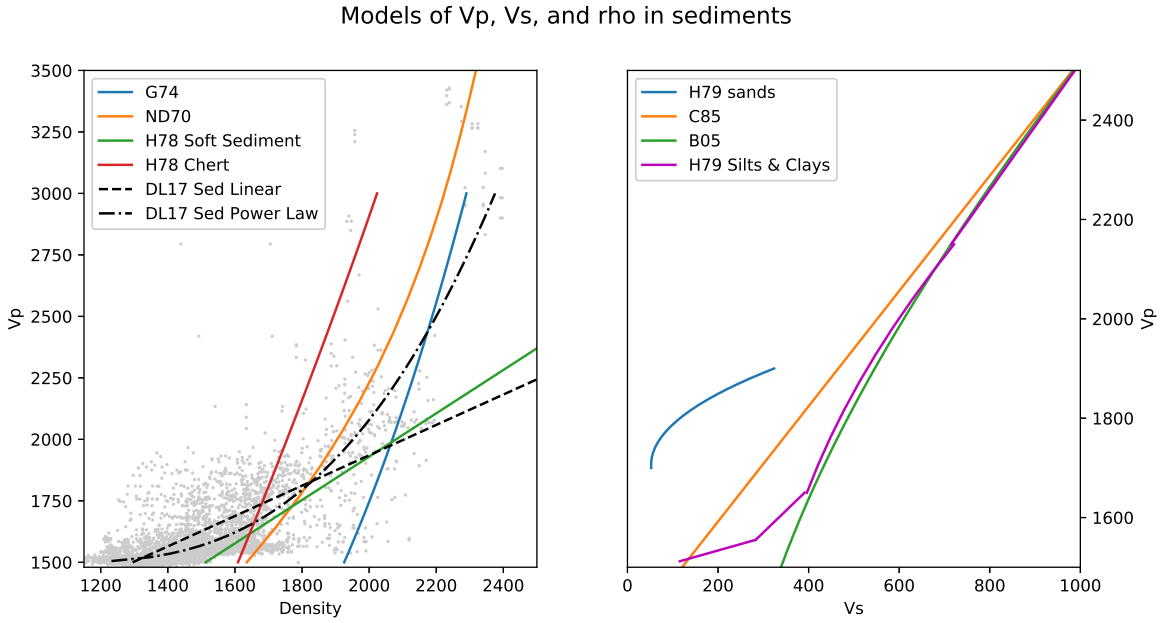

Figure C.2: Scaling relations between physical parameters in sediments. (A) α as a function of ρ. The well data from ODP 843 are shown for reference. The published models shown are: G74 (Gardner et al., 1974), ND70 (Ludwig et al., 1970; Brocher, 2005), H78 Soft Sediment (Hamilton, 1978), and H78 Chert (Hamilton, 1978). (B) α as a function of β. The published models shown are: H78 Silts & Clays (Hamilton, 1979b), H79 Sands (Hamilton, 1979b), C85 (Castagna et al., 1985), and B05 (Brocher, 2005). All models are proposed to be valid for α as low as 1.5 km/s, which should be the lower limit in marine sediments.

Table C.4: Equations relating α to ρ in sediments.

$\rho(\alpha)$	Source	Additional Info
$\rho(\alpha) = 1.6612\alpha - 0.4721\alpha^2 + 0.0671\alpha^3 - 0.0043\alpha^4 + 0.000106\alpha^5$	Ludwig et al. (1970); Brocher (2005)	Valid for $1.5 < \alpha < 8.5$
$\rho(\alpha) = 1.74\alpha^{0.25}$	Gardner et al. (1974); Brocher (2005)	Valid for $1.5 < \alpha < 6.1$
$\rho(\alpha) = 1.135\alpha - 0.190$	Hamilton (1978)	Soft marine sediments 0-500m thick
$\rho(\alpha) = 1.124\alpha + 0.347\alpha - 0.0157\alpha^2$	Hamilton (1978)	Valid for orcelanite-chert-quartz

Table C.5: Equations relating α to β in sediments.

$\beta(\alpha)$	Source	Additional Info
$\beta(\alpha) = (\alpha - 1.36)/1.16$	Castagna et al. (1985); Brocher (2005)	'Mudrock line' valid for $1.5 < \alpha < 4.25$
$\beta(\alpha) = 0.7875 - 1.2344\alpha + 0.7949\alpha^2 - 0.1238\alpha^3 + 0.0064\alpha^4$	Brocher (2005)	Valid for $1.5 < \alpha < 8.0$
$\beta(\alpha) = 21.05 - 24.617\alpha + 7.215\alpha^2$	Hamilton (1979b)	Valid in marine sands. α, β in km/s
$\beta(\alpha) = 3.884\alpha - 5.757$	Hamilton (1979b)	Valid for $1.512 < \alpha < 1.555$
$\beta(\alpha) = 1.137\alpha - 1.485$	Hamilton (1979b)	Valid for $1.555 < \alpha < 1.650$
$\beta(\alpha) = 0.991 - 1.136\alpha + 0.47\alpha^2$	Hamilton (1979b)	Valid for $1.650 < \alpha < 2.150$
$\beta(\alpha) = 0.78\alpha - 0.962$	Hamilton (1979b)	Valid for $\alpha > 2.150$

1.2 Crust

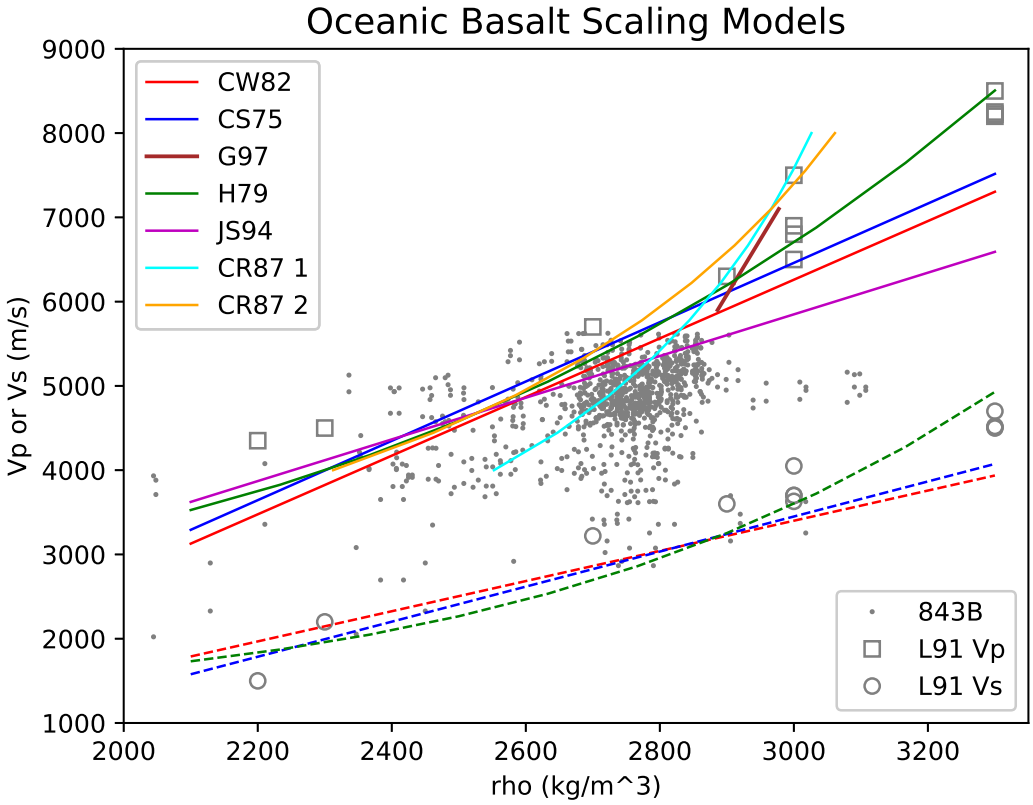

Figure C.3: α and β as a function of ρ in the basaltic crust. Solid lines represent α and dashed lines represent β. The scaling models shown are: CW (Christensen and Wilkens, 1982), CS75 (Christensen and Salisbury, 1975), G97 (Godfrey et al., 1997), H79 (Hamilton, 1979b), JS94 (Johnson and Semyan, 1994), CR87 1 (Carlson and Raskin, 1984, porous basalts), and CR87 2 (Carlson and Raskin, 1984, laboratory measurements). The gray squares and circles represent α and β values, respectively, from the Hawaiian crustal model of Lindwall (1991), and the dots represent point measurements logged from hole ODP 843B (Dziewonski et al., 1992a).

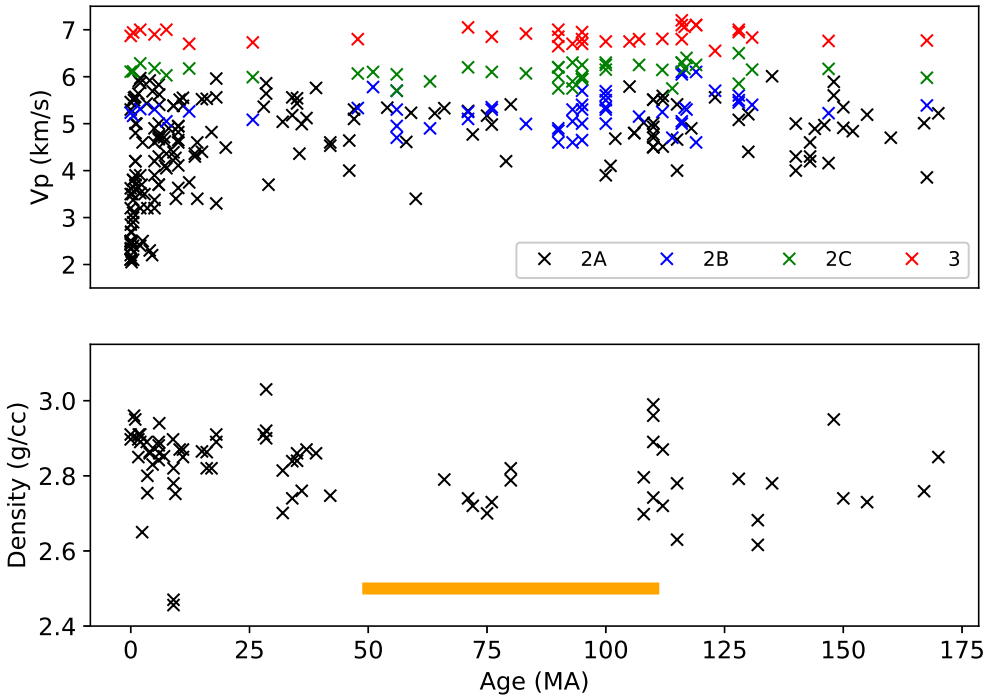

Figure C.4: Density and compressional velocity against age for oceanic layers 2A, 2B, 2C, and 3. Data are compiled from Jarrard et al. (2003), Johnson and Semyan (1994), Carlson (1998), and Houtz (1976). The yellow bar marks the approximate crustal ages covered by the PLUME network.

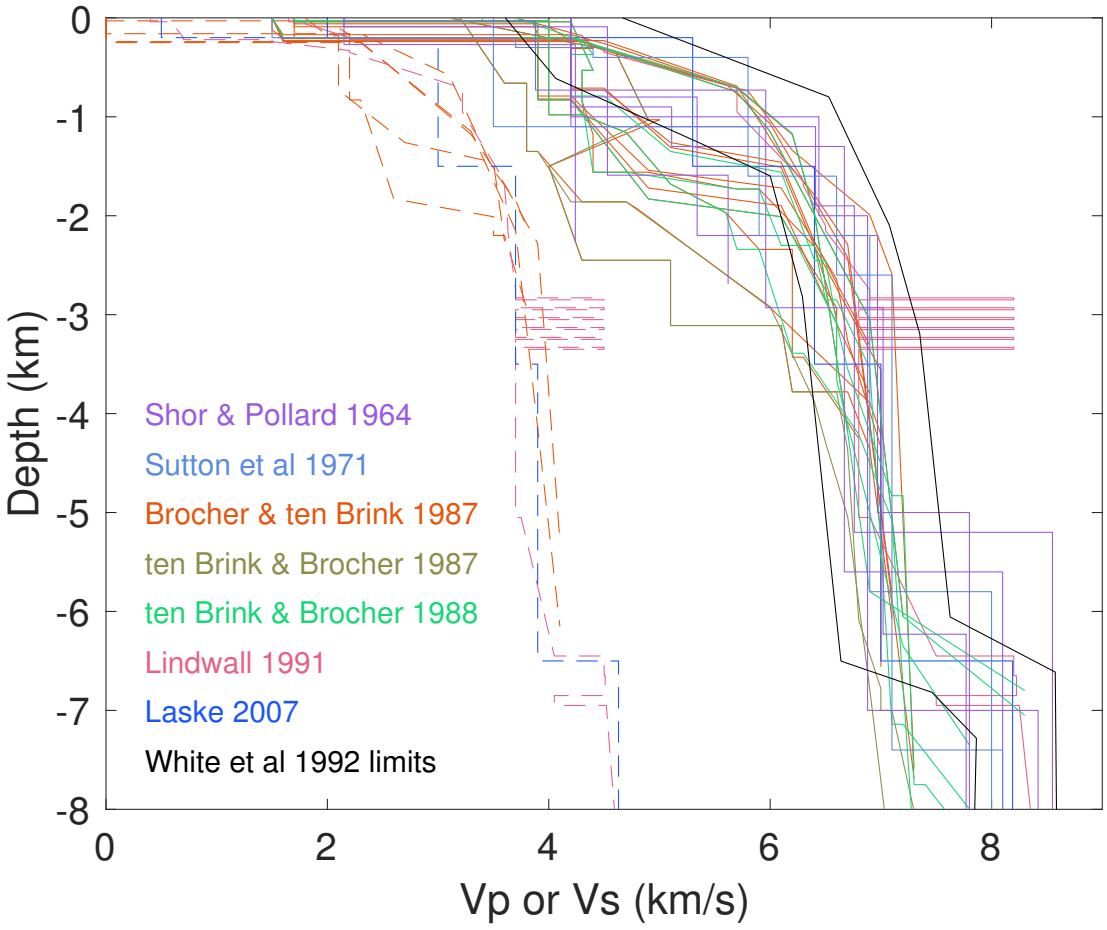

Figure C.5: A sample of the range of inferred crustal models across the Hawaiian Swell. The crustal models are presented by Shor and Pollard (1964), Sutton et al. (1971), Brocher and ten Brink (1987), ten Brink and Brocher (1987), ten Brink and Brocher (1988), Lindwall (1991), and Laske et al. (2007). The black lines represent upper and lower bounds on velocity in Pacific crust $>$ 29Ma presented by White et al. (1992). Solid lines represent α and dashed lines represent β. Dependence of the models as a function of distance from the island chain is masked in this plot, but we see general ranges of published α and β profiles.

Table C.6: Basalt relationships

	Source	Additional Info
$\alpha(\rho) = -4.18 + 3.48\rho$	Christensen and Wilkens (1982)	From basalts collected in Iceland
$\alpha(\rho) = -4.10 + 3.52\rho$	Christensen and Salisbury (1975)	From DSDP basalts collected near Iceland
$\alpha(\rho) = 2.473\rho - 1.57$	Johnson and Semyan (1994)	From DSDP and ODP sites
$\alpha(\rho) = 2.33 + 0.081\rho^{3.63}$	Hamilton (1979b)	From water-saturated DSDP basalts
$\rho(\alpha) = 3.81 - 5.99/\alpha$	Carlson and Raskin (1984)	Derived from DSDP and ophiolite samples
$\rho(\alpha) = 3.50 - 3.79/\alpha$	Carlson and Raskin (1984)	Derived for porous basalt formations
$\rho(\alpha) = 3.4372 + 0.0761\alpha$	Godfrey et al. (1997); Brocher (2005)	Valid for balsalt, diabase, and gabbro for $5.9 < \alpha < 7.1$
$\beta(\rho) = -1.97 + 1.79\rho$	Christensen and Wilkens (1982)	From Basalts collected in Iceland
$\beta(\rho) = -2.79 + 2.08\rho$	Christensen and Salisbury (1975)	From Basalts collected in Iceland
$\beta(\rho) = 1.33 + 0.011\rho^{4.85}$	Hamilton (1979b)	From water-saturated DSDP basalts

1.3 Poisson's Ratio

Hyndman (1979) finds typical poisson ratio of 0.30 in the oceanic crust, varying from 0.28 in the upper crust to 0.31 in the lower crust, and 0.24 in the upper mantle. Christensen (1996) also presents an average oceanic crustal Poisson of 0.3 Several studies have found very low Poisson's ratios (σ between 0.20-0.25) in layer 2 in Pacific crust (e.g., Spudich and Orcutt, 1980a,b; Au and Clowes, 1984), significantly less than most laboratory studies. Shearer (1988) found this can be explained by cracking of the media and not different lithology, although was not able to prove conclusively this was the cause. Collier and Singh (1998) find a Poisson's ratio of 0.48 at the very top of the oceanic crust and one that remains above 0.4 throughout layer 2A, but drops down to 0.25 in layer 2B. Brocher (2005) and Ludwig et al. (1970) present Vp/Vs as a function of Vp, finding values between 1.75 and 1.8 for α between 5.5 and 8.5. Brocher's mafic line, valid for $5.25 < \alpha < 7.25$ km/s, is defined as:

$$\beta = 2.88 + 0.52(\alpha - 5.25) \tag{C.1}$$

Ludwig's empirical fit for Poisson's ratio as a function of Vp is given by:

$$\sigma = 0.769 - 0.226\alpha + 0.0316\alpha^2 - 0.0014\alpha^3 \tag{C.2}$$

Some studies suggest that Poisson's ratio reaches a minimum somewhere between 1-1.5km depth and then climbs back to 0.3 at the base of the crust; however, Shaw (1994) suggests that this effect disappears for crust older than 60Ma. There is also evidence that cracking and other factors contribute to high Poisson's ratios in the upper crust, but this can vary significantly even on the scale of tens of kilometers (Hyndman et al., 1976).

For reference Poisson's ratio is related to seismic velocity by:

$$\sigma = \frac{\alpha^2 - 2\beta^2}{2(\alpha^2 - \beta^2)} \tag{C.3}$$

Table C.7: Reference for Poisson's values

α/β	1.6	1.65	1.7	1.75	1.8	1.85	1.9	1.95	2	2.05	2.1
σ	0.179	0.210	0.235	0.258	0.277	0.294	0.308	0.321	0.333	0.344	0.353

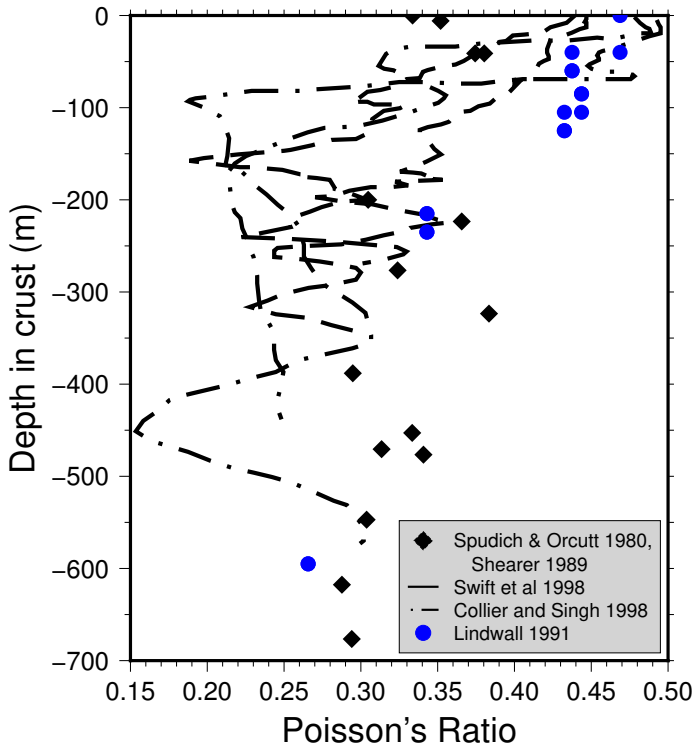

Figure C.6: Poisson's ratio as a function of depth in the upper crust. Values from Spudich and Orcutt (1980b), Shearer (1988), Swift et al. (1998), and Collier and Singh (1998). All of these solutions are for crust 15Ma or younger. Values from Lindwall (1991) are also shown (crustal age >80Ma).

2 Changes in tilt direction at PLUME instruments

2.1 Removing the tilt signal

I removed the tilt signal from the vertical acceleration data following (with a few differences noted below) the method of Bell et al. (2015a), which is a modification of the method proposed by Webb and Crawford (1999) and Crawford and Webb (2000). I rotated the horizontal data between 0 and 180 degrees, calculating the coherence between the rotated horizontal (H_1') and vertical signals at one degree increments. The angle that maximizes the average coherence below 20 mHz is taken to be the tilt direction (the 180° ambiguity is removed by examining the phase between the signals; tilting causes the signals to be out of phase). The tilt at any site is characterized by the direction ϕ_t and magnitude A_t. The transfer function is estimated by applying a Hann window (Harris, 1978) to the data and calculating:

$$T_{zh_1'}(\omega) = \frac{C_{zh_1'}(\omega)}{C_{h_1'h_1'}(\omega)} \tag{C.4}$$

where $C_{zh_1'}(\omega)$ is the cross-spectrum between the vertical and H_1' and $C_{h_1'h_1'}(\omega)$ is the power spectrum of H_1'. The coherent energy is then removed from the vertical spectrally, and the cleaned vertical signal is given as

$$Z'(\omega) = Z(\omega) - T_{zh_1'}(\omega)H_1'(\omega) \tag{C.5}$$

I removed the tilt at all frequencies below 50 mHz. Figure C.7 shows the effect of removing the tilt on the spectral energy of the vertical and on the coherence between the vertical and other signals at site PL37. No clear infragravity signal is observed before tilt is removed, and the dominating effects of tilt noise can be seen by the high coherence between the vertical and horizontal data. Once the tilt is removed, the expected signal and coherence are visible. I tested to ensure that removing the tilt doesn't bias our transfer function estimates. The improvement at

other PLUME sites is comparable or greater than that seen at PL37.

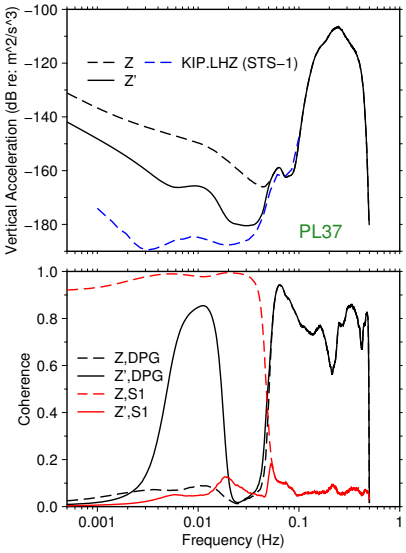

Figure C.7: Spectral power levels and coherence at site PL37 before (dashed lines) and after (solid lines) tilt removal. These spectra are calculated from the median spectra of the entire deployment. In the lower panel, the black lines represent coherence between the vertical acceleration and pressure signals, while the red lines represent coherence between the vertical acceleration and rotated horizontal signals. Removing the tilt signal from the vertical greatly improves the coherence between the vertical and the pressure signals, and also significantly reduces long-period noise, allowing the infragravity signal to become clear. I include the ambient noise model of Berger et al. (2004) at GSN site KIP (Kipapa) between 1 and 100 mHz for comparison.

2.2 Changes in tilt direction

I noticed that the tilt angle and / or direction changed at certain times for a number of PLUME stations, although I have never seen discussion of this in the literature. Figure C.9 shows typical tilt patterns at two PLUME 1 sites. After a few days tilt values settle to fairly constant values. Figure C.12 shows the median values for tilt angle and direction calculated at all WHOI PLUME sites. Although it is not shown, no significant difference is observed between deployments 1 & 2. The tilt directions appear to be randomly distributed, and the tilt angles are generally less than 1°. In general, the tilt settles asymptotically to constant values for these parameters. On several occasions, I notice sharp jumps in either or both ϕ_t and A_t

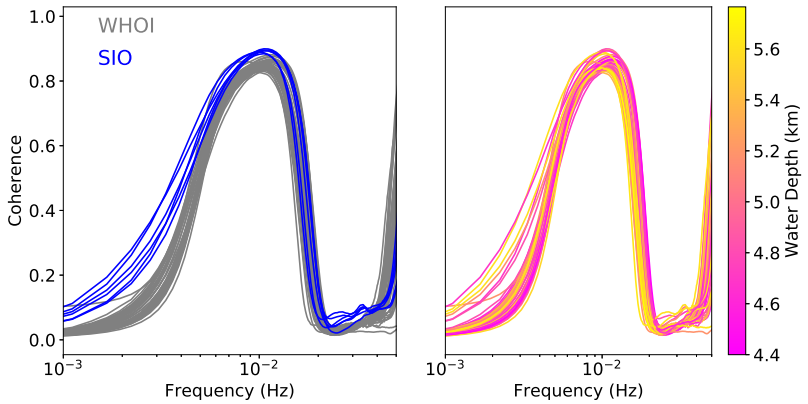

Figure C.8: Pressure-vertical acceleration coherence at all PLUME sites. Only frequencies between 1 and 50 mHz are shown. (A) Comparing coherence at SIO and WHOI sites. The SIO sites show higher coherence at lower frequencies, likely because the T240 seismometer at those stations has a lower frequency roll-off. (B) Coherence at all sites as a function of water depth. While the water depth doesn't seem to play a role at low frequencies, shallower instruments show high coherence to higher frequencies.

at one or more stations. The most significant change in the tilt parameters occurred following the Kīholo Bay earthquake. This M_W6.7 event occurred at 39km depth beneath the Island of Hawaii on 15 October 2006 (see Yamada et al. (2010) or Nakata (2007) for more information). Figure C.10 shows ϕ_t and A_t at three sites for several days before and after the event. In general, stations closer to the epicenter were more likely to experience changes in tilt. Figure C.11 shows the range of changes across the PLUME 2 network. No consistent pattern emerges, leading us to hypothesize that the tilt changes result from the instrument slightly shifting in the mud. Unfortunately at all stations experiencing a tilt change the seismic data became clipped, limiting our analysis of the waveforms. Simultaneous tilt changes also occurred at several PLUME 1 stations following the M5.1 event to the south of the big island on 17 July 2005. Fewer OBSs were affected than following the Kiholo Bay event, but some experienced significant tilt changes.

The Kiholo Bay earthquake also produced strange behavior at site PL61. This site experienced long-period ($>$ 200s) spikes on the DPG throughout the deployment, but this event appears to have altered the gain of the DPG. Figure C.14 shows the time series directly preceding and following the earthquake in three frequency bands. The gain of the data appears to

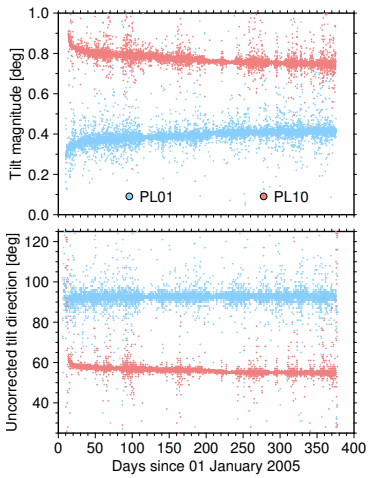

Figure C.9: Tilt values at two sites typical of the year-long deployments of the PLUME network. Both the direction and magnitude settle in the first two weeks and then continues to slowly change as the deployment continues.

roughly double following the event. Inspection of the power spectra before and after the event confirmed this.

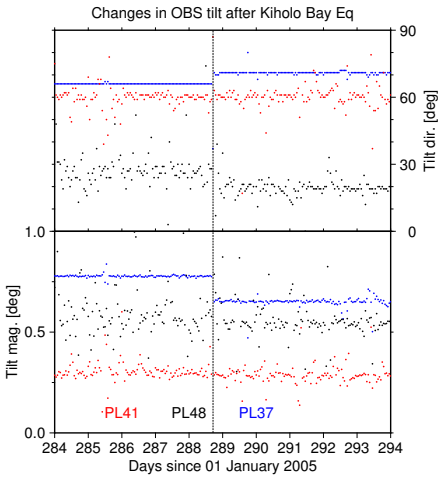

Figure C.10: Changes in tilt observed at three stations following the 15 October 2006 Kiholo Bay earthquake. PL41, situated over 400 km from the epicenter, has no obvious change in tilt parameters, but both PL48 and PL37 experience clear shifts.

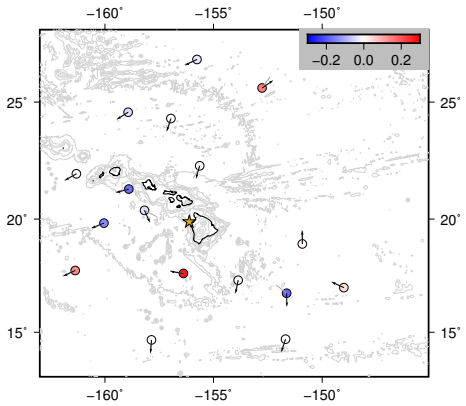

Figure C.11: Changes in tilt magnitude and direction following the 15 October 2006 Kiholo Bay earthquake for all PLUME2 WHOI sites. The change in magnitude is given by the color and the direction by the gray lines (original ϕ_t) and black lines (new ϕ_t). The tilt directions have been corrected for instrument orientations, which were determined using the methods of Laske et al. (1994) and Doran and Laske (2017). The epicenter location is marked with a yellow star.

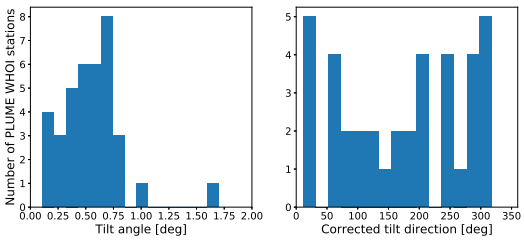

Figure C.12: Summary plot showing median tilt angle and direction for all PLUME WHOI OBSs. The vast majority of instruments used in this study have a very low tilt angle ($< 1^{\circ}$), and the tilt direction seems to be distributed randomly, consistent with free-fall deployment of OBSs. "Corrected" tilt direction indicates that the instrument orientation is included in this calculation.

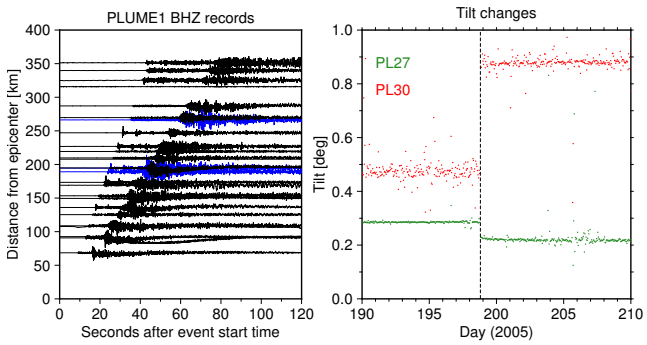

Figure C.13: Changes in tilt magnitude and direction following a $M5.1$ earthquake occurring 33km beneath the island of Hawaii on 17 July 2005. The WHOI sites are shown in black and the SIO sites are shown in blue. Two WHOI stations with tilt changes are shown on the right.

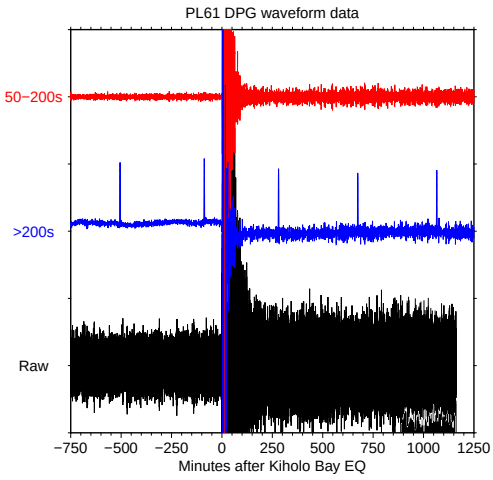

Figure C.14: Changes in DPG data concurrent with the Kiholo Bay earthquake at site PL61. Three signals are shown, and all appear to show changes to the DPG gain. Long period spikes can be seen at the lowest frequencies, further complicating compliance estimates at this station. The change in gain appears to have been caused by the earthquake, but a specific reason is not immediately obvious.

Bibliography

Agius, M. R., C. A. Rychert, N. Harmon, and G. Laske (2017), Mapping the mantle transition zone beneath Hawaii from Ps receiver functions: Evidence for a hot plume and cold mantle downwellings, Earth and Planetary Science Letters, 474, 226–236, doi: 10.1016/j.epsl.2017.06.033.

Agius, M. R., N. Harmon, C. A. Rychert, S. Tharimena, and J.-M. Kendall (2018), Sediment characterization at the equatorial MidAtlantic Ridge from PtoS teleseismic phase conversions recorded on the PILAB experiment, Geophysical Research Letters, p. doi: 10.1029/2018GL080565.

Ahern, T., R. Casey, D. Barnes, R. Benson, and T. Knight (2012), SEED reference manual, Version 2.4, Incorporated Research Institutions for Seismology.

Aki, K. (1957), Space and time spectra of stationary waves with special reference to microtremors, Bulletin of the Earthquake Research Institute, University of Tokyo, 35, 415 – 456.

An, C., C. Cai, Y. Zheng, L. Meng, and P. Liu (2017), Theoretical solution and applications of ocean bottom pressure induced by seismic seafloor motion, Geophysical Research Letters, 44, 10,272 – 10,281, doi: 10.1002/2017GL075,137.

Anderson, D. A. (2011), Hawaii, boundary layers and ambient mantle - geophysical constraints, Journal of Petrology, 52, 1547–1577, doi:10.1093/petrology/egq068.

Anderson, D. A., and J. Natland (2005), A brief history of the plume hypothesis and its competitors: Concept and controversy, Geological Society of America, (Special Paper 388), 119–145.

Anderson, P., F. Duennebier, and R. Cessaro (1987), Ocean borehole horizontal seismic sensor orientation determined from explosive charges, Journal of Geophysical Research, 92(B5), 3573–3579, doi: 10.1029/JB092iB05p03,573.

Apel, J. (1987), Principles of Ocean Physics, Academic Press, San Diego, CA.

Araki, E., M. Shinohara, S. Sacks, A. Linde, T. Kanazawa, H. Shiobara, H. Mikada, and K. Suyehiro (2004), Improvement of seismic observation in the ocean by use of seafloor boreholes, Bulletin of the Seismological Society of America, 94(2), 678–690.

Ardhuin, F., A. Rawat, and J. Aucan (2014), A numerical model for free infragravity waves: Definition and validation at regional and global scales, Ocean Modelling, 77, 20–32.

Arnulf, A. F., A. J. Harding, S. C. Singh, G. M. Kent, and W. Crawford (2012), Fine-scale velocity structure of upper oceanic crust from full waveform inversion of downward continued seismic reflection data at the Lucky Strike Volcano, Mid-Atlantic Ridge, Geophysical Research Letters, 39(L08303), doi: 10.1029/2012GL051,064.

Arnulf, A. F., A. J. Harding, S. C. Singh, G. M. Kent, and W. Crawford (2014a), Nature of upper crust beneath the Lucky Strike volcano using elastic full waveform inversion of streamer data, Geophysical Journal International, 196, 1471–1491, doi: 10.1093/gji/ggt461.

Arnulf, A. F., A. J. Harding, G. M. Kent, S. M. Carbotte, J. P. Canales, and M. R. Nedimovic (2014b), Anatomy of an active submarine volcano, Geology, 42(8), 655 – 658, doi:10.1130/G35,629.1.

Arnulf, A. F., A. J. Harding, G. M. Kent, and W. S. D. Wilcock (2018), Structure, seismicity and accretionary processes at the hotspot-influenced Axial Seamount on the Juan de Fuca Ridge, Journal of Geophysical Research: Solid Earth, p. doi: 10.1029/2017JB015131.

Astiz, L., and P. Shearer (2000), Earthquake locations in the Inner Continental Borderland, Offshore Southern California, Bulletin of the Seismological Society of America, 90(2), 425–449.

Au, D., and R. M. Clowes (1984), Shear-wave velocity sructure of the oceanic lithosphere from ocean bottom seismometer studies, Geophysical Journal of the Royal Astronomical Society, 77, 105–123.

Aucan, J., and F. Ardhuin (2013), Infragravity waves in the deep ocean: an upward revision, Geophysical Research Letters, 40(13), 3435–3439, doi: 10.1002/grl.50,321.

Baker, G., and J. Stevens (2004), Backazimuth estimation reliability using surface wave polarization, Geophysical Research Letters, 31(L09611), doi: 10.1029/2004GL019,510.

Ball, J., A. Sheehan, F. Lin, and J. Collins (2014a), Calibration of Differential Pressure Gauges at OBS stations off New Zealand, in Eos Trans. Fall meeting supplement.

Ball, J., A. Sheehan, J. Stachnik, F. Lin, and J. Collins (2014b), A joint Monte Carlo analysis of seafloor compliance, Rayleigh wave dispersion and receiver functions at ocean bottom seismic stations offshore New Zealand, Geochemistry Geophysics Geosystems, 15(12), 5051–5068, doi: 10.1002/2014GC005,412.

Ballmer, M., J. van Hunen, G. Ito, P. Tackley, and T. Bianco (2007), Non-hotspot volcano chains originating from small-scale sublithospheric convection, Geophysical Research Letters, 34(L23310), doi: 10.1029/2007GL031,636.

Ballmer, M., G. Ito, J. van Hunen, and P. Tackley (2011), Spatial and temporal variability in Hawaiian hotspot volcanism induced by small-scale convection, Nature, 4, 457 – 460.

Ballmer, M., G. Ito, C. Wolfe, and S. Solomon (2013), Double layering of a thermochemical plume in the upper mantle beneath Hawaii, Earth and Planetary Science Letters, 376, 155 – 164.

Barbour, A., and R. Parker (2014), psd: Adaptive, sine multitaper power spectral density estimation for R, Computers and Geosciences, 63, 1–8, doi: 10.1016/j.cageo.2013.09.015.

Barruol, G., and K. Sigloch (2013), Investigating La Réunion Hot Spot from crust to core, EOS, 94(23), 205 – 207.

Basuyau, C., M. Diament, C. Tiberi, G. Hetenyi, J. Vergne, and A. Peyrefitte (2013), Joint inversion of teleseismic and GOCE gravity data: application to the Himalayas, Geophysical Journal International, 193, 149–160, doi: 10.1093/gji/ggs110.

Becel, A., D. J. Shillington, M. R. Nedimovic, and S. C. W. H. Kuehn (2015), Origin of dipping structures in fast-spreading oceanic lower crust offshore Alaska imaged by multichannel seismic data, Earth and Planetary Science Letters, 424, 26 – 37, doi: 10.1016/j.epsl.2015.05.016.

Behn, M. D., M. S. Boettcher, and G. Hirth (2007), Thermal structure of oceanic transform faults, Geology, 35(4), 307–310, doi: 10.1130/G23,112A.1.

Bell, S. W., D. Forsyth, and Y. Ruan (2015a), Removing noise from the vertical component records of ocean-bottom seismometers: Results from year one of the Cascadia Initiative, Bulletin of the Seismological Society of America, 105(1), 300–313, doi: 10.1785/0120140,054.

Bell, S. W., Y. Ruan, and D. W. Forsyth (2015b), Shear velocity structure of abyssal plain sediments in Cascadia, Seismological Research Letters, 86(5), 1247–1252, doi: 10.1785/0220150,101.

Bensen, G., M. Ritzwoller, M. Barmin, A. Levshin, F. Lin, M. Moschetti, N. Shapiro, and Y. Yang (2007), Processing seismic ambient noise data to obtain reliable broad-band surface wave dispersion measurements, Geophysical Journal International, 169, 1239–1260, doi: 10.1111/j.1365–246X.2007.03,374.x.

Berger, J., P. Davis, and G. Ekström (2004), Ambient earth noise: A survey of the global seismographic network, Journal of Geophysical Research, 109(B11307), doi: 10.1029/2004JB003,408.

Berger, J., G. Laske, J. Babcock, and J. Orcutt (2016), An ocean bottom seismic observatory with near real-time telemetry, Earth and Space Science, 3, 68–77.

Berger, J., J.-R. Bidlot, M. A. Dzieciuch, W. E. Farrell, P. F. Worcester, and R. A. Stephen (2018), A deep ocean acoustic noise floor, 1-800 Hz, Journal of the Acoustical Society of America, 143, 1223 – 1233, doi: 10.1121/1.5025,042.

Beyreuther, M., R. Barsch, L. Krischer, T. Megies, Y. Behr, and J. Wassermann (2010), ObsPy: A Python toolbox for seismology, Seismological Research Letters, 81(3), 530–533, doi: 10.1785/gssrl.81.3.530.

Bowden, D., M. Kohler, V. Tsai, and D. Weeraratne (2016), Offshore southern california lithospheric velocity structure from noise cross-correlation functions, Journal of Geophysical Research: Solid Earth, 121, doi: 10.1002/2016JB012,919.

Bratt, S. R., and S. C. Solomon (1984), Compressional and shear wave structure of the East Pacific Rise at 11'20"n: Constraints from three-component ocean bottom seismometer data, Journal of Geophysical Research, 87(B7), 6095–6110.

Brenguier, F., M. Campillo, C. Hadziioannou, N. M. Shapiro, R. M. Nadeau, and E. Larose (2008), Postseismic relaxation along the san andreas fault at parkfield from continuous seismological observations, Science, 321, 1478 – 1481, doi: 10.1126/science.1160,943.

Brenguier, F., D. Rivet, A. Obermann, N. Nakata, P. Boue, T. Lecocq, M. Camipllo, and N. Shapiro (2016), 4-d noise-based seismology at volcanoes: ongoing effors at perspectives, Journal of Volcanology and Geothermal Research, 321, 182 – 195, doi: 10.1016/j.jvolgeores.2016.04.036.

Brocher, T. (2005), Empirical relations between elastic wavespeeds and density in the Earth's crust, Bulletin of the Seismological Society of America, 95(6), 2081–2092, doi: 10.1785/0120050,077.

Brocher, T., and U. S. ten Brink (1987), Variations in oceanic layer 2 elastic velocities near Hawaii and their correlation to lithspheric flexure, Journal of Geophysical Research, 92(B3), 2647–2661.

Bromirski, P. D., L. N. Frazer, and F. K. Duennebier (1992), Sediment shear Q from airgun OBS data, Geophysical Journal International, 110, 465–485.

Bromirski, P. D., O. V. Sergienko, and D. R. MacAyeal (2010), Transoceanic infragravity waves impacting antarctic ice shelves, Geophysical Research Letters, 37.

Butterfield, D. A., G. J. Massoth, R. E. McDuff, J. E. Lupton, and M. D. Lilley (1990), Geochemistry of hydrothermal fluids from axial seamount hydrothermal emissions study vent field, juan de fuca ridge: Subseafloor boiling and subsequent fluid-rock interaction, Journal of Geophysical Research, 95(B8 12,895 - 12,921).

Cacchione, D., and D. Drake (1982), Measurements of storm-generated bottom stresses on the continental shelf, Journal of Geophysical Research, 87(C3), 1952–1960.

Cadio, C., M. Ballmer, I. Panet, M. Diament, and N. Ribe (2012), New constraints on the origin of the hawaiian swell from wavelet analysis of the geoid to topography ratio, Earth and Planetary Science Letters, (359-360), 40–54, doi: 10.1016/j.epsl.2012.10.006.

Campillo, M., and A. Paul (2003), Long-range correlations in the diffuse seismic coda, Science, 299, 547–549.

Campillo, M., and P. Roux (2015), Treatise on Geophysics, vol. 1, chap. Crust and Lithospheric Structure - Seismic Imaging and Monitoring with Ambient Noise Correlations, pp. 391–417, Elsiver.

Canales, J., M. R. Nedimovic, G. M. Kent, S. M. Carbotte, and R. S. Detrick (2009), Seismic reflection images of a near-axis melt sill within the lower crust at the Juan de Fuca ridge, Nature, 460, 89 – 93, doi: 10.1038/nature08,095.

Cannata, A. (2012), Crustal changes at mt. etna volcano accompanying the 2002–2003 eruption as inferred from a repeating earthquake analysis, Geophysical Research Letters, 39(L18311), doi: 10.1029/2012GL053,185.

Carlson, R. (1998), Seismic velocities in the uppermost oceanic crust: Age dependence and the fate of layer 2A, Journal of Geophysical Research, 103(B4), 7069–7077.

Carlson, R., and G. Raskin (1984), Density of the ocean crust, Nature, 311, 555–558.

Carlson, R. L., N. I. Christensen, and R. H. Wilkins (1980), Acoustic properties of volcaniclastic sediments recovered from the floor of the Phillippine Sea, in Initial Reports of the Deep Sea Drilling Project, vol. 59, edited by L. Kroenke and R. Scott, NSF.

Castagna, J., M. Batzle, and R. Eastwood (1985), Relationships between compressional-wave and shear-wave velocities in clastic silicate rocks, Geophysics, 50, 571–581.

Chadwick, W. W., D. S. Scheirer, R. W. Embley, and H. P. Johnson (2001), High-resolution bathymetric surveys using scanning sonars: Lava flow morphology, hydrothermal vents, and geologic structure at recent eruption sites on the juan de fuca ridge, Journal of Geophysical Research, 106(B8), 16,075 – 16,099.

Chadwick, W. W., D. A. Clague, R. W. E. M. R. Perfit, D. A. Butterfield, D. W. Caress, J. B. Paduan, J. F. Martin, P. Sansnett, S. G. Merle, and A. M. Bobbitt (2013), The 1998 eruption of axial seamount: New insights on submarine lava flow emplacement from high-resolution mapping, Geochemistry Geophysics Geosystems, 14(10), 3939 – 3968, doi: 10.1002/ggge.20,202.

Chadwick, W. W., J. B. Paduan, D. A. Clague, B. M. Dreyer, S. G. Merle, A. M. Bobbitt, D. W. Caress, B. T. Phillip, D. S. Kelley, and S. L. Nooner (2016), Voluminous eruption from a zoned magma body after an increase in supply rate at Axial Seamount, Geophysical Research Letters, 43, 12,063 – 12,070, doi:10.1002/ 2016GL071,327.

Chael, E. (1997), An automated rayleigh-wave detection algorithm, Bulletin of the Seismological Society of America, 87(1), 157–163.

Chen, Y. J., and J. Lin (2004), High sensitivity of ocean ridge thermal structure to changes in magma supply: the galapagos spreading center, Earth and Planetary Science Letters, 221, 263 – 273, doi: 10.1016/S0012–821X(04)00,099–8.

Christensen, N., and M. Salisbury (1975), Structure and constitution of the lower oceanic crust, Reviews of Geophysics and Space Physics, 13, 57–86.

Christensen, N., and R. Wilkens (1982), Seismic properties, density, and composition of the icelandic crust near reydarfjordur, Journal of Geophysical Research, 87(B8), 6389–6395.

Christensen, N. I. (1996), Poisson's ratio and crustal seismology, Journal of Geophysical Research, 101(B2), 3139–3156.

Christeson, G. L., J. Goff, R. L. Carlson, and R. Reece (2017), New synthesis of ocean crust velocity structure from two-dimensional profiles, in EOS Transactions, vol. Abstract V44A-02.

Clague, D. A., B. M. Dreyer, J. B. Paduan, J. F. Martin, W. W. Chadwick, D. W. Caress, R. A. Portner, T. P. Guilderson, M. L. McGann, H. Thomas, D. A. Butterfield, and R. W. Embley (2013), Geologic history of the summit of axial seamount, Geochemistry Geophysics Geosystems, 14, 4403 – 4443, doi: 10.1002/ggge.20,240.

Clague, D. A., J. B. Paduan, D. W. Caress, W. W. Chadwick, M. L. Saout, B. M. Dreyer, and R. A. Portner (2017), High-resolution AUV mapping and targeted ROV observations of three historic lava flows at Axial Seamount, Oceanography, 30(4), 82 – 99, doi: 10.5670/oceanog.2017.426.

Codiga, D. L. (2011), Unified Tidal Analysis and Prediction Using the UTide Matlab Functions, Technical Report 2011-01, Graduate School of Oceanography, University of Rhode Island, Narragansett, RI.

Collier, J. S., and S. C. Singh (1998), Poisson's ratio structure of young oceanic crust, Journal of Geophysical Research, 103(B9), 20,981–20,996.

Collins, J. A., F. L. Vernon, J. A. Orcutt, R. A. Stephen, K. R. Peal, F. B. Wooding, F. N. Spiess, and J. A. Hildebrand (2001), Broadband seismology in the oceans: lessons from the Ocean Seismic Network Pilot Experiment, Geophysical Research Letters, 28(1), 49–52.

Constable, S., and G. Heinson (2004), Hawaiian hot-spot swell structure from seafloor MT sounding, Tectonophysics, 389, 111–124, doi: 10.1016/j.tecto.2004.07.060.

Constable, S., R. Parker, and C. Constable (1987), Occam's inversion: A practical algorithm for generating smooth models from electromagnetic sounding data, Geophysics, 52(3), 289–300.

Cox, C., T. Deaton, and S. Webb (1984), A deep-sea differential pressure gauge, J. Atmos. Oceanic Technol., 1, 237–246.

Crawford, W. (2004), The sensitivity of seafloor compliance measurements to sub-basalt sediments, Geophysical Journal International, 157, 1130–1145.

Crawford, W., and S. Singh (2008), Sediment shear properties from seafloor compliance measurements: Faroes-shetland basin case study, Geophysical Prospecting, 56, 313–325.

Crawford, W., and S. Webb (2000), Identifying and removing tilt noise from low-frequency (less than 0.1 Hz) seafloor vertical seismic data, Bulletin of the Seismological Society of America, 90(4), 952–963.

Crawford, W., and S. Webb (2002), Variations in the distribution of magma in the lower crust and at the Moho beneath the East Pacifc Rise at 9 and 10 degrees N, Earth and Planetary Science Letters, 203, 117–130.

Crawford, W., S. Webb, and J. Hildebrand (1991), Seafloor compliance observed by long-period pressure and displacement measurements, Journal of Geophysical Research, 96(B10), 151–160.

Crawford, W., S. Webb, and J. Hildebrand (1998), Estimating shear velocities in the oceanic crust from compliance measurements by 2-D finite difference modeling, Journal of Geophysical Research, 103(B5), 9895–9916.

Crawford, W., S. Webb, and J. Hildebrand (1999), Constraints on melt in the lower crust and Moho at the East Pacific Rise using seafloor compliance measurements, Journal of Geophysical Research, 104(B2), 2923–2939.

Crawford, W., R. Stephen, and S. Bolmer (2006), A second look at low-frequency marine vertical seismometer data quality at the OSN-1 site off Hawaii for seafloor, buried, and borehole emplacements, Bulletin of the Seismological Society of America, 96(5), 1952–1960.

Crawford, W., V. Ballu, X. Bertin, and M. Karpytchev (2015), The sources of deep ocean infragravity waves observed in the north atlantic ocean, Journal of Geophysical Research: Oceans, 120(7), 5120–5133.

Dahlen, F., and J. Tromp (1998), Theoretical Global Seismology, Princeton University Press.

Davis, E. E., C. R. B. Lister, and B. T. R. Lewis (1976), Seismic structure of the Juan de Fuca Ridge: Ocean bottom seismomoter results from the Median Valley, Journal of Geophysical Research, 81(20), 3541–3555.

Davis, G. E., M. F. Baumgartner, J. M. Bonnell, J. Bell, C. Berchok, J. B. Thorton, S. Brault, G. Buchanan, R. A. Charif, D. Cholewiak, C. W. Clark, P. Corkeron, J. Delarue, K. Dudzinski, L. Hatch, J. Hildebrand, L. Hodge, H. Klinck, S. Kraus, B. Martin, D. K. Mellinger, H. Moors-Murphy, S. Nieudirk, D. P. Nowacek, S. Parks, A. J. Read, A. ¿n Rice, D. Risch, A. Sirovic, M. Soldevilla, K. Stafford, J. E. Stanistreet, E. Summers, S. Todd, A. Warde, and S. M. V. Parijs (2017), Long-term passive acoustic recordings track the changing distribution of North Atlantic right whales (Eubalaena galcialis) from 2004 to 2014, Scientific Reports.

Deen, M., E. Wielandt, E. Stutzmann, W. Crawford, G. Barruol, and K. Sigloch (2017), First observation of the Earth's permanent free oscillations on ocean bottom seismometers, Geophysical Research Letters, 44, 10,988–10,966, doi: 10.1002/2017GL074,892.

Detrick, R., and S. Crough (1978), Island subsidence, hot spots, and lithospheric thinning, Journal of Geophysical Research, 83, 1236–1244.

Divins, D. L. (2003), Total sediment thickness of the world's oceans & marginal seas, Tech. rep., NOAA National Geophysical Data Center, Boulder, CO.

Dolenc, D., B. Romanowicz, D. Stakes, and P. McGill (2005), Observations of infragravity waves at the Monterey Ocean Bottom Broadband station (MOBB), G3, 6(Q09002), doi:10.1029/2005GC000,988.

Dolenc, D., B. Romanowicz, R. Uhrhammer, P. McGill, D. Neuhauser, and D. Stakes (2007), Identifying and removing noise from the Monterey Ocean Bottom Broadband Seismic Station (MOBB) data, Geochemistry Geophysics Geosystems, 8(Q02005), doi:10.1029/2006GC001,403.

Doran, A. K., and G. Laske (2016), Infragravity waves and horizontal seafloor compliance, J. Geophys. Res., 121(1), 260–278, doi: 10.1002/2015JB012,511.

Doran, A. K., and G. Laske (2017), Ocean-bottom seismometer instrument orientations via automated Rayleigh-wave arrival angle measurements, Bulletin of the Seismological Society of America, 107(2), 691–708, doi: 10.1785/012016,165.

Doran, A. K., and G. Laske (2018), Structure of the sediments and upper oceanic crust surrounding hawaii, Journal of Geophysical Research: Solid Earth.

Doran, A. K., and G. Laske (2019), Seismic structure of marine sediments and upper oceanic crust surrounding Hawaii, Journal of Geophysical Research: Solid Earth, p. doi: 10.1029/2018JB016548.

Dorman, L. (1997), Handbook of Acoustics, chap. Propagation in marine sediments, pp. 409–416, John Wiley, New York.

Duennebier, F., and G. Sutton (1995), Fidelity of ocean bottom seismic observations, Marine Geophysical Research, 17, 535–555.

Duennebier, F., and G. Sutton (2007), Why bury ocean bottom seismometers?, Geochemistry Geophysics Geosystems, 8, Q02,010, doi:10.1029/2006GC001,428.

Duennebier, F., P. Anderson, and G. Fryer (1987), Azimuth determination of and from horizontal ocean bottom seismic sensors, Journal of Geophysical Research, 92(B5), 3567–3572, doi: 10.1029/JB092iB05p03,567.

Duennebier, F., D. Harris, J. Jolly, J. Babinec, D. Copson, and K. Stiffel (2002), The hawaii-2 observatory seismic system, IEEE Journal of Oceanic Engineering, 47(2), 212–217.

Dunn, R. A., and O. Hernandez (2009), Tracking blue whales in the eastern tropical Pacific with an ocean-bottom seismometer and hydrophone array, Journal of the Acoustical Society of America, 126(3), 1084 – 1094, doi: 10.1121/1.3158,929.

Dvorkin, J. P. (2008), Yet another Vs equation, Geophysics, 73(2), E35 – E39, doi: 10.1190/1.2820,604.

Dziewonski, A., and D. Anderson (1981), Preliminary reference earth model, Physics of the Earth and Planetary Interiors, 25, 297–356.

Dziewonski, A., R. Wilkens, J. Firth, and S. S. Party (1992a), Volume 136, site 843, Tech. rep., Proceeedings of the Ocean Drilling Program Initial Reports.

Dziewonski, A., R. Wilkens, J. Firth, and S. S. Party (1992b), Background and objectives of the ocean seimographic network and leg 136 drilling results, Proceeedings of the Ocean Drilling Program Initial Report, 136, 2–8.

Efron, B. (1979), Bootstrap methods: another look at the jacknife, Annals of Statistics, 7(1), 1–26.

Egbert, G., and S. Erofeeva (2002), Efficient inverse modeling of barotropic ocean tides, J. Atmos. Oceanic Technol., 19, 183–204, doi: 10.1175/1520–0426(2002)019¡0183:EIMOBO¿2.0.CO;2.

Ekstrom, G., and R. W. Busby (2008), Measurements of seismometer orientation at usarray transportable array and backbone station, Seismological Research Letters, 79(4), 554–561, doi: 10.1785/gssrl.79.4.554.

Ekström, G., G. A. Abers, and S. C. Webb (2009), Determination of surface-wave phase velocities across USArray from noise and Aki's spectral formulation, Geophysical Research Letters, 36(L18301), doi: 10.1029/2009GL039,131.

Embly, R. W., K. M. Murphy, and C. G. Fox (1990), High-resolution studies of the summit of axial volcano, Journal of Geophysical Research, 95(B8), 12,785 – 12,812.

Essen, H.-H., I. Grevemeyer, R. Herber, and W. Weigel (1998), Shear-wave velocity in marine sediments on young oceanic crust: constraints from dispersion analysis of Scholte waves, Geophysical Journal International, 132, 227 – 234.

Ewing, J., M. Ewing, T. Aitken, and W. J. Ludwig (1968), North pacific sediment layers measured by seismic profiling, in The crust and upper mantle of the Pacific area, vol. Monograph 12, edited by L. Knopoff, C. L. Drake, and P. J. Hart, pp. 147 – 173, Am. Geophysical Union.

Filloux, J. (1983), Pressure fluctuations on the open ocean floor off the gulf of california: Tides, earthquakes, tsunamis, Journal of Physical Oceanography, 13, 783–786.

Fontaine, F. J., M. Rabinowicz, and M. Cannat (2017), Can high-temperature, high-heat flux hydrothermal vent fields be explained by thermal convection in the lower crust along fast-spreading mid-ocean ridges?, Geochemistry Geophysics Geosystems, 18, 1907–1925, doi:10.1002/ 2016GC006,737.

Foster, A., G. Ekstrom, and V. Hjorleifsdottir (2014a), Arrival-angle anomalies across the USArray Transportable Array, Earth and Planetary Science Letters, 402, 58–68, doi: 0.1016/j.epsl.2013.12.046.

Foster, A., M. Nettles, and G. Ekstrom (2014b), Overtone interference in array-based love-wave phase measurements, Bulletin of the Seismological Society of Americ, 104(5), 2266–2277, doi: 10.1785/0120140,100.

French, S., and B. Romanowicz (2015), Broad plumes rooted at the base of the Earth's mantle beneath major hotspots, Nature, 525, 95 – 99.

Gardner, G., L. Gardner, and A. Gregory (1974), Formation velocity and density - the diagnostic basics for stratigraphic traps, Geophysics, 39, 770–780.

Godfrey, N., B. Beaudoin, and S. Klemperer (1997), Ophiolitic basement to the Great Valley forearc basin, California, from seismic and gravity data: Implications for crustal growth at the North American continental margin, Geological Society of America Bulletin, 109(12), 156–152.

Godin, O., N. Zabotin, A. Sheehan, Z. Yang, and J. Collins (2013), Power spectra of infragravity waves in a deep ocean, Geophysical Research Letters, 40, 2159–2165, doi:10.1002/grl.50,418.

Godin, O. A., and I. M. Fuks (2012), Transmission of acoustic-gravity waves through gas-liquid interfaces, Journal of Fluid Mechanics, 709.

Godin, O. A., N. A. Zabotin, A. F. Sheehan, and J. A. Collins (2014), Interferometry of infragravity waves off New Zealand, Journal of Geophysical Research: Oceans, 119, 1103 – 1122, doi: 10.1002/2013JC009,395.

Goes, S., R. Govers, and P. Vacher (2000), Shallow mantle temperatures under Europe from p and s wave tomography, Journal of Geophysical Research, 105(B5), 11,153 – 11,169.

Gomberg, J., and G. Masters (1988), Waveform modelling using locked-mode synthetic and differential seismograms: Application to determination of the structure of Mexico, Geophysical Journal International, 94(2), 193–218.

Grant, W., and O. Madsen (1979), Combined wave and current interaction with a rough bottom, Journal of Geophysical Research, 84(C4), 1797–1808.

Hamilton, E. (1976a), Variations of density and porosity with depth in deep-sea sediments, Journal of Sedimentary Petrology, 46(2), 280–300.

Hamilton, E. (1976b), Shear-wave velocity versus depth in marine sediments: A review, Geophysics, 41(5), 985–996.

Hamilton, E. (1978), Sound velocity-density relations in sea-floor sediments and rocks, Journal of the Acoustical Society of America, 63, 366–377, doi: 10.1121/1.381,747.

Hamilton, E. (1979a), Vp/vs and poisson's ratios in marine sediments and rocks, Journal of the Acoustical Society of America, 66(4), 1093–1101.

Hamilton, E. (1979b), Vp / Vs and Poisson's ratios in marine sediments and rocks, J. Acoust. Soc. Am., 66(4), 1093–1101.

Hamilton, E. (1979c), Sound velocity gradients in marine sediments, Journal of the Acoustical Society of America, 65, 909–922, doi: 10.1121/1.382,594.

Hammond, W., and E. Humphreys (2000), Upper mantle seismic velocity: Effects of realistic partial melt geometries, Journal of Geophysical Research, 105(B5), 10,975 – 10,986.

Haney, M. M., and V. Tsai (2017), Perturbational and nonperturbational inversion of Rayleigh-wave velocities, Geophysics, 82(3), F15 – F28, doi: 10.1190/GEO2016–0397.1.

Harding, A. (2001), Encyclopedia of Ocean Siences, chap. Seismic Structure, pp. 361–366, doi: 10.1016/B978–012374,473–9.00,258–7, second ed., Academic Press.

Harmon, N., D. Forsyth, and S. Webb (2007a), Using ambient seismic noise to determine short-period phase velocities and shallow shear velocities in young oceanic lithosphere, Bulletin of the Seismological Society of America, 97(6), 2009 – 2023, doi: 10.1785/0120070,050.

Harmon, N., D. W. Forsyth, R. Lamm, and S. C. Webb (2007b), P and S wave delays beneath intraplate volcanic ridges and gravity lineations near the East Pacific Rise, Journal of Geophysical Research, 112(B03309), doi: 10.1029/2006JB004,392.

Harris, F. (1978), On the use of windows for harmonic analysis with the discrete fourier transform, Proceedings of the IEEE, 86(1), 51–83, doi: 10.1109/PROC.1978.10,837.

Hauri, E. (1996), Major-element variability in the Hawaiian mantle plume, Nature, 382, 415 – 419.

Hein, J. R., D. A. Clague, R. A. Koski, R. W. Embley, and R. E. Dunham (2008), Metalliferous sediment and a silica-hematite deposit within the Blanco Fracture Zone, Northeast Pacific, Marine Georesources & Geotechnology, 26(4), 317 – 339, doi: 10.1080/10641190802430,986.

Henig, A. S., D. K. Blackman, A. J. Harding, J.-P. Canales, and G. M. Kent (2012), Downward continued multichannel seismic refraction analysis of Atlantis Massif oceanic core complex, 30 N, Mid-Atlantic Ridge, Geochemistry Geophysics Geosystems, 13(Q0AG07, doi:10.1029/2012GC004059).

Herbers, T., S. Elgar, and R. Guza (1995a), Generation and propagation of infragravity waves, Journal of Geophysical Research, 100(C12), 24,863–24,872.

Herbers, T., S. Elgar, R. Guza, and E. Thornton (1995b), Infragravity-frequency (0.00590.05 hz) motions on the shelf, ii, free waves, Journal of Physical Oceanography, 25, 1063–1079.

Herceg, M., I. Artemieva, and H. Thybo (2016), Sensitivity analysis of crustal correction for calculation of lithospheric mantle density from gravity data, Geophysical Journal International, 204, 687–696, doi: 10.1093/gji/ggv431.

Holcomb, R. T., J. G. Moore, P. W. Lipman, and R. H. Belderson (1988), Voluminous submarine lava flows from hawaiian volcanos, Geology, 16, 400 – 404.

Hooft, E. E., and R. S. Detrick (1995), The role of density in the accumulation of basaltic melts at mid-ocean ridges, Geophysical Research Letters, 20(6), 423 – 426.

Houtz, R. (1976), Seismic properties of layer 2A in the Pacific, Journal of Geophysical Research, 81(35), 6321–6331.

Hulme, T., W. Crawford, and S. Singh (2005), The sensitivity of seafloor compliance to two-dimensional low-velocity anomalies, Geophysical Journal International, 163, 547–558, doi: 10.1111/j.1365–246X.2005.02,753.x.

Hyndman, R. (1979), Poisson's ratio in the oceanic crust - a review, Tectonophysics, 59(1), 321–333.

Hyndman, R. D., F. Aumento, W. G. Melson, J. M. Hall, H. Bougault, L. Dmitriev, J. F. Fisher, M. Flower, R. C. Howe, G. A. Miles, P. T. Robinson, and T. L. Wright (1976), Seismic structure of the oceanic crust from deep drilling on the mid-atlantic ridge, Geophysical Research Letters, 3(3), 201–204.

Iassonov, P., and W. Crawford (2008), Two-dimensional finite-difference model of seafloor compliance, Geophysical Journal International, 174, 525–541.

Jackson, D. D., and M. Matsu'ura (1985), A Bayesian approach to nonlinear inversions, Journal of Geophysical Research, 90(B1), 581–591.

Janiszewski, H., and G. Abers (2015), Imaging the plate interface in the cascadia seismogenic zone: new constraints from offshore receiver functions, Seismological Research Letters, 86(5), 1261–1269, doi: 10.1785/0220150,104.

Jarrard, R., L. Abrams, R. Pockalny, R. Larson, and T. Hirono (2003), Physical properties of upper oceanic crust: Ocean Drilling Program Hole 801C and the waning of hydrothermal circulation, Journal of Geophysical Research, 108(B4), doi:10.1029/2001JB001,727.

Jin, G., and J. Gaherty (2015), Surface wave phase-velocity tomography based on multichannel cross-correlation, Geophysical Journal International, 201, 1383–1398, doi: 10.1093/gji/ggv079.

Johnson, H., and S. Semyan (1994), Age variation in the physical properties of oceanic basalts: Implications from crustal formation and evolution, Journal of Geophysical Research, 99(B2), 3123–3134.

Johnston, J. E., and N. I. Christensen (1997), Seismic properties of layer 2 basalts, Geophysical Journal International, 128, 285 – 300.

Karney, C. F. F. (2013), Algorithms for geodesics, Journal of Geodesy, 87(1), 43–55, doi: 10.1007/s00,190–012–0578–z.

Kelley, D. S., J. R. Delaney, and S. K. Juniper (2014), Establishing a new era of submarine volcanic observatories: Cabling axial seamount and the endeavour segment of the juan de fuca ridge, Marine Geology, 352, 426 – 450, doi: 10.1016/j.margeo.2014.03.010.

Kenter, J. A. M., and M. Ivanov (1995), Parameters controlling acoustic properties of carbonate and volcaniclastic sediments at sites 866 and 869, in Proceedings of the Ocean Drilling Program, vol. 143, edited by E. L. Winterer, W. W. Sager, J. V. Firth, and J. M. Sinton, Scientific Reports.

Kohler, M., K. Booth, C. Sun, C. Curl, C. Finnell, P. Shute, W. Prine, J. Ramos, and W. Brown (2010), Albacore obs deployment cruise report, Tech. Rep. 27 pp, R/V Melville Cruise MV1010.

Kohler, M., K. Brunner, M. Donohue, D. Weaver, T. Chi, and M. Breen (2011), Albacore obs recovery cruise report, Tech. Rep. 35 pp, R/V New Horizon Cruise NH1111.

Krischer, L., T. Megies, R. Barsch, M. Beyreuther, T. Lecocq, C. Caudron, and J. Wassermann (2015), ObsPy: a bridge for seismology into the scientific Python ecosystem, Computational Science and Discovery, 8(1), 014,003, doi: 10.1088/1749–4699/8/1/014,003.

Larson, E., and G. Ekstrom (2002), Determining surface wave arrival angle anomalies, Journal of Geophysical Research, 107(B6), doi: 10.1029/2000JB000,048.

Larson, E., J. Tromp, and G. Ekstrom (198), Effects of slight anisotropy on surface waves, Geophysical Journal International, 132, 654–666.

Laske, G. (1995), Global observation of off-great-circle propagation of long-period surface waves, Geophysical Journal International, 123(1), 245–259, doi: 10.1111/j.1365–246X.1995.tb06,673.x.

Laske, G., and G. Masters (1996), Constraints on global phase velocity maps from long-period polarization data, Journal of Geophysical Research, 101(B7), 16,059–16,075, doi: 10.1029/96JB00,526.

Laske, G., and G. Masters (1997), A global digital map of sediment thickness, EOS Transactions AGU, 78(F483).

Laske, G., and G. Masters (1998), Surface-wave polarization data and global anisotropic structure, Geophysical Journal International, 132(3), 508–520, 10.1046/j.1365–246X.1998.00,450.x.

Laske, G., and R. Widmer-Schnidrig (2015), Treatise on Geophysics, vol. 1, chap. Theory and Observations: Normal Mode and Surface Wave Observations, pp. 117–167, Elsiver.

Laske, G., G. Masters, and W. Zurn (1994), Frequency-dependent polarization measurments of long-period surface waves and their implications for global phase-velocity maps, Physics of the Earth and Planetary Interiors, 84, 111–137.

Laske, G., J. Phipps Morgan, and J. Orcutt (2007), The Hawaiian SWELL pilot experiment - Evidence for lithosphere rejuvination from ocean bottom surface wave data, Geological Society of America, Special Paper 430.

Laske, G., J. Collins, C. Wolfe, S. Solomon, R. Detrick, J. Orcutt, D. Berovici, and E. Hauri (2009), Probing the Hawaiian hot spot with new ocean bottom instruments, EOS Transactions, 90(41), 362–363, doi: 10.1029/2009EO410,002.

Laske, G., A. Markee, J. Orcutt, C. Wolfe, J. A. Collins, S. Solomon, R. Detrick, D. Bercovici, and E. Hauri (2011), Asymmetric shallow mantle structure beneath the Hawaiian Swell - evidence from Rayleigh waves recorded by the PLUME network, Geophysical Journal International, 187, 1725–1742, doi: 10.1111/j.1365–246X.2011.05,238.x.

Laske, G., G. Masters, Z. Ma, and M. Pasyanos (2013), Update on CRUST1.0 - A 1-degree global model of the Earth's crust, in Geophys. Res. Abstracts, 15, Abstract EGU2013-2658.

Latychev, K., and R. Edwards (2003), On the compliance method and the assessment of three-dimensional seafloor gas hydrate deposits, Geophysical Journal International, 155, 923–952.

Leahy, G., J. Collins, C. Wolfe, G. Laske, and S. Solomon (2010), Underplating of the Hawaiian Swell: Evidence from teleseismic receiver functions, Geophysical Journal International, 183, 313–329.

Lecocq, T., C. Caudron, and F. Brenguier (2014), MSNoise, a Python package for monitoring seismic velocity changes using ambient seismic noise, Seismological Research Letters, 85(3), 715 – 726, doi: 10.1785/0220130,073.

Legg, M., M. Kohler, N. Shintaku, and D. Weeraratne (2015), High-resolution mapping of two large-scale transpressional fault zones in the california continental borderland: santa cruz-catalina ridge and ferrelo faults, Journal of Geophysical Research: Solid Earth, 120, 915–942, doi:10.1002/2014JF003,322.

Leslie, S. C., G. F. Moore, J. K. Morgan, and D. J. Hills (2002), Seismic stratigraphy of the Frontal Hawaiian Moat: implications for sedimentary processes at the leading edge of an oceanic hotspot trace, Marine Geology, 184, 143–162.

Levshin, A., T. L. Yanavskaya, A. V. Lander, B. G. Bukchin, M. P. Barmin, L. I. Ratnikova, and E. N. Its (1989), Seismic surface waves in a laterally inhomogeneous Earth, Kluwer Academic, Norwell, Mass.

Li, X., R. Kind, X. Yuan, I. Wolbern, and W. Hanka (2004), Rejuvenation of the lithosphere by the Hawaiian plume, Nature, 427, 827–829.

Lin, F.-C., M. H. Ritzwoller, and N. M. Shapiro (2006), Is ambient noise tomography across ocean basins possible, Geophysical Research Letters, 33(L14304), doi: 10.1029/2006GL026,610.

Lin, F.-C., M. Moschetti, and M. Ritzwoller (2008), Surface wave tomography of the western united states from ambient seismic noise: Rayleigh and love wave phase velocity maps, Geophysical Journal International, 173, 281–298.

Lin, P., J. Gaherty, G. Jin, J. Collins, D. Lizarralde, R. Evans, and G. Hirth (2016), High-resolution seismic constraints on flow dynamics in the oceanic asthenosphere, Nature, 535, 538 – 541, doi: 10.1038/nature18,012.

Lindner, F., G. Laske, F. Walter, and A. K. Doran (2018), Crevasse-induced rayleigh- wave azimuthal anisotropy on Glacier de la Plaine Morte, Switzerland, Annals of Glaciology, pp. 1 – 16, doi: 10.1017/aog.2018.25.

Lindwall, D. (1991), Old Pacific crust near Hawaii: A seismic view, Journal of Geophysical Research, 96(B5), 8191–8203.

Lodewyk, J., and D. Sunny (2015), Cascadia amphibious array ocean bottom seismograph horizontal orientations, 2013-2014 obs deployments, Version 2.1 24pp, OBSIP Management Office, IRIS.

Lodewyk, J., and B. Woodward (2014), Cascadia amphibious array ocean bottom seismograph horizontal orientations, 2012-2013 obs deployments, Version 1.0 25pp, OBSIP Management Office, IRIS.

Lodewyk, J., A. Frassetto, A. Adinolfi, and B. Woodward (2014), Cascadia amphibious array ocean bottom seismograph horizontal orientations, 2011-2012 obs deployments, Version 3.0 23pp, OBSIP Management Office, IRIS.

Ludwig, W., J. Nafe, and C. Drake (1970), The Sea, vol. 4, chap. Seismic refraction, pp. 53–84, Wiley-Interscience, New York.

Ma, Z., and G. Masters (2014), A new global Rayleigh- and Love-wave group velocity dataset for constraining lithosphere properties, Bulletin of the Seismological Society of America, 104(4), 2007–2026, doi: 10.1785/0120130,320.

Ma, Z., G. Masters, G. Laske, and M. Pasyanos (2014), A comprehensive dispersion model of surface wave phase and group velocity for the globe, Geophysical Journal International, 119(1), 113–135, doi: 10.1093/gji/ggu246.

Mainprice, D. (1997), Modeling the anisotropic seismic properties of partially molton rocks found at mid-ocean ridges, Tectonophysics, 279, 161 – 179.

Marjanovic, M., N. Fuji, S. Singh, T. Belahi, and J. Escartin (2017), Seismic signatures of hydrothermal pathways along the east pacific rise between 9°160 and 9°560n, Journal of Geophysical Research: Solid Earth, 122, 10,241 – 10,262, doi: 10.1002/2017JB015,004.

Marone, F., and B. Romanowicz (2007), Non-linear crustal corrections in high-resolution regional waveform seismic tomography, Geophysical Journal International, 170, 460–467, doi: 10.1111/j.1365–246X.2007.03,399.x.

Matthews, K. J., R. D. Müller, P. Wessel, and J. M. Whittaker (2011), The tectonic fabric of the ocean basins, Journal of Geophysical Research, 116(B12109, doi: 10.1029/2011JB008413).

Mavko, G. (1980), Velocity and attenuation in partially molten rocks, Journal of Geophysical Research, 85(B10), 5173 – 5189.

McManus, D., R. Burns, C. von der Borch, R. Goll, E. Milow, R. Olsson, T. Vallier, and O. Weser (1970), Volume 5, site 43, Tech. rep., Deep Sea Drilling Project Reports and Publications.

Megies, T., M. Beyreuther, R. Barsch, L. Krischer, and J. Wassermann (2011), ObsPy - what can it do for data centers and observatories?, Annals of Geophysics, 54(1), 47–58, doi: 10.4401/ag–4838.

Montagner, J., J. Karczewski, B. Romanowicz, S. Bouaricha, P. Lognonne, G. Roult, E. Stutzmann, J. Thirot, J. Brion, B. Dole, D. Fouassier, J. Koenig, J. Savary, L. Floury, J. Dupond, A. Echardour, and H. Floc'h (1994), The french pilot experiment ofm-sismobs: first scientific results on noise level and event detection, Physics of the Earth and Planetary Interiors, 84, 321–336.

Montagner, J. P., and N. Jobert (1988), Vectorial tomography - II. application to the Indian Ocean, Geophysical Journal International, 94, 309–344.

Moore, J., D. Clague, R. Holcomb, P. Lipman, W. Normark, and M. Torresan (1989), Prodigious submarine landslides on the Hawaiian Ridge, Journal of Geophysical Research, 94(B12), 17,465–17,484.

Moore, J., W. Normark, and R. Holcomb (1994), Giant Hawiian landslides, Annual Reviews of Earth and Planetary Sciences, 22, 119–144.

Müller, R., M. Sdrolias, C. Gaina, and W. Roest (2008), Age, spreading rates and spreading symmetry of the world's ocean crust, Geochem. Geopyhs. Geosys., 9(G04006), doi:10.1029/2007GC001,743.

Munk, W. H. (1949), Surf beats, EOS Transactions, 30, 849–854.

Mutter, C., and J. Mutter (1993), Variations in thickness of layer-3 dominate oceanic crustal structure, Earth and Planetary Science Letters, 117, 295–317.

Nafe, J., and C. Drake (1957), Variation with depth in shallow and deep water marine sediments of porosity, density, and the velocities of compressional and shear waves, Geophysics, 22(3), 523–552.

Naka, J., E. Takahashi, D. Clague, M. Garcia, T. Hanyu, E. Herrero-Bervera, J. Ishibashi, O. lshizuka, K. Johnson, T. Kanamatsu, I. Kaneoka, P. Lipman, A. Malahoff, G. McMurtry, B. Midson, J. Moore, J. Morgan, T. Naganuma, K. Nakajima, T. Oomori, A. Pietruszka, K. Satake, D. Sherrod, T. Shibata, K. Shinozaki, T. Sisson, J. Smith, S. Takarad, C. Thomber, F. Trusdell, N. Tsuboyama, T. Ui, S. Umino, K. Uto, and H. Yokose (2000), Tectono-magmatic processes investigated at deep-water flanks of Hawaiian volcanoes, EOS Transactions, AGU, 81(20), 221–232.

Naka, J., T. Kanamatsu, P. Lipman, T. Sisson, N. Tsuboyama, J. Morgan, J. Smith, and T. Ui (2002), Deep-sea volcaniclastic sedimentation around the southern flank of Hawaii, Hawaiian volcanoes: Deep underwater Perspectives, Geophysical Monograph 128.

Nakata, J. S. (2007), Hawaiian Volcano Observatory seismic data: January to December 2006, U.S. Geological Survey Open File Report, 2007-1073.

Natland, J., and E. Winterer (2005), Fissure control on volcanic action in the Pacific, Geological Society of America, (Special Paper 388), 687–710.

Nedimovic, M. R., S. M. Carbotte, A. J. Harding, R. S. Detrick, J. Canales, J. B. Diebold, G. M. Kent, M. Tischer, and J. M. Babcock (2005), Frozen magma lenses below the oceanic crust, Nature, 436, 1149 – 1152, doi: 10.1038/nature03,944.

Nishimura, C. E., and D. W. Forsyth (1989), The anisotropic structure of the upper mantle in the Pacific, Geophysical Journal International, 96, 203–229.

Niu, F., and L. Li (2011), Component azimuths of the cearray stations estimated from p-wave particle motion, Earthquake Science, 24(1), 3–13, doi: 10.1007/s11,589–011–0764–8.

Nolet, G., and L. Dorman (1996), Waveform analysis of Scholte modes in ocean sediment layers, Geophysical Journal International, 125, 385–396.

Nooner, S. L., and W. W. Chadwick (2009), Volcanic inflation measured in the caldera of axial seamount: Implications for magma supply and future eruptions, Geochemistry Geophysics Geosystems, 10(2), Q02,002, doi: 10.1029/2008GC002,315.

Nooner, S. L., and W. W. Chadwick (2016), Inflation-predictable behavior and co-eruption deformation at Axial Seamount, Science, 354(6318), 1399 – 1403, doi: 10.1126/science.aah4666.

Olson, P. (1990), Hot spots, swells, and mantle plumes, in Magma transport and storage, edited by M. Ryan, John Wiley.

Olson, P., E. Reynolds, L. Hinnov, and A. Goswami (2016), Variation of ocean sediment thickness with crustal age, Geochemistry Geophysics Geosystems, 17, 1349 – 1369, doi: 10.1002/2015GC006,143.

Orcutt, J. (1987), Structure of the earth: Oceanic crust and the uppermost mantle, Reviews of Geophysics, 25(6), 1177–1196.

Phipps Morgan, J., and Y. J. Chen (1993), The genesis of oceanic crust: Magma injection, hydrothermal circulation, and crustal flow, Journal of Geophysical Research, 98(B4), 6283 – 6297.

Phipps Morgan, J., and D. W. Forsyth (1988), Three-dimensional flow and temperature perturbations due to a transform offset: Effects on oceanic crustal and upper mantle structure, Journal of Geophysical Research, 93(B4), 2955–1966.

Phipps Morgan, J., W. J. Morgan, and E. Price (1995), Hotspot melting generates both hotspot volcanism and a hotspot swell?, Journal of Geophysical Research, 100(B5), 8045–8062.

Purdy, G. M. (1983), The seismic structure of 140 Mya old crust in the western central Atlantic Ocean, Geophysical Journal of the Royal Astronomical Society, 72(115-137).

Raitt, R. W. (1963), The Sea, vol. 3, chap. The crustal rocks, pp. 85–102, John Wiley.

Rees, B., R. Detrick, and B. Coakley (1993), Seismic stratigraphy of the Hawaiian flexural moat, Geological Society of America Bulletin, 105, 189–205.

Reeves, Z., V. Lekic, N. Schmerr, M. Kohler, and D. Weeraratne (2015), Lithospheric structure across the california continental borderland from receiver functions, Geochemistry Geophysics Geosystems, 16, 246–266, doi: 10.1002/2014GC005,617.

Rehm, E., and P. Halbach (1982), Hawaiian-derived volcanic ash layers in equatorial northeastern Pacific sediments, Marine Geology, 50, 25–40.

Rhie, J., and B. Romanowicz (2006), A study of the relation between ocean storms and the earth's hum, Geochemistry Geophysics Geosystems, 7, Q10,004, doi:10.1029/2006GC001,274.

Rhie, J., D. Dolenc, and B. Romanowicz (2008), Long-period seismic nosie at the farallon islands: island's tilting due to infragravity waves as a possible source of earth's horizontal hum, in AGU Abstract S34A-05.

Riedel, K., and A. Sidorenko (1995), Minimum bias multiple taper spectral estimation, IEEE Transactions on Signal Processing.

Riedel, M., M. Cote, P. Neelands, G. Middleton, G. Standen, R. Iuliucci, M. Ulmi, C. Stacey, R. Murphy, D. Manning, C. Brillon, and G. Spence (2014), 2012 haida gwaii mw 7.7 earthquake response - ocean bottom seismometer relocation and geophone orientation analysis and quality control of wide-angle p-wave refraction data, Geological Survey of Canada, Open File 7632, 79pp, doi: 10.4095/295,551.

Ringler, A. T., C. R. Hutt, K. Persefield, and L. S. Gee (2013), Seismic station installation orientation errors at ANSS and IRIS/USGS stations, Seismological Research Letters, 84(6), 926 – 931, doi: 10.1785/0220130,072.

Ritsema, J., and R. Allen (2003), The elusive mantle plume, Earth and Planetary Science Letters, 207, 1 – 12.

Romanowicz, B. (2002), Inversion of surface waves: A review, in International Handbook of Earthquake Engineering Seismology, vol. 81A, edited by W. Lee, H. Kanamori, P. Jennings, and C. Kisslinger, pp. 149–173, Academic Press, Amsterdam.

Romanowicz, B., D. Stakes, D. Dolenc, D. Neuhauser, P. McGill, R. Uhrhammer, and T. Ramirez (2006), The monterey bay broadband ocean bottom seismic observatory, Annals of Geophysics, 49(2/3), 607–623, doi: 10.4401/ag–3132.

Romanowicz, B., P. McGill, D. Neuhauser, and D. Dolenc (2009), Aquiring real time data from the broadband ocean bottom seismic observatory at monterey bay (mobb), Seismological Research Letters, 80(2).

Ruan, Y., D. Forsyth, and S. Bell (2014), Marine sediment shear velocity structure from the ratio of displacement to pressure of Rayleigh waves at seafloor, Journal of Geophysical Research: Solid Earth, 119, 6357–6371, doi:10.1002/2014JB011,162.

Rychert, D., G. Laske, N. Harmon, and P. Shearer (2013), Seismic imaging of melt in a displaced Hawaiian plume, Nature Geoscience, 6, 657–660, doi: 10.1038/ngeo1878.

Sabra, K., P. Gerstoft, P. Roux, W. Kuperman, and M. Feler (2005), Extracting time-domain green's function estimates from ambient seismic noise, Geophysical Research Letters, 32(3), 1–5.

Sambridge, M. (1999a), Geophysical inversion with a neighbourhood algorithm-i, Geophysical Journal International, 138, 479 – 494, doi: 10.1046/j.1365–246X.1999.00,876.x.

Sambridge, M. (1999b), Geophysical inversion with a neighbourhood algorithm-ii, Geophysical Journal International, 138, 727 – 746, doi: 10.1046/j.1365–246x.1999.00,900.x.

Sasagawa, G., M. J. Cook, and M. A. Zumberge (2016), Drift-corrected seafloor pressure observations of vertical deformation at axial seamount 2013–2014, Earth and Space Science, 3, 381 – 385, doi: 10.1002/2016EA000,190.

Sato, H., I. Sacks, and T. Murase (1989), The use of laboratory velocity data for estimating temperature and martial melt fraction in the low-velocity zone: comparison with heat flow and electrical conductivity studies, Journal of Geophysical Research, 94(B5), 5689 – 5704.

Schaff, D. P., and G. C. Beroza (2004), Coseismic and postseismic velocity changes measured by repeating earthquakes, Journal of Geophysical Research, 109(B10302), doi:10.1029/2004JB003,011.

Schmeling, H. (1985), Numerical models on the influence of partial melt on elastic, anelastic and electric properties of rocks. part i: elasticity and anelasticity, Physics of the Earth and Planetary Interiors, 41, 34 – 57.

Schmeling, H., J. P. Kruse, and G. Richard (2012), Effective shear and bulk viscosity of partially molten rock based on elastic moduli theory of a fluid filled poroelastic medium, Geophysical Journal International, 190, 1571 – 1578, doi: 10.1111/j.1365–246X.2012.05,596.x.

Schulte-Pelkum, V., G. Masters, and P. Shearer (2001), Upper mantle anisotropy from long-period p polarization, Journal of Geophysical Research, 106(B10), 21,917–21,934, doi: 10.1029/2001JB000,346.

Sclater, J. G. (2003), Ins and outs on the ocean floor, Nature, 421, 590 – 591.

Selby, N. D. (2001), Association of rayleigh waves using backazimuth measurements: application to test ban treaty verification, Bulletin of the Seismological Society of America, 91(3), 580–593, doi: 10.1785/0120000,068.

Shapiro, N. M., and N. Campillo (2004), Emergence of broadband rayleigh waves from correlations of the ambient seismic noise, Geophysical Research Letters, 31(7), doi: 10.1029/2004GL019,491.

Shaw, P. R. (1994), Age variation of oceanc crust Poisson's ratio: Inversion and a porosity evolution model, Journal of Geophysical Research, 99(B2), 3057 – 3066.

Shearer, P. (1988), Cracked media, poisson's ratio and the structure of the upper oceanic crust, Geophysical Journal International, 92, 357–362.

Shen, Y., D. W. Forsyth, and J. Conder (1997), Investigation of microearthquake activity following an intraplate teleseismic swarm on the west flank of the Southern East Pacific Rise, Journal of Geophysical Research, 102(B1), 459 – 475.

Shor, G., and D. Pollard (1964), Mohole site selection studies north of Maui, Journal of Geophysical Research, 69(8), 1627–1637.

Singh, S. C., W. C. Crawford, H. Carton, T. Seher, V. Combier, M. Cannat, J. P. Canales, D. Dusunur, J. Escartin, and J. M. Miranda (2006), Discovery of a magma chamber and faults beneath a mid-atlantic ridge hydrothermal field, Nature, 442, 1029 – 1032, doi: 10.1038/nature05,105.

Sinton, J. M., and R. S. Detrick (1992), Mid-ocean ridge magma chambers, Journal of Geophysical Research, 97(B1), 197 – 216.

Smith, W. H. F., and D. T. Sandwell (1997), Global sea floor topography from satellite altimetry and ship depth soundings, Science, 277, 1956 – 1962.

Sobolev, S. V., H. Zeyen, G. Stoll, F. Werling, R. Altherr, and K. Fucks (1996), Upper mantle temperatures from teleseismic tomography of French Massif Central including effects of composition, mineral reactions, anharmonicity, anelasticity, and partial melt, Earth and Planetary Science Letters, 139, 147 – 163.

Soule, D. C., and W. S. D. Wilcock (2013), Fin whale tracks recorded by a seismic network on the Juan de Fuca Ridge, Northeast Pacific Ocean, Journal of the Acoustical Society of America, 133(3), 1751 – 1761, doi: 10.1121/1.4774,275.

Spudich, P., and J. Orcutt (1980a), A new look at the seismic velocity structure of the oceanic crust, Reviews of Geophysics and Space Physics, 18(3), 627–645.

Spudich, P., and J. Orcutt (1980b), Petrology and porosity of an oceanic crustal site: Results from wave form modeling of seismic refraction data, Journal of Geophysical Research, 85(B3), 1409–1433.

Stachnik, J., A. Sheehan, D. Zietlow, Z. Yang, J. Collins, and A. Ferris (2012a), Determination of new zealand ocean bottom seismometer orientation via rayleigh-wave polarization, Seismological Research Letters, 83(4), 704–712, doi: 10.1785/0220,110,128.

Stachnik, J. C., A. F. Sheehan, D. W. Zietlow, Z. Yang, J. Collins, and A. Ferris (2012b), Determination of New Zealand ocean bottom seismometer orientation via Rayleigh-wave polarization, Seismological Research Letters, 83(4), 704–712, doi: 10.1785/0220110,128.

Stakes, D., J. McClain, T. VanZandt, P. McGill, and M. Begnaud (1998), Corehole sesimometer development for low-noise seismic data in a long-term seafloor observatory, Geophysical Research Letters, 25(14), 2745–2748.

Stephen, R., J. Kasahara, G. Acton, and S. S. Party (2003a), Volume 200, site 1223, Tech. rep., Proceeedings of the Ocean Drilling Program Initial Reports.

Stephen, R. A. (1988), Lateral heterogeneity in the upper oceanic crust at Deep Sea Drilling Project site 504, Journal of Geophysical Research, 93(B6), 6571 – 6584.

Stephen, R. A., F. N. Spiess, J. A. Collins, J. A. Hildebrand, J. A. Orcutt, K. R. Peal, F. L. Vernon, and F. B. Wooding (2003b), Ocean Seismic Network Pilot Experiment, Geochem. Geopyhs. Geosys., 4(10), 1–38, doi: 10.1029/2002GC000,485.

Sugawara, T. (2000), Empirical relationships between temperature, pressure, and MgO content in olivine and pyroxene saturated liquid, Journal of Geophysical Research, 105(B4), 8457 – 8472.

Sumy, D. F., J. A. Lodewyk, R. L. Woodward, and B. Evers (2015), Ocean-bottom seismograph performance during the Cascadia Initative, Seismological Research Letters, 86, 1238 – 1246, doi: 10.1785/0220150,110.

Sutton, G. H., G. L. Maynard, and D. M. Hussong (1971), The Structure and physical properties of the Earth's Crust, Geophysical Monograph Series, vol. 14, chap. Physical Properties of the Oceanic Crust, pp. 193–209, American Geophysical Union.

Swift, S., and R. Stephen (1989), Lateral heterogeneity in the seismic structure of upper oceanic crust, western north atlantic, Journal of Geophysical Research: Solid Earth, 94(B7), 9303–9322.

Swift, S. A., D. Lizarralde, R. A. Stephen, and H. Hoskins (1998), Velocity structure in upper ocean crust at Hole 504B from vertical seismic profiles, Journal of Geophysical Research, 103(B7), 15,361 – 15,376.

Taira, T., Z. Zheng, and B. Romanowicz (2014), On the systematic long-period noise reduction on ocean floor broadband seismic sensors collocated with differential pressure gauges, Bulletin of the Seismological Society of America, 104(1), 247–259.

Taylor, J. R. (1997), An Introduction to Error Analysis, University Science Book.

Taylor, M. A. J., and S. C. Singh (2002), Composition and microstructure of magma bodies from effective medium theory, Geophysical Journal International, 149, 15 – 21.

ten Brink, U., and T. Brocher (1987), Multichannel seismic evidence for a subcrustal intrusive complex under Oahu and a model for Hawaiian volcanism, Journal of Geophysical Research, 92(B13), 13,687–13,707.

ten Brink, U., and T. Brocher (1988), Multichannel seismic evidence for variations in crustal thickness along the Molokai Fracture Zone in the Mid-Pacific, Journal of Geophysical Research, 93(B2), 1119–1130.

Toomey, D., W. Wilcock, S. Solomon, W. Hammond, and J. Orcutt (1998), Mantle seismic structure beneath the melt region of the east pacific rise from p and s wave tomography, Science, 280, 1224–1227, doi: 10.1126/science.280.5367.1224.

Toomey, D., R. M. Allen, A. H. Barclay, S. W. Bell, P. D. Bromirski, R. L. Carlson, X. Chen, J. A. Collins, R. P. Dziak, B. Evers, D. W. Forsyth, P. Gerstoft, E. E. E. Hooft, D. Livelybrooks, J. A. Lodewyk, D. S. Luther, J. J. McGuire, S. Y. Schwartz, M. Tolstoy, A. M. Trehu, M. Weirathmueller, and W. S. D. Wilcock (2014), The Cascadia Initiative: A sea change in seismological studies of subduction zones, Oceanography, 27(2), 138–150, doi: 10.5670/oceanog.2014.49.

Tucker, M. (1950), Surf beats: sea waves of 1 to 5 min. period, Proceedings of the Royal Society of London, A(202), 565–573.

Turcotte, D., and G. Schubert (2002), Geodynamics, second ed., Cambridge University Press, New York, NY.

Turcotte, D., and G. Schubert (2014), Geodynamics, third ed., Cambridge University Press.

Van Avendonk, H., M. Magnani, D. Shillington, J. Gaherty, M. Hornbach, B. Dugan, M. Long, D. Lizarralde, A. Becel, M. Benoit, S. Harder, L. Wagner, and G. Christeson (2014), Enam: A community seismic experiment targeting rifting processes and post-rift evolution of the mid atlantic us margin, in AGU Fall Meeting Abstracts, T53B-4683.

von Herzen, R., M. Cordery, R. Detrick, and C. Fang (1989), Heat flow and the thermal origin of hot spot swells: The Hawaiian Swell revisited, Journal of Geophysical Research, 94(B10), 13,783–13,799.

Wang, J., W. Chi, R. Edwards, and E. Willoughby (2010), Effects of sea states on seafloor compliance studies, Marine Geophysical Research, 31, 99–107.

Wanless, V. D., and A. M. Shaw (2012), Lower crustal crystallization and melt evolution at mid-ocean ridges, Nature Geoscience, 5, 651 – 655, doi: 10.1038/NGEO1552.

Wathelet, M., D. Jongmans, M. Ohrnberger, and S. Bennefoy-Claudet (2008), Array performances for ambient vibrations on a shallow structure and consequences over vs inversion, Journal of Seismology, 12(1 - 19).

Watts, A., U. ten Brink, P. Buhl, and T. Brocher (1985), A multichannel seismic study of lithospheric flexure across the Hawaiian-Emperor seamount chain, Nature, 315, 105–111, doi:10.1038/315,105a0.

Watts, A. B., and U. S. ten Brink (1989), Crustal structure, flexture, and subsidence history of the Hawaiian Islands, Journal of Geophysical Research, 94(B8), 10,473 – 10,500.

Webb, S. (1992), The equilibrium oceanic microseism spectrum, J. Acoust. Soc. Am., 92(4), 2141–2158.

Webb, S., and W. Crawford (1999), Long-period seafloor seismology and deformation under ocean waves, Bulletin of the Seismological Society of America, 89(6), 1535–1542.

Webb, S., and W. Crawford (2010), Shallow-water broadband OBS seismology, Bulletin of the Seismological Society of America, 100(4), 1770–1778, doi: 10.1785/0120090,203.

Webb, S., X. Zhang, and W. Crawford (1991), Infragravity waves in the deep ocean, Journal of Geophysical Research, 96(C2), 2723–2736.

Webb, S. C. (1998), Broadband seismology and noise under the ocean, Reviews of Geophysics, 36(1), 105–142, doi: 10.1029/97RG02,287.

Wessel, P., and W. H. F. Smith (1991), Free software helps map and display data, Eos Transactions, AGU, 72(441).

Wessel, P., and W. H. F. Smith (1998), New, improved version of the Generic Mapping Tools released, EOS Transactions AGU, 79(579).

Wessel, P., W. H. F. Smith, R. Scharroo, J. F. Luis, and F. Wobbe (2013), Generic mapping tools: Improved version released, Eos Transactions, AGU, 94.

West, M., W. Menke, M. Tolstoy, S. Webb, and R. Sohn (2001), Magma storage beneath Axial volcano on the Juan de Fuca mid-ocean ridge, Nature, 413.

West, M., W. Menke, and M. Tolstoy (2003), Focused magma supply at the intersection of the Cobb hotspot and the Juan de Fuca ridge, Geophysical Research Letters, 30(14), doi: 10.1029/2003GL017,104.

White, R. S., R. S. Detrick, M. C. Sinha, and M. H. Cormier (1984), Anomalous seismic crustal structure of oceanic fracture zones, Geophysical Journal of the Royal Astronomical Society, 79, 779–798.

White, R. S., D. McKenzie, and R. K. O'Nions (1992), Oceanic crustal thickness from seismic measurements and rare earth element inversions, Journal of Geophysical Research, 97(B13), 19,683–19,715.

Wilcock, W., R. P. Dziak, W. W. Chadwick, S. L. Nooner, D. R. Bohnenstiehl, J. Caplan-Auerbach, F. Waldhauser, A. F. Arnulf, C. Baillard, T.-K. Lau, J. H. Haxel, Y. J. Tan, C. Garcia, S. Levy, and M. E. Mann (2018), The recent volcanic history of axial seamount: Geophysical insights into past eruption dynamics with an eye toward enhanced observations of future eruptions, Oceanography, 31(1), 114 – 123, doi: 10.5670/oceanog.2018.117.

Wilcock, W. S. D. (2012), Tracking fin whales in the northeast Pacific Ocean with a seafloor seismic network, Journal of the Acoustical Society of America, 132(4), 2408 – 2419, doi: 10.1121/1.4747,017.

Wilcock, W. S. D., K. M. Stafford, R. K. Andrew, and R. I. Odom (2014), Sounds in the ocean at 1-100 Hz, Annual Review of Marine Science, 6, 117 – 140, doi: 10.1146/annurev–marine–121,211–172,423.

Willoughby, E., and R. Edwards (2000), Shear velocities in cascadia from seafloor compliance measurements, Geophysical Research Letters, 27(7), 1021–1024.

Willoughby, E., K. Latychev, R. Edwards, K. Schwalenberg, and R. D. Hyndman (2008), Seafloor compliance imaging of marine gas hydrate deposits and cold vent structures, Journal of Geophysical Research, 113(B7), doi: 10.1029/2005JB004,136.

Winterer, E., W. Riedel, R. Moberly, J. Resig, L. Kroenke, E. Gealy, G. Heath, P. Brönnimann, E. Martini, and T. Worsley (1971), Volume 7, site 67, Tech. rep., Deep Sea Drilling Project Reports and Publications.

Wolfe, C., S. Solomon, G. Laske, J. Collins, R. Detrick, J. Orcutt, D. Berovici, and E. Hauri (2009), Mantle shear-wave velocity structure beneath the Hawaiian hot spot, Science, 326, 1388–1390.

Wolfe, C., S. Solomon, G. Laske, J. Collins, R. Detrick, J. Orcutt, D. Bercovici, and E. Hauri (2011), Mantle P-wave velocity structure beneath the Hawaiian hotspot, Earth and Planetary science letters, 303, 267–280, doi: 10.1016/j.epsl.2011.01.004.

Wu, C., D. Delorey, F. Brenguier, C. Hadziioannou, E. G. Daub, and P. Johnson (2016), Constraining depth range of s wave velocity decrease after large earthquakes near Parkfield, California, Geophysical Research Letters, 43, 6129–6136, doi:10.1002/2016GL069,145.

Yamada, T., P. G. Okubo, and C. J. Wolfe (2010), Kiholo Bay, Hawai'i, earthquake sequence of 2006: Relationship of the main shock slip with locations and source parameters of aftershocks, Journal of Geophysical Research, 115(B08304, doi: 10.1029/2009JB006657).

Yang, Z., A. Sheehan, J. Collins, and G. Laske (2012), The character of seafloor ambient noise recorded offshore New Zealand: Results from the MOANA ocean bottom seismic experiment, Geochemistry Geophysics Geosystems, 13(Q10011), doi: 10.1029/2012GC004,201.

Yeats, R. S., and Others (1989), Initial reports of the deep sea drilling project, chap. Site 469: Base of Patton Escarpment.

Yoshizawa, K., K. Yomogida, and S. Tsuboi (1999), Resolving power of surface wave polarization data for higher-order heterogeneities, Geophysical Journal International, 138(1), 205–220, doi: 10.1046/j.1365–246x.1999.00,861.x.

Zha, Y., and S. Webb (2016), Crustal shear velocity structure in the Southern Lau Basin constrained by seafloor compliance, Journal of Geophysical Research: Solid Earth, 121, 3220–3237, doi: 10.1002/2015JB012,688.

Zha, Y., S. Webb, and W. Menke (2013), Determining the orientations of ocean bottom seismometers using ambient noise correlation, Geophysical Research Letters, 40(14), 3585–3590, doi: 10.1002/grl.50,698.

Zha, Y., S. Webb, S. Nooner, and W. Crawford (2014a), Spatial distribution and temporal evolution of crustal melt distribution beneath the East Pacific Rise at 9-10 N inferred from 3-D seafloor compliance modeling, Journal of Geophysical Research: Solid Earth, 119, 4517–4537, doi:10.1002/2014JB011,131.

Zha, Y., S. C. Webb, S. Wei, D. Wiens, D. Blackman, W. Menke, R. Dunn, and J. Conder (2014b), Seismological imaging of ridge-arc interaction beneath the eastern lau spreading center from obs ambient noise tomography, Earth and Planetary Science Letters, 408, 194–204, doi: 10.1016/j.epsl.2014.10.019.

Zucca, J. J., D. P. Hill, and R. L. Kovach (1982), Crustal structure of Mauna Loa Volcano, Hawaii, from seismic refraction and gravity data, Bulletin of the Seismological Society of America, 72(5), 1535–1550.